Cosmology and the Dusty Universe via VST ATLAS and ALMA

ANSARINEJAD, BEHZAD

Cosmology and the Dusty Universe via VST ATLAS and ALMA

Behzad Ansarinejad

Abstract: Clustering analyses of the large-scale structure of the Universe provide a powerful tool for testing the current standard model of cosmology (ΛCDM). To this end, we exploit the multi-band optical imaging from the VST ATLAS survey, which covers $\sim 4700\,\mathrm{deg}^2$ of the southern sky. Our main goals are to create a galaxy cluster catalogue and use it to test the predictions of ΛCDM; to use the cross-correlation of various ATLAS galaxy samples with the CMB as a probe dark energy, and to study star formation in the most massive halos in the early Universe which are the progenitors of present-day clusters. We find the ATLAS galaxy cluster catalogue to be more complete than the SDSS RedMapper cluster sample at $z < 0.35$. We use this catalogue to improve the completeness of the Planck SZ cluster sample by identifying 11 SZ sources with no confirmed optical counterparts, for which we obtain spectroscopic redshifts and cluster mass measurements. The ATLAS cluster mass functions prefer a value of $S_8 = \sigma_8\sqrt{\Omega_\mathrm{m}/0.3} = 0.77 \pm 0.03$, which is in good agreement with various other low-redshift analyses of the large-scale structure, but $\sim 2\sigma$ lower than the latest Planck CMB measurement. We then measure the Integrated Sachs-Wolfe (ISW) effect based on the cross-correlation of ATLAS galaxies and the Planck CMB temperature map. Combining our results with previous measurements from SDSS, we detect the ISW signal at 2.6σ at $z < 0.55$, in agreement with the ΛCDM model. However, at $z = 0.68$, we find the measured ISW amplitude to be $\sim 2\sigma$ lower than the ΛCDM predictions. Future confirmation of these results based on SKA, DESI or LSST observations, could open the door to alternatives to dark energy, including modified gravity. Finally, using ALMA observations of four $z > 6$ and two $z \sim 2.5$ sub-mm galaxies, we demonstrate that AGN rather than star formation, are the dominant dust-heating mechanism in these sources.

Cosmology and the Dusty Universe via VST ATLAS and ALMA

Behzad Ansarinejad

A thesis presented for the degree of
Doctor of Philosophy

Centre for Extragalactic Astronomy
Department of Physics
Durham University
United Kingdom

February 2021

Contents

List of Figures

List of Tables

Declaration

The work in this thesis is based on research carried out in the Centre for Extragalactic Astronomy, Department of Physics, Durham University, United Kingdom. No part of this thesis has been submitted elsewhere for any other degree or qualification and it is all my own work unless referenced to the contrary in the text.

The content presented in Chapter 6 and some content appearing in Chapter 2 have been published in:

Ansarinejad B., Mackenzie R., Shanks T., Metcalfe N., "*Cross-correlating Planck with VST ATLAS LRGs: a new test for the ISW effect in the Southern hemisphere*", 2020, MNRAS, 493, 4830.

The author of the thesis was primarily responsible for all aspects of this publication.

The contents of Chapters 3, 4, 5 and 7 are in preparation for submission to MNRAS. The author of this thesis was primarily responsible for all aspects of the work presented in these Chapters.

Acknowledgements

Personal acknowledgements: First and foremost, I would like to thank my parents, Simin Hamed and Mozafar Ansarinejad, for their continuous and unconditional support which enabled me to follow my passion for astronomy. I am also grateful to my uncle, Majid Hamed, for sparking my curiosity into the world of physics at a young age. I would also like to thank my PhD supervisor, Tom Shanks, for always being a source of inspiration, support and motivation. I can never thank you enough for sharing your decades of experience with me and for your patience and dedication in seeing me through my PhD. In addition, I am grateful to my second supervisor, Nigel Metcalfe, as well as Ruari Mackenzie, David Murphy, Rich Beilby and Ben Chehade for teaching me many of the research skills which made this body of work possible. I am also forever grateful to Mathilde Jauzac and Alastair Edge for all their help, inspiration and guidance in preparing me for the next step of my career in Astronomy. I will never forget your generosity and kindness, which inspires me to do my best to help others in the same way in the future. I am also thankful to Peter Draper, Lydia Heck and Alan Lotts for their invaluable help and advice on the high-performance computing and programming aspects of this research.

I would also like to thank the Royal Astronomy Society for their generous travel grant in support of an observing trip to La Silla, which provided valuable data used in this research. I am also thankful to the science and operations teams at La Silla, and Paranal Observatories for their hospitality and expert support during our observing runs. And of course, I would be remiss if I do not mention my Chilean friends Felipe Lobos, Ismael Gaete and Patricio Vial; thank you for keeping me company and introducing me to the best bars Santiago had to offer. Our gatherings were always the best way to end my long observing runs on the Chilean mountains.

I consider myself lucky for having met and worked with so many wonderful members of the Durham astronomy department. I will always be grateful for your friendship, company and the many good memories we shared. Thank you for making the years of my PhD some of

the most enjoyable in my life. Finally, I owe a great deal of gratitude to my dear friend and housemate, Alina Talmantaite, for her continuous moral support and useful discussions on the various topics covered in this thesis.

Software, computing resources & online database: This research has made extensive use of Python 2 & 3 (Van Rossum & Drake Jr 1995; Van Rossum & Drake 2009), IPython (Perez & Granger, 2007), Matplotlib (Hunter, 2007), SciPy (Virtanen et al., 2020), NumPy (van der Walt et al., 2011), pandas (Wes McKinney, 2010), AstroPy (Price-Whelan et al., 2018), as well as TOPCAT & STILTS[1] packages (Taylor, 2005).

This work used the DiRAC@Durham facility managed by the Institute for Computational Cosmology on behalf of the STFC DiRAC HPC Facility (www.dirac.ac.uk). The equipment was funded by BEIS capital funding via STFC capital grants ST/P002293/1 and ST/R002371/1, Durham University and STFC operations grant ST/R000832/1. DiRAC is part of the National e-Infrastructure.

This research has made use of the NASA/IPAC Extragalactic Database, which is funded by the National Aeronautics and Space Administration and operated by the California Institute of Technology, as well as the "Aladin sky atlas" developed at CDS, Strasbourg Observatory, France.

Data & public surveys: Elements of this work are based on observations collected at the European Southern Observatory under ESO programmes 0102.A-0865(C), 0101.A-0851(C) and 0102.A-0865(B).

I would like to thank Matt Hilton and the ACT collaboration for providing me with early access to the AdvACT cluster catalogue, prior to its public release.

Funding for the Sloan Digital Sky Survey IV has been provided by the Alfred P. Sloan Foundation, the U.S. Department of Energy Office of Science, and the Participating Institutions. SDSS-IV acknowledges support and resources from the Center for High-Performance Computing at the University of Utah. The SDSS web site is www.sdss.org.

SDSS-IV is managed by the Astrophysical Research Consortium for the Participating Institutions of the SDSS Collaboration including the Brazilian Participation Group, the Carnegie Institution for Science, Carnegie Mellon University, the Chilean Participation Group, the French Participation Group, Harvard-Smithsonian Center for Astrophysics, Instituto de Astrofísica de Canarias, The Johns Hopkins University, Kavli Institute for the Physics and Mathematics

[1] http://www.star.bris.ac.uk/ mbt/topcat/sun253/index.html

of the Universe (IPMU) / University of Tokyo, the Korean Participation Group, Lawrence Berkeley National Laboratory, Leibniz Institut für Astrophysik Potsdam (AIP), Max-Planck-Institut für Astronomie (MPIA Heidelberg), Max-Planck-Institut für Astrophysik (MPA Garching), Max-Planck-Institut für Extraterrestrische Physik (MPE), National Astronomical Observatories of China, New Mexico State University, New York University, University of Notre Dame, Observatário Nacional / MCTI, The Ohio State University, Pennsylvania State University, Shanghai Astronomical Observatory, United Kingdom Participation Group, Universidad Nacional Autónoma de México, University of Arizona, University of Colorado Boulder, University of Oxford, University of Portsmouth, University of Utah, University of Virginia, University of Washington, University of Wisconsin, Vanderbilt University, and Yale University.

The Pan-STARRS1 Surveys (PS1) and the PS1 public science archive have been made possible through contributions by the Institute for Astronomy, the University of Hawaii, the Pan-STARRS Project Office, the Max-Planck Society and its participating institutes, the Max Planck Institute for Astronomy, Heidelberg and the Max Planck Institute for Extraterrestrial Physics, Garching, The Johns Hopkins University, Durham University, the University of Edinburgh, the Queen's University Belfast, the Harvard-Smithsonian Center for Astrophysics, the Las Cumbres Observatory Global Telescope Network Incorporated, the National Central University of Taiwan, the Space Telescope Science Institute, the National Aeronautics and Space Administration under Grant No. NNX08AR22G issued through the Planetary Science Division of the NASA Science Mission Directorate, the National Science Foundation Grant No. AST-1238877, the University of Maryland, Eotvos Lorand University (ELTE), the Los Alamos National Laboratory, and the Gordon and Betty Moore Foundation.

This publication makes use of data products from the Wide-field Infrared Survey Explorer, which is a joint project of the University of California, Los Angeles, and the Jet Propulsion Laboratory/California Institute of Technology, funded by the National Aeronautics and Space Administration.

Chapter 1

Introduction

1.1 An overview of modern cosmology

The groundwork for our understanding of modern cosmology was laid by Isaac Newton in his 1687 '*Philosophiæ Naturalis Principia Mathematica*'[1], which provided the first description of a universal law of gravity. The inception of modern cosmology however, is often attributed to Albert Einstein's 1917 paper, '*Cosmological Considerations in the General Theory of Relativity*' (Einstein, 1917)[2], which introduced the first relativistic model of the Universe. The notion of a cosmological constant (Λ), which we shall revisit later, was also first introduced in this work in order to satisfy Einstein's assumption that the Universe is static with a uniform matter distribution, by providing a repulsive force which contracts the effects of gravity. However, this model was later shown to be unstable as a slight increase in the density of matter would cause the Universe to contract, while a slight decrease would lead to a runaway expansion.

Observationally, in 1913, Vesto Slipher obtained the first spectroscopic measurement of the Andromeda galaxy (M31), observing a Doppler shift in the spectral lines which indicated the M31 was moving towards us (Slipher, 1913). However, Slipher soon realised that most "spiral nebulae" similar to Andromeda (now known as spiral galaxies) are moving away from the earth based on their redshifted spectra (Slipher 1915; Slipher 1917). Slipher however, did not realise the significance of his observations which provided the first observational evidence for an expanding Universe. It is also believed that Einstein was unaware of Slipher's observations

[1] See Newton (1999) for a modern publication of this work.

[2] English translation: `https://einsteinpapers.press.princeton.edu/vol6-trans/433`, also see O'Raifeartaigh et al. (2017) for a detailed review of this paper.

when assuming a static Universe, as he was developing his model in 1917. Indeed until years later, it remained a matter of great debate (Shapley & Curtis, 1921) whether or not these observed nebulae were distant galaxies separate from our own. This debate was finally settled based on Hubble's observations of Cepheid variables in M31 and M33 galaxies (Hubble, 1925), which provided distances to these galaxies placing them outside of the Milky Way.

In 1929, based on observations of Cepheid variables and radial velocities for a sample of 24 galaxies, Hubble provided the first conclusive observational evidence showing a relationship between galaxy recession velocities and distances (Hubble, 1929). This relationship, which is now known as Hubble's law is given by:

$$v = H_0 \times d, \tag{1.1.1}$$

where v and d are the recession velocity and the distance of an object moving away from the observer due to the expansion of the Universe. Here, the *Hubble constant*, H_0, is the present day value of the *Hubble parameter*, H, with dimensions of inverse time. Over the years, the value of H_0 has been the subject of much debate and as we will discuss later, tensions between measurements of this value obtained using different techniques remain to this day. For this reason, the Hubble constant is often parameterised as:

$$H_0 = 100h \text{ km s}^{-1}\text{Mpc}^{-1}, \tag{1.1.2}$$

with h allowing for adjustments to the value of the Hubble constant in the absence of a consensus on the precise value of H_0.

1.1.1 The expansion history & geometry of the Universe

Hubble's 1929 observations gave credence to Alexander Friedmann's 1922 cosmological model of an expanding Universe, which he derived from Einstein's field equations (Friedmann, 1922)[3]. A similar model was independently developed by Georges Lemaître in which he suggested the Universe began with a big bang (Lemaître, 1927)[4]. Modifications of these models, which were further developed and proved by Howard P. Robertson and Arthur G. Walker in the 1930's (Robertson 1935; Walker 1937), are now known as the Friedmann – Lemaître – Robertson – Walker (FLRW) space-time metric, which can describe a homogeneous, isotropic, expanding Universe, thus providing the best approximation for the observed

[3]See Friedmann (1999) for an English translation.
[4]See Lemaître (1931) for an English translation.

Universe at the time. In *comoving* spherical coordinates (r_c, θ_c and ϕ_c), the FLRW metric takes the form:

$$(ds)^2 = (cdt)^2 - a^2(t)\left[\frac{dr_c^2}{1-kr_c^2} + r_c^2(d\theta_c^2 + \sin^2\theta_c d\phi_c^2)\right], \tag{1.1.3}$$

where ds is the space-time line element, c is the speed of light and $a(t)$ is the *scale factor* of the Universe. The scale factor links the *proper distance*, $d(t)$, between two objects which are moving away from each other due to the expansion of the Universe at time t, to their *comoving distance*, r_c, which remains constant as the Universe expands (as it is defined in a coordinate system expanding at the same rate as the Universe). In effect, $a(t)$ describes the expansion history of the Universe and by definition, the present day (t_0) value of the scale factor is $a(t_0) = 1$. The k term in the FLRW metric is a constant with units of [length]$^{-2}$, which describes the geometry of the Universe, often referred to as the 'curvature'. The three possible spatial geometries of the Universe are: $k > 0$ denoting a spherical geometry or a closed Universe, $k = 0$ giving a flat geometry and Universe or a $k < 0$ curvature, corresponding to an open Universe with hyperbolic geometry.

As the redshift (z) of an object is defined as the ratio of its observed wavelength (λ_{obs}) to its emitted wavelength (λ_{em}), in cases where the object is moving away from the observer due to the expansion of the Universe, (or with the 'Hubble flow'), we can link the redshift of an object with the scale factors of the Universe at the time when the object's light was emitted $a(t_{em})$ and observed $a(t_{obs})$:

$$1 + z \equiv \frac{\lambda_{obs}}{\lambda_{em}} = \frac{a(t_{obs})}{a(t_{em})} = \sqrt{\frac{1+v/c}{1-v/c}}. \tag{1.1.4}$$

The final expression which applies in the special relativistic regime links the redshift of an object to its recession velocity, v, with this relation simplifying to $z = v/c$ in cases where $v << c$. However, there is a second component to the motion of objects referred to as peculiar velocity, v_{pec}. This velocity is due to local gravitational forces acting on the object (e.g. in case of a galaxy residing in a cluster due to the gravitational potential energy of the halo and gravitational forces from nearby galaxies). As a result, the observed redshift of an object is given by $(1 + z_{obs}) = (1 + z_{cos})(1 + z_{pec})$ where z_{cos} is the cosmological redshift of the object due to the expansion of the Universe, while z_{pec} is the Doppler shift due to the object's peculiar velocity (see Appendix 1 of Davis & Scrimgeour (2014) for a derivation of this equation). For the remainder of this Section we assume $z = z_{cos}$, (with $z_{cos} >> z_{pec}$).

We now introduce another set of key cosmological equations, known as the Friedmann equations. These equations were first derived by Alexander Friedmann (Friedmann, 1922) in the framework of general relativity by solving the Einstein field equations (Einstein, 1916). The Friedmann equations link the expansion of space-time to the comoving density ρ, pressure p and geometry of the Universe:

$$H^2(a) = \left(\frac{\dot{a}}{a}\right)^2 = \frac{8\pi G}{3}\rho - \frac{kc^2}{a^2} + \frac{\Lambda c^2}{3}, \tag{1.1.5}$$

$$\frac{\ddot{a}}{a} = -\frac{4\pi G}{3}\left(\rho + \frac{3p}{c^2}\right) + \frac{\Lambda c^2}{3}, \tag{1.1.6}$$

where $H(a)$ is the Hubble parameter, G is the gravitational constant and Λ is a cosmological constant with units of $[\text{length}]^{-2}$. We note that these equations hold under the assumption that we live in an isotropic and homogeneous Universe where on large scales, pressure and matter density are the same everywhere. As we mentioned earlier, the cosmological constant Λ was first introduced by Einstein in order to balance the effect of k and ρ to achieve a static Universe where $H = 0$. We will shortly explore the implications of different values of Λ on the evolution of the Universe.

The density term in the Friedmann equations is composed of two components with $\rho(a) = \rho_{\rm m}(a) + \rho_r(a)$, where the evolution of *matter density*, $\rho_{\rm m}(a)$, with the expansion of the Universe is given by:

$$\rho_{\rm m}(a) = \frac{\rho_{\rm m_0}}{a^3}, \tag{1.1.7}$$

with ρ_{m_0} denoting the present-day value of the matter density, and the *radiation density* evolves with:

$$\rho_{\rm r}(a) = \frac{\rho_{\rm r_0}}{a^4}, \tag{1.1.8}$$

with $\rho_{\rm r_0}$ being the present-day value of the radiation density. The difference in the proportionality of the two densities with the scale factor is due to the fact that as the Universe expands, its total matter content remains constant and the matter density decreases at a rate proportional to the increasing volume; however, in the case of radiation the expansion of space also causes the wavelength of photons to be redshifted to lower energies, introducing a further factor of a which accounts for this additional reduction in the radiation energy density.

The above densities are often expressed as dimensionless quantities, relative to the *critical density* of the Universe, $\rho_{\rm c}$, which is the density required for a flat Universe with the curvature

parameter $k = 0$. The critical density of the present-day Universe is given by:

$$\rho_{\rm c}(t_0) = \frac{3H_0^2}{8\pi G}, \tag{1.1.9}$$

and the *density parameter*, Ω, is defined as:

$$\Omega \equiv \frac{\rho}{\rho_{\rm c}}. \tag{1.1.10}$$

Using the above definition (see also Peebles 1993, pp. 310-321; Hogg 1999, eq. 14), one can express Equation 1.1.5, in terms of redshift and the present-day values of various density parameters (denoted below by the subscript zero):

$$E(z) \equiv \frac{H(z)}{H_0} = \sqrt{\Omega_{\rm m_0}(1+z)^3 + \Omega_{\rm r_0}(1+z)^4 + \Omega_{\rm k_0}(1+z)^2 + \Omega_{\Lambda_0}}, \tag{1.1.11}$$

with

$$\Omega_{\rm m_0} \equiv \frac{8\pi G\rho_{\rm m_0}}{3H_0^2}, \tag{1.1.12}$$

$$\Omega_{\rm r_0} \equiv \frac{8\pi G\rho_{\rm r_0}}{3H_0^2}, \tag{1.1.13}$$

$$\Omega_{\rm k_0} \equiv -\frac{kc^2}{H_0^2}, \tag{1.1.14}$$

$$\Omega_{\Lambda_0} \equiv \frac{\Lambda c^2}{3H_0^2}. \tag{1.1.15}$$

1.1.2 Cosmological distances

In this Section, we define various cosmological distances used in this thesis. These definitions largely follow those given by Hogg (1999), and we refer the reader to this paper and the references therein (in particular Peebles 1993 and Weinberg 1972), for further details and derivations of the cosmological distances presented here. Furthermore, as we assume a flat Universe with $\Omega_{\rm k} = 0$ throughout this thesis, we only present cosmological distances corresponding to this specific case. However, one can find variations of these expressions corresponding to an $\Omega_{\rm k} > 0$ or $\Omega_{\rm k} < 0$ Universe in Hogg (1999) and elsewhere in the literature.

Equipped with Equation 1.1.11, one can obtain the *line-of-sight comoving distance* $r_{\rm c}(z)$ to redshift z using:

$$r_{\rm c}(z) = D_{\rm H}\int_0^z E^{-1}(z)dz, \tag{1.1.16}$$

where $D_{\rm H}$ is the *Hubble distance* given by $D_{\rm H} = c/H_0 = 3000h^{-1}$Mpc.

Another key cosmological distance is the *angular diameter distance*, $D_{\rm A}(z) = l/\theta$, defining the ratio of an object's transverse physical size l, to its observed angular size on the sky θ (in units of radians). In the case of a flat universe, the angular diameter distance is given by:

$$D_{\rm A}(z) = \frac{r_{\rm c}(z)}{1+z}, \tag{1.1.17}$$

(Weinberg 1972, pp. 421–424; Peebles 1993, pp. 325–327; Hogg 1999, eq. 18). Next, we define the *luminosity distance*, $D_{\rm L}(z)$, which links an object's *bolometric luminosity*, L, in units of $[W]$, to its bolometric flux, F, in $[Wm^{-2}]$:

$$D_{\rm L}(z) \equiv \sqrt{\frac{L}{4\pi F}} = (1+z)r_{\rm c}(z) = (1+z)^2 D_{\rm A}(z), \tag{1.1.18}$$

(Weinberg 1972, pp. 420–424; Hogg 1999, eqs. 20, 21). The luminosity distance is also used to define the *distance modulus*, $\mu = m - M$, which is the difference between the *apparent magnitude*, m, of an object (i.e. its observed magnitude), and its *absolute magnitude*, M, (i.e. the apparent magnitude an objected would have if it was observed from a distance of 10 parsecs, assuming no extinction due to dust). The distance modulus is given by:

$$m - M = 5log_{10}\left(\frac{D_{\rm L}(z)}{10pc}\right). \tag{1.1.19}$$

Finally, we define the *comoving volume*, $V_{\rm c}$, (i.e. a volume in which the number density of non-evolving objects locked into Hubble flow is constant at different redshifts). The comoving volume element in redshift dz and solid angle interval $d\Omega$ is given by:

$$dV_{\rm c}(z) = D_{\rm H}\frac{(1+z)^2 D_{\rm A}^2}{E(z)} d\Omega dz. \tag{1.1.20}$$

1.2 ΛCDM: the current standard cosmological model

The ΛCDM model provides the current best description of the expansion history and the large-scale structure features of the Universe. This model, also referred to as the standard model of cosmology, describes the bulk of the matter content of the Universe as a collisionless dark matter with no electromagnetic interactions with ordinary matter, i.e. cold dark matter (CDM). The first evidence for the existence of dark matter came from the observation of the

motion of galaxies in the Coma cluster by Zwicky (1933), which revealed that these galaxies were moving with velocities that are too high for the cluster to remain bound, given the mass of the cluster estimated based on its observed luminous matter. On this basis, Zwicky posited that the missing cluster mass may be in the form of a non-luminous, 'dark matter'. A key piece of observational evidence supporting Zwicky's hypothesis was later discovered by Rubin et al. (1978) whose observation of the flat rotation curve of the Andromeda galaxy pointed to the existence of a dark matter halo encompassing the galaxy which extends further in space than the galaxy's visible component. Later on, multi-wavelength observations and weak lensing analysis of a merging galaxy cluster known as the 'Bullet cluster' (1E 0657-56; Markevitch et al. 2004; Clowe et al. 2004; Clowe et al. 2006) provided additional evidence for the existence of dark matter while providing direct constraints on the dark matter self-interaction cross-section.

The other main component of the ΛCDM model attributes the majority of the energy density of the Universe to a cosmological constant, Λ, which is associated with dark (or vacuum) energy, describing the accelerating expansion of the Universe. The first piece of observational evidence supporting the existence of the cosmological constant causing the accelerated expansion of the Universe came from standard candle observations of type Ia supernovae (SNe Ia) by Riess et al. (1998), finding them to be on average $10 - 15\%$ farther than predicted based on the assumption of a low mass-density Universe with no cosmological constant. These measurements have since been confirmed and improved using alternative calibrations of SNe Ia standard candle distance measurements, using Cephid variables and the tip of the red giant branch (see e.g. Riess et al. 2016; Riess et al. 2019; Freedman et al. 2019). The existence of dark energy has also been confirmed via various other means including observations of the CMB by Planck Collaboration et al. (2020) which estimated the content to of the Universe to be made up of 68.3% dark energy, 26.8% dark matter and 4.9% baryonic matter, in good agreement with distance measurements using the Baryon Acoustic Oscillations (BAO) feature in the clustering of galaxies and quasars (e.g. eBOSS Collaboration et al. 2020). The ΛCDM model has therefore had astonishing success in providing a comprehensive statistical description of the large-scale structure and expansion history of the Universe.

1.2.1 The Cosmic Microwave Background: A powerful tool for cosmology

The analysis of the Cosmic Microwave Background (CMB) is one of the most useful tools in testing different cosmological models. Indeed the discovery of the CMB provided a second

key piece of evidence, which along with the discovery of the expansion of the Universe, led to the widespread acceptance of the inflationary big bang model, providing the basis of ΛCDM. After the big bang, the Universe consisted of a hot, dense plasma in which photons and baryonic matter were coupled together and existed in thermal equilibrium. At this time the interaction between photons and electrons was primarily due to Thompson scattering, while Coulomb interactions between electrons and protons kept protons in thermal equilibrium with radiation. As the Universe expanded, the energy density of the plasma was reduced, allowing electrons and protons to combine and form hydrogen atoms. This in turn permitted photons to stream freely through space resulting in the decoupling of matter and radiation. At this point the Universe became transparent, releasing the radiation that eventually became the CMB shown in Figure 1.1a. On angular scales of $\sim$ 1 degree, the observed temperature anisotropies of the CMB provide a snapshot of the slight inhomogeneities in the distribution of matter in the early Universe. The CMB anisotropies originate during matter-radiation decoupling, with photons moving away from slightly denser regions of space losing a fraction of their energy as they climb out of the gravitational potential of the dense region, leaving them with a slightly lower temperature compared to the average temperature of CMB photons. The opposite effect takes place in case of photons emitted in regions of space with lower than average densities, causing these photons to have slightly higher temperatures than average.

The CMB power spectrum provides a quantitative measure of the relative strength of the CMB anisotropies, as a function of angular separation (or multipole moments l). As such, the CMB power spectrum provides a unique observational signature that needs to be described by any viable cosmological model, making it one of the most important cosmological tools. Measurements of the CMB temperature power spectrum (shown in Figure 1.1b) highlight the success of the ΛCDM model in providing an excellent fit to the observations of CMB by various surveys including the Wilkinson Microwave Anisotropy Probe (WMAP; Hinshaw et al. 2013), Planck (Planck Collaboration et al., 2014b), South Pole Telescope (SPT; Story et al. 2013) and The Atacama Cosmology Telescope (ACT; Das et al. 2014), at a wide range of angular separations.

The observed peaks in the CMB power spectrum are caused by the counteracting forces of gravity and radiation pressure leading to the formation of acoustic oscillations in the plasma of the early Universe. As we will discuss in the next Section, measurements of the positions and amplitudes of these peaks can provide precise constraints on the key parameters of ΛCDM.

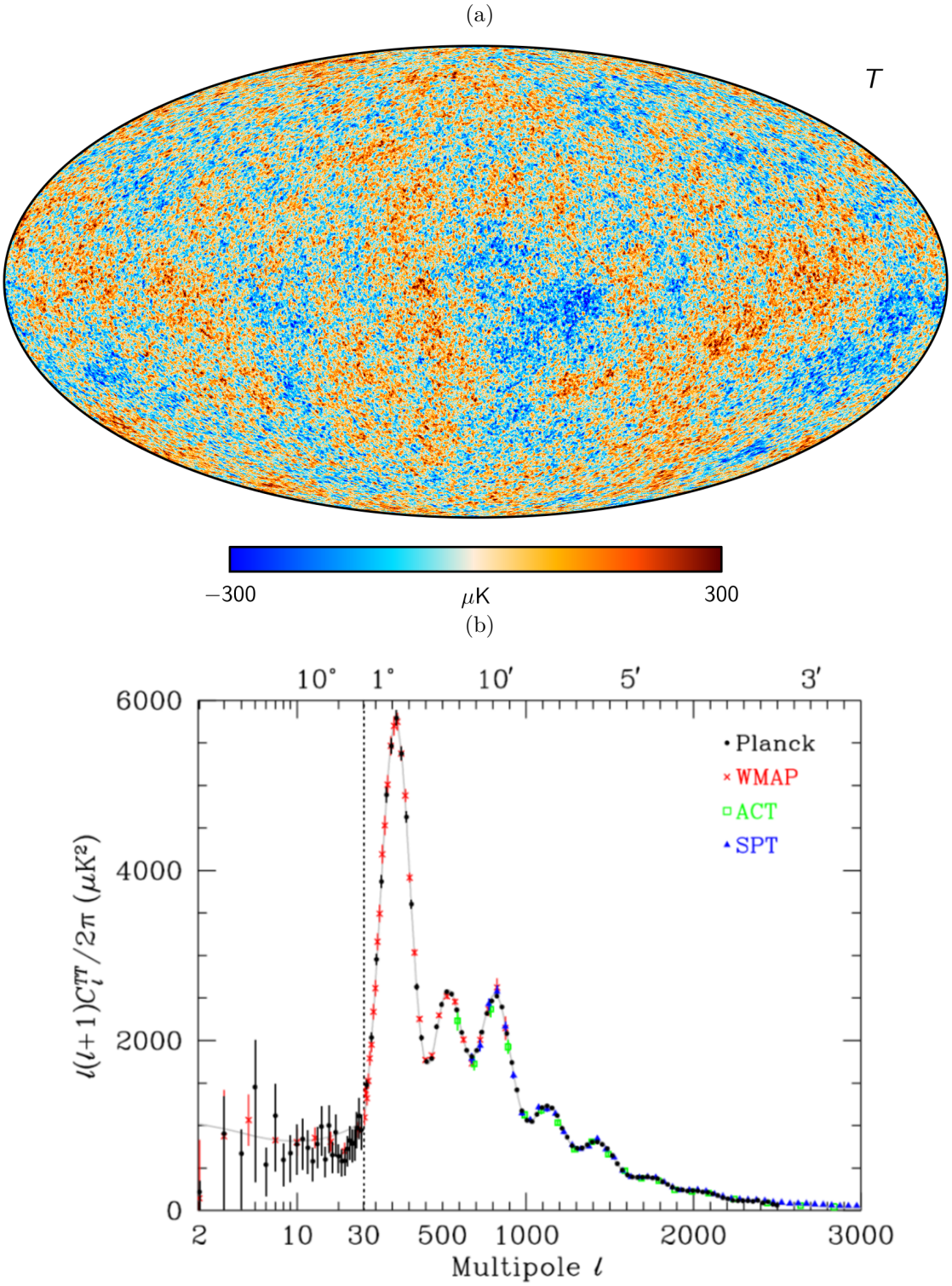

Figure 1.1: (a) The Planck 2018 map of CMB temperature anisotropies based on the CMB component separation of the COMMANDER algorithm. (Figure from Planck Collaboration et al. 2018). (b) Measurements of the CMB temperature power spectrum (TT) by the WMAP, Planck, SPT and ACT collaborations, with the best-fit Planck ΛCDM model shown by the solid curve. The dotted line separates regions of the horizontal axes plotted in linear and logarithmic scales. (Figure from Zyla et al. 2020).

Similar power spectra measurements can be obtained from the CMB polarisation maps which consist of two components (E and B-modes). However, the CMB polarisation anisotropy E-modes are weak relative to the CMB temperature anisotropies, making the E-mode power spectrum harder to measure. The CMB polarisation B-modes have an even lower amplitude than the E-modes, requiring extremely sensitive measurement and careful foreground subtraction which could interfere with this signal. Nonetheless, detection of the CMB B-modes remains a key goal of future CMB experiments, as it can provide the smoking gun evidence for inflation via the detection of signatures of primordial gravitational waves (see, e.g. Abazajian et al. 2015).

1.2.2 Parameters of ΛCDM

The ΛCDM model requires measurements of only six independent parameters to fully define a cosmological paradigm. Although there is some freedom in the choice of these six parameters, CMB measurements (e.g. Planck Collaboration et al. 2020) have provided some of the most precise constraints on the parameters of the ΛCDM model to date[5]. Consequently, the parameters used to define the ΛCDM model are often expressed in terms of quantities which are directly measurable from the observations of CMB.

A key parameter of the standard model is the acoustic scale angle θ_*, which is given by the ratio of the sound horizon (r_s), to the angular diameter distance to the surface of last scattering. The sound horizon is the distance acoustic oscillations of a particular frequency would have travelled to reach maximum compression at the time the CMB radiation was emitted. We can therefore determine r_s by measuring the position of the first acoustic peak in the CMB temperature power spectrum (located at an angular scale of $\sim 0.9°$, see Figure 1.1b). Due to the dependence of the angular diameter distance on the curvature of the Universe Ω_k, the measurements of the position of the first acoustic peak could provide tight constraints on Ω_k. A universe with a positive curvature would have a peak that is shifted to larger angular separations compared to the position of the peak for a flat universe, while a negative curvature would result in the peak being shifted to lower angular separations.

Other defining parameters of the ΛCDM model are the amplitude of the initial curvature perturbations A_s, which is given by the power spectrum amplitude measured at a particular scale, and the scalar spectral index n_s which describes the variation of density fluctuations

[5]However, as we will discuss in Section 1.2.3, there are remaining tensions between the Planck CMB measurements of some of these parameters and those obtained from other cosmological probes.

as a function of angular scale. In other words, the scalar spectral sets the "slope" of the CMB power spectrum as a function of angular separation, with an increase in the value of $n_{\rm s}$, tilting the amplitude of the power spectrum lower at very large angular separations, and higher at very small angular separations. Other parameters of ΛCDM include $\Omega_{\rm b}h^2$ and $\Omega_{\rm c}h^2$, which are the densities of baryonic matter and cold dark matter, (with the total matter density of the Universe given by $\Omega_{\rm m} = \Omega_{\rm b} + \Omega_{\rm c}$). Constraints on these parameters can be obtained from the CMB power spectrum as an increase in $\Omega_{\rm b}$ will lead to an increase in the enhancement of the power spectrum compression peaks (odd-numbered peaks), over rarefaction peaks (even-numbered peaks), (i.e. the second peak would be suppressed relative to the first and the third). Another consequence of an increase in $\Omega_{\rm b}$ would be a decrease in the frequency of the oscillations. On the other hand, an increase in the total matter density $\Omega_{\rm m}$, results in a decrease in the overall amplitude of the CMB power spectrum. As a result, one can determine the ratio of the baryon to dark matter content of the Universe, based on the ratio of the amplitudes of the first and second peaks. The sixth key parameter of ΛCDM measured from the CMB power spectrum is the optical depth to reionization τ, measuring the line of sight free-electron opacity to the surface of last scattering. As the optical depth impacts the level at which the primary CMB anisotropies are scattered as the CMB radiation travels to the observer, higher values of τ result in a reduction of the amplitude of the power spectrum peaks[6].

The Planck 2018 CMB constraints (Planck Collaboration et al., 2020) on the above cosmological parameters are: $\Omega_{\rm b}h^2 = 0.02233 \pm 0.00015$, $\Omega_{\rm c}h^2 = 0.02233 \pm 0.00015$, $100\theta_* = 1.04108 \pm 0.00031$, $\tau = 0.0540 \pm 0.0074$, $\ln(10^{10}A_{\rm s}) = 1.04108 \pm 0.00031$ and $n_{\rm s} = 0.9652 \pm 0.0042$. A final commonly used cosmological parameter is σ_8, which in linear perturbation theory, is the present-day root-mean-square variance of the matter density field averaged over spheres of radius $r = 8h^{-1}$Mpc, (setting the amplitude of the linear matter power spectrum $P(k)$ at a scale of $8h^{-1}$Mpc). The value of σ_8 has a major influence on the determination of the rate of structure growth in the early Universe, with the Planck Collaboration et al. (2020) analysis of the CMB giving a σ_8 constraint of 0.811 ± 0.006. Accurate measurement of this parameter is crucial, as its local value should be consistent with that predicted based on gravitational growth of primordial fluctuations, which are measured using CMB anisotropies. However, as we will see in the next Section, tensions between the early-time measurements of σ_8 (and H_0) from the CMB and their late-time measurements from analyses of the large-scale

[6]For animated illustrations of the impact of variations of the above parameters on the shape of the CMB temperature power spectrum visit: `https://space.mit.edu/home/tegmark/cmb/movies.html`

structure (LSS) have persisted in the past decade, presenting an ongoing challenge for the ΛCDM model.

1.2.3 Challenges to ΛCDM and other unsolved mysteries

We now present a brief overview of a number of current challenges to the ΛCDM model arising from measurements of different cosmological probes at various points during the history of the Universe. Perhaps the greatest remaining challenge to the flat ΛCDM model is the H_0 tension, where a growing number of low redshift measurements of the expansion of Universe have been found to be significantly discrepant from the early-time constraint on H_0 based on the Planck CMB analysis (Planck Collaboration et al., 2020), (for a recent review of the this issue see Verde et al. 2019).

In recent years, increasingly precise measurements of H_0 obtained from probes of expansion in the local Universe and the constraints from CMB experiments, have revealed a statistically significant tension between late and early-time measurements of H_0. The latest distance ladder measurements provided by the 'Supernovae, H0, for the Equation of State of Dark Energy' (SH0ES; Riess et al. 2016; Riess et al. 2018) team have in particular offered improvements on the measurements of expansion rate both in terms of precision and controlling of systematics. As shown in Figure 1.2 combining the SH0ES H_0 measurement of Riess et al. (2019) which is based on observations of Cepheids in the Large Magellanic Cloud (LMC), and the 'H0 Lenses in COSMOGRAIL's Wellspring' (H0LiCOW) collaboration's independent constraint on the expansion rate based on observations of lensed quasars (Wong et al., 2020), results in a 5.3σ tension between late and early-Universe measurements of H_0, with values of 73.8 ± 1.1 and 67.4 ± 0.5 respectively.

Several studies have suggested that the H_0 tension could be in part due to unaccounted systematics in the local or CMB measurements of the expansion rate (e.g. Rigault et al. 2015; Bernal et al. 2016; Addison et al. 2018; Rose et al. 2019; Shanks et al. 2019). However, there is currently no consensus that systematics could entirely explain the tension between the early and late-Universe measurements, as multiple probes with independent systematics produce similar values of H_0 both in the early and local Universe. A solution to the H_0 tension may also come from other independent probes of the expansion rate (or alternative routes to calibrating the local distance ladder), such as analysis of Baryon Acoustic Oscillations (BAO) and galaxy clustering (e.g. eBOSS Collaboration et al. 2020; Abbott et al. 2018b), observations of water masers (e.g. Braatz et al. 2018; Reid et al. 2019), X-ray observations

of SZ clusters (Kozmanyan et al., 2019), the analysis of CMB polarisation (Henning et al., 2018), extra-galactic background light γ-ray attenuation (Domínguez et al., 2019) and gravitational waves standard siren measurements (see, e.g. Chen et al. 2018; Di Valentino et al. 2018; Soares-Santos et al. 2019; The LIGO Scientific Collaboration et al. 2019). Although the precision of H_0 constraints based on these measurements is currently lower than those obtained from SH0ES or Planck, with the availability of larger datasets and higher quality observations, in the future a resolution to the current H_0 tension may emerge from these alternative probes. However, if the H_0 tension persists in future measurements, it could also be indicative of new physics favouring cosmologies beyond the standard flat ΛCDM model.

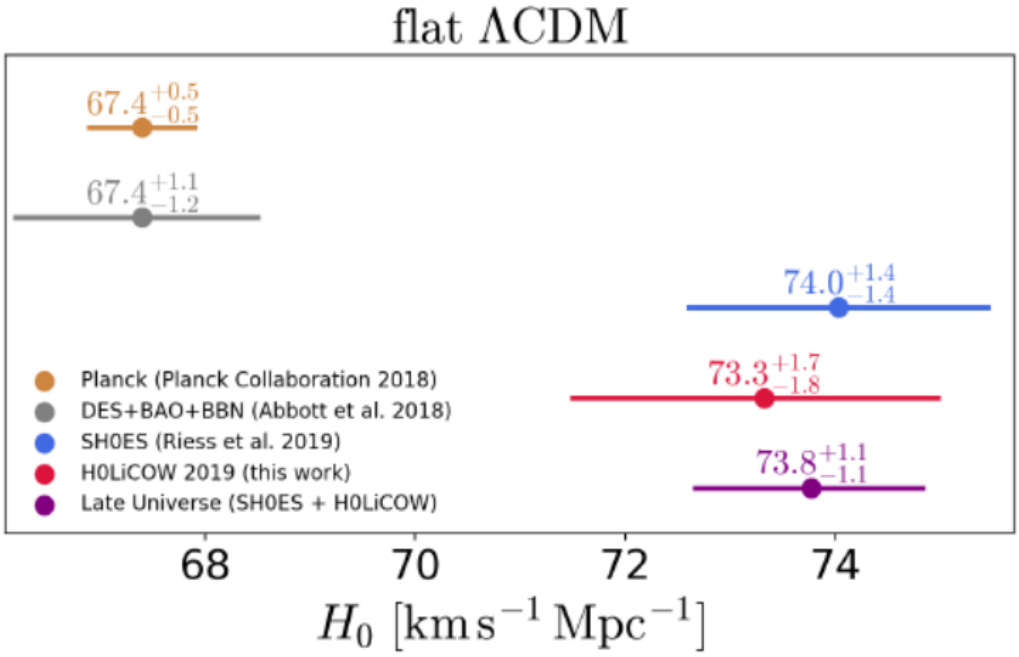

Figure 1.2: Figure 12 of Wong et al. (2020) showing H_0 constraints from early-time Planck Collaboration et al. (2020) CMB and Abbott et al. (2018b) DES clustering, weak lensing, BAO, and big bang nucleosynthesis measurements. Also shown are the H_0 constraints of Riess et al. (2019) based on observations of Cepheids in the Large Magellanic Cloud, as well as Wong et al. (2020) H_0 measurements from lensed quasars. The combination of these two measurements from the late Universe results in a $> 5\sigma$ tension with the H_0 constraint from Planck.

It is also possible to solve the H_0 tension by introducing a dynamical form of dark energy (see, e.g. Copeland et al. 2006; Di Valentino et al. 2017, Figure 1.3; Zhao et al. 2017). The standard parametrisation of the dynamical dark energy equation of state is:

$$\omega(a) = \omega_0 + (1 - a)\omega_a, \tag{1.2.1}$$

where a is the scale factor of the Universe, ω_0 is the present-day value of the equation of state,

and ω_a describes the variation of the equation of state with time, with $\omega = -1$ corresponding to a cosmological constant. Here a value of $w_a < 0$ corresponds to a model where ω increases with a, while $w_a > 0$ means ω becomes more negative with a. For models with $w < -1$, the dark energy density increases with time leading to the expansion of the Universe in excess of the predictions of the cosmological constant, thus providing a resolution to the current H_0 tension (see, e.g. Risaliti & Lusso 2019; Alestas et al. 2020).

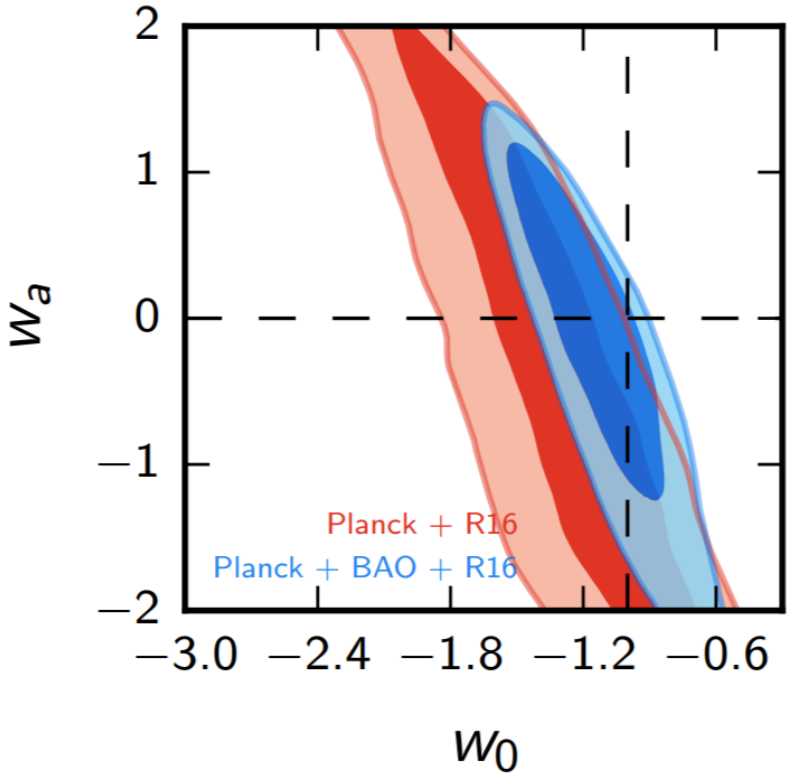

Figure 1.3: Figure 1 of Di Valentino et al. (2017), showing constrains on the dynamical dark energy parameters ω_a and ω_0, based on Planck Collaboration et al. (2016f) CMB analysis, local H_0 constraints of Riess et al. (2016) and combined BAO constraints from the analysis of 6dFGS (Beutler et al., 2011), SDSS (Ross et al., 2015) and BOSS (Anderson et al., 2014) galaxy samples. The cross corresponds to values of ω_a and ω_0 in the standard ΛCDM model with the dark energy equation of state $\omega = -1$ corresponding to a cosmological constant.

In the past decade, another challenge to the ΛCDM model has emerged in the form of a statistically significant tension between the CMB and late-Universe constraints on σ_8. An early indication of this tension came from the comparison of the Planck σ_8 constraints based on the analysis of SZ cluster counts and the CMB (see Figure 1.4a; Planck Collaboration et al. 2014d; Planck Collaboration et al. 2016d). This discrepancy could be as high as 3.7σ depending on the chosen method of calibrating the Planck SZ cluster masses.

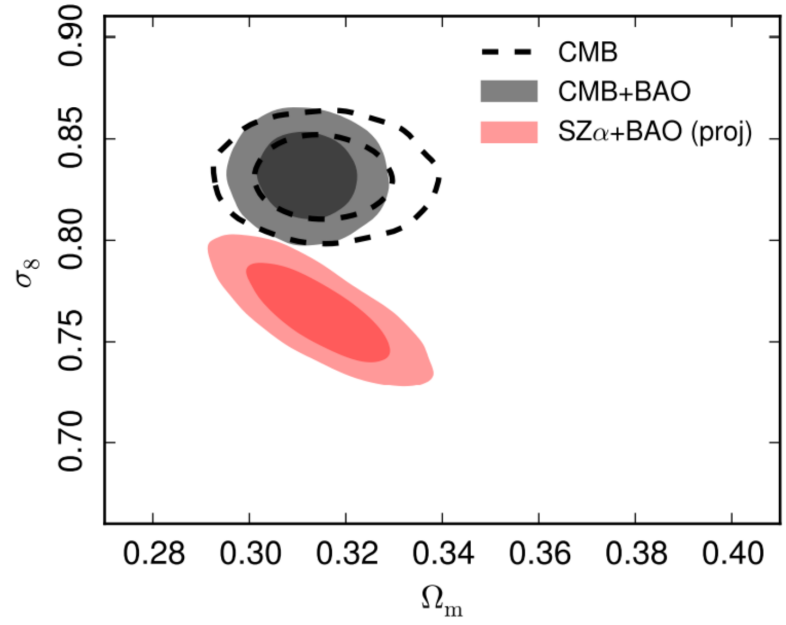

(a)

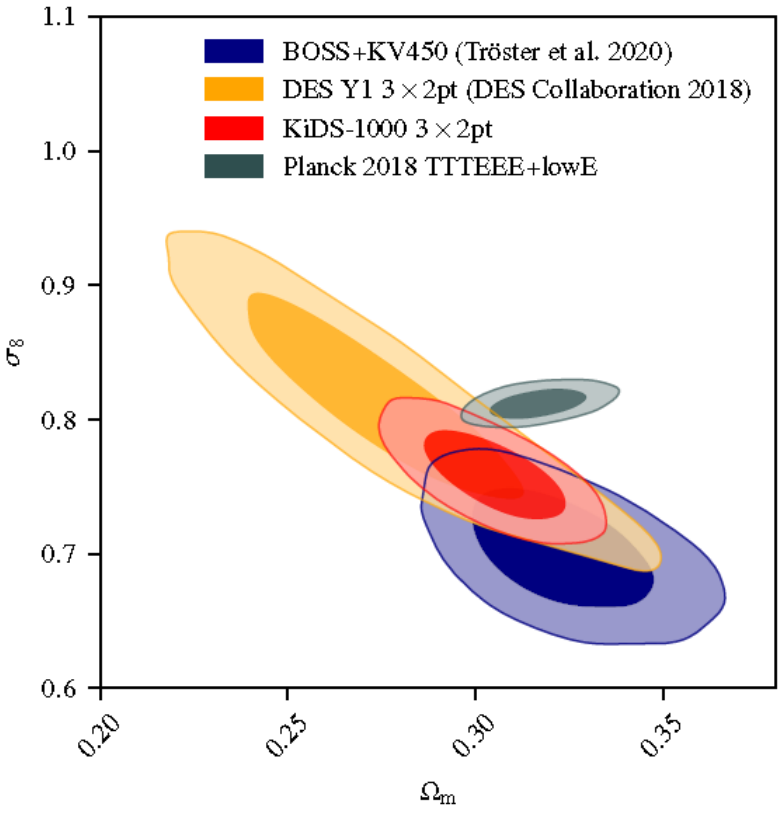

(b)

Figure 1.4: (a) Figure 13 of Planck Collaboration et al. (2016d) showing the tension between the combined Planck SZ cluster count and BAO constraint on σ_8, and the measurement based on the Planck CMB analysis. (b) Figure 8 of Heymans et al. (2020) showing the tension between the Planck CMB (Planck Collaboration et al., 2020) constraints on σ_8, and the weak lensing and galaxy clustering constraints from the KiDS (Heymans et al., 2020) and DES (Abbott et al., 2018b) surveys, as well as those from joint analysis of BOSS and KiDS surveys (Tröster et al., 2020).

However, as shown in Figure 1.4b, recent low redshift measurements of σ_8 including the KiDS-1000 galaxy clustering and weak lensing (3×2pt) analysis of Heymans et al. (2020), the DES Year 1 3×2pt analysis of Abbott et al. (2018b) and the joint BOSS and KiDS-450 analysis of Tröster et al. (2020) remain in tension with the results of the Planck CMB analysis. In Chapters 4 and 5 we present discussions of potential systematics[7] that could be responsible for the σ_8 tensions. The σ_8 tension, however, could also be an indication of new physics, requiring modifications to the standard model. For instance, a solution to both σ_8 and H_0 tensions could come from interactions between dark matter and dark energy (Di Valentino et al., 2020a), while Kreisch et al. (2020) suggest neutrino self-interactions as a joint solution to both tensions.

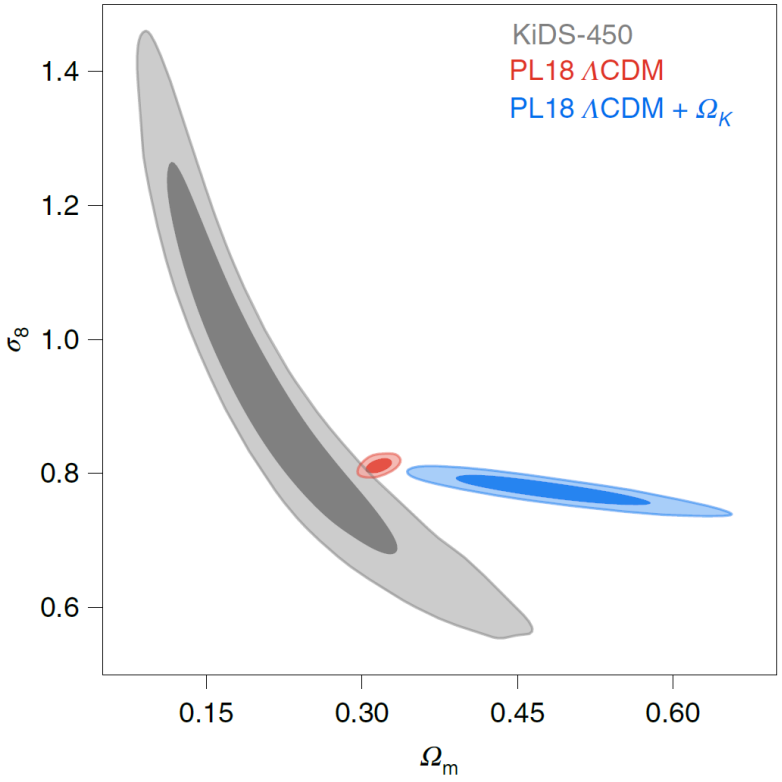

Figure 1.5: Figure 6 of Di Valentino et al. (2020b) showing the increased tension between the Planck 2018 σ_8-Ω_m constraints (red contours) and the weak lensing constraints from the KiDS-450 (Hildebrandt et al., 2017) cosmology (grey contours) as a result of incorporating Ω_k in the Planck analysis (blue contours). Here the contours represent the 1 and 2σ error regions.

[7]For an interesting discussion of the potential interplay between the H_0 and σ_8 tensions see Sanchez (2020) who suggests that expressing σ_8 in units of h^{-1}Mpc could be in part responsible for aggravating the tension between local and early Universe constraints on this parameter. Instead, the author recommends expressing the amplitude of the matter power spectrum as σ_{12} (i.e. the mass fluctuation in spheres of 12Mpc in radius). We note, however, that Heymans et al. (2020) found a similar tension between their low redshift constraints on σ_{12} and those given by the Planck analysis.

Another challenge to the flat ΛCDM model is highlighted by a recent work by Di Valentino et al. (2020b), where they suggest that the enhanced lensing amplitude observed in the Planck 2018 (PL18) CMB power spectra result in a preference for a closed universe with ($\Omega_K < 0$) at a confidence level of 99.985%. As shown in Figure 1.5 the inclusion of Ω_k in the PL18 analysis results in an increased tension between the late and early-Universe constraints on the σ_8-Ω_m parameter space (in the case of KiDS-450 and PL18 comparison, increasing the tension from 2.3σ to $> 3.5\sigma$). The inclusion of Ω_k in the PL18 analysis also results in significant tensions with lower redshift BAO measurements. The authors consequently suggest that the assumption of a flat Universe may be masking a possible crisis for the ΛCDM model, making this a vital topic of research for future CMB experiments which can determine if the observed enhancement of the lensing amplitude is due to undetected systematics or a statistical fluctuation, or indicative of deviations from a flat ΛCDM model.

Another conundrum facing the ΛCDM model, often referred to as the *fine-tuning* or *cosmological constant problem*, arises as the observed value of Λ is 120 orders of magnitude smaller than the theoretical prediction from quantum field theory, with large amounts of fine-tuning of initial conditions required to explain the late-time accelerating expansion of the Universe (see Weinberg 1989; Adler et al. 1995; Carroll 2001; Sahni 2002). Although there are many proposed solutions to this problem, including invocation of the anthropic principle (e.g. Banks et al. 2001; Garriga & Vilenkin 2001), scalar field models of dark energy (Copeland et al., 2006); modified gravity models (e.g. Sotiriou & Faraoni 2010; Bamba et al. 2012; Clifton et al. 2012) and cosmological model beyond ΛCDM (e.g. Bull et al. 2016; Marsh 2016). However, the community is yet to achieve a consensus on a resolution to this conundrum.

1.3 Thesis motivation and outline

The first aim of this thesis is to test the predictions of the standard model against the observed clustering of the large-scale structure (LSS) of the Universe. To this end, we make use of data from the recently completed VST ATLAS survey, which is described in Chapter 2. The ATLAS survey provides multi-band optical coverage of large, previously unmapped areas of the Southern sky, making it an ideal dataset for performing cosmological tests based on analysis of the LSS. We then compare our results to the predictions of the standard model, as well as those obtained from other datasets.

In Chapter 3, we introduce a new cluster catalogue obtained in the VST ATLAS survey. We present details of our cluster richness and photometric redshift estimation and assess the

completeness and purity of our sample by comparing it to other optical, SZ and X-ray cluster samples.

In Chapter 4, we present our spectroscopic observations and cluster mass estimates for a sample of previously unidentified Planck SZ sources with counterpart optical detections in the VST ATLAS cluster catalogue.

In Chapter 5, we present details of the calibration of the ATLAS cluster mass-richness scaling relation based on comparison to external optical, X-ray and SZ cluster masses. We then compare the mass functions of our clusters to those obtained from other optical and SZ samples, and the predictions of ΛCDM at different redshifts.

In Chapter 6, we obtain new measurements of the Integrated Sachs-Wolfe (ISW) effect (which probes the late time accelerating expansion of the Universe), based on the cross-correlation of various ATLAS galaxy samples and the Planck CMB temperature map. We then compare our results with previous measurements from the SDSS survey as well as the predictions of the ΛCDM model at different redshifts.

In Chapter 7, we exploit ALMA observations of our samples of $z > 6$ and $z \sim 2$ sub-mm galaxies in order to calculate their star formation rate surface densities. We then use these measurements as a proxy to identify whether AGN or star formation is the dominant fueling mechanism of these sources.

We conclude this thesis in Chapter 8 by presenting a summary and discussion of the cosmological implications of our findings, as well as the scope for future work.

Chapter 2

The VST ATLAS survey

2.1 Introduction

The VST ATLAS (Shanks et al., 2015) is an European Southern Observatory (ESO) public survey of the southern sky, designed to provide optical imaging in *ugriz* bands to similar depths as The Sloan Digital Sky Survey (SDSS; Eisenstein et al. 2011) in the north. The data is taken using the Very Large Telescope (VLT) Survey Telescope (VST; Schipani et al. 2012) a 2.61-m telescope with a $1\,\mathrm{deg}^2$ field of view located at the Paranal observatory. The telescope is equipped with the 268 megapixel OmegaCAM camera (Kuijken, 2011), composed of a mosaic of 32 CCDs. Figure 2.1 shows a comparison of the VST ATLAS and SDSS *ugriz* band transmission curves. The VST and Sloan telescopes have a similar throughput in *ugri* bands, while the VST z band has a throughput approximately twice that of the Sloan telescope.

The processing of the raw data is performed by the Cambridge Astronomy Survey Unit (CASU[1]), providing catalogues with $\sim 5\sigma$ detections, fixed aperture fluxes and morphological classifications which we use for star-galaxy separation. The CASU morphological classification relies on the curve of growth of each detected source (i.e. variations in the object's brightness with varying aperture size) as described in detail in Section 3.1 of González-Solares et al. (2008). The data provided by CASU is de-biased using nightly calibration images and flat-fielding is performed using monthly stacked twilight sky flats. The CASU sky estimation is performed using an automatic 2-D background following algorithm, as described in section

[1] `http://casu.ast.cam.ac.uk/`, we also refer the reader to `http://casu.ast.cam.ac.uk/surveys-projects/vst/technical/catalogue-generation` for additional information on the source catalogue parameters provided in by CASU.

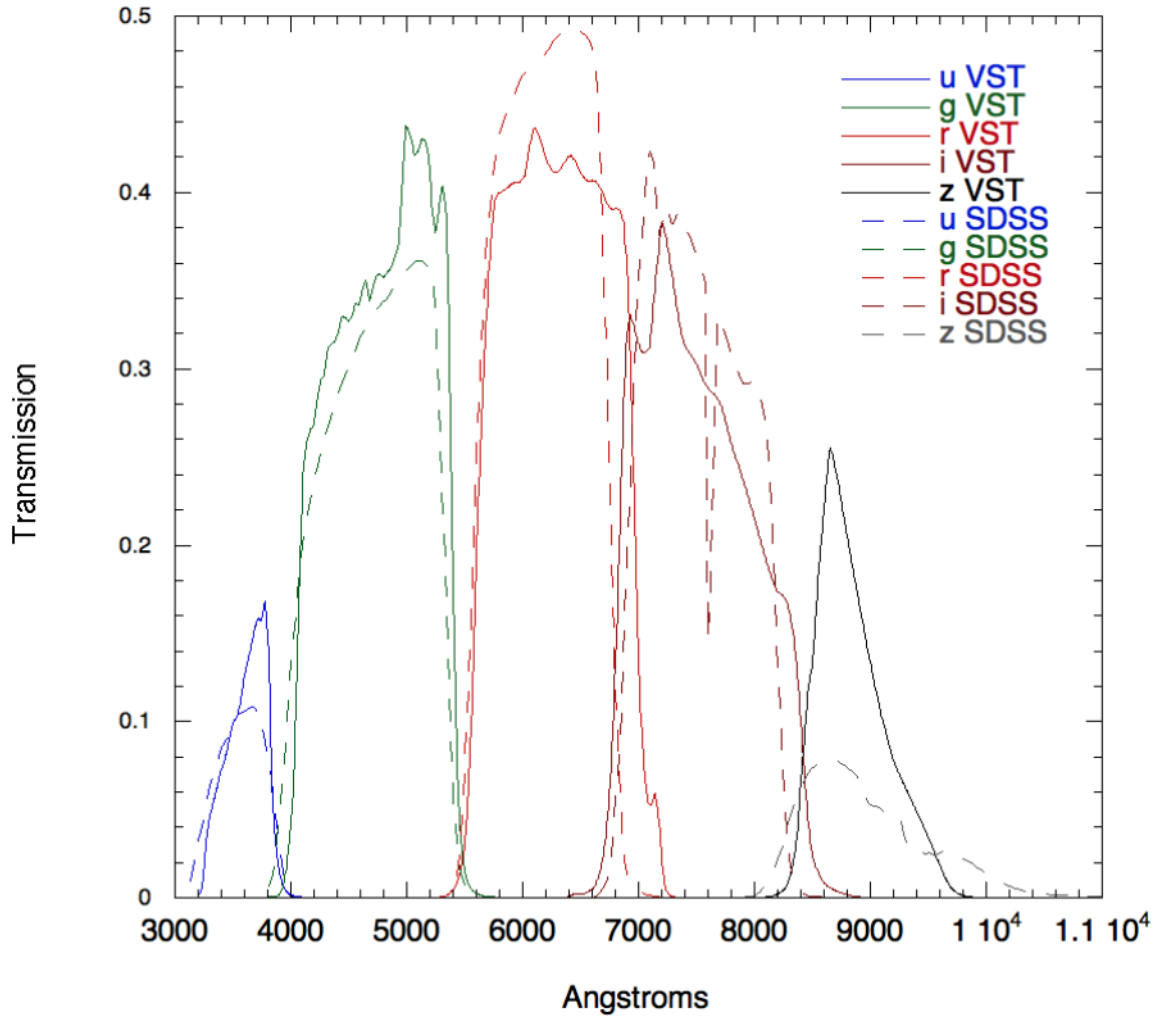

Figure 2.1: Filter, telescope and atmosphere corrected transmission curves, calculated at airmass of 1.3, for the VST ATLAS and SDSS *ugriz* bands. Figure from Shanks et al. (2015).

3 of González-Solares et al. (2008). Further details of the CASU data reduction pipeline and VST ATLAS zero-point calibration are provided in Shanks et al. (2015) and improved global photometric calibration using the Gaia survey (Gaia Collaboration et al., 2018) is now publicly available with the fourth Data Release (DR4) of the survey[2].

2.2 Survey coverage & observing strategy

The total survey area consists of 4711 deg^2, with 2087 deg^2 in the NGC and 2624 deg^2 in the SGC. Figure 2.2 shows the coverage of the VST ATLAS survey compared to the DES (The Dark Energy Survey Collaboration, 2005), DESI (DESI Collaboration et al., 2016), KiDS (de

[2]https://www.eso.org/sci/publications/announcements/sciann17211.html

Jong et al., 2013) and eROSITA (Merloni et al., 2012) surveys. In the future, the 4MOST (de Jong et al., 2019), Euclid (Laureijs et al., 2011) and LSST (LSST Dark Energy Science Collaboration, 2012) surveys will also provide multi-wavelength imaging and spectroscopic coverage of the VST ATLAS survey area. The survey is now complete in *ugriz* in both galactic caps, while an ongoing Chilean observing program will double the *u*-band exposure over the full survey footprint[3].

Figure 2.3 shows an example of a VST ATLAS r-band image, composed of images taken by OmegaCAM's 32 CCD chips, covering a 1 deg^2 area. The CCD gaps are covered by taking two sub-exposures for each tile, with a dither of 25″ in RA and 85″ in DEC. This approach also removes the impact of cosmic rays and bad pixels. The *u* and *g*-band exposures consist of 2×60s and 2×50s stacked sub-exposures, respectively, while *riz*-band stacks are composed of 2×45s sub-exposures.

The ATLAS observations are taken in blocks of 17 tiles (or a concatenation) in the RA direction while keeping DEC constant, with a 2′ overlap in RA and DEC between tiles. For all ATLAS bands, the seeing and airmass are required to be $< 1.4''$ and < 1.4, respectively, while observing conditions are required to be $< 10\%$ cloud cover, with transparency variations of $< 10\%$.

2.3 ATLAS seeing and magnitude limits

Figure 2.4 shows the seeing histograms of the ATLAS g, r, i and z bands. Table 2.1 summarises the median ATLAS and SDSS seeing in these bands and compares the magnitude limits of the two surveys. (Note that we do not show similar information for the *u*-band as it is not used in the analysis of this thesis).

2.4 Band-merged catalogue generation

Based on the ATLAS DR4 data, we produce a band-merged *griz* catalogue[4] using a pipeline developed with the 'Starlink Tables Infrastructure Library Tool Set' (STILTS; Taylor 2006)

[3]The latest survey progress maps are available at `http://astro.dur.ac.uk/Cosmology/vstatlas/`

[4]For each 1 deg^2 ATLAS tile, CASU provides catalogues of the detected sources in separate bands (often observed on different nights). The band merging process is therefore performed independently of CASU to generate a source catalogue containing data from all ATLAS bands, prior to using the data for the analysis of this thesis. Here, the band-merged catalogue refers to a fits table where each row contains relevant information for a detected object, including the object's measured magnitudes and morphological classifications in different bands (which are presented in the columns of the table).

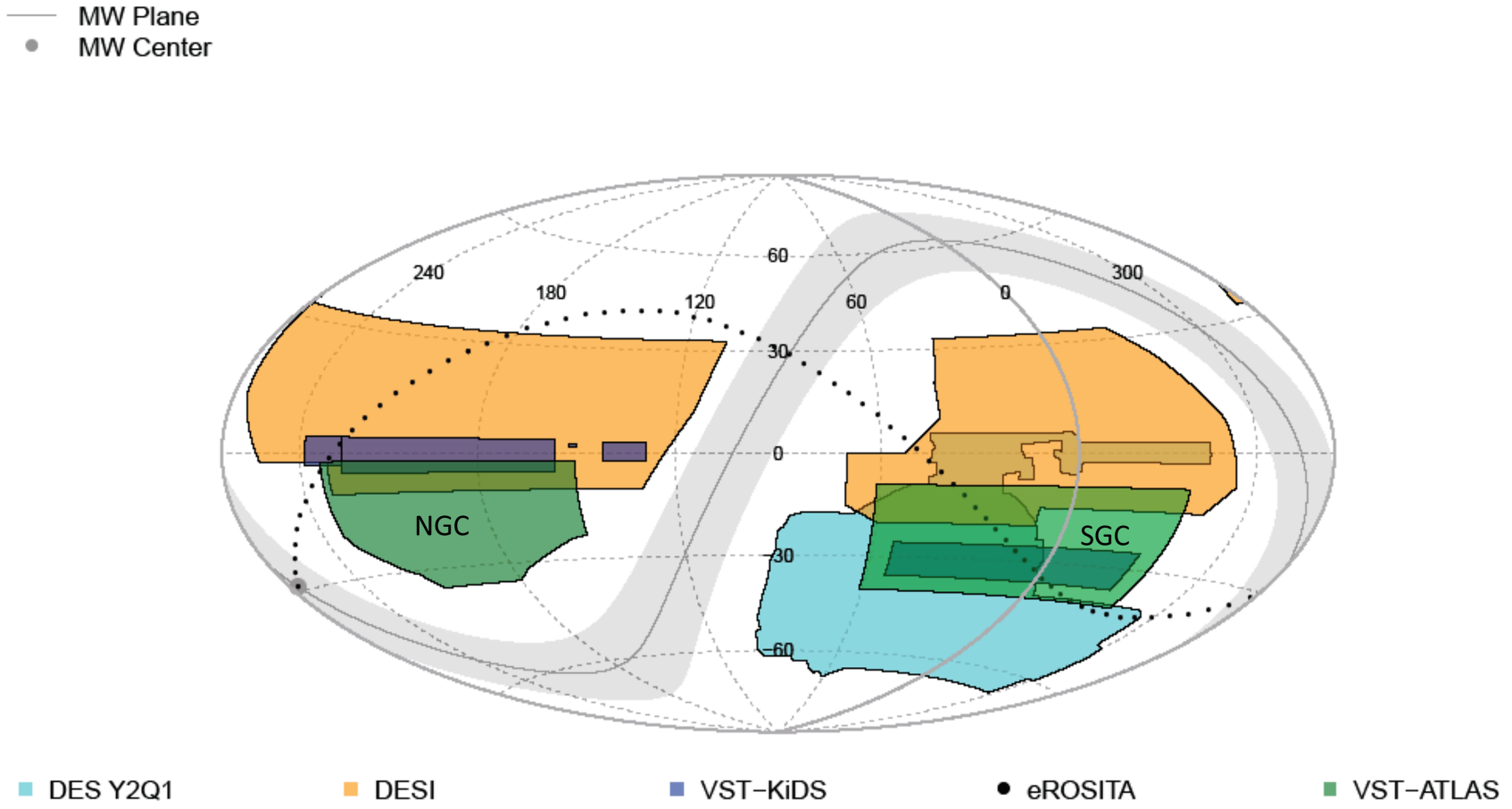

Figure 2.2: Coverage map of the VST ATLAS in comparison to the DES, DESI VST-KiDS and eROSITA surveys. The dotted line separates the German and Russian halves of the eROSITA survey, with the Milky Way galactic plane shown by the grey region. Figure generated with AstroMap (`http://astromap.icrar.org`).

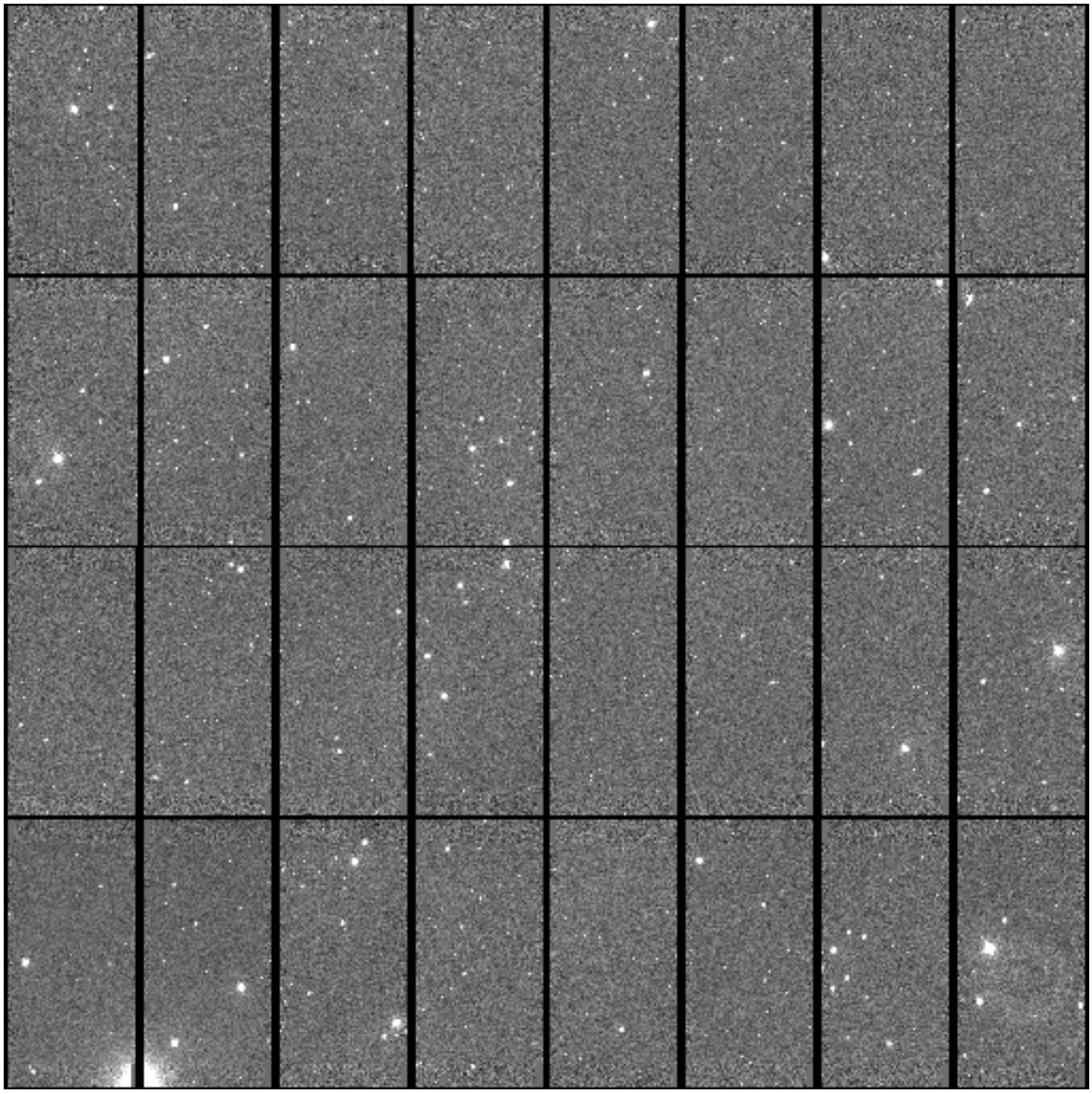

Figure 2.3: Example of an ATLAS r-band tile (o20120114_00055) with 0.9″ seeing. The gaps between the 32 OmegaCAM CCD chips are covered by a second exposure with a 25″ × 85″ dither in RA and DEC. The two exposures are then stacked to provide the final image for each tile.

framework. The pipeline first merges the CASU *griz*-band catalogues on a tile by tile basis, keeping a subset of relevant columns from the tables for each object. During band-merging, we include all objects with detections in a minimum of two bands. We then concatenate the band-merged catalogues generated for the individual tiles and remove duplicate detections of the same objects in the tile overlap areas based on an internal match with a radius of 0.7″.

In this work, we utilise the VST ATLAS aperture magnitudes provided by CASU for obtaining galaxy colours while relying on the CASU Kron pseudo-total magnitude for imposing magnitude limits on our galaxy samples. The ATLAS Kron magnitudes are measured using

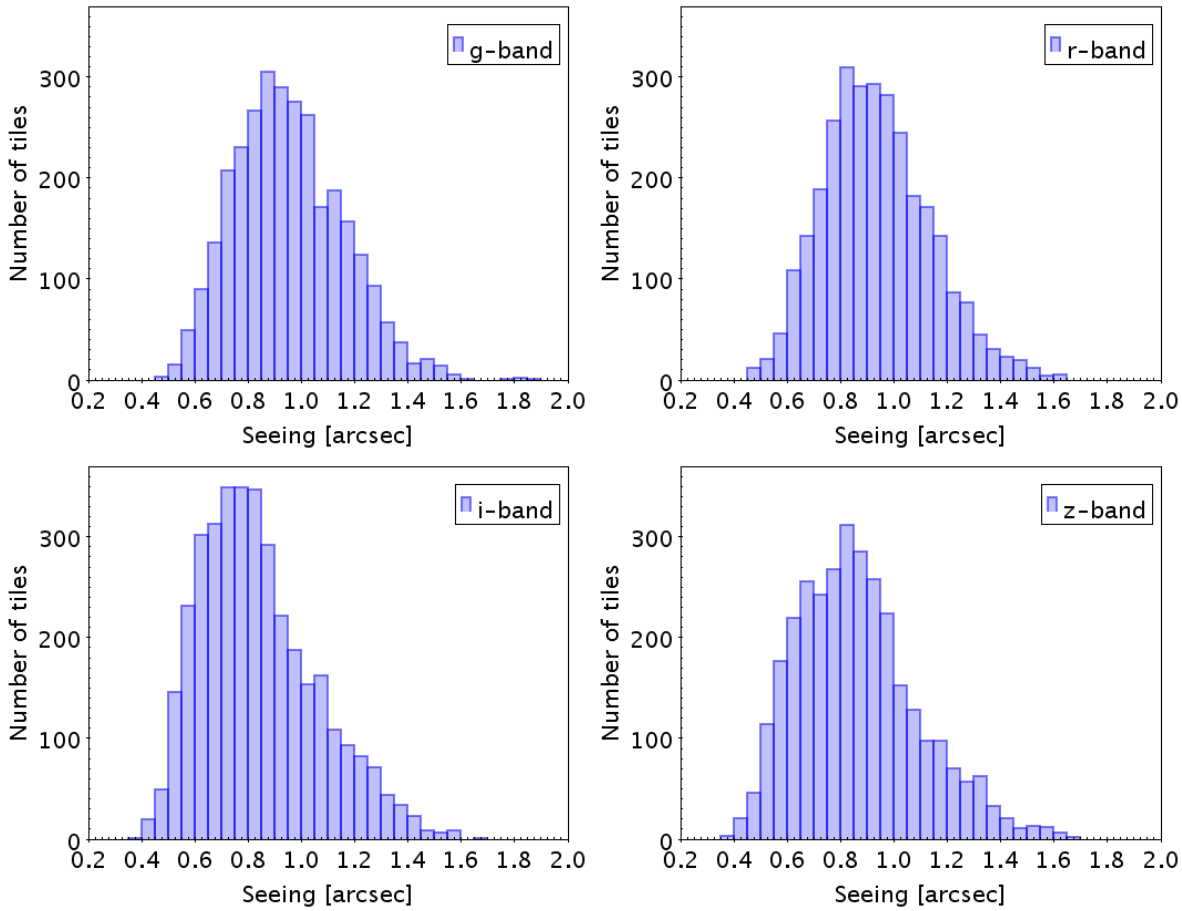

Figure 2.4: Seeing distributions of the VST ATLAS g, r, i and z bands. Bins are 0.05 arcsecs in width.

Band	g	r	i	z
ATLAS Seeing [″]	0.99	0.96	0.84	0.87
SDSS Seeing [″]	1.36	1.24	1.18	1.20
ATLAS Mag. Lim.	22.7	22.2	21.4	20.2
SDSS Mag. Lim.	22.7	22.3	21.7	20.1

Table 2.1: Comparison of VST ATLAS and SDSS median seeing in g, r, i, z bands. Also shown are the ATLAS median 5σ magnitude limits for galaxies and SDSS 5σ point source magnitude limits, with all magnitudes given in the AB system. All values presented here are taken from Table 1 of Shanks et al. (2015), with the exception of ATLAS seeing values which have been updated to include the latest observations.

circular apertures of $2\times$ the Kron radius, with the definition of the Kron radius given by Bertin & Arnouts (1996). The use of Aperture magnitudes to measure galaxy colours was motivated by the inspection of the red-sequence of rich, spectroscopically confirmed Abell clusters as well as comparison of galaxy colours between ATLAS Kron and Aperture magnitudes and SDSS model magnitudes in a ~ 200 deg^2 overlap area between the two surveys. These tests showed that aperture magnitudes have a lower level scatter than Kron around

the red-sequence and when compared to SDSS. This is most likely due to fact that unlike aperture magnitudes which are measured within fixed radii, for individual objects Kron radii can vary in different bands making the colour measurements noisier. On the other hand comparison between ATLAS and SDSS shows that Kron magnitudes provide a more reliable measure of the galaxies' total magnitudes compared to aperture magnitudes, which could miss a larger fraction of the galaxy flux (see also Shanks et al. 2015). We denote aperture magnitudes corresponding to the ATLAS `Aperture flux 3`, and `Aperture flux 5` using subscripts 'A3' and 'A5'. These apertures have radii of 1 and 2″ respectively and we apply their associated aperture corrections labelled as `APCOR` in the CASU catalogue. For g, r, i and z bands, the mean values of `APCOR3` are 0.45, 0.42, 0.35 and 0.38 mags, while mean values of `APCOR5` are 0.12, 0.12, 0.11 and 0.12 mags. Although these aperture corrections are derived for stars, they also provide a first-order seeing correction for faint galaxies, and overall, we find that aperture magnitudes appear to give the most consistent galaxy colours compared to SDSS model magnitudes. Where Kron pseudo-total magnitudes are used, we correct these to total magnitude for galaxies by applying a -0.15 offset. This value is chosen based on an empirical comparison of the ATLAS Kron and SDSS model magnitudes for galaxies in an overlap area between the two surveys as shown by Shanks et al. (2015).

We correct all magnitudes for Galactic dust extinction $A_{\rm x} = C_{\rm x} E(B-V)$, with x representing a filter ($griz$), taking the SDSS $C_{\rm x}$ values presented in Schneider et al. (2007) (3.793, 2.751, 2.086, and 1.479 for $griz$ respectively) and using the Planck $E(B-V)$ map (Planck Collaboration et al. 2014a).

2.4.1 Morphological classifications

In order to isolate galaxies from stars in the ATLAS data, we use the default morphological classifications supplied in CASU catalogues (see the top panel of Figure 2.5), a description of which can be found in González-Solares et al. (2008). The performance of the CASU morphological classification is reduced at fainter magnitudes, approaching magnitude limits of the survey. In such cases, plots of ATLAS Aperture vs. Kron magnitudes, in which stars and galaxies appear as distinct populations, can be used to further remove stellar contamination from galaxies. In the upcoming chapters, we explicitly mention the cases where this approach is implemented to further improve on the star-galaxy separation provided by CASU.

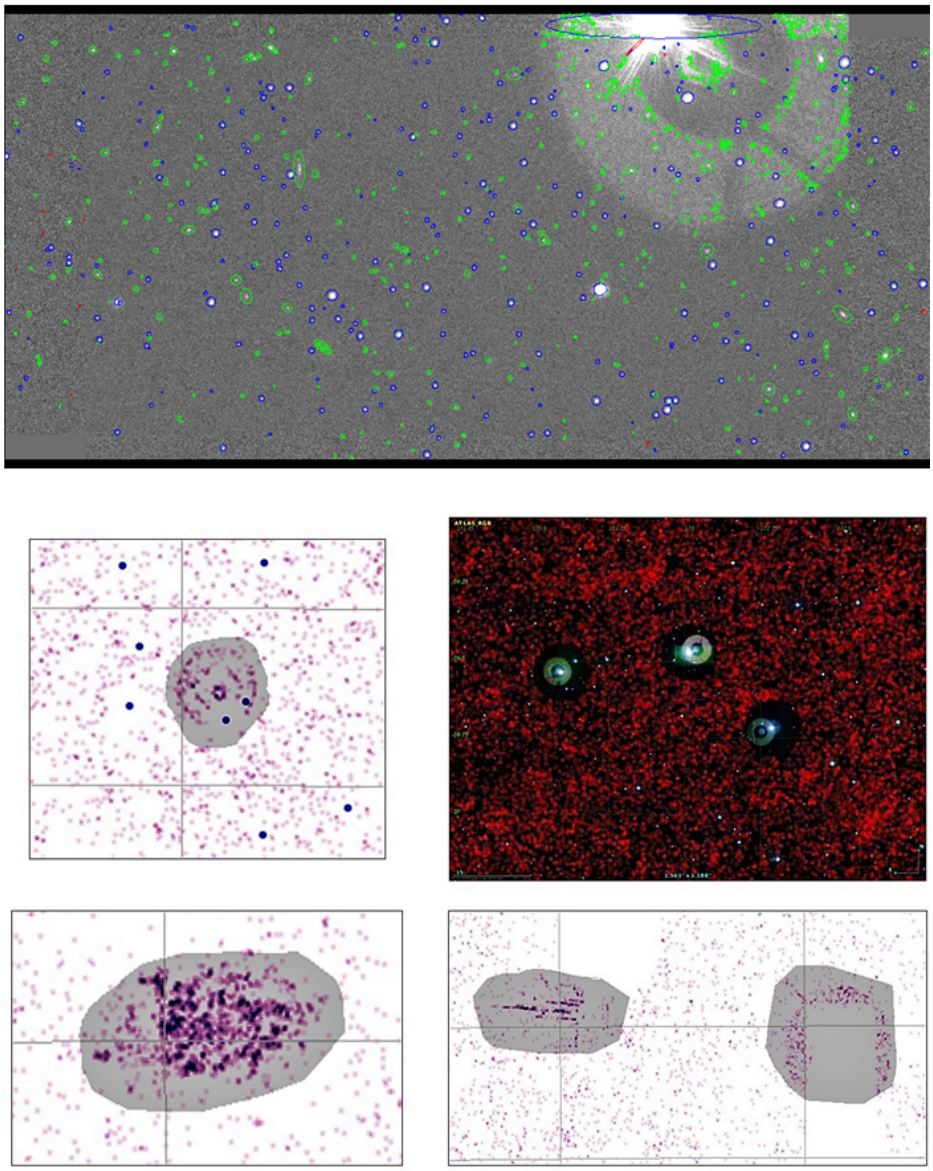

Figure 2.5: Top panel: An ATLAS i-band image with the CASU morphological classifications for the detected objects overlayed (blue: point-like sources; green: extended sources; red: noise). Here, we can see how a halo caused by reflection from a bright star can be misclassified as multiple extended sources in the CASU catalogue. Middle right: an ATLAS RGB image showing multiple bright star halos. Here, objects classified as galaxies are plotted by red dots. It can be seen that our match to the TYCHO2 bright stars catalogue has successfully masked these bright star halos. However, in some cases, the matching radii are not sufficient to remove the entire halo (middle left). Here blue dots are bright stars in the TYCHO2 catalogue and pink dots are objects classified as galaxies in our ATLAS input catalogue. These cases as well as nearby galaxies (bottom left) and other remaining artefacts (bottom right) are manually masked (grey regions).

2.4.2 Removal of artefacts

Reflections from bright stars in the VST ATLAS data could lead to the formation of circular halos which in some cases can be misidentified as multiple extended sources and misclassified as galaxies by the CASU source detection algorithm (see top panel of Figure 2.5). To overcome this, we mask circular regions around these bright stars based on cross-matching the input catalogue to the Tycho-2 Catalogue of the 2.5 million brightest stars (Høg et al., 2000). The Tycho bright stars are masked with radii varying according to their V-band magnitudes. For this purpose we choose the following radii based on visual inspection of stars with various magnitudes: $V < 8$: $340''$; $8 < V < 9$: $80''$; $9 < V < 10$: $45''$; $10 < V < 11$: $30''$; $V > 11$: $20''$. However, depending on the position of the star on the CCD chip, in some cases the halo can be off-centred from the stars. The remaining stellar halos and other major remaining artefacts such as nearby galaxies or satellite trails are manually removed by performing a visual inspection of the data (see Figure 2.5).

Chapter 3

The VST ATLAS Southern galaxy cluster catalogue

3.1 Introduction

In the context of hierarchical structure formation, primordial peaks in the density field of the early Universe collapse and merge, leading to the incremental formation of gravitationally bound halos of increasing mass (Peebles, 1980). Galaxy clusters are the largest of these gravitationally bound structures in the Universe, occupying the extreme tail of the halo mass function. As a result, the evolution of galaxy cluster abundance with mass and redshift is extremely sensitive to variations in cosmological parameters. Precise observations of large numbers of clusters over a range of redshifts can therefore provide powerful cosmological constraints (see reviews by Allen et al. 2011; Weinberg et al. 2013). In the context of the ΛCDM model, the study of galaxy clusters can place independent constraints on Ω_m, the matter density parameter (Evrard 1997; Schuecker et al. 2003), Ω_Λ, the dark energy density parameter and ω, the dark energy equation of state parameter (Morandi & Sun 2016), as well as σ_8, the normalization of the matter power spectrum on the scale of 8 h^{-1}Mpc (White et al. 1993; Croom & Shanks 1999). Furthermore, extensions to ΛCDM such as massive neutrinos can be investigated via the study of galaxy cluster number counts (Costanzi et al. 2013; Roncarelli et al. 2015), while non-standard modified gravity models can be constrained via the study of cluster properties (Brownstein 2009; Llinares & Mota 2013; Planck Collaboration et al. 2016b; Bocquet et al. 2019). Galaxy clusters and groups also provide useful tools in studying galaxy evolution in extreme environments and their physical properties could aid our understanding of structure formation, providing vital information on collapse of dark

matter and evolution of baryons in dark matter potentials (see reviews in Rosati et al. 2002; Voit 2005 and Kravtsov & Borgani 2012).

As the most prominent features visible in the large-scale structure, galaxy clusters are observationally accessible by various means. Galaxy clusters consist of multiple components, including dark matter (which contains most of the cluster mass), stars, cold gas and dust in the galaxies, as well as large quantities of intracluster medium (ICM), in the form of ionized diffuse hot gas containing the bulk of the baryonic matter in the cluster. The presence of large quantities of dark matter makes galaxy clusters ideal sites for identifying strongly-lensed background galaxies (Smail et al., 2007), providing a window into star formation in the early Universe (Swinbank et al., 2010), as well as an independent method of measuring cluster masses (Hoekstra et al., 2013). Due to the multi-component nature of clusters, they can be detected in multiple wavelengths, with galaxies emitting in optical and infrared, while the ICM is detectable in X-ray via thermal bremsstrahlung and line emission. Furthermore, inverse Compton scattering due to interaction with high energy electrons in the ICM provides a boost in energy to the cosmic microwave background (CMB) photons passing through the clusters, making them detectable via a phenomenon known as the Sunyaev-Zel'dovich (SZ) effect (Sunyaev & Zeldovich 1980). In what follows, we provide a brief overview of various historical and modern cluster detection techniques in different wavelengths.

3.1.1 Optical detection

Optically, galaxy clusters are revealed as overdensities in the projected distribution of galaxies on the sky, and due to their distinct appearance as concentrations of galaxies, their initial detection dates back as far as the 18th century (Biviano, 2000). The study of physical properties of clusters, however, began in the early 20th century leading to substantial astronomical advancements including the discovery of dark matter in the Coma cluster by Zwicky (1933). This was followed by more comprehensive statistical studies of clusters, leading to the creation of the earliest cluster catalogues. These early catalogues were based on visual inspection of a series of photographic plates, combined to cover large areas of the sky in search of galaxy overdensities identified using uniform selection methods. Amongst the most famous of these early efforts is Abell's all-sky catalogue of 4073 clusters (Abell 1958; Abell et al. 1989), in which clusters were defined as overdensities of 30 or more galaxies within a fixed radius of $1.5h^{-1}$Mpc, each no more than 2 magnitudes fainter than the third brightest cluster member. Furthermore, clusters were placed in distinct classes based on an estimate of their distance

given by the magnitude of the 10th brightest cluster member. This distance indicator was later improved upon by defining distance in terms of redshift rather than magnitude. Similar catalogues with different selection criteria were also independently developed by Zwicky et al. (1961).

The Abell catalogue has had significant influence in the field, providing the basis for a wide variety of research including the first studies of the large-scale matter distribution of the Universe (Bahcall & Soneira 1983; Postman et al. 1992), as well as utilisation of the Brightest Cluster Galaxies (BCGs) in construction of Hubble diagrams (Gunn & Oke 1975; Postman & Lauer 1995). Despite these successes, however, the Abell catalogue is affected by projection effects, where un-associated foreground and background field galaxies can contaminate the result of measured properties of the clusters such as richness or estimated distance (see Sutherland 1988). Moreover, apparent overdensities in projection which are not gravitationally bound can be identified as false clusters (Lucey, 1983), while further uncertainties can arise in the selection function as a consequence of reliance on visual cluster identification.

To overcome these limitations, later efforts focused on the construction of new optically selected cluster samples using digitized photographic plates (such as the Automated Plate Measurement (APM) galaxy survey; Dalton et al. 1992), along with automated cluster selection techniques (Lumsden et al. 1992; Dalton et al. 1994; Gal et al. 2003). Further instrumental advancements led to the availability of wide-field surveys containing vast samples of galaxies with multi-band CCD imaging. Amongst the first of these surveys was Sloan Digital Sky Survey (SDSS; York et al. 2000), a subset of which was used to generate an input catalogue of 2.3×10^7 galaxies with *ugriz* photometry which form the basis of the MAXBCG (Koester et al., 2007) and redMaPPer (Rykoff et al., 2014) cluster catalogues. The VST ATLAS survey (Shanks et al., 2015), which is the basis of this work later provided coverage of ~ 4700 deg^2 over the southern sky to similar depths as SDSS (but with superior seeing). Other notable ongoing and upcoming photometric surveys include Dark Energy Survey (DES; The Dark Energy Survey Collaboration 2005; Rykoff et al. 2016), Pan-STARRS (Kaiser et al. 2002; Ebeling et al. 2013), the Kilo-Degree Survey (KiDS; de Jong et al. 2013; Radovich et al. 2017), the Hyper-Suprime Camera (HSC; Aihara et al. 2017), and the Large Synoptic Survey Telescope (LSST; LSST Dark Energy Science Collaboration 2012) and Euclid (Laureijs et al., 2011), providing enormous quantities of data upon which the search for clusters of galaxies has and will be based.

With the availability of such vast quantities of data, comes the demand for fully automated

galaxy cluster detection techniques and algorithms that could analyse the data to identify uniform, pure and complete samples of clusters. In the absence of spectroscopic redshifts, galaxy redshifts can be estimated photometrically based on techniques such as SED template fitting (e.g. Hyperz; Bolzonella et al. 2000), using Bayesian probabilistic methods (e.g. BPZ; Benítez 2011) or via machine learning approaches utilising artificial neural networks or boosted decision trees (e.g. ANNz2; Sadeh et al. 2016). Due to their large uncertainties (often many times larger than the physical size of clusters), photometric redshifts alone are not sufficient for accurate identification of galaxy clusters via 3D reconstruction of the distribution of galaxies. However, many cluster detection algorithms rely on photometric redshifts (photo-z's) as part of their cluster identification process (see, e.g. van Breukelen & Clewley 2009; Durret et al. 2011; Wen et al. 2012), often with a combination of other techniques including matched filter (Milkeraitis et al. 2010; Szabo et al. 2011) and Voronoi Tessellation methods (Ramella et al. 2001; Soares-Santos et al. 2011).

Another approach to detecting clusters in the optical regime, as proposed by Gladders & Yee (2000), is based on taking advantage of the cluster *red sequence* (Baum 1959; Bower et al. 1992). The red sequence refers to the tight correlation followed by the cluster galaxies in the colour-magnitude space, this feature arises due to galaxy clusters mostly containing early-type elliptical and lenticular galaxies which consist of passively evolving stellar populations giving rise to strong metal absorption lines at wavelengths blue-wards of 4000Å. As a result, the majority of cluster members appear red in colour and occupy a narrow ridge in the colour-magnitude space, when viewed through broadband photometric filters that straddle the 4000Å break. In this way cluster galaxies can be isolated from active, star forming field galaxies. The 4000Å break evolves red-ward with increasing redshift allowing for identification of clusters across a range of redshifts using a combination of filters at various wavelengths in order to track this evolution. Algorithms utilising the red sequence for cluster detection include Koester et al. (2007); Gladders et al. (2007); Thanjavur et al. (2009); Hao et al. (2010); Rykoff et al. (2014) as well as The Overdense Red-sequence Cluster Algorithm (ORCA; Murphy et al. 2012) used in this work.

3.1.2 X-ray detection

Galaxy clusters have also been detected in X-ray exploiting the radiation from the hot ICM (Cavaliere & Fusco-Femiano 1976; Allen et al. 2002) with several catalogues constructed based on the ROSAT All-Sky Survey (Voges et al. 1999; Ebeling et al. 1998; Reiprich &

Böhringer 2002; Böhringer et al. 2004; Böhringer et al. 2016), as well as deeper observations of high-redshift clusters (Burenin et al. 2007; Ebeling et al. 2010; Mehrtens et al. 2012).

The main advantage of X-ray compared to optical cluster samples is their significantly lower vulnerability to line of sight projection effects. This is a consequence of the dependence of X-ray signal on electron density squared which makes the signal more peaked at the cluster centre relative to the projected cluster galaxy distribution in optical observations (see e.g. Ebeling et al. 2010; Allen et al. 2011). On the other hand, in the X-ray regime, AGN present the main challenge for cluster samples. This is because AGN significantly outnumber galaxy clusters and their superposition can be a source of contamination in X-ray cluster samples, especially in X-ray observations with a lower resolution (see e.g. Böhringer et al. 2014; Biffi et al. 2018; Finoguenov et al. 2020).

In this work, we compare our optically detected cluster catalogue with The MCXC: a meta-catalogue of X-ray detected clusters of galaxies (Piffaretti et al. 2011; which contains 1743 clusters based on publicly available ROSAT All Sky Survey-based (NORAS, REFLEX, BCS, SGP, NEP, MACS, and CIZA) samples and serendipitous (160SD, 400SD, SHARC, WARPS, and EMSS) cluster catalogues. In the near future, an ongoing all-sky X-ray survey eROSITA (Merloni et al., 2012) with the aim of detecting $\sim 100,000$ galaxy clusters out to $z > 1$ will significantly increase the cluster sample size in the X-ray regime. The cluster catalogue introduced in this work will provide a valuable resource which could be used to better characterise the selection function of the eROSITA cluster in terms of sample completeness and purity.

3.1.3 SZ detection

With the benefit of a detection signature that is essentially independent of redshift, the SZ effect offers a new window on the cluster population providing a nearly mass-limited sample at high redshifts, where cluster abundance can place sensitive constraints on cosmological parameters (Carlstrom et al. 2002; Planck Collaboration et al. 2014d). In recent years, several SZ surveys have been undertaken with South Pole Telescope (SPT; Carlstrom et al. 2011) survey, the Atacama Cosmology Telescope (ACT; Fowler et al. 2007), and Planck (Tauber et al., 2010), providing the first SZ-selected cluster samples (Vanderlinde et al. 2010; Menanteau et al. 2010; Planck Collaboration et al. 2011; Reichardt et al. 2013; Hasselfield et al. 2013). In Section 3.4.1, we also draw a comparison between our cluster catalogue and The second Planck catalogue of Sunyaev-Zeldovich sources (henceforth Planck SZ; Planck Collaboration et al. 2016e), which contains 1653 detections, out of which 1203 are confirmed

clusters based on identification of counterparts in external datasets. Similarly, we compare the ATLAS cluster catalogue with SZ detections from the AdvACT sample (Hilton et al., 2020), which has a large overlap with the SGC of ATLAS. The AdvACT sample contains over 4000 cluster detections in a survey area of $13,168$ deg^2, probing lower cluster masses than the Planck SZ sample.

The layout of this Chapter is as follows: In Section 3.2 we describe the VST ATLAS survey galaxy input catalogue, followed by Section 3.3, where we present a brief description of the ORCA algorithm, as well as a description of our machine learning approach to obtaining photometric redshifts for our clusters. We then present a description of our cluster richness estimation. In Section 3.4, we present the ATLAS cluster catalogue and compare our results with external multi-wavelength cluster samples, providing estimates of the completeness and purity of the ATLAS cluster catalogue. Finally, we conclude this work by presenting a summary in Section 3.5.

3.2 Dataset

The input catalogue given to ORCA for cluster detection consists of objects detected in two adjacent bands (i.e. g & r, r & i, or i & z which are used for cluster red-sequence detection). We also require objects to be classified as galaxies in a minimum of two bands. Here, we only require objects to be classified as galaxies in two bands as demanding a galaxy classification in all bands was deemed too strict, resulting in a $\sim 10\%$ decrease in the overall sample size. The slight increase in stellar contamination introduced in this approach is unlikely to be a problem in our cluster detection, due to ORCA's reliance on the red sequence in selecting cluster members (see Section 3.3.1). We do not include the u band due to its shallow depth and the incompleteness of the u-band observations resulting in large gaps in across the survey area at the time of conducting this work.

As the VST ATLAS survey observations are conducted in 17 deg^2 concatenations (in DEC), taking data in a single band at a time, nightly variations in seeing, sky brightness and other observing conditions can result in slight variations in survey depth across different concatenations. After band merging, these slight fluctuations in object densities in some concatenations could result in artificial inhomogeneities across the sky. Consequently, we select magnitude limits of $g_{\rm Kron} < 22.0$; $r_{\rm Kron} < 21.6$; $i_{\rm Kron} < 21.1$; $z_{\rm Kron} < 19.9$ as a compromise between increasing the survey depth and increasing homogeneity between concatenations. The fi-

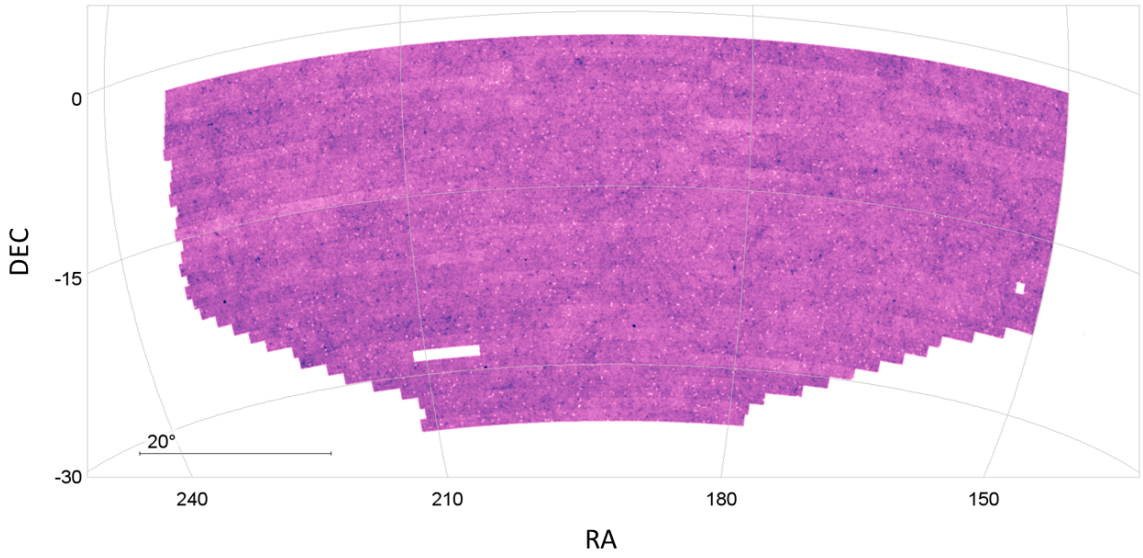

(a) VST ATLAS NGC

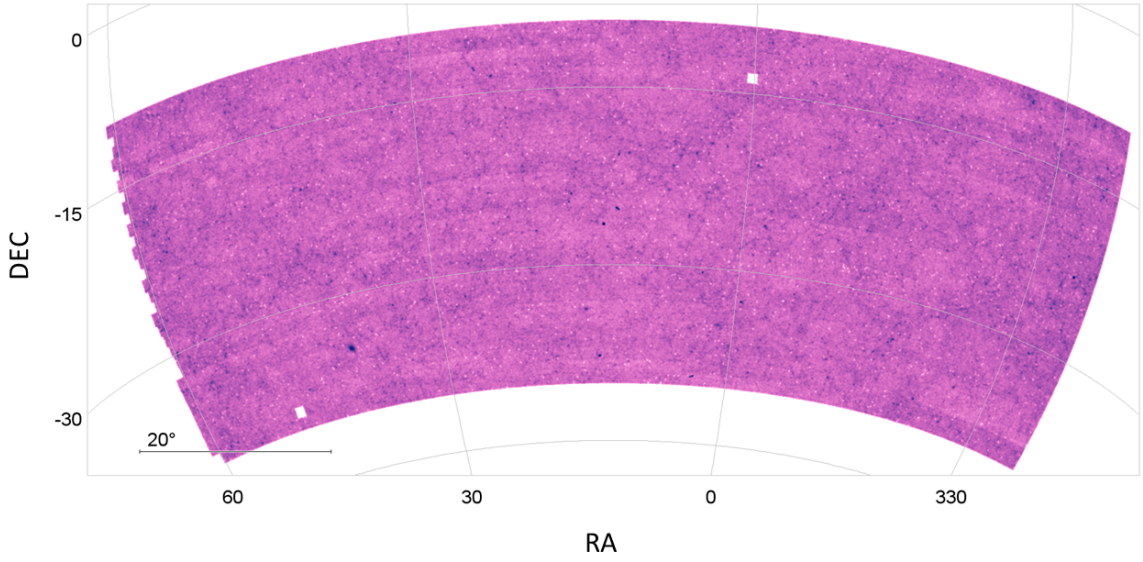

(b) VST ATLAS SGC

Figure 3.1: The ORCA galaxy input catalogues in the NGC and SGC of the VST ATLAS survey. The input catalog contains objects classified as galaxies in two bands, with magnitude limits of $g < 22.0$; $r < 21.6$; $i < 21.1$; $z < 19.9$. Here the darker colours represent denser regions.

nal input catalogues contain $\sim 8,740,000$ galaxies in the SGC, $\sim 7,825,000$ in the NGC. Figure 3.1 shows the ORCA input catalogues in the NGC and SGC of the ATLAS survey.

In order to impose magnitude limits on the input catalogues, we make use of the VST ATLAS Kron pseudo-total magnitudes, adding an offset to total of -0.15mag (see discussion in Section 2.4 and Section 3.3 of Shanks et al. (2015) for the origin of this offset). The Kron magnitudes provide the most reliable measure of the galaxies' total magnitudes in comparison to SDSS model magnitudes, with a lower level of dispersion compared to VST ATLAS Petrosian magnitudes. However, when measuring the galaxy colours, we make use of the ATLAS Aperture 5 magnitudes which provide the most consistent colours compared to SDSS. The ATLAS Aperture 5 has a radius of $2''$, and we add the associated VST ATLAS aperture corrections (`APCOR5`) with mean values -0.12, -0.12, -0.11 and -0.12mag to the $g_{\rm A5}$, $r_{\rm A5}$, $i_{\rm A5}$, $z_{\rm A5}$ respectively.

3.3 Methodology

3.3.1 ORCA: The cluster detection algorithm

A detailed description of the 'Overdense Red-sequence Cluster Algorithm' (ORCA) which is used to create the ATLAS cluster catalogue can be found in Murphy et al. (2012). Figure 1 of the reference paper (shown as Figure 3.2 here), provides an illustration of five main stages involved in ORCA's cluster detection. The algorithm detects the red sequence in pairs of adjacent bands or *colours* (i.e. $g-r$, $r-i$ or $i-z$). In the first stage, the algorithm applies a selection function to the input catalogue in the form of narrow slices in the colour-magnitude space. This photometric filtering separates galaxies within a specific redshift range from foreground and background objects, broadly isolating the cluster galaxies via the 4000Å break. By detecting clusters in two colours concurrently, fore- and background contamination can be significantly reduced, as galaxies follow unique tracks in different colour-redshift spaces (see Figure 3.3). During this stage, the red sequence is isolated across a range of redshifts, through modifications of the colour slice in successive runs of the algorithm in order to systematically scan the entire photometric space.

Upon the application of the photometric filtering, the algorithm estimates the surface density of the remaining galaxies by calculating the Voronoi diagram of their projected distribution on the sky. The Voronoi cells are then separated into overdense and underdense cells based on a user-specified probability threshold ($P_{\rm thresh}$), related to how likely they are to belong to

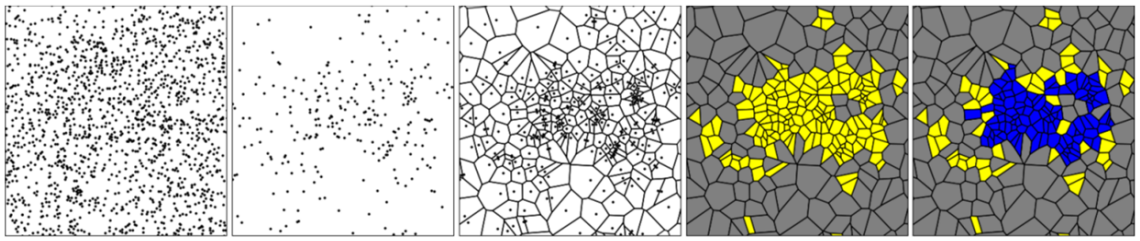

Figure 3.2: Figure 1 of Murphy et al. (2012) illustrating the five stages of the ORCA cluster detection algorithm based on a $9' \times 9'$ region of the SDSS Stripe 82. The first panel on the left shows the distribution of galaxies in this region. In the second panel, galaxies are isolated in a specific redshift range based on a photometric colour selection. In the third panel the Voronoi diagram and surface densities of these galaxies are calculated. The galaxies are then divided into overdense (yellow) and underdense (grey) cells, as shown in the fourth panel. In the final panel ORCA's Friends-Of-Friends algorithm connects the overdense cells until the density of the whole system falls below a user-specified density threshold. The system is then considered a cluster if there are at least $N_{\rm min}$ linked members, where the value of $N_{\rm min}$ is also specified by the user.

a random distribution (for more details, see Section 3.4 of Murphy et al. 2012). Finally using the Friends-of-friends technique, the algorithm connects adjacent overdense cells until the density of the whole system falls below a user-defined critical density ($\sum_{\rm crit}$). At this stage if the system has at least $N_{\rm gals}$ linked galaxies (in this case we set $N_{\rm gals} = 5$), it is defined as a cluster.

We optimize the $P_{\rm thresh}$ and $\sum_{\rm crit}$ parameters for performance on VST ATLAS based on multiple runs of the ORCA algorithm on a $\sim$ 300 deg^2 area and assessing its performance based on recovering the Abell, MCXC, RedMapper and Planck SZ clusters in this region. We then set $\sum_{\rm crit} = 2.5\bar{\sum}$ (where $\bar{\sum}$ is the mean galaxy density), and $P_{\rm thresh} = 0.0125$, using the default for other adjustable parameters of the algorithm as these do not have a major effect on improving the results.

As the adjustment to the colour slice is by design less than the width of the red sequence, the same cluster can be identified multiple times in successive runs of the algorithm. However, multiple detections are identified and merged into one in the final stage of the algorithm in a process described in Section 3.6 of Murphy et al. (2012). Attached to each merged cluster in the final catalogue is a list of the candidate cluster galaxies considered by ORCA in separate runs, which were not merged into a final cluster. These are referred to as *associate cluster members* and in some cases could contain actual cluster members which for instance could be identified with the help of photo-z's. These cluster associates will be released in a supplementary catalogue in conjunction with the ATLAS cluster catalogue.

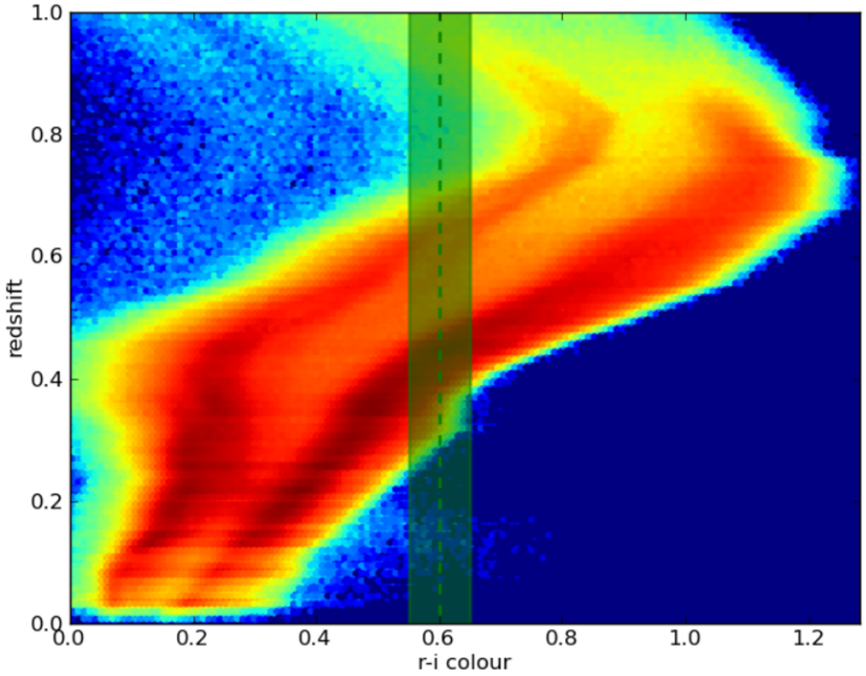

Figure 3.3: Figure 2 of Murphy et al. (2012) showing the redshift evolution of the mock galaxy r-i colours. Here blue indicates low and red indicates high-density regions. By selecting galaxies in the narrow colour slices as shown by the shaded region, ORCA is able to isolate galaxies within a specific redshift range. Furthermore, concurrent detection of the red-sequence in two colours (e.g. g-r and r-i) significantly reduces contamination from fore- and background galaxies.

3.3.2 ANNz2: Photometric redshift estimation

We make use of the publicly available ANNz2[1] (Sadeh et al., 2016) algorithm in order to obtain photometric redshift estimates for the VST ATLAS cluster members. For this purpose, we simultaneously make use of a combination of two machine learning methods offered by the algorithm; Artificial Neural Networks (ANNs) and Boosted Decision Trees (BDTs). After performing various tests, this approach was shown to produce the best RMS scatter in comparison to using ANNs or BDTs alone. Here the RMS error is given by:

$$\sigma_{\Delta z/(1+z)} \equiv \sqrt{\frac{1}{n_{\rm gals}} \sum_{\rm gals} \left(\frac{z_{\rm photo} - z_{\rm spec}}{1 + z_{\rm spec}} \right)^2}, \tag{3.3.1}$$

where $n_{\rm gals}$ is the number of galaxies in the training set and $z_{\rm photo}$ and $z_{\rm spec}$ are estimated photometric and measured spectroscopic redshifts of these galaxies, respectively. We define outliers following the conventional form as galaxies where

$$\frac{\mid z_{\rm photo} - z_{\rm spec} \mid}{1 + z_{\rm spec}} > 0.15, \tag{3.3.2}$$

and assess the photometric redshift estimation performance with and without including these outliers.

To estimate photometric redshifts using machine learning, we are required to provide the algorithm with a training sample of galaxies with measured redshifts, which overlap the VST ATLAS survey area. For this purpose, we make use a total of 21,114 galaxies with redshifts obtained from various surveys as detailed in Table 3.1. In cases where the same objects have redshifts provided by more than one survey, we keep the redshift with the smaller uncertainty. Figure 3.4 shows the redshift distribution of the galaxies included in the training set used in our photometric redshift estimation.

In order to improve our photometric redshift training, in addition to the ATLAS *griz* bands, we add the W1 and W2 magnitudes from the "unblurred coadds of the WISE imaging" catalogue (unWISE; Schlafly et al. 2019)[2]. Here we use a $2''$ radius to match ATLAS and unWISE sources and we correct for galactic dust extinction in W1 and W2 bands by subtracting $0.18 \times E(B-V)$ and $0.16 \times E(B-V)$ from the W1 and W2 magnitudes respectively.

[1] `https://github.com/IftachSadeh/ANNZ`

[2] We note that despite the $6''$ WISE PSF, thanks to the improved modelling of the blended sources in the unWISE catalogue, the addition of W1 and W2 information to our machine learning training still proved useful in improving our photo-z RMS scatter.

Table 3.1: Details of the samples used in our photometric redshift training. Here the redshift coverage, the mean redshift of the samples, and the number of galaxies corresponds to the number of objects with redshifts with counterparts identified as ATLAS cluster members by the ORCA algorithm.

Sample	Redshift coverage	$\bar{z}$	Number of galaxies	Reference
2dFGRS	$0.00 < z < 0.30$	0.13	9,426	Colless et al. (2003)
SDSS DR12	$0.05 < z < 0.35$	0.15	5,260	Alam et al. (2015)
GAMA G23	$0.05 < z < 0.50$	0.21	3,008	Liske et al. (2015)
Primus	$0.05 < z < 0.60$	0.24	177	Cool et al. (2013)
2dFLenS	$0.05 < z < 0.75$	0.26	2,717	Wolf et al. (2017)
BOSS LOWZ	$0.05 < z < 0.45$	0.26	375	Dawson et al. (2013)
BOSS CMASS	$0.40 < z < 0.75$	0.52	141	Dawson et al. (2013)

These $E(B-V)$ values are taken from the same Planck dust map (Planck Collaboration et al., 2014d) used to correct the ATLAS magnitudes for galactic dust extinction and the 0.18 and 0.16 coefficients are taken from Yuan et al. (2013).

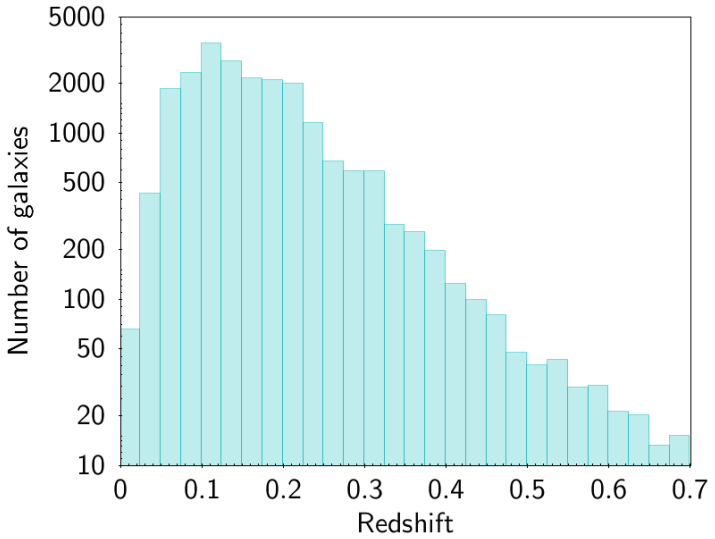

Figure 3.4: The redshift distribution of the training sample used to estimate the photometric redshifts of the ATLAS galaxy cluster members by ANNz2.

Finally, we calculate the weighted mean photometric redshift of our clusters using:

$$\bar{z} = \frac{\sum z_i/{\sigma_i}^2}{\sum 1/{\sigma_i}^2}, \tag{3.3.3}$$

where z_i and σ_i are the photometric redshift and photometric redshift error of the i-th cluster member. The error on the weighted mean redshift of each cluster is then given by:

$$\sigma_{\bar{z}} = \sqrt{\frac{1}{\sum 1/{\sigma_i}^2}}. \tag{3.3.4}$$

3.3.3 Cluster catalogue post-processing

As discussed in 3.6 of Murphy et al. (2012), multiple detections of the same cluster found in different colour-magnitude spaces are merged together by ORCA based on five tests of 'cluster similarity'. These criteria are based on the similarity of the clusters' red-sequence, the extent of spatial overlap and the number of common galaxies between the two detections.

In this work, we utilise our photometric redshifts to further merge overlapping cluster detections that are likely to belong to the same system based on the following criteria:

- **Spatial overlap:** A cluster centre lies within the cluster radius of a nearby cluster. Here, the cluster centre is defined as the mean RA and DEC of its cluster member and cluster radius is defined as the angular separation between the furthest cluster member and the cluster centre. In addition, we require at least one of the below criteria to be satisfied in order for overlapping detections to be considered as part of the same system.
- **Photometric redshift overlap:** The error weighted mean cluster photometric redshift lies within 3σ of another spatially overlapping cluster. Here σ is defined as the error on the weighted mean cluster redshift (with an average value of 0.007 ± 0.003).
- **Red-sequence overlap:** The mean colour of a cluster's members (in either $g-r$, $r-i$ or $i-z$) is within one standard error of another overlapping cluster's mean colour.

Requiring the combination of spatial overlap, with either photometric redshift or red-sequence overlap, results in the merging of 9% of the clusters in the catalogue. Figure 3.5 shows an example of merged overlapping clusters based on the above criteria.

3.3.4 Cluster richness (N_{200})

In order to provide an estimate of cluster richness, we first count the number of galaxies within a $1h^{-1}$ Mpc aperture of the cluster centre, $N_{1\mathrm{Mpc}}$, which are fainter than the BCG, and brighter than $0.4L_*$. Here L_* is the characteristic luminosity in the Schechter luminosity function, and following Reyes et al. (2008), we take the $z = 0.1$, i-band value of $L_* = 2.08 \times 10^{10} h^{-2} \mathrm{L}_\odot$. To calculate the K-corrections, we make use of the 'K-corrections calculator' Python algorithm[3], which is based on the procedure described in Chilingarian et al. (2010).

[3] http://kcor.sai.msu.ru/getthecode/

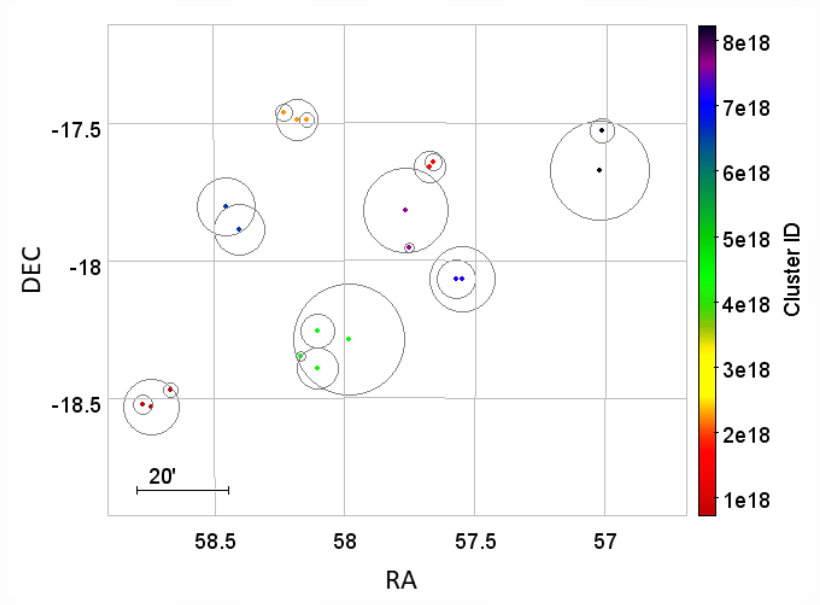

Figure 3.5: The outcome of merging overlapping clusters based on spatial and photometric redshift, or red-sequence overlap. The cluster centres of the merged overlapping clusters are coloured by their newly assigned cluster IDs, with the circles showing the corresponding cluster radii used to identify spatially overlapping clusters.

Once the values of $N_{1\mathrm{Mpc}}$ are determined, we calculate the cluster radius R_{200}, defined as the radius within which the cluster galaxy number density is $200\Omega_{\mathrm{m}}^{-1}$ times the mean galaxy density of the present Universe. We calculate R_{200} (in units of h^{-1}Mpc) using an empirical relation presented by Hansen et al. (2005):

$$R_{200} = (0.142 \pm 0.004) N_{1\mathrm{Mpc}}^{0.6\pm0.01}, \tag{3.3.5}$$

based on their analysis of the SDSS maxBCG clusters. R_{200} is in turn used to obtain the final cluster richness N_{200} which is calculated in the same way as $N_{1\mathrm{Mpc}}$, but now using R_{200} as the aperture within which the cluster members are counted as opposed to the fixed aperture of 1 Mpc.

3.3.5 Scaling N_{200} by $n(z)$

Due to the magnitude limits of our data, our ability to detect fainter cluster members is reduced as a function of redshift, which could lead to an under-estimation of our cluster N_{200} values at higher redshifts. In order to correct for the impact of the survey magnitude limits on our N_{200} and subsequent cluster mass (M_{200}) estimation, we up-weight our N_{200} values by a theoretical galaxy $n(z)$ curve which gives the relative number of galaxies detectable as a function of redshift, given our $i < 21.1$ magnitude limit. This theoretical $n(z)$ is obtained

based on a luminosity function which assumes a Schechter (1976) function, with the i-band, 'red' galaxy values of $\alpha = -0.46$ and the $z = 0.1$ value of $M^* - 5\log h = -20.63$ taken from table 3 of Loveday et al. (2012), k and evolution corrected (with a characteristic time-scale of $\tau = 2.5$ Gyr), using the Stellar population synthesis model of Bruzual & Charlot (2003).

Figure 3.6a shows the cluster membership of our ORCA clusters (as well as ORCA clusters matched to Planck, AdvACT, MCXC and Abell cluster samples) as a function of redshift. Here, we are also plotting the theoretical $n(z)$ described above, normalized to match our maximum value of $N_{\rm gal} = 220$ at $z = 0.1$. Also shown is a fitted curve to the theoretical n(z) which is used to obtain the scaling factor, $C(\bar{z})$, applied to our N_{200} in the $z > 0.1$ redshift range, where the number of our cluster members begin to drop as a function of redshift. This scaling factor takes the form of:

$$C(\bar{z}) = 220/(571.7\bar{z}^2 - 819\bar{z} + 292.8), \tag{3.3.6}$$

i.e. the ratio of $N_{\rm gal} = 220$ to our normalized theoretical $n(z)$ at each redshift and is shown in Figure 3.6b as a function of redshift.

In order to apply the $C(\bar{z})$ scaling to our N_{200} values, we first scale our $N_{\rm 1Mpc}$ values which are used to estimate the value of R_{200} for each cluster. We then count the number of cluster galaxies within R_{200} to obtain N_{200}. The N_{200} values are then scaled by the $C(\bar{z})$ scaling factor to give the scaled N_{200} values plotted in Figure 3.7a as a function of redshift. The uncertainty on the scaled N_{200} is then given by propagation of the $\sqrt{n}$ error on N_{200} and the uncertainty on $C(\bar{z})$:

$$\sigma_{N_{200}} = 2200\sqrt{\frac{4N_{200}^2(5717\bar{z} - 4095)^2\sigma_{\bar{z}}^2 + \sqrt{N_{200}}^2(5717\bar{z}^2 - 8190\bar{z} + 2928)^2}{(5717\bar{z}^2 - 8190\bar{z} + 2928)^4}}. \tag{3.3.7}$$

Note that in the above equation the N_{200} values are not scaled by $C(\bar{z})$. For the remainder of this work however, unless otherwise specified, our use of N_{200} refers to these $n(z)$ scaled N_{200} values.

We note that our cluster mass estimates and the resulting mass functions (see Chapter 5) are not very sensitive to the chosen value of normalisation and exact parameters of equation 3.3.6. This is because any systematic offsets introduced during the $n(z)$ scaling is removed when we calibrate our cluster mass-richness scaling relation to masses from external samples (in Section 5.2). However, in future works, we shall verify the performance of our cluster detection algorithm, as well as our richness estimation and $n(z)$ scaling, by injecting mock clusters and redshifted versions of nearby clusters with few members preserved. This has the potential to

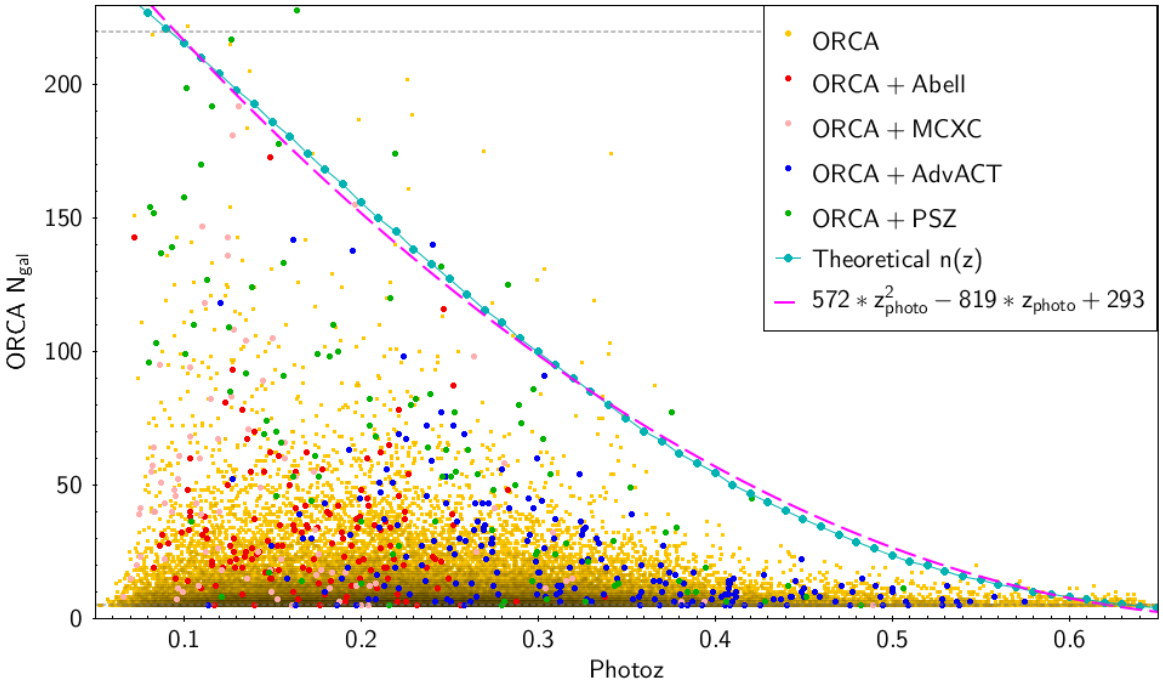

(a)

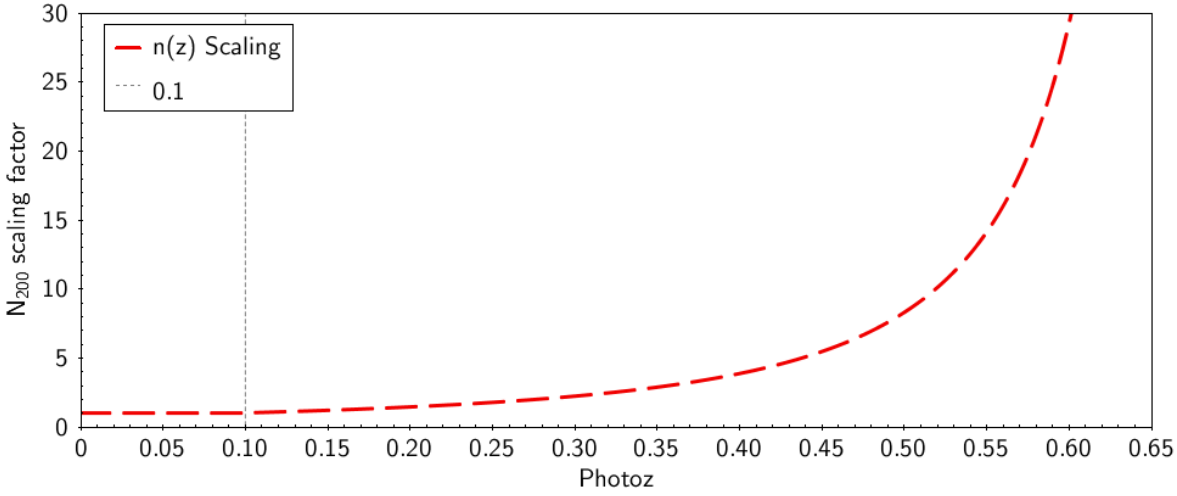

(b)

Figure 3.6: (a) ORCA cluster membership $N_{\rm gal}$ as a function of photometric redshift. Also shown are ORCA clusters with counterparts in Planck SZ, MCXC, AdvAct and Abell cluster catalogues. The best fit curve (dashed pink line), fitted to the normalized theoretical $n(z)$ described in Section 3.3.5 is used to determine the redshift dependent N_{200} scaling factor shown in panel (b).

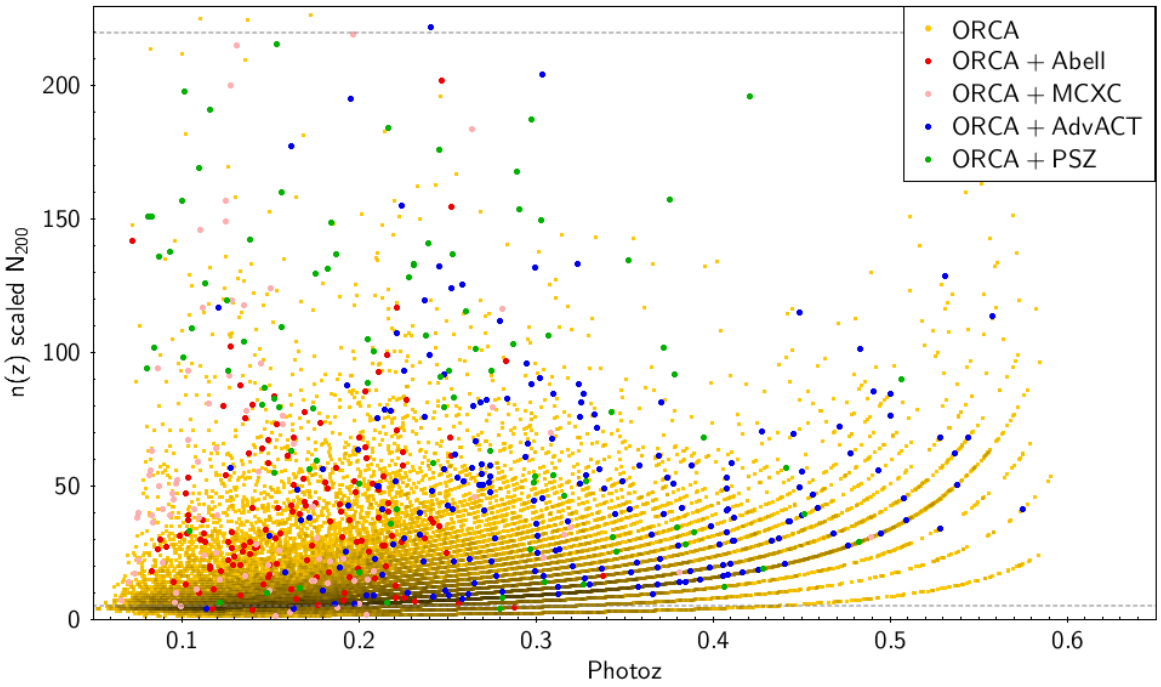

(a)

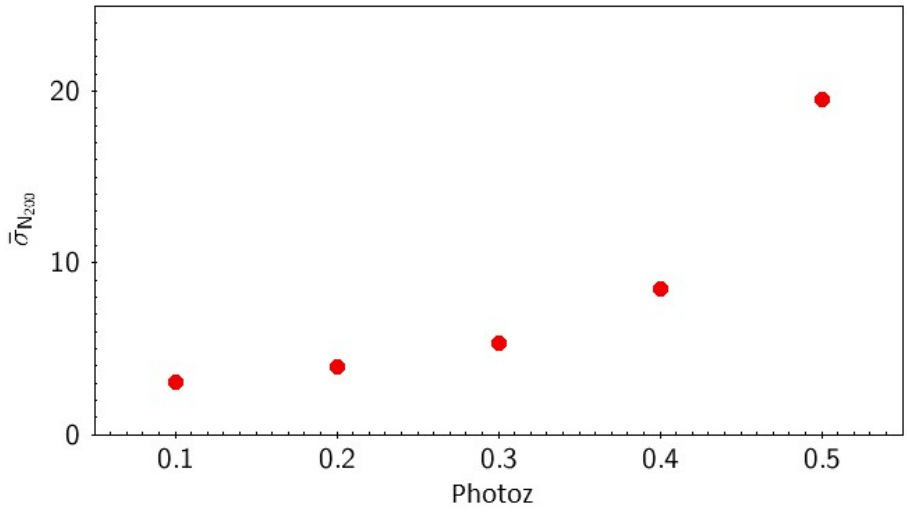

(b)

Figure 3.7: (a) $n(z)$ scaled N_{200} values as a function of photometric redshift. A comparison of this plot with Figure 3.6a shows that this scaling has compensated for our tendency to under-estimate cluster richness values with increasing redshift. For clarity we do not show the error bars on the scaled N_{200} values in panel (a). However, in panel (b) we show the mean uncertainty on the scaled N_{200} values as a function of cluster photometric redshift.

improve the accuracy of our cluster mass estimates by revealing any unknown systematics that might be present in our analysis, in a manner that is independent of other cluster samples which could suffer from their own systematics.

3.3.6 Cluster quality flags

We assign a quality flag to each cluster detection based on the various factors described in this Section.

- **Seeing flag, $Q_{\mathbf{seeing}}$:** Seeing is the main observing condition that could impact our cluster detection success rate, and perhaps to a greater extent, the number of galaxies identified as cluster members by ORCA. As discussed in Section 3.2, seeing variations across different ATLAS concatenations (series of 17 tiles forming an ATLAS Observing Block), could result in slight variations in the number of objects detected/classified as galaxies across different concatenations. In cases where these artificial inhomogeneities result in galaxy densities that are lower than the mean galaxy density across the survey, the number of cluster detections (and the richness of the cluster) can be underestimated. In order to provide a measure of which clusters may be impacted in such a way by below average seeing, we assign a seeing flag to each cluster ranging from 0 to 1, based on the mean of the tile seeing in g, r, i and z-bands, with clusters detected in the tile with the best mean seeing being assigned a seeing flag of 1.

- **Photometric redshift flag $Q_{\mathbf{photoz}}$:** A second detection quality flag (once again ranging in value from 0 to 1) is assigned to each detection based on the uncertainty on the weighted mean photo-z of each cluster. As we later show in Figure 3.11d, the error on the mean photometric redshift of our clusters increases with increasing redshift, so in order to take this into account we first divide our clusters into six redshift bins covering the range $0.05 < z < 0.65$ with bin widths of $\Delta z = 0.1$. We then remove any 3σ redshift outliers from each cluster, recalculate the redshift error on the mean cluster redshift and divide the new error by the cluster R_{200}. The division by cluster radius will allow for variations in error on the redshift caused by variations in physical cluster sizes. In the final step, we rank these "R_{200} normalized" redshift errors from highest to lowest in each redshift bin, assigning a redshift flag of 1 to the cluster with the lowest normalized error on the mean redshift.

A final detection quality flag ($Q_{\rm ORCA}$) is determined by taking the mean of $Q_{\rm seeing}$ and $Q_{\rm photoz}$ providing a measure of the quality of each detection based on variations in seeing and the level of scatter on the cluster photometric redshift.

3.4 Results and discussion

3.4.1 The VST ATLAS cluster catalogue

The sky distribution of ATLAS clusters in the SGC and NGC of the survey are shown in Figures 3.8 and 3.9, respectively. For clarity we limit the clusters to those with richness $N_{200} > 15$. For comparison, we also include the ABELL, MCXC, Planck SZ and AdvACT cluster samples in the VST ATLAS coverage areas. In Section 3.4.4, we assess the completeness of the ATLAS cluster sample as a function of cluster mass and redshift by drawing comparison to these four cluster samples.

Figure 3.10 shows the number of ATLAS clusters as a function of cluster richness ($N200$). A similar histogram showing the richness (λ) of the SDSS RedMapper sample is also added for comparison. Although RedMapper clusters with ($\lambda < 20$) are not available with the public release of the catalogue, it can be seen that in both samples follow similar cluster richness distributions with thousands of clusters in bins of richness smaller than ~ 40, hundreds in richness bins between ~ 40 and 80, and tens of clusters in bins of richness ranging from $\sim 80 - 140$. The ATLAS sample however contains a slightly larger number of richer clusters ($\sim 10\%$), which is likely due to differences in the definitions of cluster richness between the two samples.

We present a more detailed comparison of various properties of the ATLAS and RedMapper samples in Section 3.4.5, where we also obtain an estimate of the purity of the ATLAS samples based on this comparison.

3.4.2 Photometric redshifts

Following the procedure described in Section 3.3.2, we use ANNz2 to obtain photo-z estimates for our cluster galaxies with an RMS scatter of ~ 0.024 (see Figure 3.11a), upon removing the outliers as defined in Equation 3.3.2. Inclusion of outliers results in an RMS of ~ 0.026. The photometric redshift distribution of BCGs of the full ATLAS sample containing $\sim 53,000$ ORCA detections, as well as $\sim 22,000$ clusters with $N_{200} > 10$ and $9,000$ clusters with

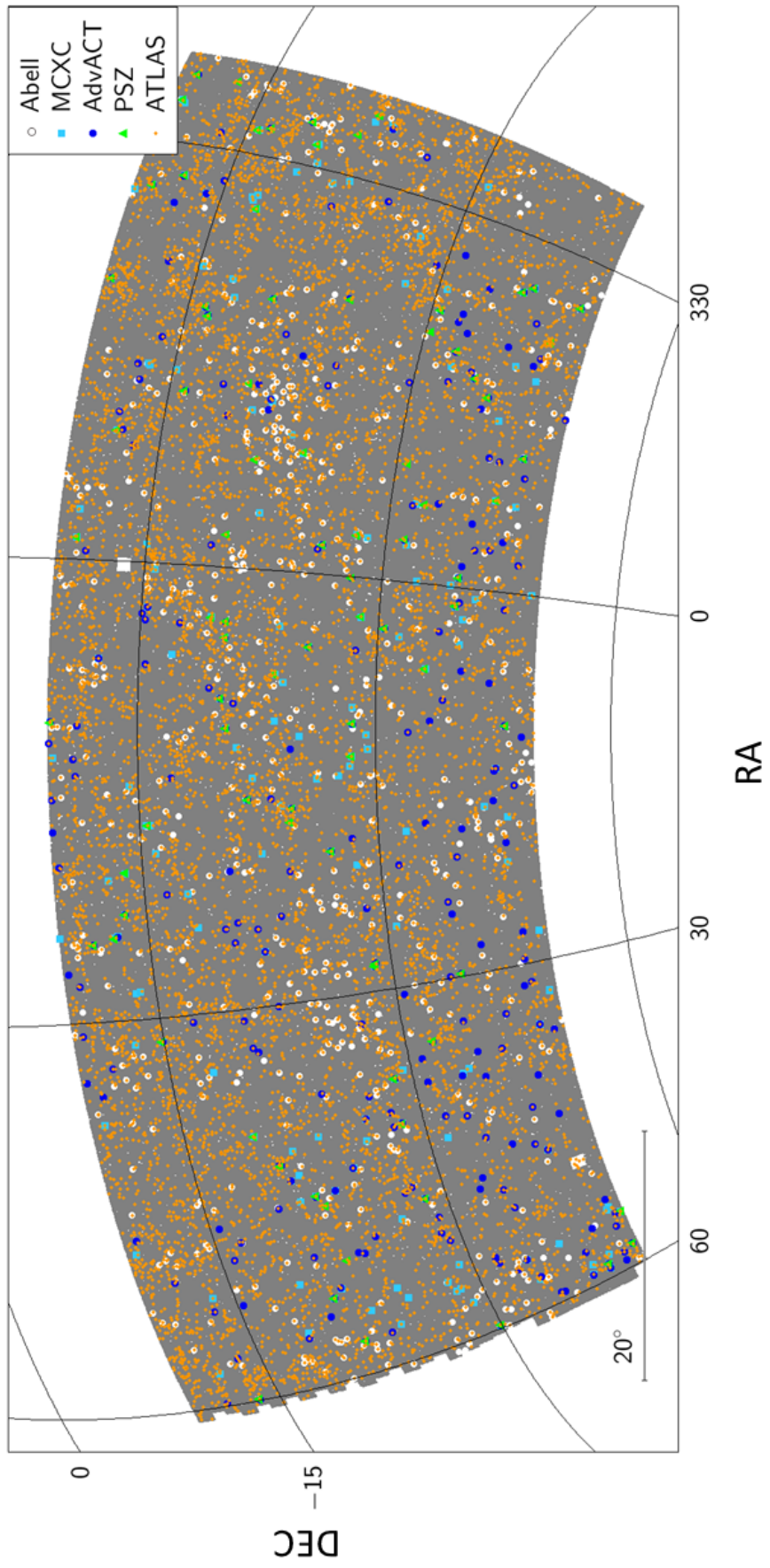

Figure 3.8: The distribution of ATLAS clusters in the Southern Galactic Cap (SGC) of the survey in comparison with clusters from the Abell, MCXC, AdvACT and Planck SZ catalogues. For clarity, here we limit the ATLAS clusters to those with $N_{200} > 15$.

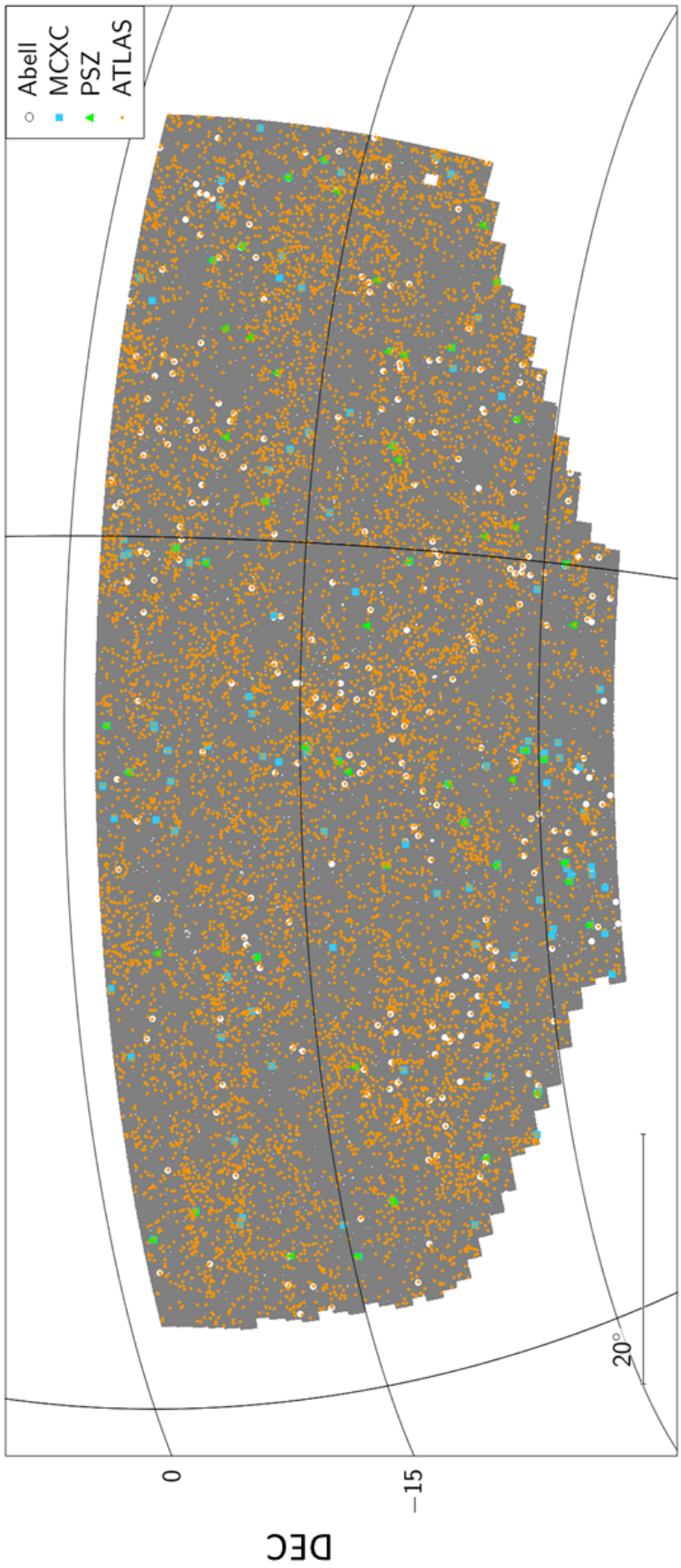

Figure 3.9: Same as Figure 3.8, but for the Northern Galactic Cap (NGC) of the ATLAS survey. Due to the small overlap between ATLAS and the AdvACT cluster catalogue in the NGC, we do not include the AdvACT clusters here for comparison.

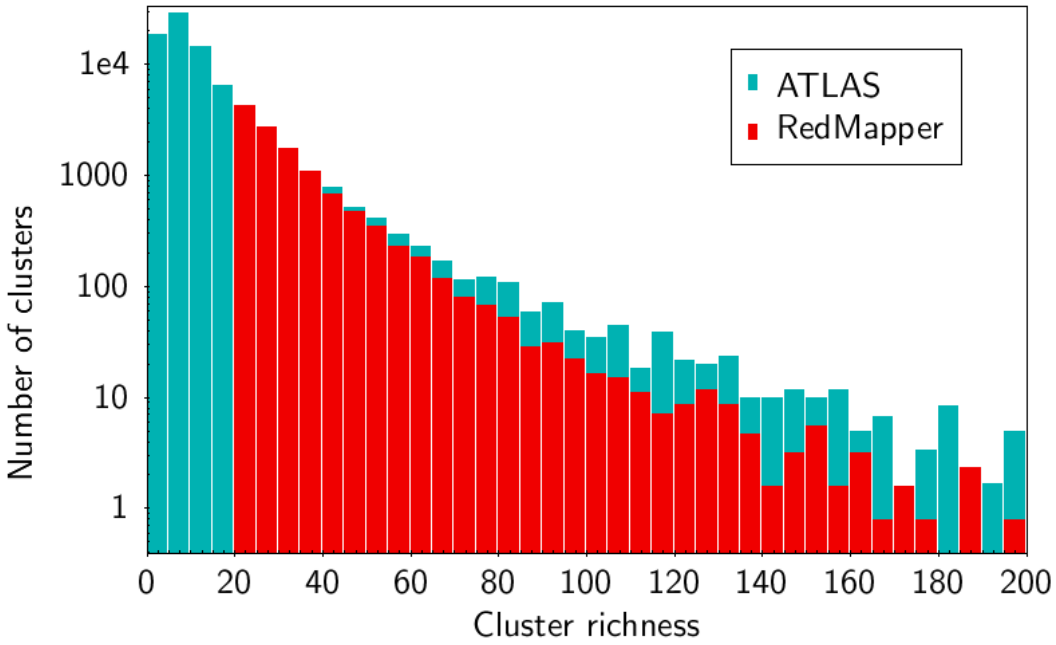

Figure 3.10: ATLAS cluster richness N_{200} distribution in comparison to SDSS RedMapper cluster richness λ. Here both samples are limited to the redshift range $0.1 < z < 0.4$, and the RedMapper histogram is scaled down by a factor of 2.2 to account for the differences between survey areas.

$N_{200} > 20$ are shown in Figure 3.11b. Here, the peaks of the distributions lie at $z \sim 0.25$ and clusters are detected up to $z \sim 0.7$, (or $z \sim 0.6$ for clusters with $N_{200} > 20$).

Figure 3.11c shows the distribution of the error on the weighted mean cluster redshift peaking at ~ 0.006 for the full sample, with errors of ~ 0.004 and 0.003 for clusters with $N_{200} > 10$ and $N_{200} > 20$ respectively. Finally, for the full sample, we show the error on the mean cluster photometric redshifts as a function of redshift in Figure 3.11d, with the error gradually increasing from ~ 0.005 at $z = 0.1$ to 0.015 at $z = 0.6$.

In Figure 3.12 we compare the photometric redshift of our ATLAS clusters with spectroscopic redshifts from their cluster counterparts from MCXC, SDSS RedMapper, Planck and AdvACT samples. While we find a general agreement between the ATLAS photometric redshifts and the spectroscopic redshifts from external samples, we find the rms scatter on this comparison to external sample to be $\sim 3\times$ higher than our estimated error on the cluster weighted mean photometric redshifts (shown in Figure 3.11d). This indicates that the error on the weighted mean given by Equation 3.3.4 tends to underestimate the uncertainty on the cluster redshift. Prior to the public release of the cluster catalogue, we shall perform a detailed study of alternative approaches to estimating the cluster photometric redshift uncertainties (such as standard error, jackknife and bootstrap techniques) that could provide a

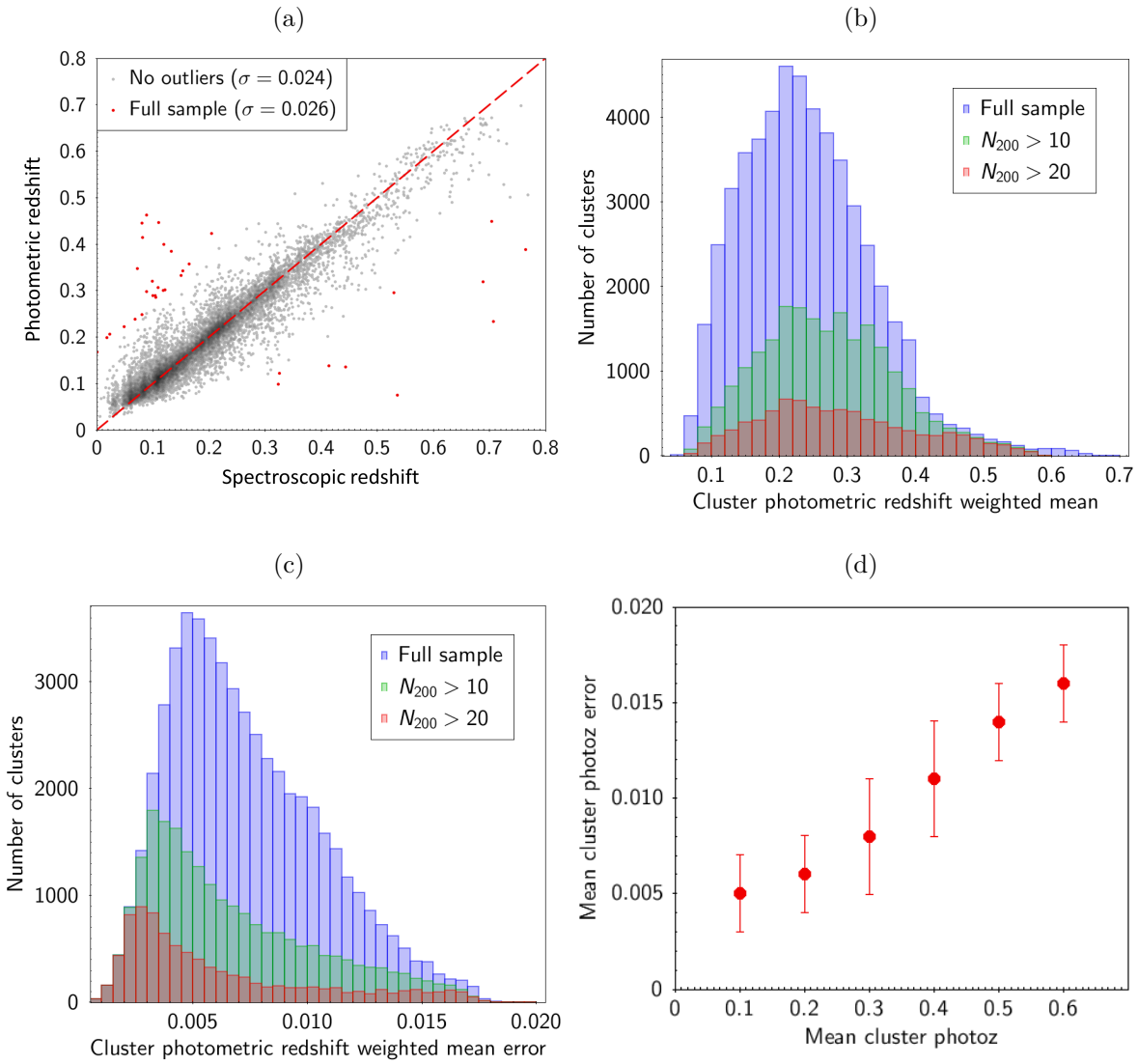

Figure 3.11: (a) Photometric vs. spectroscopic redshift of the ORCA cluster members. The photometric redshifts are calculated following the procedure described in Section 3.3.2. Outliers (red) are defined in Equation 3.3.2. (b) The distribution of the (error-weighted) mean photometric redshift of the VST ATLAS clusters, with the error on the weighted mean photometric redshift shown in panel (c). (d) The error on the mean cluster photometric redshifts as a function of redshift. Here the error bars represent the standard deviation in each bin.

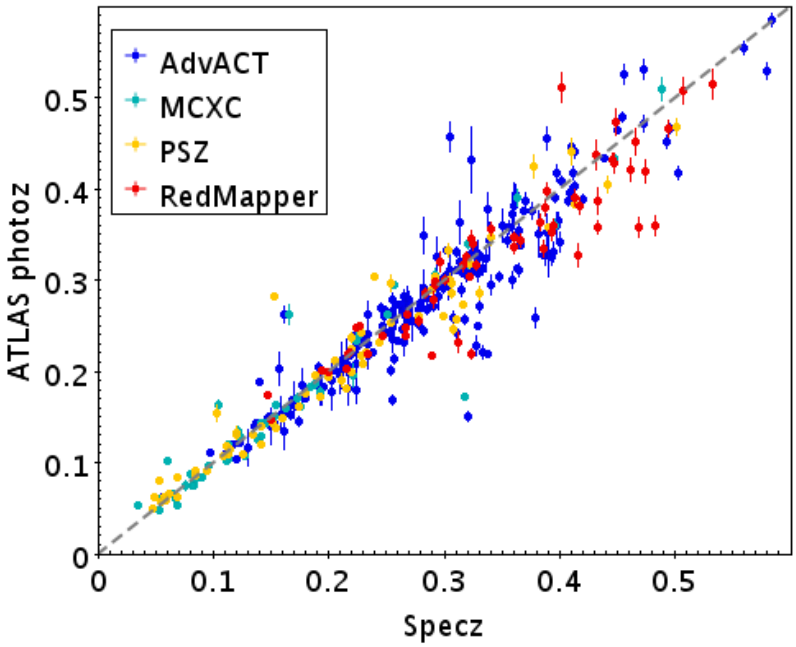

Figure 3.12: A comparison of our ATLAS cluster photometric redshifts to spectroscopic redshifts from the MCXC, SDSS RedMapper, Planck and AdvACT SZ cluster samples.

more realistic estimate of the error.

In the future, it may be possible to improve on our current photometric redshifts by adding J, Y, H and K bands from the VHS survey to aid our machine learning training at higher redshifts. Another improvement will come from the increased size of the high redshift spectroscopic training samples from surveys including Euclid and 4MOST. Finally, photometric redshift improvements may also be achieved by using different machine learning algorithms such as GPZ (Almosallam et al., 2016), or more novel deep learning approaches (e.g. D'Isanto & Polsterer 2018).

3.4.3 ATLAS cluster catalogue columns

Table 3.2 provides a description of the ATLAS catalogue columns, detailing the various properties of clusters including redshift, richness, cluster radius and cluster mass. For each catalogue column, we provide the column title given in the catalogue, the corresponding symbol as used in the text of this work, followed by the units and a description of the values in each column.

Table 3.2: A description of the columns of the ATLAS cluster catalogue. For each catalogue column, the symbols column of this table shows the corresponding symbol used in the text and figures of this thesis.

Column	Symbol [units]	Description
ClusterID	—	A unique cluster identification number assigned to each cluster by the ORCA cluster detection algorithm.
RA	[Degrees J2000]	Right Ascension of the cluster centre (mean RA of cluster members).
DEC	[Degrees J2000]	Declination of the cluster centre (mean DEC of cluster members).
Photoz	$\bar{z}$	Error-weighted mean photometric redshift of the cluster (given by Equation 3.3.3).
Photoz_err	$\sigma_{\bar{z}}$	Error on the weighted mean cluster photometric redshift (given by Equation 3.3.4).
ORCA_Ngal	$N_{\rm gal}$	The number of cluster galaxies detected by ORCA.
R_ORCA	$R_{\rm ORCA}$ [arcmin]	The projected radius of the ORCA cluster on the sky, defined as the angular separation between the cluster centre and the furthest cluster galaxy.
N_1Mpc	$N_{\rm 1Mpc}$	The number of cluster galaxies detected by ORCA within a radius of $1h^{-1}$Mpc from the centre of the cluster. This number is scaled by the theoretical $n(z)$ following Equation 3.3.6.
R_200	R_{200} [h^{-1}Mpc]	The radius from the cluster centre within which the density is 200× the mean density of the Universe (given by Equation 3.3.5.
N_200	N_{200}	The number of cluster galaxies within a radius of R_{200} from the centre of the cluster. This number is scaled by the theoretical $n(z)$ following Equation 3.3.6.
N_200_err	$\sigma_{N_{200}}$	The error on N_{200} given by Equation 3.3.7.

Continued on next page

Table 3.2 – *Continued from previous page*

Column	Symbol [units]	Description
M_200	M_{200} [$10^{14}\mathrm{M}_{\odot}$]	The cluster mass enclosed within a radius of R_{200} from the centre of the cluster (given by Equation 5.2.1). The cluster masses in our catalogue are measured with respect to the mean density of the Universe (often represented using the symbol $M_{200\mathrm{m}}$ in literature).
M_200_err	$\sigma_{M_{200}}$ [$10^{14}\mathrm{M}_{\odot}$]	The error on the M_{200} cluster mass given by Equation 5.2.2.
Q_ORCA	[Q_{seeing}, Q_{photoz}, Q_{ORCA}]	Tuple containing seeing, photometric redshift and overall cluster detection quality flag (see Section 3.3.6).
Notes	—	(If present) 'Lensed?': Previously unpublished candidate strong lensing cluster, 'Lensed': Spectroscopically confirmed / published strong lensing cluster (see Section 3.4.6 for details); 'Ext: Abell, RM, PSZ, AdvACT, MCXC', representing cluster counterparts in Abell, SDSS RedMapper, PSZ, AdvAT and MCXC cluster catalogues, respectively (within R_{ORCA}).

Table 3.3 provides a description of the columns in the ATLAS cluster members catalogues providing unique identifiers, coordinates and photometric redshifts of each cluster galaxy.

3.4.4 Mass and redshift completeness

Figure 3.13a shows the fraction of clusters from the SDSS RedMapper, AdvACT, Planck, MCXC and Abell catalogues overlapping the ATLAS coverage area, that are detected in the ATLAS cluster catalogue. This provides a measure of the completeness of the ATLAS cluster sample as a function of redshift. Here we use the ORCA cluster radius (R_{orca}) as our matching radius for the AdvACT, RedMapper, MCXC and Abell cluster catalogues, while using the Planck position error on the SZ cluster centre as the matching radius. In the case of the AdvACT and Planck samples, we limit the match to clusters with SZ detections with $SNR > 5$. In all cases, the cluster samples are limited to clusters with masses greater than $1 \times 10^{14}\mathrm{M}_{\odot}$, roughly corresponding to the lower mass limit of the ATLAS clusters.

Table 3.3: A description of the columns of the ATLAS cluster members catalogue. For each catalogue column, the symbols column of this table shows the corresponding symbol used in the text and figures of this Chapter.

Column	Symbol [units]	Description
ClusterID	—	A unique cluster identification number assigned to each cluster by the ORCA cluster detection algorithm.
ObjID	—	A unique object identification number assigned to each cluster galaxy by the ORCA cluster detection algorithm.
RA	[Degrees J2000]	Right Ascension of the cluster member.
DEC	[Degrees J2000]	Declination of the cluster member.
Photoz	z	Cluster galaxy photometric redshift as determined by ANNz2 machine learning algorithm (see Section 3.3.2).
Photoz_err	$\sigma(z)$	Error on cluster galaxy photometric redshift as determined by ANNz2.

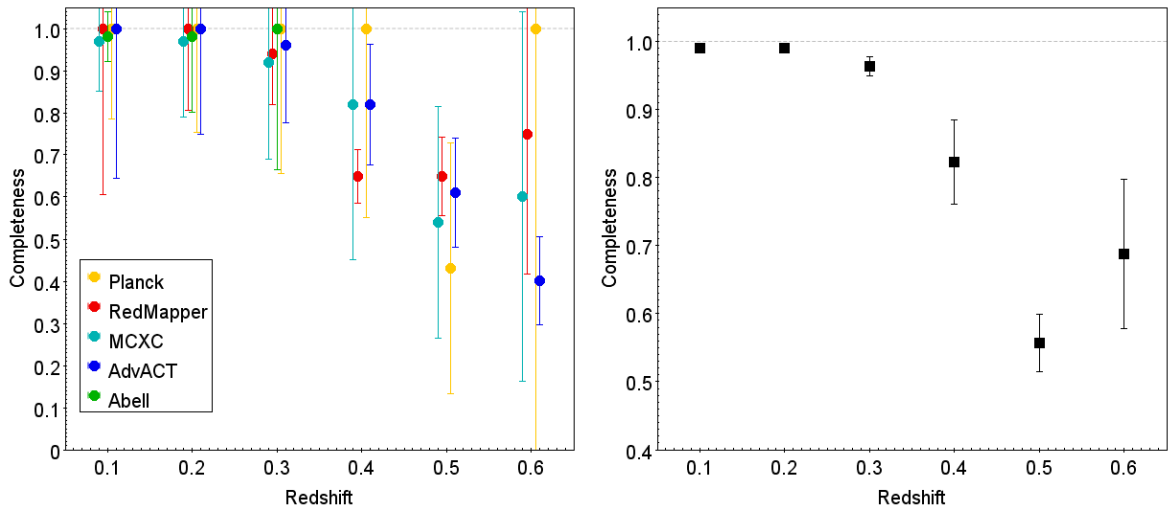

(a) Relative redshift completeness

(b) Mean redshift completeness

Figure 3.13: (a) The redshift completeness of the ATLAS cluster sample, based on the fraction of the recovered SDSS RedMapper, AdvACT, Planck, MCXC and Abell clusters overlapping the ATLAS coverage area (see text for selection and matching criteria). The error bars are given by the propagation of $\sqrt{n}$ error estimates and for clarity, the data points corresponding to different datasets have been slightly shifted along the x-axis. (b) The mean redshift completeness of the ATLAS clusters sample based on the comparison to external clusters in panel (a). Here, the error bars being given by the standard error on the mean.

Figure 3.13b shows the mean completeness of the ATLAS cluster samples as a function of redshift, where the sample is $> 95\%$ complete in the range $z < 0.3$ and $> 80\%$ complete up to $z = 0.4$. We note that the sharp fall in our completeness comparison to Planck at $z = 0.5$ is due to small number statistics of the Planck sample at this redshift range where we detect 3/7 Planck SZ clusters overlapping the ATLAS coverage area.

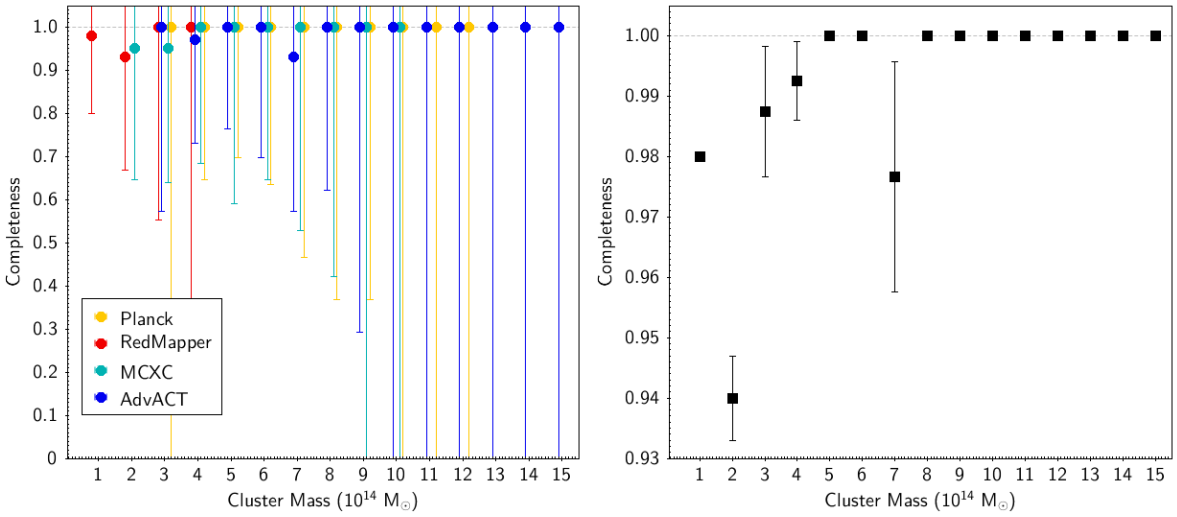

(a) Relative cluster mass completeness (b) Mean cluster mass completeness

Figure 3.14: (a) The fraction of SDSS RedMapper, AdvACT, Planck and MCXC clusters overlapping the ATLAS coverage area which are detected in the ATLAS cluster catalogue. This provides an estimate of the completeness of the ATLAS cluster sample as a function of mass. The error bars shown in this panel are given by the propagation of $\sqrt{n}$ error estimates and for clarity, the data points corresponding to different datasets have been slightly shifted along the x-axis. (b) The mean completeness of the ATLAS sample as a function of cluster mass, based on comparison to the samples shown in panel (a). Here, the error bars given by the standard error on the mean.

Figure 3.14a shows the mass completeness of the ATLAS cluster catalogue by assessing the fraction of SDSS RedMapper, AdvACT, MCXC and Planck clusters detected in the ATLAS sample as a function of cluster mass. Here, all samples are limited to the redshift range $0.1 < z < 0.3$ in order to ensure the mass completeness is not impacted by our reduced completeness at higher redshifts. Figure 3.14b shows the mean cluster mass completeness of the ATLAS sample, with the sample being $> 95\%$ complete across the full $1 \times 10^{14} - 1.5 \times 10^{15} M_\odot$ mass range, with a near full recovery rate of external clusters for masses $> 5 \times 10^{14} M_\odot$.

3.4.5 Comparison to RedMapper

In Figure 3.15, we show a comparison of the ATLAS and SDSS RedMapper cluster catalogues in the regions where the two surveys overlap. We note the caveat that the comparison performed in this Section is limited to an overlap area of ~ 200 deg^2 between the ATLAS and RedMapper cluster samples (i.e. $\sim 4\%$ and $\sim 2\%$ of the ATLAS and SDSS survey areas respectively), with the overlap area being situated at the edge of both surveys. Furthermore, While we remove any cluster that lies within $5'$ of the boundaries of the two survey coverage areas, given the limited overlap area and potential "edge effects", one should keep in mind that

the comparison performed here may not be representative of the complete cluster samples.

Here, we limit the ATLAS and RedMapper clusters to those with richness greater than 30 to match the richness lower limit of the Abell clusters which are added along with clusters from the AdvACT catalogue for comparison. For reasons that we will explore in more detail later, in the redshift range $0.05 < z < 0.35$ ATLAS appears to perform better than RedMapper in recovering Abell and AdvACT clusters[4]. In the $0.35 < z < 0.55$ redshift range, however, RedMapper appears to recover a larger fraction of AdvACT clusters than ATLAS. We also note that at higher redshifts there appears to be a larger number of RedMapper clusters with no detections in ATLAS or AdvACT catalogues compared to lower redshift ATLAS clusters with no detections in the other catalogues.

Table 3.4 shows a comparison of the sky density of the ATLAS cluster catalogue to the SDSS RedMapper catalogue in five bins of redshift ranging from $z = 0.05 - 0.55$. For the purposes of this comparison, we limit the ATLAS sample to clusters with richness $N_{200} > 20$, to allow for direct comparison with the sky densities of the RedMapper sample, given their similar $\lambda > 20$ richness cut. Similar to what we saw in Figure 3.15, one can see here that the ATLAS catalogue has a higher sky density of clusters compared to RedMapper, in the redshift range $z < 0.25$ while the situation is reversed in the redshift at $z > 0.35$.

Table 3.4: Number and sky density (number of clusters per square degree) of ATLAS and SDSS RedMapper cluster samples in different redshift bins. Here, we apply a richness cut of $N_{200} > 20$ to our ATLAS sample, to match the RedMapper richness cut of $\lambda > 20$.

	Number of clusters		Sky density	
Redshift	ATLAS	RedMapper	ATLAS	RedMapper
$0.05 < z < 0.15$	41	17	0.19	0.08
$0.15 < z < 0.25$	127	71	0.59	0.33
$0.25 < z < 0.35$	112	127	0.52	0.59
$0.35 < z < 0.45$	67	215	0.31	1.00
$0.45 < z < 0.55$	41	99	0.19	0.46

A similar pattern can be seen in Figure 3.16a where we compare the photometric redshift distributions of ATLAS and RedMapper samples for clusters with richness greater than 20. To further examine this, we calculate the detection rate of Abell clusters (which are classified as clusters with 30 or more members), by the RedMapper catalogue across the full SDSS

[4]We note that the Abell sample is not as complete as the ATLAS and RedMapper samples as the latter surveys have the advantage of detecting clusters in multiple colours, (with both catalogues detecting $\sim 3 - 4$ times as many clusters as the Abell sample across their full survey footprints in the $z < 0.3$ redshift range). However, Abell is still a useful sample for comparison to ATLAS and RedMapper, as clusters detected in both ATLAS and Abell samples are likely to be genuine rich clusters which should be detected by RedMapper within its $\lambda > 20$ limit

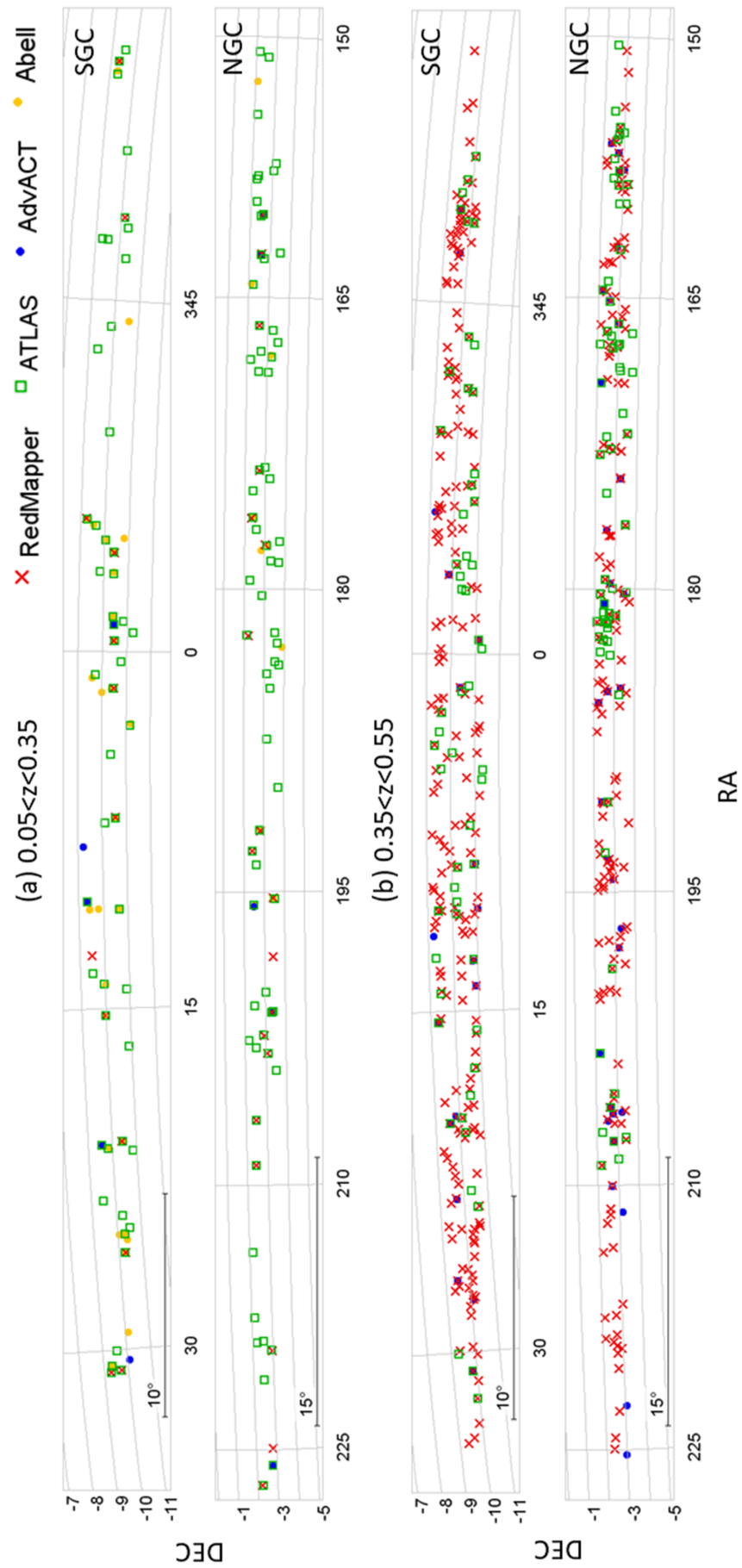

Figure 3.15: (a) Comparison of ATLAS, RedMapper and Abell clusters limited to the redshift range $0.05 < z < 0.35$ in the overlapping areas of ATLAS and SDSS. (b) Same as (a) but now ATLAS and RedMapper are compared to AdvACT clusters with all samples limited to the redshift range $0.35 < z < 0.55$. In all cases, ATLAS and RedMapper clusters are limited to those with richness greater than 30 to match the richness lower limit of the Abell catalogue. We also note that the number density of Abell clusters in the ATLAS-SDSS overlap area in the NGC is $\sim 50\%$ lower compared to the SGC.

survey footprint. We find that RedMapper only recovers $\sim$ 60% of the $0.05 < z < 0.3$ Abell clusters, compared to a $\sim$ 80% recovery rate in the ATLAS sample with a richness cut of $N_{200} > 20$. Consequently, the higher number of ATLAS detections in this redshift range relative to RedMapper is likely to be predominantly due to the incompleteness of the RedMapper sample at lower redshifts.

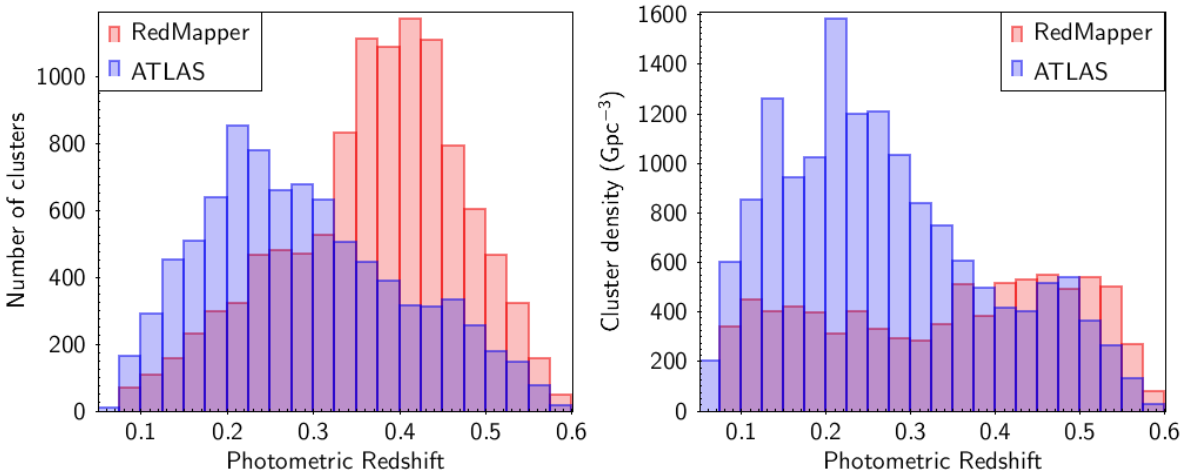

(a) (b)

Figure 3.16: (a) A comparison of the photometric redshift distribution of ATLAS and SDSS RedMapper cluster catalogues. Here, the ATLAS samples is restricted to clusters with richness $N_{200} > 20$ to roughly match the RedMapper richness cut of $\lambda > 20$. The RedMapper histogram is scaled down by a factor of 2.2 to account for the difference between survey areas. (b) The number density of ATLAS and RedMapper clusters per Gpc^3. Here, in addition to the richness>20 cuts imposed in panel (a), the two samples are limited to clusters with masses $M_{200} > 3 \times 10^{14} h^{-1} \mathrm{M}_\odot$ for the purpose of comparison to the cluster mass functions later presented in Chapter 5.

In Figure 3.16b we compare the redshift distributions of the ATLAS and RedMapper samples per unit volume and impose a mass cut of $M_{200} > 3 \times 10^{14} h^{-1} \mathrm{M}_\odot$ on both samples (details of our cluster mass calibrations are presented in Section 5.2), in addition to limiting them to clusters with richness>20. Here, the better agreement between the ATLAS and RedMapper redshift histograms at $z > 0.35$ compared to Figure 3.16a, suggests that the majority of the additional RedMapper detections at higher redshifts are clusters with $M_{200} < 3 \times 10^{14} h^{-1} \mathrm{M}_\odot$.

We now explore the completeness and purity of the ATLAS sample based on direct comparison to RedMapper across the full range of cluster masses. In column (2) of Table 3.5, we calculate the fraction of SDSS RedMapper clusters (within the ATLAS coverage area) that are also detected by ORCA using the ATLAS data[5]. Here, our aim is to simply compute the likelihood

[5]Similar to Section 3.4.4, we use the ORCA radius R_{ORCA} as our matching radius here and throughout the rest of this Section when comparing the two catalogues.

that a SDSS RedMapper cluster detection is also identified by ORCA in the ATLAS data; as such, when performing the matching, we only impose a redshift cut on the RedMapper catalogue to allow for matches to be made in cases where the two catalogues assign the same cluster to different redshift bins. We also remind the reader that in the public release of the RedMapper catalogue a richness cut of $\lambda > 20$ has been imposed on the clusters, however, for the purpose of this comparison we do not disregard successful matches between RedMapper and ATLAS clusters that have an estimated richness of $N_{200} < 20$.

With these caveats in mind, we convert the recovery fractions shown in column (2) to percentages giving an estimate of the completeness of the ATLAS catalogue as a function of redshift (under the assumption that the RedMapper sample is 100% pure with accurate estimates of photometric redshift). Based on this comparison, we find that the ATLAS sample is 100% complete up to $z < 0.25$, with a slight reduction in completeness to 95% between $0.25 < z < 0.35$ and a further reduction down to 65% completeness at $z > 0.35$. Although these values are presented here to show a full comparison of the two samples, we note that the mean completeness shown in Figure 3.13b is likely to be a more reliable estimate of the completeness of the ATLAS cluster sample than estimates based on comparison to any one external sample alone.

Table 3.5: Various comparisons of the intersections between the ATLAS and SDSS RedMapper cluster catalogues.

Redshift (1)	AT/RM (2)	AT Comp. (3)	RM/AT (4)	VI (5)	AT Purity (6)	RM Comp. (7)
$0.05 < z < 0.15$	13/13	100%	16/37	+18/37	34/37 (92%)	16/34 (47%)
$0.15 < z < 0.25$	54/54	100%	60/95	+20/95	80/95 (84%)	60/80 (75%)
$0.25 < z < 0.35$	118/126	94%	71/100	+14/100	85/100 (85%)	71/85 (84%)
$0.35 < z < 0.45$	172/262	65%	53/91	+7/91	60/91 (66%)	53/60 (88%)
$0.45 < z < 0.55$	79/122	65%	19/58	+6/58	25/58 (43%)	19/25 (76%)

Notes. (columns 2 & 3) Fraction & percentage of SDSS RedMapper clusters with detections in the ATLAS cluster catalogue. (4) The fraction of ATLAS clusters with counterpart detections in the RedMapper catalogue. (5) Among the ATLAS clusters not matched to RedMapper in column (4), how many clusters we constitute as genuine and rich detection clusters based on Visual Inspection (VI) of their photo-z $n(z)$. (6) The fraction of ATLAS detections that are either detected by RedMapper or appear as likely detections based on the VI of the cluster $n(z)$s. (7) An estimate of the completeness of the RedMapper based on the ratio of RedMapper cluster detections to the number of "pure" ATLAS detections (from column 6).

In columns (4, 5 & 6) of Table 3.5, we estimate the purity of the ATLAS cluster catalogue based on comparison to the cluster detections by RedMapper in the overlap region between SDSS and ATLAS. As a richness cut of $\lambda > 20$ is imposed on the RedMapper sample, here,

we are also limited to the richness range $N_{200} > 20$ when estimating the purity of our cluster detections. As we are interested in assessing our sample purity as a function of redshift, we limit the ATLAS sample to photometric redshift bins shown in column (1) and look for confirmation that the ATLAS detection is also identified by RedMapper in SDSS as a cluster with $\lambda > 20$. The fraction of ATLAS detections confirmed by RedMapper in this way at each redshift bin is shown in column (4).

We note, however, that without access to the full RedMapper catalogue we have no way of checking whether our $N_{200} > 20$ clusters with no successful matches to RedMapper may have been detected and classified by RedMapper as clusters with $\lambda < 20$. To overcome this limitation, in the next step we visually inspect the photometric redshifts of the clusters that were detected as $N_{200} > 20$ systems in ATLAS, but did not have a successful match in RedMapper. We also count our cluster detections as "pure" (i.e. non-spurious detections) if $> 50\%$ of the cluster members appear concentrated in a histogram with a width of $z \pm 0.025$ (corresponding to the ATLAS RMS error on cluster galaxy photometric redshifts). The choice of this criterion was motivated based on visual inspection of the photometric redshift histograms of ATLAS clusters with successful matches to RedMapper, where almost all clusters detected in both catalogues had ATLAS or SDSS photometric redshift histograms which were centred around a redshift with more than half of cluster members lying within $z \pm 0.025$ of the histogram peak. Figure 3.17 shows colour images and photometric redshift histograms of two $N_{200} > 20$ ATLAS clusters with no SDSS RedMapper detections, which were confirmed as pure following the procedure described above.

The fraction of additional clusters confirmed as genuine cluster detections based on visual inspection is presented in column (5), with column (6) showing the sum of the fractions in columns (4 & 5) with the percentages in this column providing an estimate of the purity of the ATLAS cluster detections. Based on this estimate we find our cluster sample to be $> 90\%$ pure at $z < 0.15$, and $\sim 85\%$ pure in the redshift range $0.15 < z < 0.35$. The purity of the sample then falls to 66% and 43% in our final two redshift bins. This reduction of sample purity with increasing redshift could be partially due to the fact that as we reach the magnitude limits of the ATLAS and SDSS surveys the likelihood of real but faint cluster members not being detected by RedMapper increases, bringing clusters with richness greater than 20, below their $\lambda > 20$ limit. Similarly, the increase in the uncertainty on our estimated photometric redshifts with increasing redshift, reduces the number of clusters classified as pure on the basis of their photo-z histograms in column (5). On the other hand, it is also possible that at higher redshifts RedMapper performs better than ORCA in overcoming

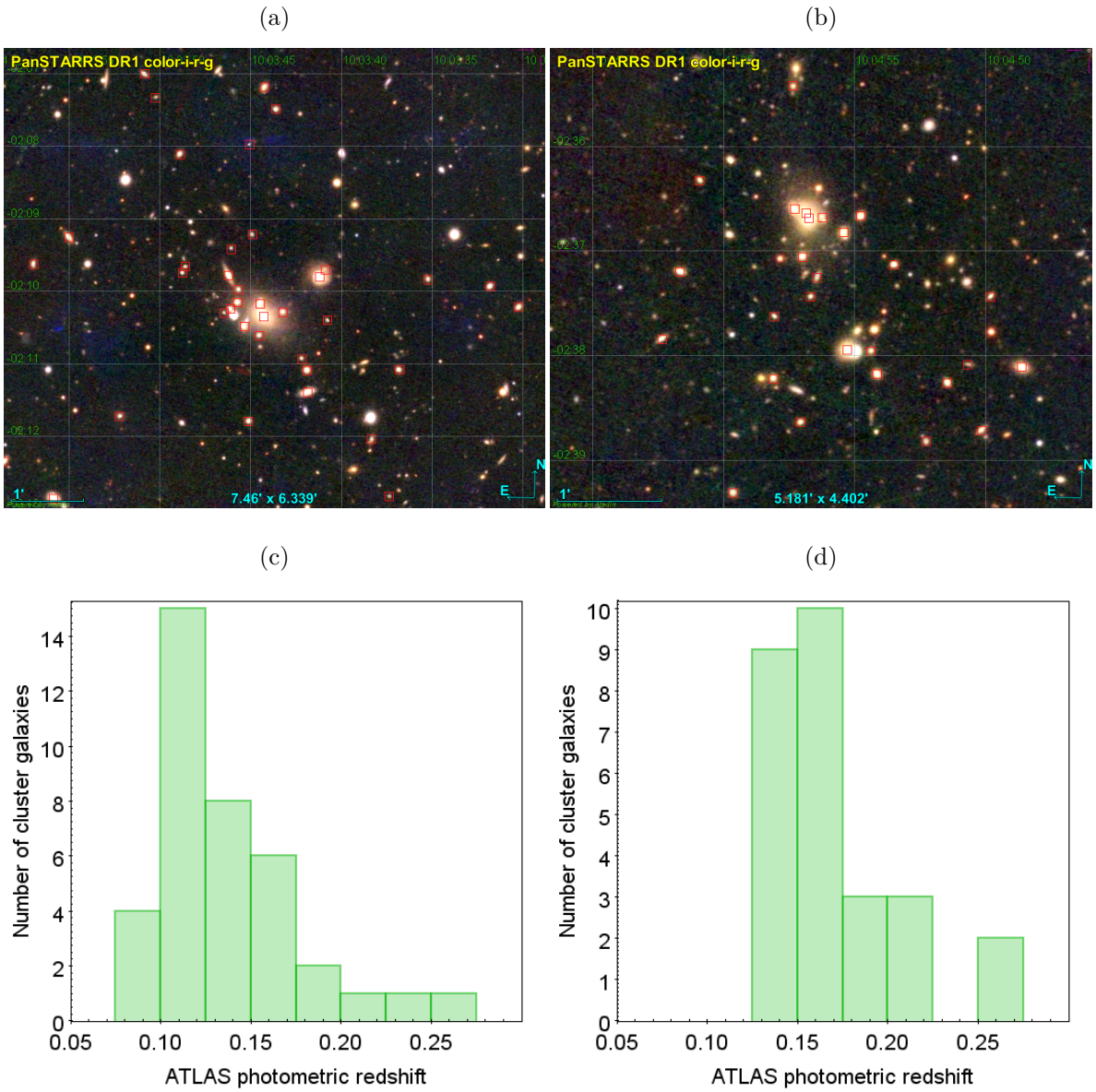

Figure 3.17: (a & b) PanSTARRS colour images of two $N_{200} > 20$ ATLAS clusters with no RedMapper detections in SDSS. Here the cluster members identified in ORCA are shown by the red squares. (c & d) The photometric redshift histograms for clusters in panels (a & b) respectively.

projection effects which could artificially increase the richness of our clusters, or result in false cluster detections. We refer the reader to Section 6.4.3 of Murphy et al. (2012), for a different analysis of the purity of ORCA cluster detections as a function of cluster mass and redshift, based on comparison to SDSS-like simulated mock cluster catalogues. Based on this comparison, the purity of ORCA detections at the median redshift of the survey was shown to be $> 70\%$ across all cluster masses.

Column (7) of Table 3.5 shows an estimate of the completeness of the RedMapper sample, which is defined as the fraction of "pure" ATLAS detections co-detected by RedMapper[6]. Here, we find the completeness of RedMapper to gradually increase from 47% in the $z = 0.1$ bin to 88%, in the $z = 0.4$ bin, before falling down to 76% at $z = 0.5$. At this point we remind the reader that although we were able to estimate the completeness of the ATLAS sample in column (3) by including successful matches between ATLAS and RedMapper in cases where a $\lambda > 20$ RedMapper cluster had an ATLAS detection with $N_{200} < 20$, we are unable to do the reverse in column 6. So while it is possible that some of our $N_{200} > 20$ ATLAS detections may have RedMapper counterparts with $\lambda < 20$ which would increase the RedMapper completeness estimate; we have no way of verifying this. Nonetheless, the information in column (7) provides a useful estimate of the percentage of low-redshift ATLAS clusters with richness $N_{200} > 20$ that are missed by RedMapper, (possibly due to differences in our definitions of cluster richness and what constitutes a "pure" cluster detection). The increased RedMapper completeness with redshift could be due to the reduced completeness of the ATLAS sample as a function of redshift, or due to the fact that at higher redshifts ATLAS and RedMapper tend to contain a larger fraction of clusters with higher masses which are easier to detect. However, this could also be indicative of a genuine improvement in the completeness of the RedMapper sample with redshift.

To summarise, comparison of the ATLAS cluster catalogue to RedMapper shows that at $z < 0.35$ the ATLAS sample is highly complete, and the majority of our clusters appear to be genuine detections. At $z < 0.3$ we also find that a number of $N_{200} > 20$ ATLAS clusters (which were visually confirmed as rich clusters) are not detected as $\lambda > 20$ clusters by RedMapper. Similarly, we found that ATLAS generally performs better than RedMapper at recovering $z < 0.35$ Abell and AdvACT clusters, with ATLAS recovering $\sim 80\%$ of $0.05 < z < 0.3$ Abell clusters while RedMapper only recovers $\sim 60\%$ of Abell clusters. At $z > 0.35$ while ATLAS appears to be less complete (65%) compared to RedMapper, Figure 3.16b suggests that the additional RedMapper cluster detections at higher redshifts tend to be clusters of lower mass with a good agreement being found between the $n(z)$ of the two samples for clusters with masses $M_{200} > 3 \times 10^{14} h^{-1} \mathrm{M}_{\odot}$.

[6]We refer the reader to Section 11 of Rykoff et al. (2014) for a more systematic analysis of the completeness of the RedMapper sample.

3.4.6 New gravitational lensing systems

As shown in Table 3.2, in the 'notes' column of the cluster catalogue, we flag any clusters identified as candidate strong lensing systems. In order to identify giant lensing arc candidates, we visually inspect the ATLAS clusters with richness $N_{200} > 20$ using *gri* colour images from DES DR1 (Abbott et al., 2018a) and *grz* colour images from DECaLS DR5 (Dey et al., 2019) surveys. These surveys offer the advantage of being deeper than ATLAS, making it possible to identify strong lensing arcs that are too faint to be visible in the ATLAS data. However, in areas where these surveys do not overlap with ATLAS, we rely on ATLAS and Pan-STARRS (Chambers et al., 2016) *gri* colour images. Our visual inspection was conducted using the ALADIN V10.0 software (Bonnarel et al., 2000) which provided the DES, DECaLS and Pan-STARRS colour imaging data, with an interactive user interface allowing for fast visual inspection of a large number of clusters. This results in the detection of 23 previously unpublished strongly lensed candidates, four of which are shown in Figure. 3.18.

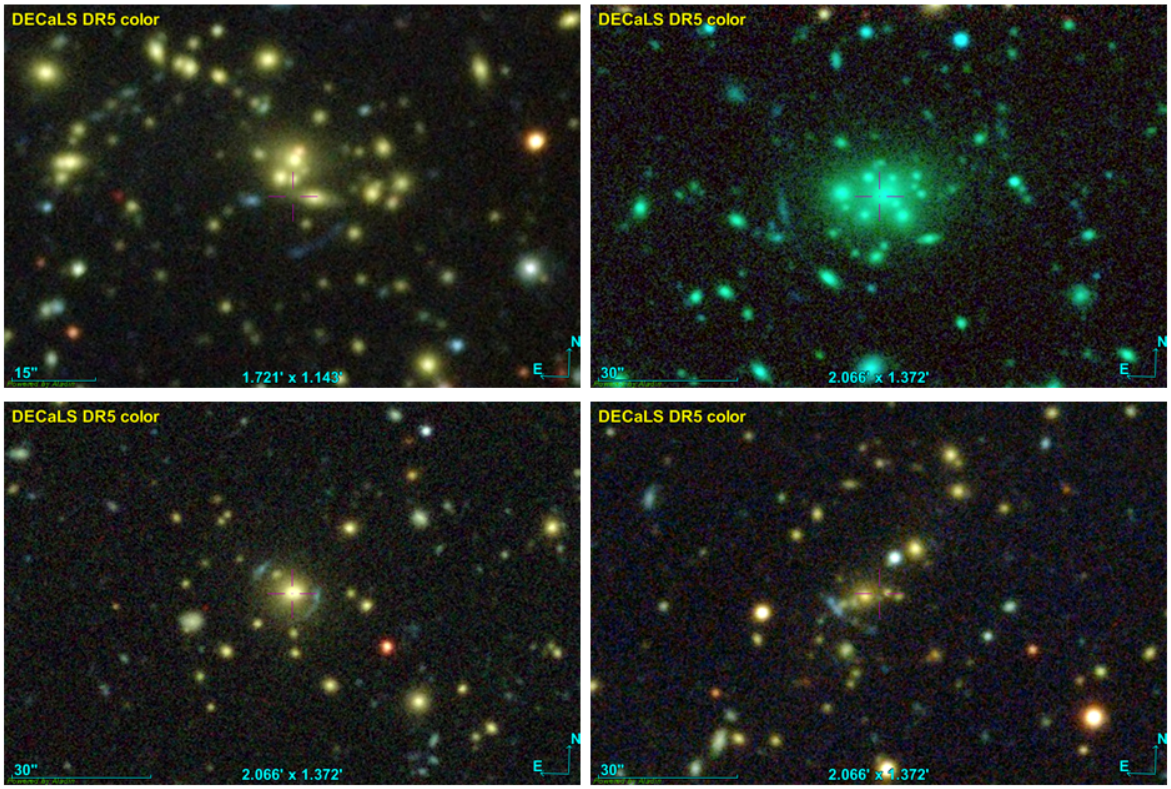

Figure 3.18: Four newly discovered strong lensing ATLAS clusters. Note that the colours images shown here are composed of DECaLS *grz* data which are deeper than ATLAS imaging, thus allowing for the detection of lensing arcs that are too faint to be seen in ATLAS imaging.

With the aid of the ATLAS cluster catalogue, in the future machine learning algorithms (e.g. Jacobs et al. 2017; Huang et al. 2020) can be implemented to identify many more cluster lenses in ATLAS imaging, in a more systematic and automated manner. These lensed clusters can then be modelled in bulk using automated machine learning algorithms such as Hezaveh et al. (2017). More detailed analyses of these clusters can also be conducted using algorithms such as HYBRID-LENSTOOL (Niemiec et al., 2020) which can provide cluster masses with an average precision of 5% using a combination of strong lensing in the cluster core and weak lensing in the cluster outskirts, providing a valuable sample for improved calibration of SZ and X-ray cluster masses.

3.5 Conclusions

In this Chapter, we have presented a new catalogue of photometrically detected galaxy groups and clusters, using the ORCA cluster detection algorithm in combination with the *griz* bands of the VST ATLAS survey, covering ~ 4700 deg^2 of the Southern sky. The catalogue contains $\sim 9,000$ clusters with richness $N_{200} > 20$. We obtained photometric redshifts for our cluster members using the ANNz2 machine learning algorithm. This resulted in photometric redshifts with an RMS of ~ 0.025 for our cluster galaxies and a mean redshift uncertainty of ~ 0.005 for our clusters with richness $N_{200} > 20$. The photometric redshift of our sample peaks at $z \sim 0.25$, extending up to $z = 0.7$.

We presented a discussion of our calculations of cluster richness (N_{200}) which we shall later use to obtain estimates of our cluster masses (M_{200}) in Chapter 5. We then assessed the completeness of our cluster sample based on comparison to external cluster catalogues, finding our sample to be complete at $> 95\%$ in the range $z < 0.35$, $> 80\%$ complete up to $z = 0.45$, and $\sim 60\%$ complete in the $0.45 < z < 0.65$ redshift range. In terms of cluster mass, we found our sample to be greater than $\sim 95\%$ complete in the mass range $1 \times 10^{14} - 1.5 \times 10^{15} \mathrm{M}_{\odot}$, with near full completeness in the $> 5 \times 10^{14} \mathrm{M}_{\odot}$ mass range. Based on a comparison to the SDSS RedMapper cluster detections as well as visual inspection of our clusters, we estimate the purity of our cluster detections with richness $N_{200} > 20$ to be 92% in the range $z < 0.15$, 85% at $0.15 < z < 0.35$, 66% at $0.35 < z < 0.45$ and 43% at $0.45 < z < 0.55$.

Our comparison to the RedMapper catalogue showed that in the $0.05 < z < 0.35$ redshift range, the ATLAS sample contains a larger number of cluster detections and recovers a larger fraction of Abell and AdvACT clusters compared to RedMapper. At higher redshifts ($0.35 <$

$z < 0.55$) the RedMapper catalogue appears to perform better than ATLAS at recovering AdvACT clusters, but also detects a large number of clusters not found in the AdvACT sample. At $z > 0.35$ we also find a good agreement between the redshift distributions of the ATLAS and RedMapper samples above a mass limit of $M_{200} > 3 \times 10^{14} h^{-1} \mathrm{M}_{\odot}$, indicating that the difference in the number of cluster detections between ORCA and RedMapper at higher redshifts is limited to relatively low mass clusters.

Finally, based on visual inspection of our rich ATLAS clusters, using DES, DECaLS, Pan-STARRS and ATLAS imaging, we identified 23 previously unpublished strong lensing cluster candidates. With future follow-up spectroscopic observations these clusters can yield high-precision masses which could be used to improve the ATLAS cluster mass calibrations.

Chapter 4

Spectroscopic follow-up of Planck SZ clusters

4.1 Introduction

The Sunyaev–Zeldovich (SZ; Sunyaev & Zeldovich 1972; Sunyaev & Zeldovich 1980) effect originates due to inverse Compton scattering of CMB photons as they pass through galaxy clusters and interact with the high-energy electrons in the intracluster medium (ICM). On average, this scattering results in a boost to the energy of the CMB photon, causing a small, frequency-dependent distortion of the CMB spectrum observed through the cluster, known as the thermal SZ (tSZ) effect. The magnitude of this effect is proportional to the product of the ICM electron density and temperature, integrated along the line of sight and provides a powerful tool for detection of galaxy clusters (Allen et al., 2011).

The SZ temperature distortion, ΔT, at a frequency ν is given by:

$$\Delta T(\nu) = \bar{T}_{\rm CMB} f_{\rm SZ}(x) \int n_e \frac{K_{\rm B} T_{\rm e}}{m_{\rm e} c^2} \sigma_{\rm T} dl \equiv \bar{T}_{\rm CMB} f_{\rm SZ}(x) Y_{\rm SZ}, \tag{4.1.1}$$

where the mean CMB temperature $\bar{T}_{\rm CMB} = 2.7260 \pm 0.0013$ (Fixsen, 2009), $x = h\nu / k_{\rm B} \bar{T}_{\rm CMB}$, h is Planck's constant, $k_{\rm B}$ is the Boltzmann constant, c is the speed of light, $n_{\rm e}$, $T_{\rm e}$ and $m_{\rm e}$ are the electron density, temperature and mass respectively, $\sigma_{\rm T}$ is the Thomson cross-section, and the integration is performed along the line of sight. $f_{\rm SZ}(x)$ encapsulates the frequency dependence of the SZ effect with:

$$f_{\rm SZ}(x) = \left(x \frac{e^x + 1}{e^x - 1} - 4 \right) (1 + \delta_{\rm rc}), \tag{4.1.2}$$

where $\delta_{\rm rc}$ encompasses relativistic corrections (Nozawa et al., 2000).

A secondary, smaller distortion of the CMB is caused by the kinetic SZ (kSZ) effect which arises due to the peculiar motion of a galaxy cluster with respect to the CMB rest frame, with a magnitude proportional to the peculiar velocity of the cluster. We refer the reader to Carlstrom et al. (2002) for a review of the SZ effect and its applications in cosmology.

In this chapter, we present our follow-up spectroscopic observations of 11 Planck SZ sources with no previous cluster identification or redshifts, with optical counterparts identified via the VST ATLAS cluster catalogue. Our targeting of these clusters was primarily motivated by the tension found between the constraint on σ_8 obtained from Planck SZ cluster counts and the constraint based on Planck analysis of primary fluctuations in the CMB (see Figure 13 of Planck Collaboration et al. 2016d). The source of this tension could be attributed to incompleteness of the Planck SZ sample, or biases in the scaling relations used to convert the SZ signal to cluster masses (which are discussed in detail in Planck Collaboration et al. 2020). Currently 365 ($\sim$ 25%) of Planck SZ sources have no redshift measurements or confirmed counterparts in external cluster samples, with 41 of these sources[1] overlapping the ATLAS survey coverage area. By obtaining multi-object spectroscopic observations of these clusters we will be able to confirm the mean cluster redshift, enabling us to estimate the cluster mass based on its Planck SZ flux, which we can compare to the second estimate of the cluster masses based on the velocity dispersion of the cluster galaxies.

In Section 4.2, we provided a list of our 11 observed clusters for which we have successfully obtained redshifts, velocity dispersions and cluster masses. We also provide a summary of other Planck SZ clusters targeted in our observations which require further analysis and may be published in future works. Section 4.3 contains a description of our observations, data reduction, spectra extraction and template fitting, followed by details of how our cluster mass estimates based on the Planck SZ flux and cluster member velocity dispersions are obtained. In Section 4.4, we compare the spectroscopic redshifts of our observed clusters to the photometric redshifts from the ATLAS cluster catalogue. We then compare the SZ flux-based masses of our observed clusters to those based on velocity dispersions, as well as masses obtained from our ATLAS cluster richness estimates (see Section 5.2). We then provide further analysis of the reliability of our measured spectroscopic redshifts by plotting a Hubble diagram of our cluster BCGs and discuss why we believe we have correctly identified the optical cluster counterparts to our targeted SZ source. Finally, we present a summary of

[1]Here we limit SZ sources to those with a SNR$>$ 5 or a neural network quality flag $Q_{\rm NEURAL} > 0.9$.

our results in Section 4.5 and discuss their implications for future works.

4.2 Target List

In Table 4.1 we provide general details of 10 low redshift (LOZ) and one high redshift (HIZ) Plank SZ clusters which were targeted and spectroscopically confirmed by our EFOSC2 and FORS2 MOS observations as described in Section 4.4.1. The information provided in this table is taken from the PSZ2 cluster catalogue (Planck Collaboration et al., 2014a). In all cases, our chosen targets have SNR$>$ 5 or a neural network quality flag $Q_{\rm NEURAL} > 0.9$ (see the reference paper for a detailed definition of $Q_{\rm NEURAL}$), making it unlikely that these sources are spurious Planck SZ detections.

Here, we defined our low redshift targets as those with matches in the ATLAS cluster catalogue and photometric redshifts $z < 0.5$. Our high redshift targets are assumed to have a redshift $z > 0.5$ and were chosen on the basis of their lack of detection in the ATLAS cluster catalogue (and imaging), but faint detection in the Vista Hemispheric Survey (VHS; McMahon et al. 2013) J and K imaging, indicating their high redshift. Another two high redshift cluster candidates were selected for observations from outside the ATLAS survey area, following the suggestion of the Planck team. Figure 4.1 shows an example of a Planck SZ cluster candidate (shown by the red square) in the ATLAS coverage area, with no previous spectroscopically confirmed optical counterpart. Here, the yellow circles indicate the galaxies identified as cluster members by ORCA using ATLAS imaging.

The results presented in this Chapter are a subset of a larger sample of 35 low redshift and 4 high redshift clusters which were among the target list for our multi-object spectroscopy observations. Table 4.2 shows a summary of the Planck SZ clusters with ATLAS cluster counterparts that were amongst our EFOSC2 and FORS2 target list, but with no successful redshift confirmation. In each case the 'Notes' column indicates the reason why we have not presented a redshift for these clusters along with our results in Chapter 4. We were not able to observe 6/35 low redshift targets due to unsuitable observing conditions i.e. high cloud coverage or high winds requiring telescope dome closure. Furthermore, the pipeline reduction failed for 2 low redshift targets requiring manual reduction, with a further 4 low redshift and 3 high redshift clusters requiring further customisation of the pipeline settings (or manual reduction) in order to improve the sky subtraction, as the sky lines currently dominate the spectra for these clusters. For the remaining 13 low redshift clusters, we were unable to obtain

Table 4.1: Details of our observed Planck SZ clusters.

Target ID (1)	Name (2)	RA (3)	DEC (4)	SNR (5)	$Q_{\rm NEURAL}$ (6)	$Y_{5\rm R500}$ (7)
LOZ-1	PSZ2 G013.06-75.46	23:47:24.63	-31:09:03.1	5.29	0.95	1.75 ± 0.73
LOZ-2	PSZ2 G029.66-47.63	21:45:44.22	-21:46:48.8	5.74	0.94	1.25 ± 0.39
LOz-3	PSZ2 G025.89-46.67	21:38:42.60	-23:59:05.8	4.93	0.93	2.41 ± 1.2
LOZ-4	PSZ2 G043.44-41.27	21:36:44.07	-10:17:47.8	5.55	0.97	1.54 ± 0.59
LOZ-5	PSZ2 G317.79+26.63	13:55:58.09	-34:22:01.1	5.76	0.45	4.17 ± 1.79
LOZ-6	PSZ2 G269.02+46.30	11:19:10.48	-10:23:55.2	4.67	0.90	0.82 ± 0.22
LOZ-7	PSZ2 G278.92+31.06	11:18:57.03	-27:27:28.1	5.18	0.99	1.07 ± 0.32
LOZ-8	PSZ2 G270.88+37.23	11:05:19.48	-18:56:55.0	5.48	0.99	4.03 ± 2.29
LOZ-9	PSZ2 G253.43+30.57	10:00:22.09	-15:24:36.4	4.94	0.90	1.88 ± 0.80
LOZ-10	PSZ2 G210.02-56.38	03:16:27.66	-20:46:40.3	4.73	0.99	4.78 ± 2.75
HIZ-1	PSZ2 G208.61-74.39	02:00:14.95	-24:54:24.1	4.86	0.97	0.94 ± 0.25

Notes. (1) Cluster short name (LOZ: low redshift candidate, HIZ: high redshift candidate), (2) Planck SZ catalogue name, (3 & 4) SZ coordinates, (5) Signal to noise ratio, (6) Neural network quality flag, (7) SZ flux in terms of the total integrated Comptonization parameter.

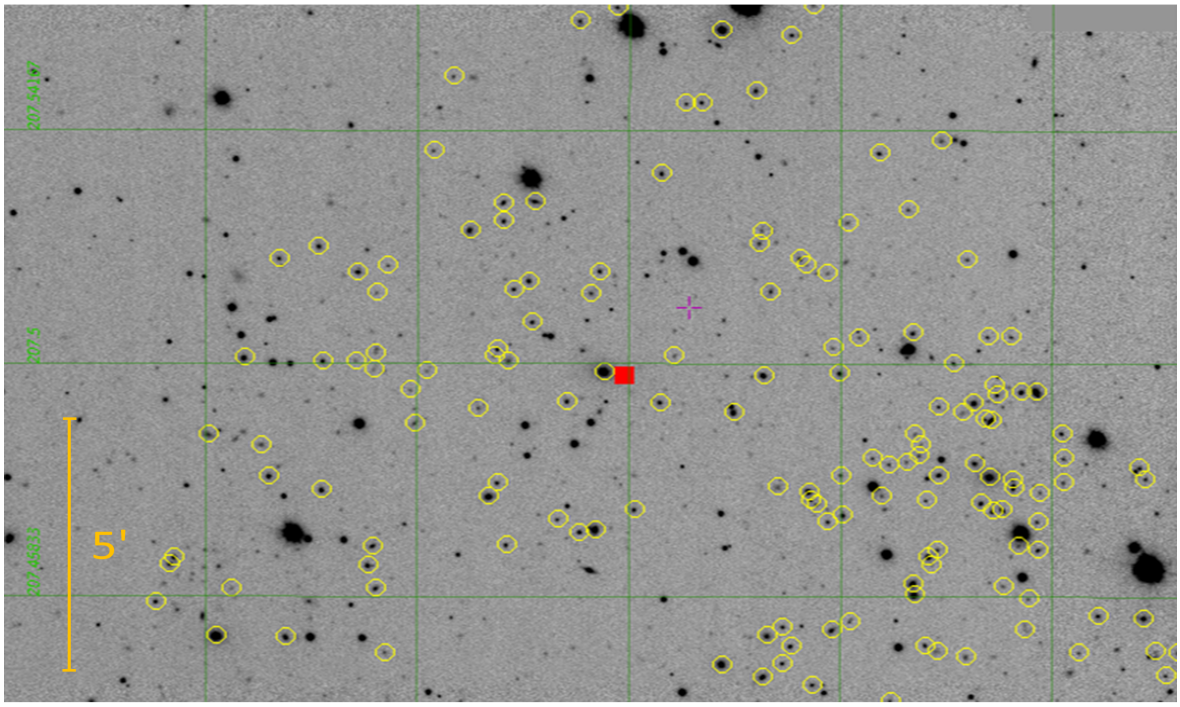

Figure 4.1: The VST ATLAS cluster counterpart to a previously unconfirmed Planck SZ source. Here the g-band image is shown with the ORCA detected cluster galaxies circled in yellow and the Planck SZ source indicated by the red square.

accurate redshifts due to the relatively low S/N ratios (due to factors including bad seeing, presence of bright stars close to our targeted cluster or high sky brightness in cases where

some of the observations had to be taken close to twilight). Some of these clusters, along with those that require re-reduction may be published in future works upon more careful manual analysis of the data. The ATLAS cluster counterparts to the SZ targets without successful spectroscopic redshifts measurements vary in richness from 5-102 (with a mean richness of 33 ± 9) and have photometric redshifts in the range of 0.12-0.44 (with a mean of 0.28 ± 0.02). We do not find a significant difference between these values and the mean redshift (0.26 ± 0.03) and richness (46 ± 11) of the spectroscopically confirmed SZ clusters.

Table 4.2: Details of the additional Planck SZ clusters in our EFOSC2 / FORS2 target list, which either could not be observed or require further analysis.

Target ID	Name	RA	DEC	SNR	$Q_{\rm NEURAL}$	$Y_{\rm 5R500}$	Notes
(1)	(2)	(3)	(4)	(5)	(6)	(7)	(8)
LOZ-11	PSZ2 G017.72-51.40	21:54:59.82	-30:07:56.9	4.54	0.98	2.32 ± 1.11	NO
LOZ-12	PSZ2 G026.34-58.64	22:30:37.72	-26:15:58.9	4.55	0.97	0.85 ± 0.26	RR
LOZ-13	PSZ2 G018.76-61.65	22:42:32.87	-30:18:54.2	5.04	0.94	1.55 ± 0.65	UR
LOZ-14	PSZ2 G014.72-62.49	22:46:32.03	-32:12:04.0	5.21	0.98	2.63 ± 1.27	NO
LOZ-15	PSZ2 G035.89-61.39	22:47:02.24	-22:13:41.7	4.73	0.96	7.51 ± 4.44	UR
LOZ-16	PSZ2 G051.40-61.15	22:58:11.53	-15:16:20.7	4.60	0.97	5.93 ± 3.52	UR
LOZ-17	PSZ2 G027.99-69.85	23:20:50.11	-27:01:47.9	5.18	0.99	1.07 ± 0.32	UR
LOZ-18	PSZ2 G006.16-69.49	23:22:09.00	-34:34:30.8	4.55	0.93	1.33 ± 0.68	RR
LOZ-19	PSZ2 G355.22-70.03	23:31:19.63	-37:54:41.2	4.68	0.99	1.07 ± 0.47	MR
LOZ-20	PSZ2 G003.21-76.04	23:53:24.29	-33:17:35.7	4.79	0.84	1.04 ± 0.38	RR
LOZ-21	PSZ2 G315.71-83.81	00:44:55.01	-33:08:48.2	4.55	0.89	2.63 ± 1.28	UR
LOZ-22	PSZ2 G180.74-85.21	01:09:13.90	-24:30:38.8	5.17	0.99	2.15 ± 1.01	UR
LOZ-23	PSZ2 G224.86-79.51	01:38:19.58	-28:48:26.6	4.98	0.89	0.88 ± 0.25	UR
LOZ-24	PSZ2 G240.71-74.03	01:59:20.36	-33:32:22.3	5.25	0.79	1.54 ± 0.72	UR
LOZ-25	PSZ2 G204.91-69.71	02:18:46.13	-22:37:21.0	4.77	0.99	1.04 ± 0.61	NO
LOZ-26	PSZ2 G256.41+32.31	10:13:01.09	-15:53:29.6	4.95	0.88	1.57 ± 0.60	RR
LOZ-27	PSZ2 G261.11+34.90	10:32:23.72	-16:26:38.7	4.68	0.67	0.74 ± 0.16	UR
LOZ-28	PSZ2 G263.65+27.87	10:21:17.19	-23:18:53.6	5.19	0.99	0.99 ± 0.31	UR
LOZ-29	PSZ2 G271.53+36.41	11:05:29.39	-19:55:07.5	5.19	0.93	3.32 ± 1.27	NO
LOZ-30	PSZ2 G289.50+32.71	11:59:54.46	-28:48:16.8	4.97	0.98	4.97 ± 2.65	UR
LOZ-31	PSZ2 G297.91+31.43	12:31:24.79	-31:14:31.8	4.96	0.93	2.33 ± 1.37	NO
LOZ-32	PSZ2 G323.96+43.81	13:54:06.11	-16:28:57.3	4.97	0.67	3.62 ± 1.85	MR
LOZ-33	PSZ2 G325.19+49.12	13:49:59.50	-11:11:57.5	4.62	0.98	2.12 ± 1.06	UR
LOZ-34	PSZ2 G096.14+56.24	14:35:56.21	-28:17:01.4	6.58	9.97	4.00 ± 1.48	UR
LOZ-35	PSZ2 G349.18+38.66	15:11:53.38	-11:16:42.5	5.15	0.99	4.04 ± 1.50	NO
HIZ-2	PSZ2 G201.20-42.83	03:58:49.74	-10:12:58.5	4.70	0.92	1.94 ± 1.11	RR
HIZ-3	PSZ2 G194.68-49.76	03:25:22.01	-09:40:49.6	5.71	0.80	1.40 ± 0.44	RR
HIZ-4	PSZ2 G045.96-26.94	20:50:08.37	-01:35:25.9	5.10	0.96	1.73 ± 0.71	MR

Notes. (1) Cluster short name (LOZ: low redshift candidate, HIZ: high redshift candidate), (2) Planck SZ catalogue name, (3 & 4) SZ coordinates , (5) Signal to noise ratio, (6) Neural network quality flag, (7) SZ flux in terms of the total integrated Comptonization parameter, (8) Reason for not including this cluster in our analysis; NO: Not Observed; MR: Manual Reduction required due to data reduction pipeline failure; RR: Data needs to be Re-Reduced with further tweaks to the pipeline settings to improve sky subtraction / spectra extraction; UR: Uncertain Redshift (mostly due to low S/N of the spectra caused by bright twilight sky, faint galaxies or bright stars in the MOS field).

4.3 Methodology

4.3.1 Spectroscopic observations of Planck SZ clusters

In this Section, we describe our observations and data reduction, followed by our spectra fitting procedure used to extract the redshifts of our clusters. We then provide a description of our cluster velocity dispersion and mass calculations.

When targeting our cluster candidates for Multi-Object Spectroscopy (MOS) observations, we first need to design MOS masks with slits assigned to the cluster galaxies for which we intend to obtain a redshift. In designing our MOS masks, we first place the slits on the brightest identified cluster members which would give the highest S/N spectra, and where slit overlaps do not allow for targeting of an ORCA identified cluster member, we place the slit on galaxies with similar colour and brightness to those identified as cluster members.

We conduct the spectroscopic observations of our low redshift Planck SZ clusters, using the ESO NTT EFOSC2 (Buzzoni et al., 1984) instrument. The EFOSC2 MOS mask slits are made using punch head no. 7 with a width and length of $1.34''$ and $8.6''$ respectively. Given the $4.1 \times 4.1'$ field of view of the instrument, on average, this allows us to target ~ 15 galaxies per cluster. Note that at least 3 slits need to be assigned to bright reference stars in the telescope field of view to allow for the alignment of the mask on the sky by taking short exposures during target acquisition. Our choice of the slit width combined with the EFOSC2 no. 1 grism will allow us to cover the $4000 - 10000$Å wavelength range with a resolution of 58Å FWHM.

In the case of our MOS observations of high redshift Planck SZ cluster candidates, we use the VLT FORS2 (Appenzeller et al., 1998) instrument. Here, we punch the MOS mask with slits of $1''$ in width and $4''$ in length. This choice of slit width, combined with the $6.8 \times 6.8'$ FORS2 field of view, allows us to target up to ~ 150 objects in the instrument field of view. By using the FORS2 GRIS-300I+11+OG590 grism in combination with our chosen slit width we are able to cover the $6000 - 11000$Å wavelength range with a resolution of 12.5Å FWHM.

Figure 4.2 shows an example of one of our FORS2 masks targeting a high redshift Planck cluster candidate. The blue square shows the focal field projected on the CCD, with the crosses on the two sides of the box marking the "forbidden" target selection areas where the spectra of objects with slits placed in these regions will be cut by the CCD edge. In this case, we target over 100 galaxies in the field of view, with ~ 25 of these being placed on candidate cluster members in the centre of the field. Both FORS2 and EFOSC2 MOS observations

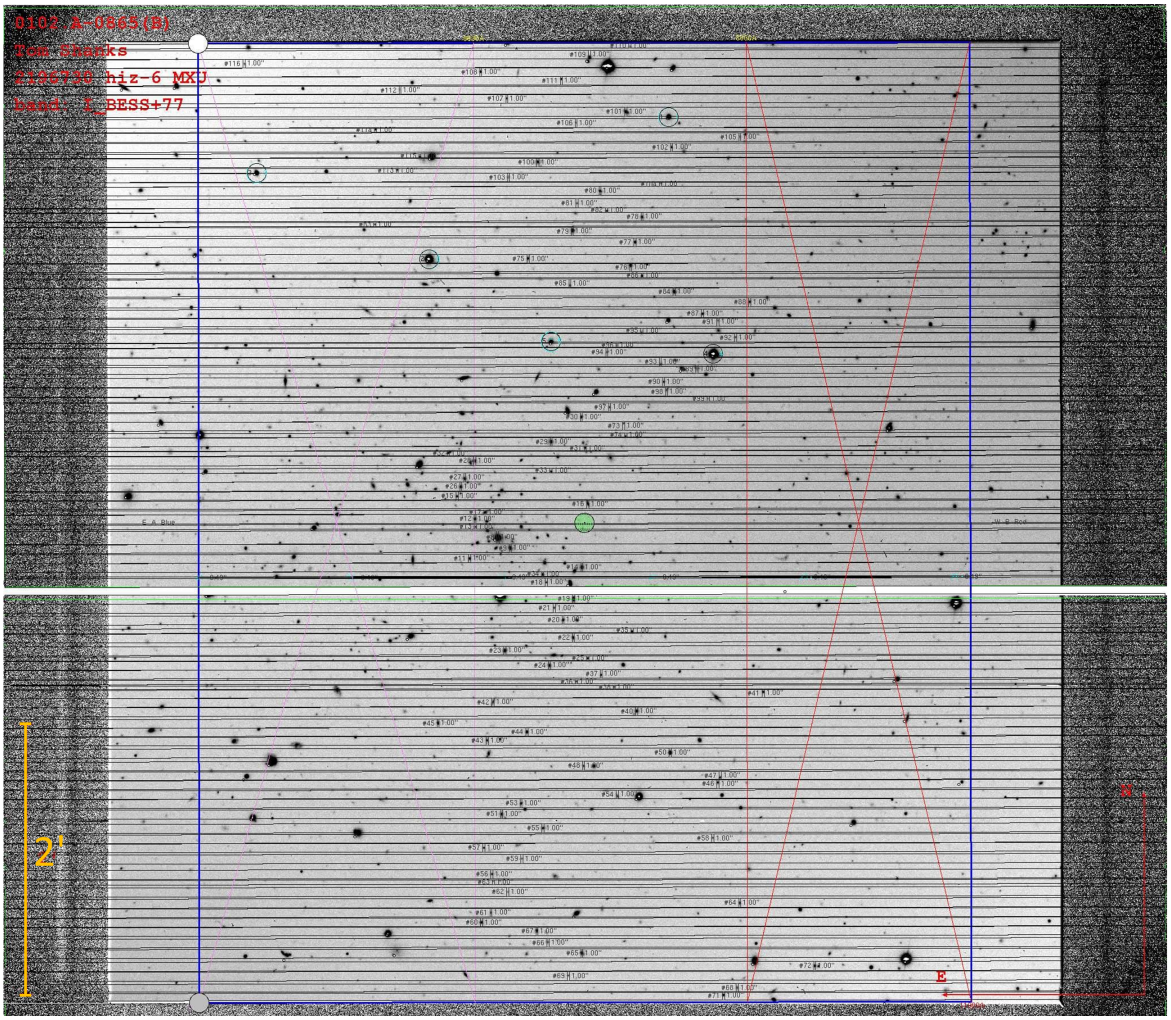

Figure 4.2: One of our FORS2 MOS masks with the mask slits labelled by different numbers and the black horizontal lines indicating the area where the spectra of each object will be projected. The background image is a 5 minute, i-band exposure taken by FORS2. Here, 5 bright reference stars used for aligning the mask on the sky during target acquisition are marked by the large empty circles.

require pre-images taken using the instrument. In both cases we take 5 minute exposures in the i-band reaching magnitude limits of $i_{\rm AB} = 21.4$ and $i_{\rm AB} = 24$ in our EFOSC2 and FORS2 pre-imaging respectively. Furthermore, during target selection for MOS observations, we use the Data release 2 of the GAIA catalogue (Gaia Collaboration et al., 2018) in order to avoid accidentally targeting any stars that may appear as red or yellow extended sources (which could be confused with cluster galaxies) in our field of view.

We reduce our MOS observations using the ESO GASGANO software[2], and the redshift of our targeted galaxies are determined by fitting templates using the publicly available MARZ[3]

[2] https://www.eso.org/sci/software/gasgano.html
[3] https://samreay.github.io/Marz/#/overview

algorithm (Hinton et al., 2016). Figure 4.3 shows an example of a $z = 0.24$ EFOSC2 and a $z = 0.71$ FORS2 cluster galaxy spectra. In both cases, the redshifts are obtained by fitting an early-type galaxy template using MARZ. In the case of the low-redshift EFOSC2 observations, as the spectra have a lower resolution relative to the FORS2 observations, we primarily make use of the H, K and Mg absorption lines (as well as the position of the cross-correlation peak provided by MARZ) in order to determine the redshift of each object.

As our MOS observations are conducted in three individual 20-minute exposures, we extract and fit the spectra from the individual exposures, as well as a combined 60-minute exposure, which is the mean of these three frames. The redshift is then taken to be the mean of the redshifts from the individual frames or the redshift from the combined frame for galaxies that are only detected in the combined frame. The redshift errors are then given by the standard error on the mean in cases where spectra are extracted from multiple frames and where an object is only detected in an individual frame they are estimated based on a linear fit to the relationship between redshift errors and the height of the spectra-template cross-correlation peak given by MARZ.

4.3.2 Cluster velocity dispersions and masses

We now convert the redshift of each galaxy to peculiar velocities $v_{\rm p}$, following Equation 16 of Davis & Scrimgeour (2014), with:

$$v_{\rm p} = c\left(\frac{z_i - \bar{z}}{1 + \bar{z}}\right), \tag{4.3.1}$$

where z_i is the redshift of the i-th cluster galaxy and $\bar{z}$ is the mean cluster redshift.

Following the approach of Caldwell et al. (2016), we then use the 'gapper' estimator of Wainer & Thissen (1976) to calculate cluster velocity dispersions based on the peculiar velocities of the cluster galaxies. The gapper estimator is calculated based on the weighted average of the gaps of an ordered statistic $(x_i, x_{i+1}, ..., x_n)$ and we choose this estimator due to its efficiency in cases with deviations from a Gaussian distribution and robustness at low richness (Beers et al., 1990). In order to obtain an estimate of the velocity dispersions using this method, we first remove any galaxies with redshifts $> 3\sigma$ away from the mean cluster redshift (where σ is the standard error on the mean redshift). The velocities are then sorted in ascending order and the velocity dispersion is given by:

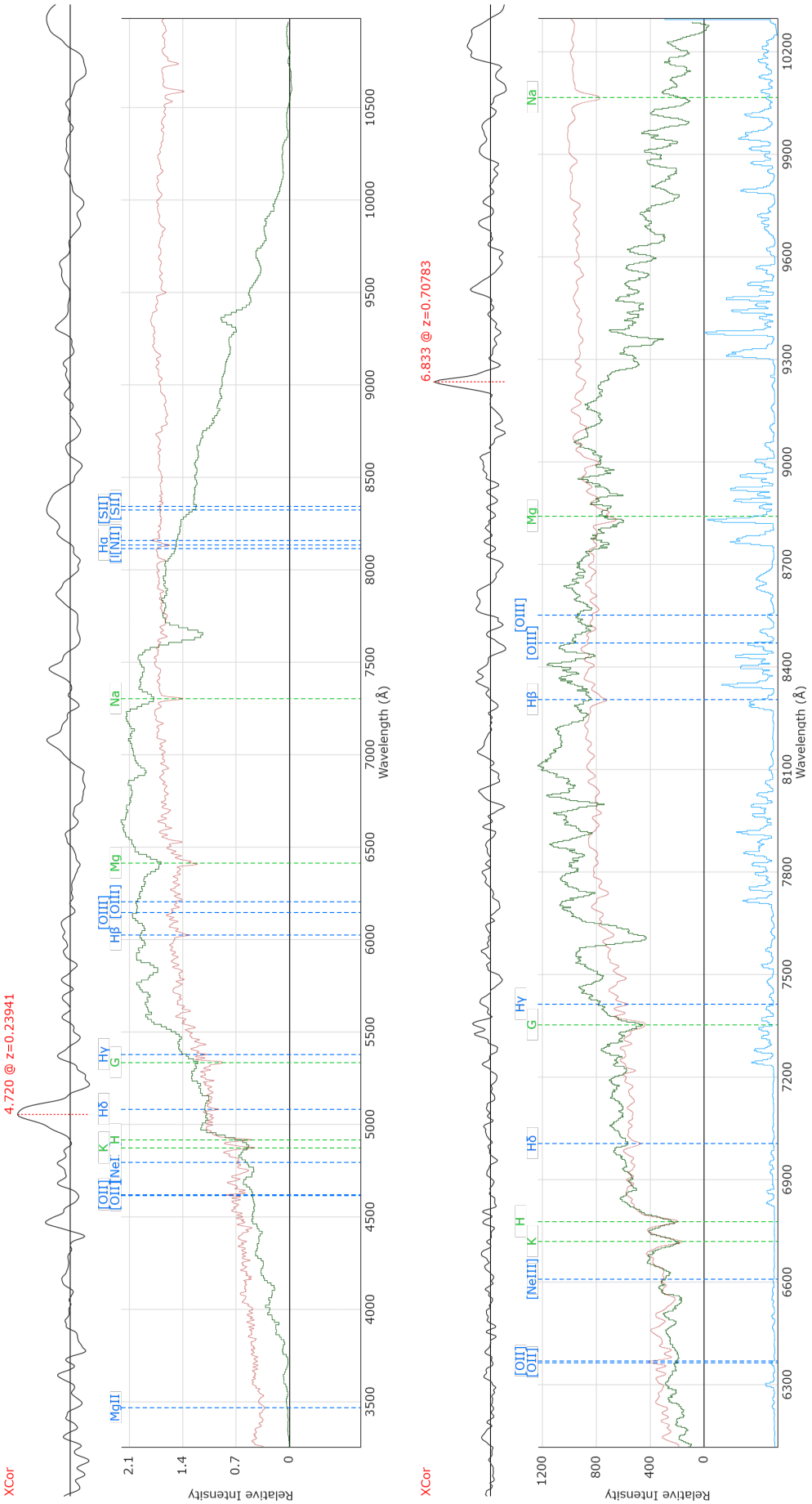

Figure 4.3: A typical EFOSC2 (a) and FORS2 (b) spectra of a $z = 0.24$ and $z = 0.71$ redshift cluster galaxy. The observed spectra are shown in green, and the fitted MARZ early-type galaxy templates are shown in red. The observed spectra-template cross-correlation peaks shown at the top of each panel are used to determine the best-fit redshift of each galaxy.

$$\sigma_{\rm gap} = \frac{\sqrt{\pi}}{N(N-1)} \sum_{i=1}^{N-1} \omega_i g_i, \tag{4.3.2}$$

where N is the number of galaxies in the cluster, the weights are given by $\omega_i = i(N-i)$, and the gaps are defined as $g_i = v_{i+1} - v_i$, where v_i is the velocity of the ith cluster galaxy, ranked by increasing velocity. Following Caldwell et al. (2016) and Eke et al. (2004), we then multiply $\sigma_{\rm gap}$ by a factor of $\sqrt{N/(N-1)}$. This is to account for the fact that the central galaxy is moving at the centre-of-mass velocity of the halo, which is not typical of the velocities of the satellite galaxies.

Following Section 4.2 of Ruel et al. (2014) which presents a detailed analysis of the uncertainties on the measured cluster velocity dispersions in cases with few spectroscopically confirmed cluster galaxies, we define the uncertainty on $\sigma_{\rm gap}$ as:

$$\Delta\sigma_{\rm gap} = \frac{C_{\rm gap}\sigma_{gap}}{\sqrt{N-1}}. \tag{4.3.3}$$

The value of the constant $C_{\rm gap}$ is determined to be 0.91 based on resampling of 1000 pseudo-observations (i. e. subsamples) with varying number of cluster members from a stacked cluster[4]. Ruel et al. (2014) find that their $\sigma_{\rm gap}$ uncertainties (while well captured by Equation 4.3.3), are $\sim 30\%$ larger than estimates commonly obtained in the velocity dispersion literature based on the jackknife or bootstrap techniques. Ruel et al. (2014) attribute these larger uncertainties to non-Gaussianity in the measured velocity distributions, as well as their use of 3σ cluster membership selection (similar to our approach in this work) which could lead to an increased scatter in the measured dispersion by removing genuine cluster members or including non-members.

We then convert $\sigma_{\rm gap}$ to cluster dynamical mass using the scaling relation from Ruel et al. (2014) and Saro et al. (2013):

$$M_{200,\rm gap} = \left(\frac{\sigma_{\rm gap}}{A \times h_{70}(z)^c}\right)^B 10^{15}{\rm M}_\odot, \tag{4.3.4}$$

where $A = 939$, $B = 2.91$ and $C = 0.33$. The errors on $M_{200,dyn}$ are calculated based on the propagation of velocity dispersion errors using the Python UNCERTAINTIES package[5].

[4]The stacked cluster was constructed in order to examine confidence intervals on the velocity dispersion measurements in clusters with few spectroscopically confirmed members. We refer the reader to Section 3.2.1 of Ruel et al. (2014) for a description of how this stacked cluster was constructed using observations of 48 SPT SZ clusters.

[5]`http://pythonhosted.org/uncertainties/`

As well as masses based on velocity dispersions, we use the observed redshift of our clusters to obtain cluster masses based on the SZ flux of each system. To do this, we follow the SZ observable-cluster mass scaling relation given by Equation 7 of Planck Collaboration et al. (2016d), with:

$$E^{-\beta}(z)\left[\frac{D_{\rm A}^2(z)\bar{Y}_{500}}{10^{-4}{\rm Mpc}^2}\right] = Y_*\left[\frac{h}{0.7}\right]^{-2+\alpha}\left[\frac{(1-b)M_{500}}{6\times10^{14}{\rm M}_\odot}\right], \tag{4.3.5}$$

where $E(z) \equiv H(z)/H_0$, $D_{\rm A}(z)$ is the angular diameter distance, $\bar{Y}_{500}$ is the SZ signal strength in terms of the Compton y-profile integrated within a sphere of radius R_{500}, $\beta = 0.66 \pm 0.5$, $\log Y_* = -0.19 \pm 0.02$, $\alpha = 1.79 \pm 0.8$ and $(1-b) = 0.8$.

Here, the "mass bias" parameter b, is a key parameter of the mass scaling relation which directly impacts the determination of cosmological parameters including Ω_m and σ_8 from cluster counts analysis. This parameter is introduced to correct for differences between the true halo mass (M_{500}) and X-ray calibrated cluster masses (M_X) (obtained based on the scaling relation of Arnaud et al. 2010) which are known to be biased towards lower masses (see e.g. Nagai et al. 2007), with $M_X = (1-b)M_{500}$.

The mass bias parameter is assumed to be independent of mass and redshift, however, as discussed in Planck Collaboration et al. (2016d), this assumption is merely due to the fact that the statistics of the current lensing samples make it difficult to constrain any mass or redshift dependence. This limitation is however likely to be removed with the availability of future CMB lensing surveys and larger weak lensing samples from surveys such as LSST and Euclid.

We refer the reader to Section 5.7 of Planck Collaboration et al. (2020) for a full review of the current constraints on $(1-b)$ obtained through various techniques. In short, Planck Collaboration et al. (2020) derive a value of $(1-b) = 0.62 \pm 0.03$ based on TT,TE,EE+lowE+lensing likelihood combined with the Planck cluster counts, which is at the lower limit of current weak lensing cluster mass estimates (e.g. Sereno et al. 2017) and roughly 2σ lower than the value found based on the Planck CMB lensing mass calibration reported by Planck Collaboration et al. (2016d). For consistency, here we decide to use the base-line value of $(1-b) = 0.8$ from Planck Collaboration et al. (2014c) which was used to determine the M_{SZ} masses provided in the Planck 2015 catalogue of SZ sources (Planck Collaboration et al., 2016e), which remains the most up to date Planck SZ cluster catalogue.

A final consideration in our calculation of the Planck cluster masses, based on the SZ flux, is that the 2015 Planck SZ catalogue (Planck Collaboration et al., 2016e) only provides

estimates of the SZ strength parameter Y_{5R500} (as defined by Equation 5 of the reference paper), with accurate conversion to Y_{500} requiring the use of conversion coefficients derived from the model which was assumed during extraction of the SZ signal (see the discussion in Section 5.2 of the reference paper), which are not included in the public release of the Planck SZ catalogue. Empirically, we find that using the Planck Y_{5R500} values instead of $\bar{Y}_{500}$ in Equation 4.3.5 results in masses larger than the M_{SZ} masses supplied in the Planck catalogue by a mean value of 2.07 ± 0.01. We therefore apply this scaling to the SZ flux-based masses of our observed Planck clusters when presenting our results.

4.4 Results and Discussion

4.4.1 Spectroscopic confirmation of ATLAS cluster counterparts to Planck SZ sources

We present the spectroscopic redshifts and peculiar velocities of our observed cluster galaxies in Table A.1 of Appendix A. Table 4.3 shows a summary of the number of spectroscopically confirmed galaxies for each of our observed clusters in comparison to the number of cluster galaxies detected by ORCA, as well as the number of ORCA detected cluster galaxies within the radii of 1 Mpc and R_{200} from cluster centres (where the final two richness estimates are scaled by Equation 3.3.6, as described in Section 3.3.5). This comparison shows that with the exception of LOZ-1 and LOZ-6, all of our target clusters appeared as relatively rich clusters with $N_{200} \sim 30$ or higher based on their ORCA detections, increasing our confidence that our targeted clusters are associated with the Planck SZ detections. Furthermore, visual inspection of LOZ-6 in the imaging data reveals it as a bright cluster, with no other visible clusters appearing within a Planck positional error of the SZ source. In the case of LOZ-1, although the cluster lies in a busier field compared to LOZ-6, we see no evidence of brighter, lower redshift, clusters that could be associated with the SZ source. We remind the reader that due to its high redshift, the HIZ-1 cluster is not detected by ORCA in the ATLAS data and was targeted as a high redshift candidate on this basis.

We present the mean redshift of our observed Planck SZ clusters in column (2) of Table 4.4. In Figure 4.4 we compare these redshifts with the photometric redshifts estimated for these clusters based on their ORCA detection in ATLAS (as described in Section 3.3.2), finding a good agreement between the two measurements sets. A second test of our measured cluster redshifts is performed in Figure 4.5 where we plot the Hubble diagram of the ATLAS BCGs

Table 4.3: Planck SZ cluster candidates vs. ORCA counterpart memberships.

Target ID (1)	$N_{\rm spec}$ (2)	$N_{\rm ORCA}$ (3)	$N_{\rm 1Mpc}$ (4)	N_{200} (5)
LOZ-1	9	7	19	10
LOZ-2	3	55	125	127
LOz-3	11	28	41	41
LOZ-4	12	10	33	33
LOZ-5	6	36	51	51
LOZ-6	6	8	6	6
LOZ-7	7	72	100	105
LOZ-8	12	78	103	117
LOZ-9	5	102	124	130
LOZ-10	14	64	86	107
HIZ-1	17	-	-	-

Notes. (1) Cluster short name, (2) Number of spectroscopically confirmed cluster members, (3) number of ORCA cluster galaxies detected by ORCA, (4) number of ORCA cluster members within $1h^{-1}$ Mpc of the cluster centre, scaled by Equation 3.3.6, (6) number of ORCA cluster members within R_{200} of the cluster centre, scaled by Equation 3.3.6.

with $N_{200} > 20$ and spectroscopic redshifts from external samples. Here, the BCGs of our observed clusters appear to follow the same trend in redshift and magnitude as the larger population of ATLAS BCGs, with no evidence that our cluster redshifts have been misidentified.

Column (3) of Table 4.4 shows the gapper velocity dispersion estimate for each cluster, which is calculated using Equation 4.3.2. The cluster masses based on these velocity dispersions (obtained using Equation 4.3.4), are presented in column (4). Column (5) shows the Planck SZ flux proxy, which is converted to SZ masses in column (6) by evaluating Equation 4.3.5 at redshifts presented in column (2). Due to the low number of spectroscopically confirmed cluster galaxies, we can see that the magnitude of the uncertainties on the cluster masses estimated from velocity dispersions are comparable to the cluster masses themselves. Indeed, for a typical cluster with a velocity dispersion of ~ 1000 kms^{-1} one would need to measure redshifts for ~ 100 members per cluster in order to obtain cluster masses with a precision of $\sim 20\%$. On the other, hand as one can see in column 6 of Table 4.4, the precision of Planck SZ flux measurements combined with our mean cluster redshifts measured at a $< 1\%$ level, allows us to obtain SZ mass estimates with a precision of $\sim 20\%$.

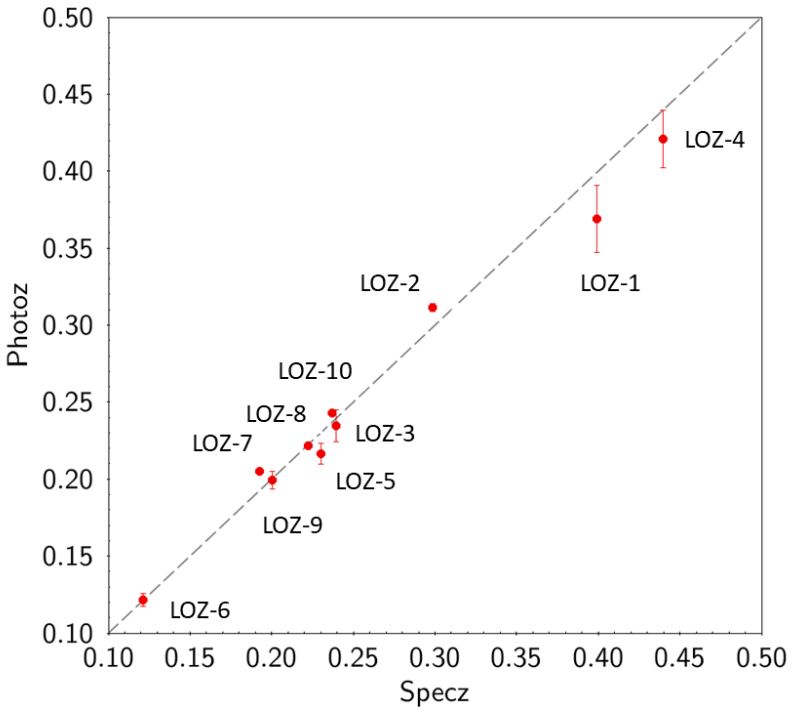

Figure 4.4: A comparison of the spectroscopic redshifts of our observed Planck SZ clusters (column 2 of Table 4.4) to the ANNz2 photometric redshifts obtained for these clusters based on their ORCA detection in ATLAS.

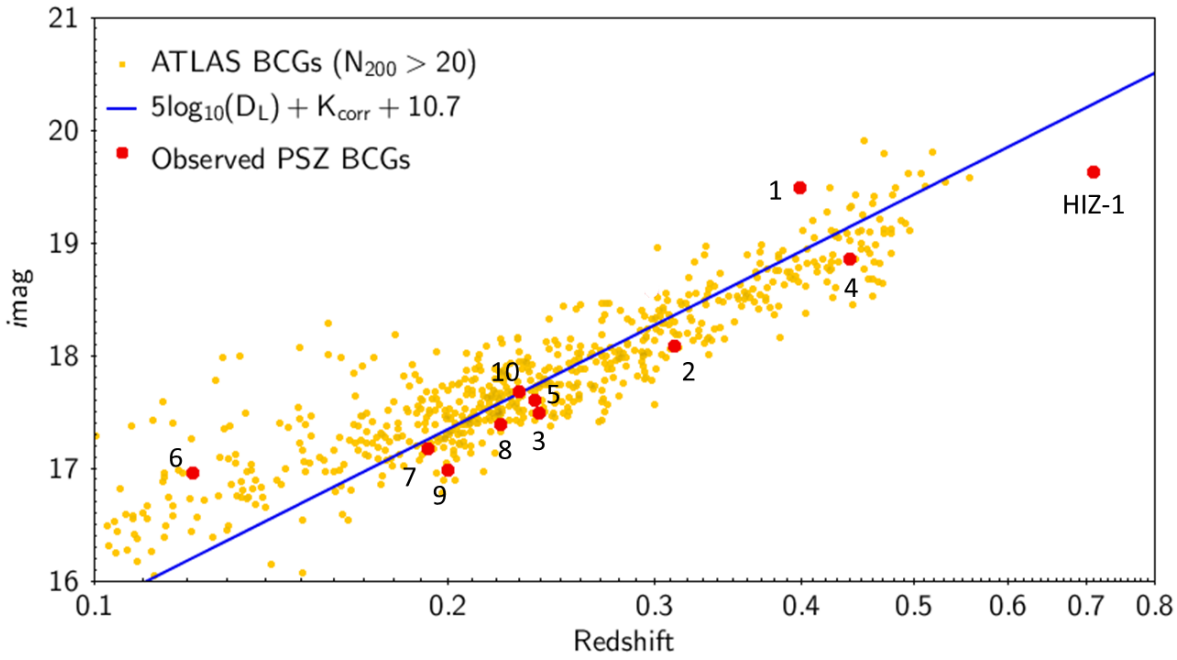

Figure 4.5: A Hubble diagram of our cluster BCGs with richness $N_{200} > 20$, compared to our observed Planck SZ cluster BCGs. Here only ATLAS BCGs with spectroscopic redshifts from external sources are shown.

Figure 4.6 shows a comparison of the SZ flux-based masses of our observed clusters and the cluster masses based on the richness of the ORCA detections of these clusters in ATLAS.

Table 4.4: Planck SZ cluster candidate redshifts, velocity dispersions and cluster masses.

Target ID	$\bar{z}$	$\sigma_{\rm gap}$ (kms^{-1})	$M_{200,\rm gap}$ ($10^{14}M_\odot$)	$Y_{5\rm R500}$	$M_{\rm SZ}$ ($10^{14}M_\odot$)	$M_{200,\rm ATLAS}$ ($10^{14}M_\odot$)
(1)	(2)	(3)	(4)	(5)	(6)	(7)
LOZ-1	0.3991 ± 0.0013	940 ± 300	8.5 ± 7.9	1.75 ± 0.73	5.8 ± 1.4	1.5 ± 0.2
LOZ-2	0.2986 ± 0.0020	620 ± 400	2.7 ± 5.0	1.25 ± 0.39	4.0 ± 0.7	9.1 ± 0.8
LOZ-3	0.2396 ± 0.0008	640 ± 180	3.0 ± 2.5	2.41 ± 1.2	4.9 ± 1.4	2.6 ± 0.3
LOZ-4	0.4399 ± 0.0011	840 ± 230	5.9 ± 4.7	1.54 ± 0.59	5.8 ± 1.2	3.2 ± 0.4
LOZ-5	0.2301 ± 0.0012	900 ± 360	8.0 ± 9.5	4.17 ± 1.79	6.5 ± 1.5	3.0 ± 0.3
LOZ-6	0.1214 ± 0.0013	410 ± 160	0.9 ± 1.1	0.82 ± 0.22	1.5 ± 0.2	1.1 ± 0.1
LOZ-7	0.1926 ± 0.0010	620 ± 70	2.8 ± 0.9	1.07 ± 0.32	2.6 ± 0.4	5.5 ± 0.5
LOZ-8	0.2224 ± 0.0011	930 ± 260	9.1 ± 7.2	4.03 ± 2.29	6.2 ± 2.0	6.4 ± 0.6
LOZ-9	0.1995 ± 0.0008	330 ± 170	0.9 ± 1.5	1.88 ± 0.80	3.7 ± 0.9	5.9 ± 0.5
LOZ-10	0.2372 ± 0.0007	740 ± 190	4.6 ± 3.4	4.78 ± 2.75	7.1 ± 2.3	6.3 ± 0.6
HIZ-1	0.7100 ± 0.0011	900 ± 200	6.2 ± 4.0	0.94 ± 0.25	5.3 ± 0.8	—

Notes. (1) Cluster short name, (2) Mean cluster redshift and standard error on the mean, (3) gapper velocity dispersion, (4) Cluster masses, (5) Planck SZ flux in terms of the total integrated Comptonization parameter, (6) Planck SZ cluster mass based on $Y_{5\rm R500}(\bar{z})$ evaluated at redshifts presented in column 2. (7) M_{200} masses based on ATLAS cluster richness N_{200}.

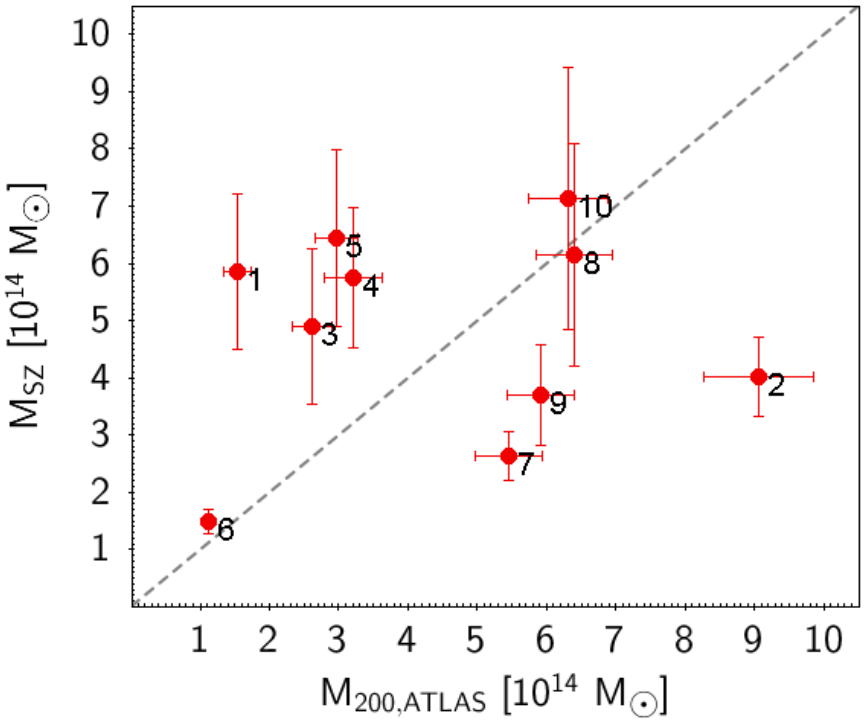

Figure 4.6: Comparison of the SZ flux-based masses of our observed clusters to masses based on cluster richness from the ATLAS cluster catalogue.

Here, the discrepancy between our richness based mass estimates and the SZ masses is generally in line with the level of scatter we found in Figure 5.2a, after calibrating our ATLAS M_{200} masses to masses from external catalogues. In the case of LOZ-2 however, (where the

ATLAS cluster mass appears to be overestimated by a factor of three), this is indicative of an overestimation of our cluster richness. A visual inspection of the cluster imaging suggests that this could be due to the presence of contamination in ORCA's assignment of cluster galaxies to this system as the cluster lies in a busy field where two or more clusters with similar colours may have been detected as one. However, the reasonable agreement between the velocity dispersion and SZ flux masses of this cluster, combined with the fact that we targeted the most localized cluster lying within the $3.2'$ positional error on the Planck SZ source, makes it unlikely that our observed cluster is not associated with the SZ source.

Although the observations presented in this Chapter are not enough to significantly impact the Planck cluster count cosmological results; in the coming years, similar observational campaigns (guided by optical cluster catalogues) could provide spectroscopic confirmation for the remaining $\sim 25\%$ of sources in the Planck SZ sample, with no current cluster counterparts. We can then repeat the cosmological analyses of the Planck SZ cluster counts with a better grasp of the survey completeness and systematics.

4.5 Conclusions

In this Chapter, we presented the results of our MOS follow-up of 11 Planck clusters with no previous spectroscopic confirmation, which were optically identified with the aid of the ATLAS cluster catalogue. We found a good agreement between the measured spectroscopic redshifts and our estimated photometric redshifts for these clusters. We then obtained two estimates of the cluster mass, based on our measured velocity dispersions and conversion of the Planck SZ flux to cluster mass using our measured redshifts.

Due to our low number of spectroscopically confirmed galaxies per cluster, we found the uncertainties on the velocity dispersion based cluster mass estimates to be comparable to the cluster masses. However, we provide SZ mass estimates for our observed clusters at a $\sim 20\%$ level, comparable to the precision of other SZ mass estimates in the literature (e.g. Bleem et al. 2015; Bocquet et al. 2019).

Besides the 11 Planck clusters presented here, we observed 14 additional low redshift ($z < 0.5$) and 2 high redshift ($z > 0.5$) Planck SZ cluster candidates. Although we were unable to obtain reliable redshifts for these clusters (due to various reasons discussed in Section 4.4.1), upon re-reduction and more detailed, manual analysis of the spectra, redshift confirmation and cluster masses for some of these systems may be released in future works.

The cluster counterparts to Planck SZ sources presented in this Chapter had most likely remained unconfirmed due to the lack of multi-wavelength imaging in the southern sky prior to the completion of the ATLAS survey. As we will discuss in the next Chapter, the tension between the Planck SZ cluster counts and CMB measurements of σ_8 is most likely dominated by remaining systematics in the calibration of Planck SZ flux-cluster mass scaling relation. We note, however, that $\sim 1/4$ of Planck SZ sources currently do not have redshift confirmations and this lack of sample completeness is also likely to contribute to the SZ cluster count-CMB σ_8 discrepancy. As such, future spectroscopic follow-up of cluster counterparts to Planck SZ sources such as those presented in this Chapter remains a worthwhile endeavour. Follow-up of higher redshifts ($z > 0.4$) Planck SZ cluster candidates are of particular importance, as at these redshifts, the Planck sample currently contains fewer detections due to the increase in the survey's lower limit of SZ detection with redshift.

Chapter 5

Cluster masses & the evolution of cluster mass function

5.1 Introduction

In the hierarchical theory of structure formation, galaxy clusters are the culmination of structure growth processes and as such their observed number densities as a function of mass and redshift (i.e. the cluster mass function) can provide stringent tests of cosmological models. In particular, cluster abundances are highly sensitive to the values of cosmological parameters including $\Omega_{\rm m}$, σ_8, potential redshift evolution of dark energy and extensions to the standard model such as massive neutrinos (see, e.g. Huterer et al. 2015; Planck Collaboration et al. 2016b; Bocquet et al. 2019; DES Collaboration et al. 2020).

The first analytical estimation of the cluster mass function was obtained by Press & Schechter (1974), by linking the linear matter power spectrum to the halo mass function, under the assumption that mass fluctuations follow a Gaussian distribution. The Press–Schechter formalism was found to be in general agreement with observed mass functions and results from various numerical simulations (e.g. White et al. 1993; Lacey & Cole 1994 and Reiprich & Böhringer 2002).

More recent numerical N-body simulations include those that focus on the friends-of-friends (FoF; Davis et al. 1985) definition of the halo mass (e.g. Sheth & Tormen 1999; Jenkins et al. 2001; Reed et al. 2003; Warren et al. 2006; Lukić et al. 2007; Reed et al. 2007; Crocce et al. 2010; Bhattacharya et al. 2011; Angulo et al. 2012), as well as those that are defined in terms of spherical or virial overdensities (e.g. Tinker et al. 2008; Watson et al. 2013; Bocquet et al. 2016; Despali et al. 2016; Comparat et al. 2017).

Our aim in this chapter is to compare the observed mass function of the ATLAS cluster catalogue to theoretical predictions of ΛCDM based on the Tinker et al. (2008) model and other cluster samples. The Tinker et al. (2008) model is based on measurements of dark matter halos in 18 sets of N-body cosmological simulations of a flat ΛCDM cosmology generated using the Hashed Oct-Tree (HOT) code of Warren & Salmon (1993), the Adaptive Refinement Technique (ART) code of Kravtsov et al. (1997) and the GADGET2 code of Springel (2005). Based on these simulations, Tinker et al. (2008) successfully calibrated the mass function at $z = 0$ for halos of $10^{11}h^{-1}\mathrm{M}_{\odot} \leq M \leq 10^{15}h^{-1}\mathrm{M}_{\odot}$ at $\lesssim 5\%$.

Unlike earlier studies of the halo mass function which usually identified halos using the friends-of-friends algorithm, Tinker et al. (2008) adopted the spherical overdensity (SO) halo finder (Lacey & Cole, 1994), which defines halos in simulations as spherical regions of specific overdensities. Tinker et al. (2008) argued that masses measured using the spherical overdensity method are more directly linked to cluster observables than those obtained using the FoF technique, making them more suitable for providing accurate forecasts of cluster abundances.

One of the key features of the Tinker et al. (2008) mass function which set it apart from previous analyses based on the FoF method, is a monotonically decreasing amplitude of the mass function with increasing redshift, with the high-mass end of the mass function evolving faster than the low-mass end. In the past decade the Tinker et al. (2008) mass function has been one of the most commonly used models to provide theoretical predictions of cluster abundances based on the ΛCDM model (see e.g. Vikhlinin et al. 2009; Allen et al. 2011; Bleem et al. 2015; Planck Collaboration et al. 2016d; Bocquet et al. 2019; DES Collaboration et al. 2020).

The layout of this Chapter is as follows: in Section 5.2, we obtain estimates of cluster masses for the ATLAS sample, using a mass-richness scaling relation calibrated to cluster masses from the MCXC, AdvACT, Planck and SDSS RedMapper samples. Section 5.3 provides a description of the Tinker et al. (2008) mass function models which are generated assuming a ΛCDM cosmology with the Planck 2018 (Planck Collaboration et al., 2020) parameters. In Section 5.4, we compare the observed cluster mass functions of the ATLAS, RedMapper, Planck and AdvACT samples, with theoretical predictions of the Tinker et al. (2008) model. In all cases, the comparisons are performed in five redshift bins covering the range $0.05 < z < 0.55$ in order to examine the evolution of the cluster mass functions. Finally, we conclude by presenting a summary of our results and the scope for future works in Section 5.5.

5.2 ATLAS cluster mass-richness scaling relation

Using our N_{200} estimates from Section 3.3.4, along with the mean photometric redshifts of our clusters $\bar{z}$, we provide cluster masses M_{200} (in units of $10^{14}\mathrm{M}_{\odot}$) based on the following scaling relation:

$$M_{200} = \left(\frac{N_{200}}{20}\right)^{1.1} \times 3\bar{z}^{\,0.9} + 1. \tag{5.2.1}$$

The form and parameters of this relation are chosen based on comparison[1] of the resulting ATLAS cluster mass estimates to masses of 626 clusters from external samples. These include 218 AdvACT and 95 Planck SZ clusters, 185 SDSS RedMapper clusters and 118 MCXC X-ray clusters. The error on our cluster masses are then approximated using:

$$\sigma_{M_{200}} = \sqrt{0.015\sigma^2_{N_{200}} N_{200}^{0.2}\bar{z}^{1.8} + \frac{0.01N_{200}^{2.2}\sigma^2_{\bar{z}}}{\bar{z}^{0.2}}}, \tag{5.2.2}$$

where $\sigma_{\bar{z}}$ and $\sigma_{N_{200}}$ are the uncertainties on $\bar{z}$ and N_{200} respectively. The derivation of the above expression can be found in Appendix B.1.

Figure 5.1 shows the redshift and mass distribution of the clusters from these four samples. The combination of these samples provide a reasonable number of counterparts to ATLAS clusters across the redshift range of $0.05 < z < 0.55$ and the mass range of $10^{14} - 10^{15}$ $\mathrm{M}_{\odot}$. Here, we calibrate the parameters in our cluster mass-richness scaling relation (Equation 5.2.1) using all available cluster masses from these four samples simultaneously, to avoid biasing our masses towards the range of masses covered by the individual samples.

We obtain the masses of the RedMapper clusters using the weak lensing calibrated mass-richness scaling relation of Simet et al. (2016), where:

$$M_{200\mathrm{m}} = 10^{14.344}\left(\frac{\lambda}{40}\right)^{1.33}. \tag{5.2.3}$$

Here, $M_{200\mathrm{m}}$ is the M_{200} cluster mass with respect to the mean density of the universe (in units of $10^{14}h^{-1}\mathrm{M}_{\odot}$) and λ is the richness of RedMapper clusters as defined by Rykoff et al. (2014). Similarly, we use the $M_{200\mathrm{m}}$ cluster masses from the AdvACT catalogue. As the MCXC cluster masses are defined as M_{500}, we multiply these by a factor of 1.5 in order to remove the mean offset found between the MCXC M_{500} masses and the $M_{200\mathrm{m}}$ masses of their RedMapper and AdvACT counterparts. Similarly, we correct for the mean offset

[1]The ATLAS mass-richness scaling relation is chosen to minimise the offset and scatter in Figure 5.2a.

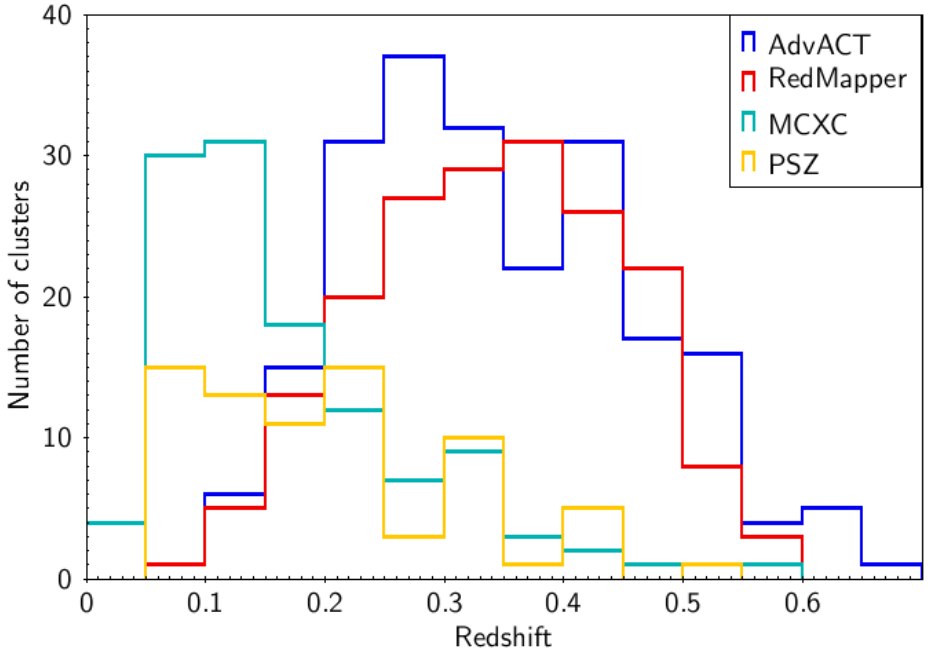

(a)

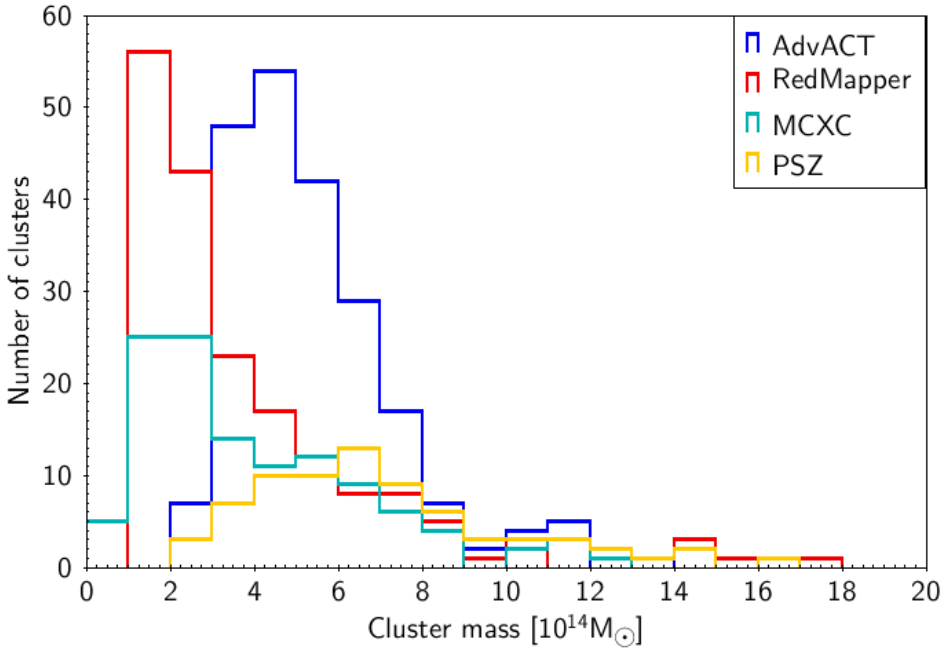

(b)

Figure 5.1: Redshift (a) and mass (b) distributions of the galaxies from the AdvACT, RedMapper, MCXC and Planck SZ cluster catalogues, used to calibrate the ATLAS cluster masses.

between the Planck SZ mass proxy values, M_{SZ}, and the $M_{200\mathrm{m}}$ masses of their RedMapper and AdvACT counterparts, by multiplying the Planck masses by a factor of 1.3. Once the Planck and MCXC masses are scaled to roughly correspond to $M_{200\mathrm{m}}$ masses, we use the masses from the four samples to calibrate the ATLAS mass-richness scaling relation following Equation 5.2.1. In the case of the AdvACT and Planck SZ samples, we limit the sources to those with a SNR>5.

The ratio of our ORCA cluster masses to masses based on their counterparts from these four samples are shown in Figure 5.2a. Our cluster masses are calibrated on the basis of minimizing the mean offset and scatter in this plot as well as the mass ratio histogram shown in Figure 5.2b. The level of scatter found in the ratio of our richness-based cluster mass estimates, to masses from external X-ray and SZ samples is comparable to that found when we compare the RedMapper richness-based cluster masses to masses from these external samples.

The photometric redshift term in our ATLAS mass-richness scaling relation (Equation 5.2.1) is added to remove a redshift dependent offset found between our M_{200} masses and the masses from the four external catalogues. This redshift dependence may be partially attributed to the Butcher-Oemler effect (Butcher & Oemler, 1978), where the fraction of late-type, blue cluster galaxies increase with redshift, causing our cluster richness values to be under-estimated at higher redshifts, (as blue galaxies will not be counted as cluster members due to ORCA's reliance on the red-sequence for cluster detection).

Another contributing factor which makes the use of this photometric redshift term necessary is the presence of a slight systematic offset towards lower redshifts in our photometric redshift estimates in the $z > 0.35$ redshift range, which is likely caused by the relatively lower number of galaxies in our spectroscopic training set in this redshift range (see Figures 3.4, 3.12 and the discussion in Section 3.4.2). The presence of such systematic offset towards lower redshift will, in turn, result in a lower $n(z)$ scaling factor being applied to the high redshift cluster richness values, biasing our estimates of N_{200} and M_{200} low.

Finally, although no evidence has been found to suggest cluster mass-to-light ratios (M/L) increase as a function of redshift (e.g. Lin et al. 2006; Muzzin et al. 2007; Soucail et al. 2015), the increase of cluster M/L as a function of cluster mass has been well established. Over a wide range of masses, various studies have found a ratio of $M/L \propto M^{\alpha}$, with α ranging from $0.2 - 0.4$ (Girardi et al. 2002; Lin et al. 2003; Rines et al. 2004; Popesso et al. 2007). Given that with increasing redshift (and in the $z > 0.3$ range in particular) due to the magnitude

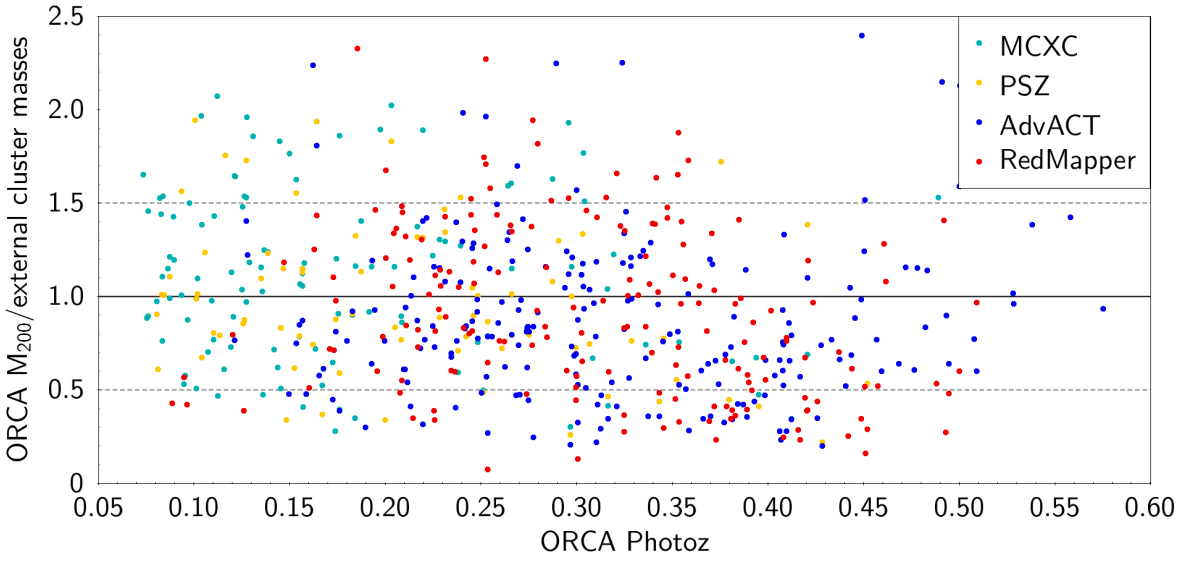

(a)

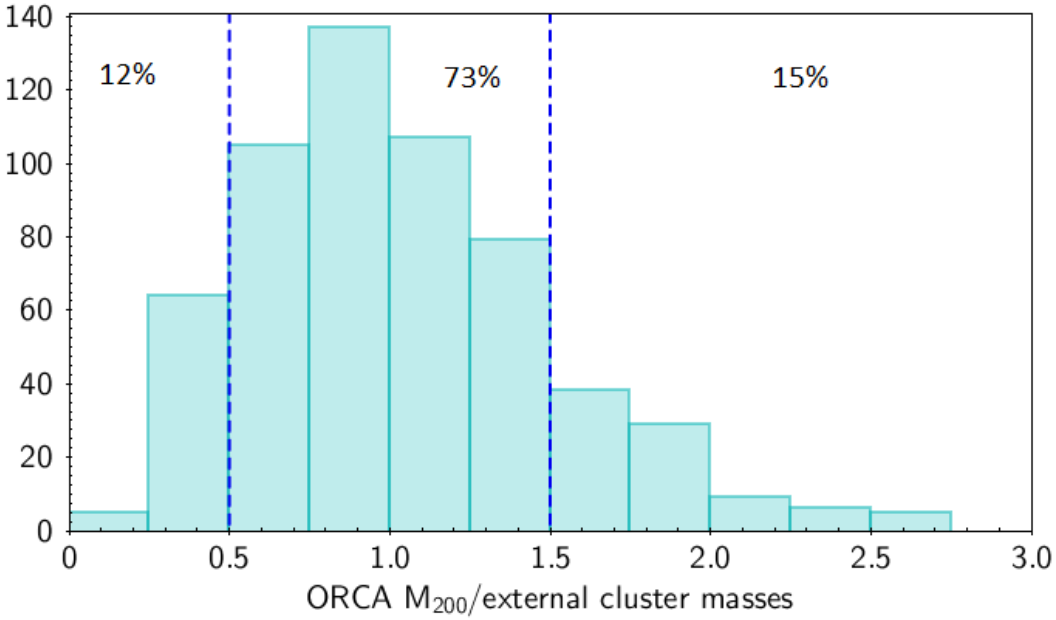

(b)

Figure 5.2: (a) The ratio of our ORCA cluster masses to masses of their cluster counterparts from external samples. The dotted lines show regions where our masses are in agreement with external masses within ±50%. (b) Histogram showing the ratio of the ORCA cluster masses to external cluster masses shown in (a). Here, we mark the percentage of clusters with mass ratios below, above and within the ±50% region.

limits of our sample we are increasingly likely to miss smaller, lower mass clusters, with the same being true (to varying degrees) for the external cluster samples used in our mass calibrations[2], the increased fraction of higher mass clusters at higher redshifts could mean that our $N - M$ scaling relation which provided a good estimate of total cluster masses at lower redshifts, is under-estimating the mass of our high redshift population which tend to have higher M/L ratios due to their higher mass.

5.3 Cluster mass function model

The Tinker et al. (2008) mass function takes the form:

$$\frac{dn}{d\ln(M)} = f(\sigma)\frac{\bar{\rho}_{\rm m}}{M}\frac{d\ln(\sigma^{-1})}{d\ln(M)}, \tag{5.3.1}$$

where $dn/d\ln(M)$ is the comoving halo number density per logarithmic mass interval in units of $(\mathrm{Mpc}/h)^{-3}$ and $\bar{\rho}_{\rm m} = \Omega_{\rm m}(z)\rho_{crit}(z) = \bar{\rho}_{\rm m}(z)(1+z)^3$ is the mean density of the universe. The Tinker et al. (2008) parametrization of the $f(\sigma)$ function is given by:

$$f(\sigma) = A\left[\left(\frac{\sigma}{b}\right)^{-a} + 1\right]e^{-c/\sigma^2}, \tag{5.3.2}$$

where the variance of the linear matter density field,

$$\sigma^2 = \int P_{\rm lin}(k)\hat{W}(kR)k^2 dk, \tag{5.3.3}$$

and $P_{\rm lin}(k)$ is the linear matter power spectrum as a function of wave-number k, which is smoothed with the Fourier transform of the real-space top-hat window function $\hat{W}$ of radius $R = (3M/4\pi\bar{\rho}_{\rm m})^{1/3}$. The redshift evolution of the $f(\sigma)$ parameters of the Tinker et al. (2008) model is given by:

$$A(z) = A_0(1+z)^{-0.14}, \tag{5.3.4}$$

$$a(z) = a_0(1+z)^{-0.06}, \tag{5.3.5}$$

$$b(z) = b_0(1+z)^{-\alpha}, \tag{5.3.6}$$

[2]This is due to the flux limit of the RedMapper and MCXC samples, and for Planck and AdvACT, due to the SZ lower-limit of cluster mass observability.

$$log\alpha(\Delta) = -\left[\frac{0.75}{\log(\Delta/75)}\right]^{1.2}, \tag{5.3.7}$$

where for an overdensity of $\Delta = 200$ (corresponding to our M_{200} cluster mass definition), the $z = 0$ values of the above parameters are: $A_0 = 0.186$, $a_0 = 1.47$, $b_0 = 2.57$. The c parameter does not evolution with redshift and takes the value of $c = 1.19$.

We generate the mass function models using the 'Halo mass function' module of the COLOSSUS[3] python package which is described by Diemer (2018) and obtain the volume of the survey elements in each redshift bin using of the COSVOL algorithm of the CELESTIAL V1.4.6[4] package, which follows Hogg (1999) and Wright (2006) in calculating cosmological volumes.

5.4 Results and discussion

5.4.1 ATLAS cluster masses

Figure 5.3 shows a comparison of the ATLAS cluster masses, obtained using Equation 5.2.1, to SZ cluster masses of the full AdvACT and Planck samples. As seen in Figure 5.3a the ATLAS cluster catalogue provides a complimentary sample to the Planck catalogue, by detecting clusters in a lower mass range than possible with Planck. As discussed in Section 4.2 of Carlstrom et al. (2002), for SZ surveys the observable lower-limit in mass is determined by factors including the effective beam size and instrument sensitivity, as well as the profile of the cluster on the sky. Following Carlstrom et al. (2002) equation 5, the integrated SZ signal over the solid angle of a cluster (with an area A on the sky), $d\Omega = dA/D_{\rm A}^2$, is given by:

$$\int \Delta T_{\rm SZ} d\Omega \propto \frac{N_{\rm e}\bar{T}_{\rm e}}{D_{\rm A}^2} \propto \frac{M\bar{T}_{\rm e}}{D_{\rm A}^2}. \tag{5.4.1}$$

Here, the CMB spectral distortion is expressed as a temperature change $\Delta T_{\rm SZ} d\Omega$, $N_{\rm e}$ represents the total number of electrons in the cluster, $\bar{T}_{\rm e}$ is the average electron temperature and M is the cluster gas mass. The angular diameter distance (i.e. the ratio of the physical size of an object to the angular size of the object on the sky) can be expressed as $D_{\rm A}(z) = D_{\rm C}/(1+z)$, where $D_{\rm C}$ is the comoving distance to the source.

Consequently, as seen in Figure 5.3a, in the $z < 0.6$ range covered by our cluster sample, the lower-limit of mass observability for the Planck SZ survey with a fixed flux sensitivity,

[3] https://bdiemer.bitbucket.io/colossus/lss_mass_function.html
[4] https://www.rdocumentation.org/packages/celestial

increases as a function of redshift due to rise in $D_{\rm A}(z)$, while optical cluster samples like ATLAS do not have the same redshift dependence on the lower-limit of cluster mass observability. On the other hand, SZ cluster surveys offer the ability to detect all clusters above a certain mass threshold with little dependence on redshift, whereas optical surveys are limited in their ability to detect clusters at higher redshifts by the magnitude limit of the survey. As a result the two approaches to cluster detection are highly complementary in maximizing the mass and redshift completeness of cluster samples.

As seen in Figure 5.3b, the ATLAS cluster sample also complements the AdvACT SZ sample in terms of detection of lower mass clusters in the redshift range $z < 0.5$. We note however, that due to it's higher angular resolution and superior flux sensitivity, AdvACT is able to detect lower mass SZ clusters than Planck. The larger Planck beam size, however, makes it more sensitive to clusters at $z < 0.05$ when compared to AdvACT (due to the larger projected area of these low redshift clusters on the sky).

Figure 5.4a shows a comparison of our ATLAS cluster masses, with X-ray cluster masses (M_{500}) from the MCXC sample. While most X-ray surveys included in the MCXC sample tend to be more sensitive to low-mass, low-redshift clusters in comparison to optical cluster catalogues, the completeness of these X-ray flux-limited cluster samples is reduced with redshift, with optical and SZ surveys providing more complete cluster samples at higher redshifts. Nevertheless, X-ray cluster samples play an important role in calibrating optical and SZ cluster masses and in determining the cluster gas fractions. The next generation of deeper X-ray cluster samples such as eROSITA will significantly improve on the completeness and statistics of current X-ray cluster samples by detecting $\sim 100,000$ galaxy clusters with masses $> 5 \times 10^{13} h^{-1} {\rm M}_{\odot}$ (Pillepich et al., 2012), a 2 orders of magnitude improvement over the MCXC cluster sample size.

Finally, we compare the ATLAS cluster masses to cluster masses from the SDSS RedMapper cluster catalogue in Figure 5.4. It can be seen that the two samples cover a similar range of cluster masses and redshifts, which is expected, given that both samples detect clusters using optical *griz* bands with a similar depth. However, as the ATLAS catalogue covers areas of the southern sky, not covered by the SDSS RedMapper catalogue, the two catalogues are highly complementary. For reasons which we discussed in Section 3.4.5, the ATLAS sample also contains a larger number of cluster detections in the redshift range $0.05 < z < 0.3$, while the RedMapper catalogue contains more cluster detections in the $0.3 < z < 0.55$ range, making this another aspect in which the two catalogues are complimentary.

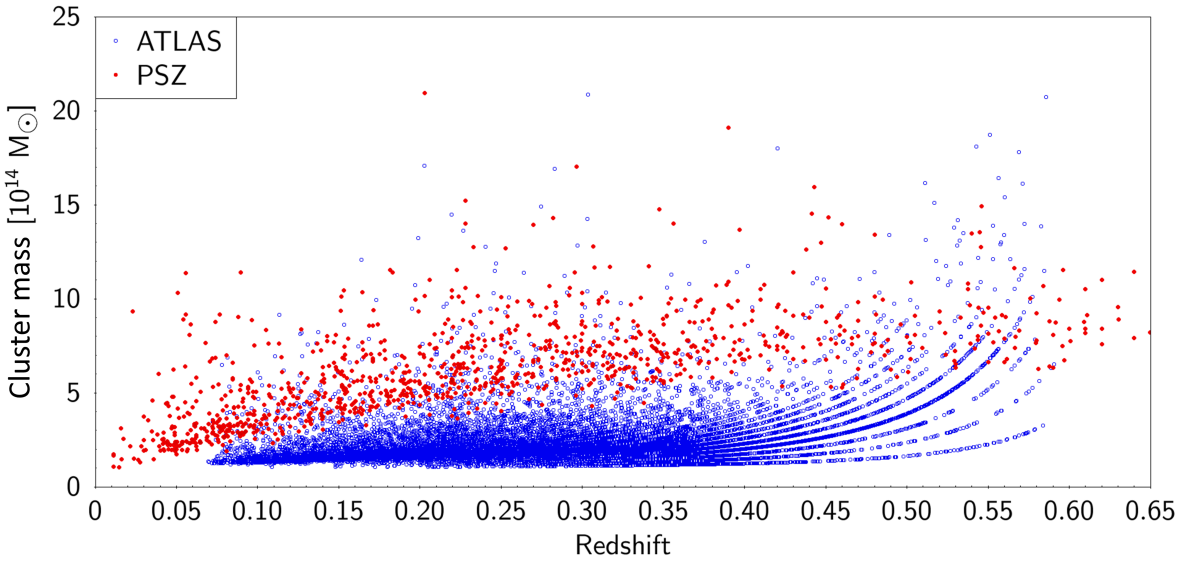

(a)

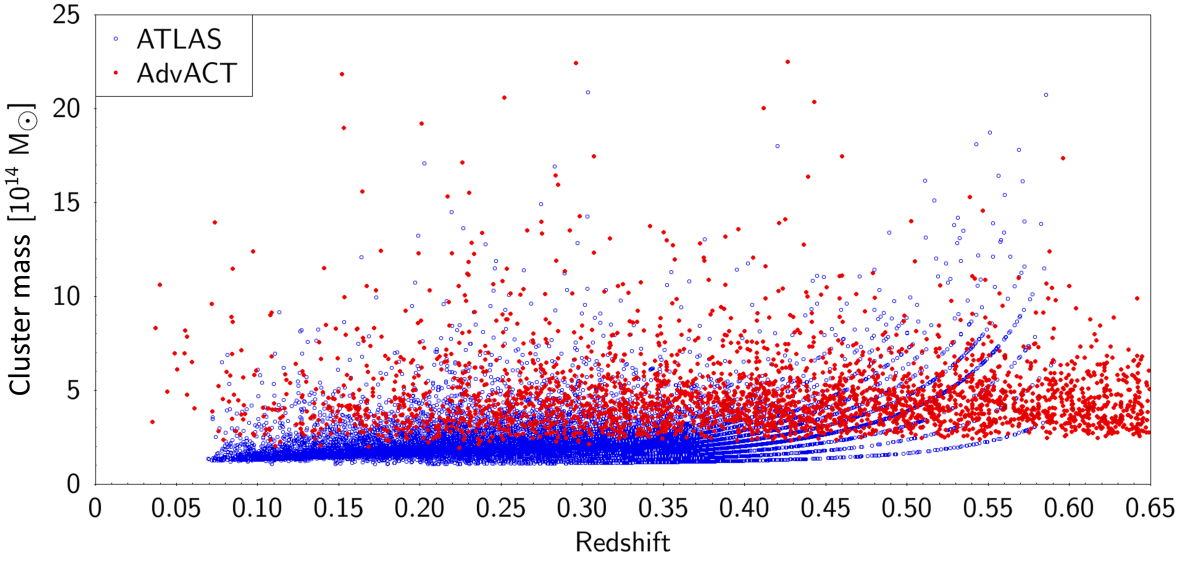

(b)

Figure 5.3: Comparison of the ATLAS $M_{200\mathrm{m}}$ cluster masses to Planck SZ masses M_{SZ} (panel a), and AdvACT $M_{200\mathrm{m}}$ SZ masses (panel b).

5.4.2 Comparison of cluster mass functions

We now compare the observed cluster mass functions of ATLAS, RedMapper, Planck and AdvACT samples to the theoretical predictions of the Tinker et al. (2008) model. The mass function models are generated for spherical overdensities defined as M_{200m}, assuming the

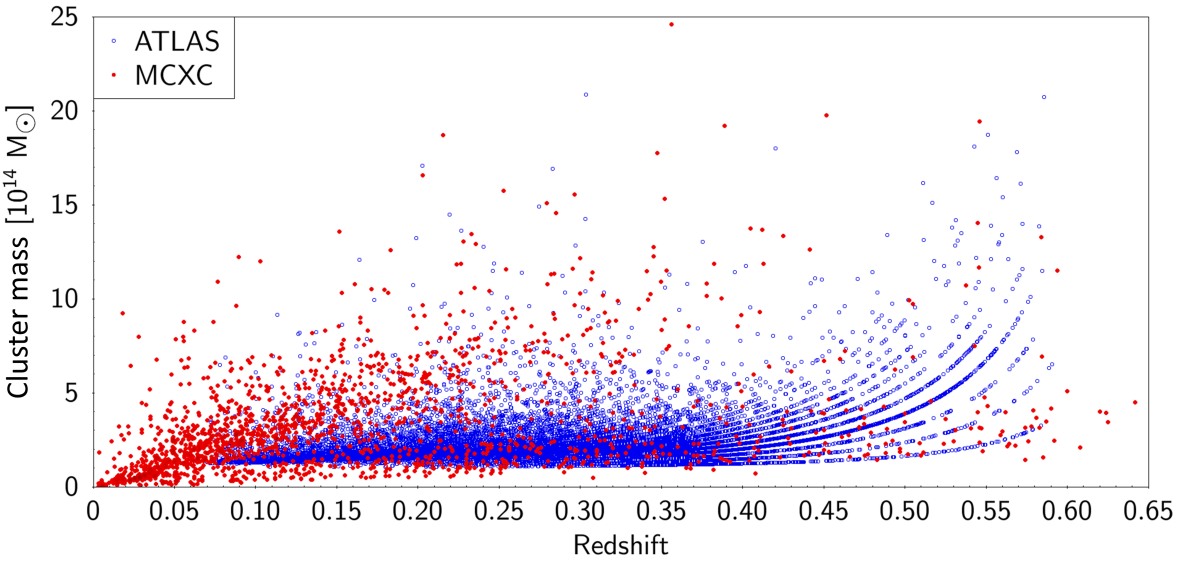

(a)

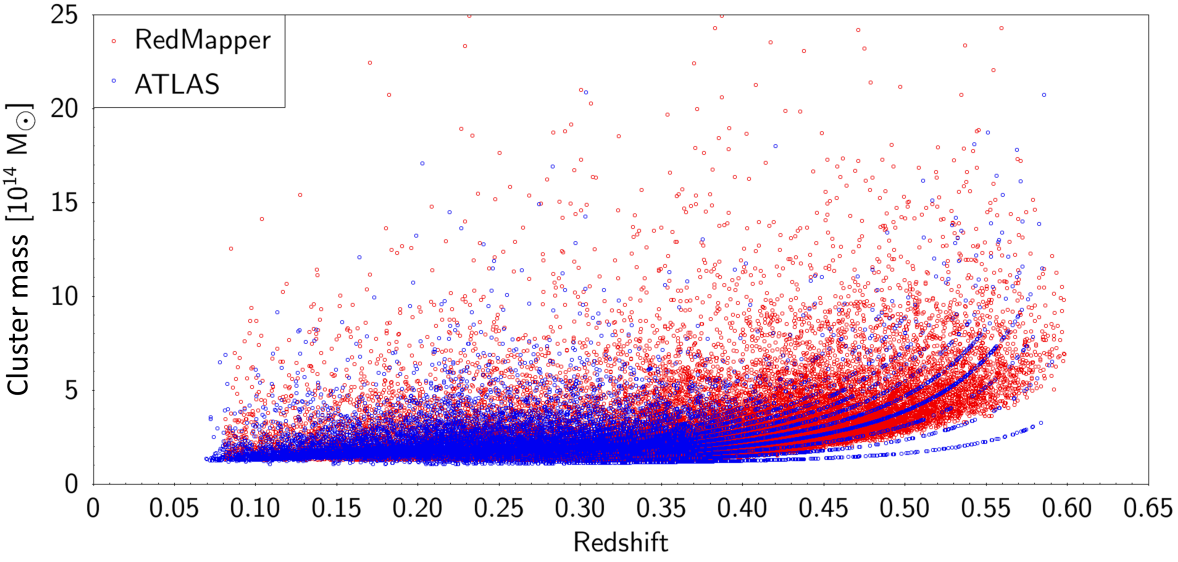

(b)

Figure 5.4: Comparison of the ATLAS M_{200m} cluster masses to MCXC M_{500} cluster masses (panel a), and SDSS RedMapper M_{200m} cluster masses (panel b), obtained using equation 5.2.3.

Planck 2015 cosmology (Planck Collaboration et al. 2016b; Table 4, column 6). We compare the observed mass functions to the models in five redshift bins, in order to examine the evolution of the cluster mass function in the redshift range $0.05 < z < 0.55$. Here, we apply a richness cut of $N_{200} > 20$ to the ATLAS clusters to match the RedMapper richness cut of

$\lambda > 20$.

In Figure 5.5 we compare the redshift evolution of observed optical and SZ cluster mass functions to the predictions of ΛCDM. Here, the fall in the amplitude of the cluster mass functions at lower masses is due to the reduced completeness of the samples as they approach their lower limit of cluster mass detection. As expected, the optical samples probe a lower range of cluster masses than the SZ masses at higher redshifts.

As seen in Figure 5.5 in the $0.05 < z < 0.35$ redshift range, we find the ATLAS cluster mass functions to have a higher amplitude relative to RedMapper, placing them in better agreement with the ΛCDM predictions. The lower amplitude of RedMapper could be in part due to an underestimation of RedMapper cluster masses at lower redshifts. This is in line with the discussion presented in Section VI.B of DES Collaboration et al. (2020), where the lower than expected $\Omega_{\rm m}$ obtained from cluster counts of the DES RedMapper sample is attributed to a possible underestimation of the RedMapper masses obtained based on the weak lensing calibration of the mass-richness scaling relation.

However, in Section 3.4.5 we also found a higher density (per unit volume) of ATLAS clusters at $z < 0.35$ compared to RedMapper. Similarly, our comparison of ATLAS and RedMapper samples to the Abell cluster catalogue at lower redshifts showed that for clusters with richness greater than 20, ATLAS recovers $\sim 80\%$ of Abell clusters, while RedMapper recovers Abell clusters at a lower rate of $\sim 60\%$. This could be taken as an indication that at lower redshifts RedMapper is likely to miss a larger fraction of genuine (and relatively rich) clusters compared to ATLAS. Consequently, RedMapper's lower completeness at $z < 0.35$ could also be an important contributing factor towards the lower amplitudes of its mass function relative to ΛCDM predictions.

As one can see in Figure 5.5, although the AdvACT survey probes a lower range of cluster masses than Planck[5], at all redshifts we find a good agreement between the mass functions of the two SZ samples in the range of masses where both surveys are complete. With the exception of the $z = 0.5$ redshift bin (Figure 5.5e), the Planck and AdvACT mass functions also appear to be in general agreement with RedMapper, placing them below the ATLAS cluster mass functions and the predictions of ΛCDM.

[5]Note that in the $z = 0.1$ bin (Figure 5.5a) the fact that Planck probes lower redshifts than AdvACT, offsets AdvACT's ability to probe clusters of lower masses, resulting in both samples having a similar completeness in the $M_{200} < 3 \times 10^{14} h^{-1} \mathrm{M}_{\odot}$ mass range.

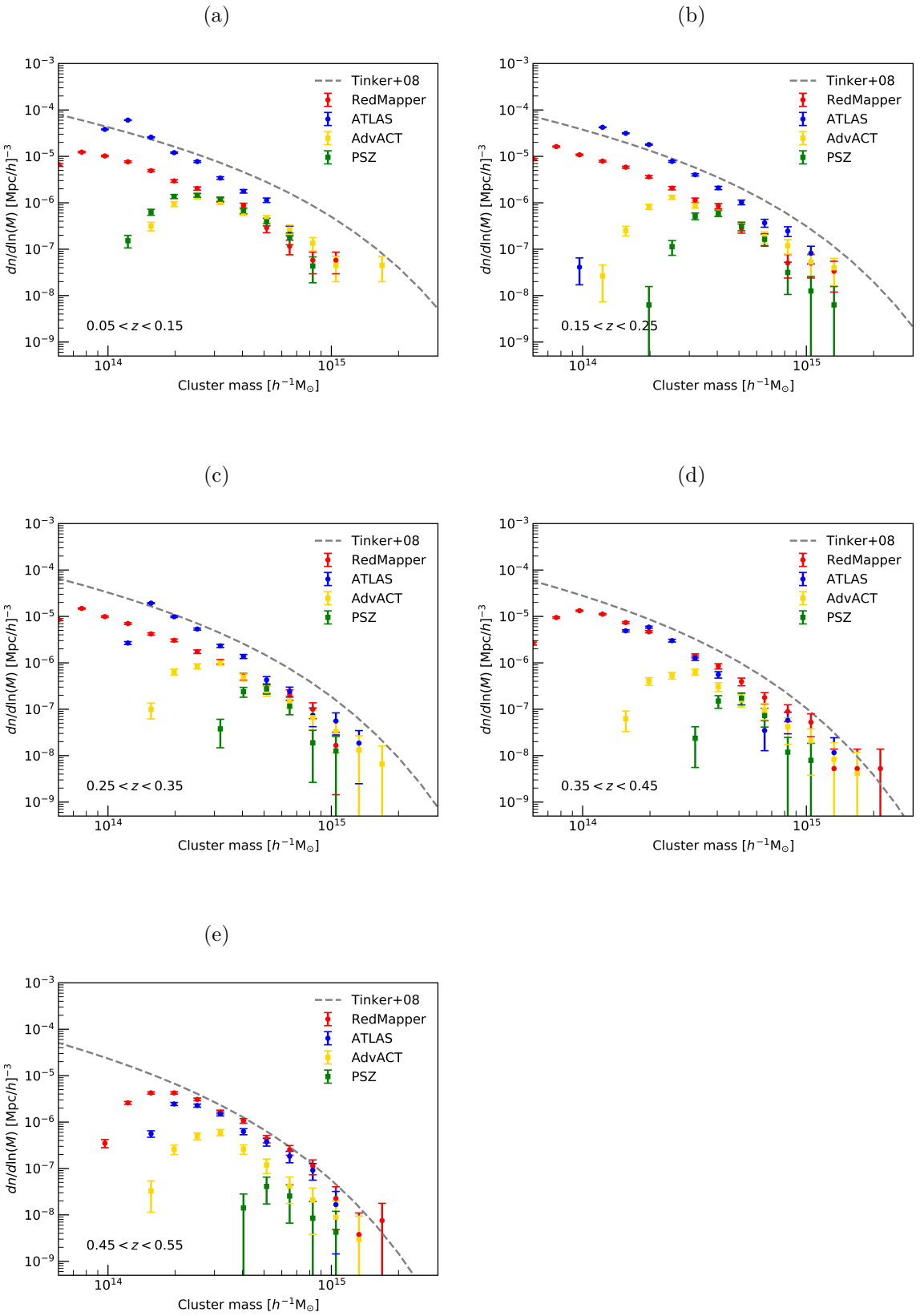

Figure 5.5: A comparison of ATLAS, RedMapper, Planck and AdvACT cluster mass functions to the theoretical predictions of the Tinker et al. (2008) ΛCDM models assuming a Planck 2015 cosmology (Planck Collaboration et al., 2016b). Here, the error bars on the observed mass functions are estimated as $\sqrt{n}$.

The lower amplitude of the SZ cluster mass functions compared to ΛCDM is likely to be due to systematics in the SZ flux-cluster mass scaling relation resulting in an under-estimation of cluster masses of these samples. Indeed, as discussed in Section 4.3.2, some SZ mass calibration techniques place the Planck cluster counts in closer agreement to the prediction of the ΛCDM model. However, as we discussed in the previous Chapter, the incompleteness of SZ samples could be another explanation for the lower amplitude of their mass functions relative to the models. To investigate this possibility, we compare the AdvACT[6] and Planck samples to the Abell clusters with richness classes > 2 and > 3, (which limit the catalogue to clusters with greater than 80 and 130 members respectively). A summary of our results is presented in Table 5.1, where we find the SZ samples to recover $\sim 30\%$ of Abell clusters with a richness class>2 and $\sim 50\%$ of Abell clusters with richness>3. Figure 5.6 shows examples of four $z \sim 0.2$ ATLAS clusters with mass estimates of $M_{200} > 4 \times 10^{14} h^{-1} \mathrm{M}_{\odot}$ placing them above the Planck lower limit on mass observability. In the future, spectroscopic follow up of SZ clusters guided by optical cluster catalogues (similar to those presented in the previous Chapter) could improve the completeness of current SZ samples. Similarly, a more detailed study of potential issues which could lead to the lack of detection of rich clusters in SZ samples based on comparison to optical catalogues such as ATLAS and RedMapper would be an interesting topic for future works.

Table 5.1: Fraction / percentage of rich Abell clusters overlapping the Planck and AdvACT surveys recovered by each SZ survey. ACO2 and ACO3 denote Abell clusters with richness class>2 and 3 respectively.

Redshift	AdvACT/ACO2	PSZ/ACO2	AdvACT/ACO3	PSZ/ACO3
$0.05 < z < 0.15$	16/73 (22%)	50/170 (29%)	4/9 (44%)	13/29 (65%)
$0.15 < z < 0.25$	34/105 (32%)	105/300 (35%)	13/28 (46%)	36/64 (56%)

Although the lower amplitude of SZ cluster mass functions relative to the ΛCDM predictions are most likely due to the issues described above, we note that a value of $\sigma_8 \approx 0.7$ (with $\Omega_{\mathrm{m}} = 0.3$), could also produce such observations. Furthermore, suppression of observed cluster mass functions compared to ΛCDM predictions at higher masses (similar to those seen in the ATLAS mass functions) could originate from primordial non-Gaussianities (Dalal et al. 2008; Verde 2010) or signal the presence of massive Neutrinos (e.g. Costanzi et al. 2013; Castorina et al. 2014; Biswas et al. 2019).

[6]We note that although Planck SZ detections with no measured redshifts are included in the catalogue used in this comparison, at the time of this writing, we only had access to AdvACT SZ detections with cluster counterparts identified based on their photometric or spectroscopic redshifts

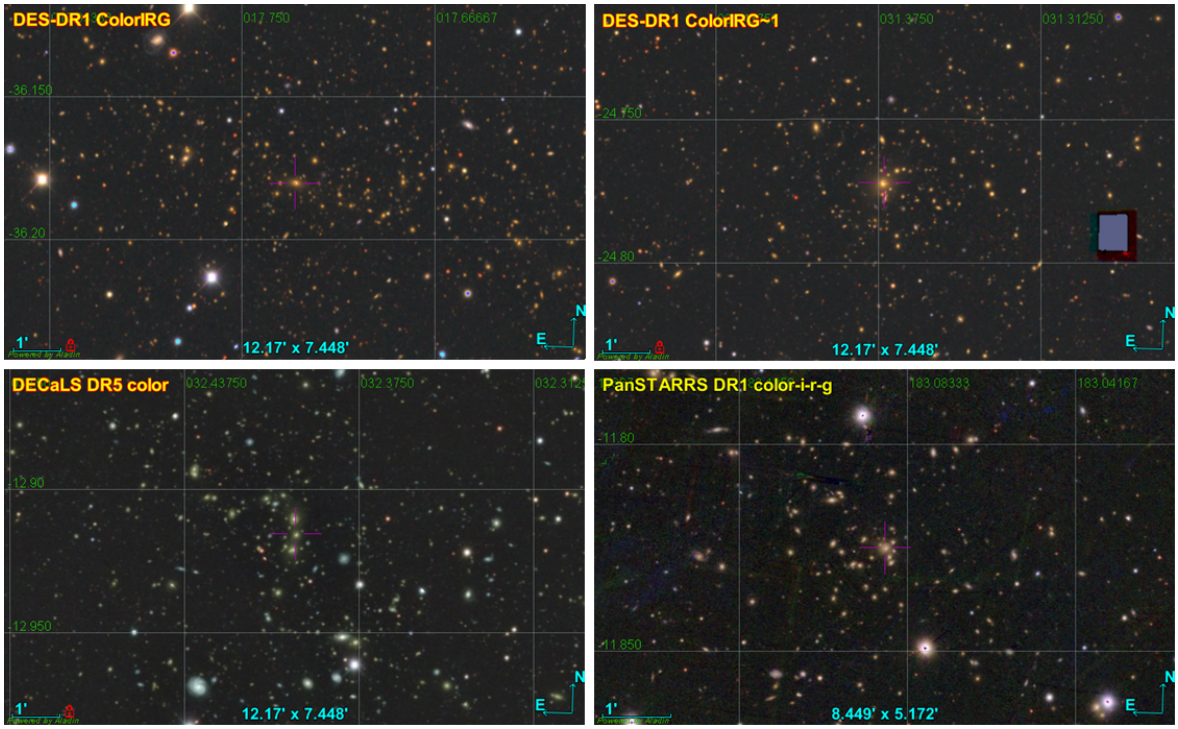

Figure 5.6: DES, DECaLS or PanSTARRS images of four $z \sim 0.2$, $M_{200} > 4 \times 10^{14} h^{-1} \mathrm{M}_{\odot}$ ATLAS clusters which are also detected in the Abell sample, with no detections in the Planck SZ catalogue.

5.4.3 σ_8 and the evolution of cluster mass function

In order to determine the value of σ_8 preferred by the data, we fit the Tinker et al. (2008) models to the observed ATLAS mass functions in each redshift bin. This is done by treating σ_8 as a free parameter when generating the mass function models at each redshift, while assuming the Planck Collaboration et al. (2016b) values for all other cosmological parameters. This results in a mean σ_8 value of $\sigma_8 = 0.76 \pm 0.02$, where the uncertainty is given by the standard error on the mean. This corresponds to $S_8 = 0.77 \pm 0.03$, where $S_8 \equiv \sigma_8 \sqrt{\Omega_\mathrm{m}/0.31}$.

In Figure 5.7, we compare the value of S_8 measured from the ATLAS cluster mass functions to various other measurements, including the Planck CMB analysis (Planck Collaboration et al., 2020), as well as the large-scale structure clustering and weak lensing analyses from the KiDS (Heymans et al., 2020), DES (Abbott et al., 2018a) and BOSS (Tröster et al., 2020) surveys. Recent measurements based on various other cluster samples, including the Planck (Planck Collaboration et al., 2016d) and SPT (Bocquet et al., 2019) SZ clusters, the DES Y1 optical cluster sample (DES Collaboration et al., 2020), and the REFLEX II X-ray cluster sample (Böhringer et al., 2014) are also shown. As we can see, the majority of S_8 measurements (blue data points) appear to be in good agreement, and taking the mean of

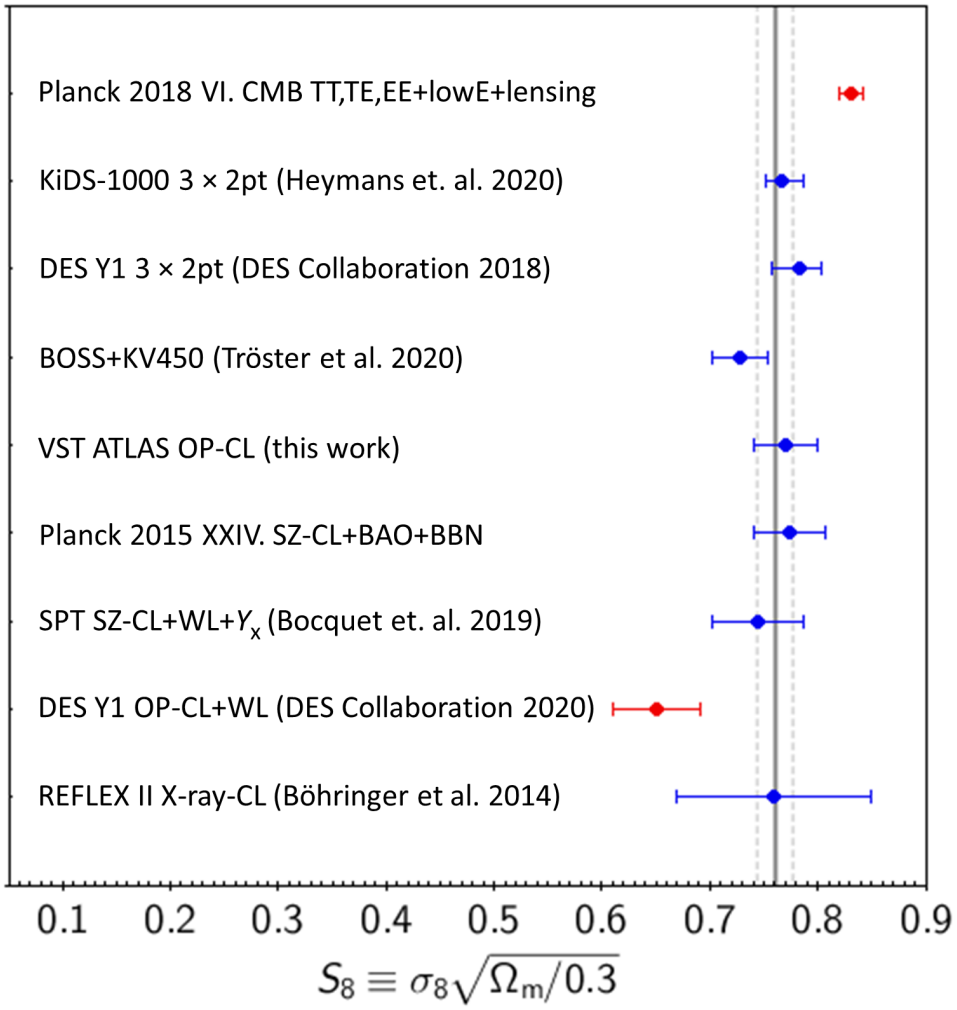

Figure 5.7: Comparison of S_8 measurements from the analysis of VST ATLAS cluster mass functions and measurements from various other surveys. Here, OP-CL, SZ-CL and X-ray-CL are used to distinguish optical, SZ and X-ray cluster samples, respectively. With the exception of the Planck 2018 CMB constraint and the weak lensing calibrated analysis of the DES Year 1 (Y1) cluster sample (red data points), the S_8 measurements from all other surveys (blue data points) appear to be in good agreement. The solid line shows the mean of the blue data points with a value of $\bar{S}_8 = 0.761 \pm 0.007$ where the uncertainty is given by the standard error on the mean. For illustration purposes, in this plot we show the standard deviation on the mean as a measure of the scatter, using the dotted lines.

these measurements results in a value of $\bar{S}_8 = 0.761 \pm 0.007$. However, the analysis of the DES Y1 cluster sample results in a S_8 value which is 2.7σ lower than $\bar{S}_8$ (this is mostly driven by their low measurement of $\Omega_m = 0.179^{+0.031}_{-0.038}$), while the Planck CMB constraint on S_8 is in a 4.6σ tension with $\bar{S}_8$. The source of the tension between Planck's early-Universe constraints on S_8 and the lower redshifts measurements from the analyses of the large-scale structure remains unknown and an important topic of study in future works.

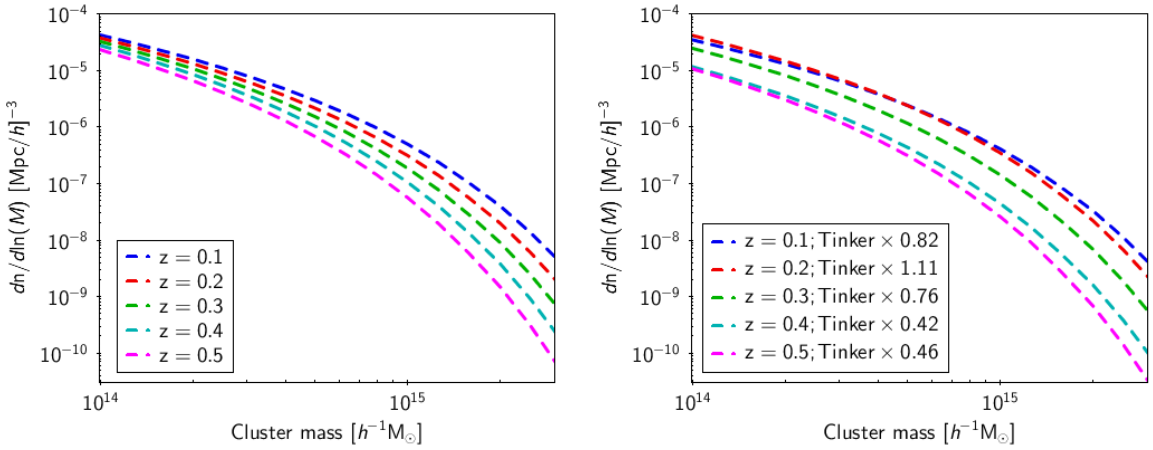

(a) (b)

Figure 5.8: (a) The redshift evolution of the Tinker et al. (2008) mass function models. (b) The redshift evolution of the Tinker et al. (2008) mass function models, fitted to ATLAS observations. At each redshift, the best-fit is obtained by varying the normalization of the models by the factors shown in the plot legend. For clarity, we do not plot the observed ATLAS mass functions here.

Figure 5.8a shows the redshift evolution of the Tinker et al. (2008) mass functions (assuming our fiducial, Planck Collaboration et al. 2016a cosmology), while Figure 5.8b shows the redshift evolution of ATLAS cluster mass functions based on the best-fit Tinker et al. (2008) models. Here, instead of varying σ_8 (which modifies the shape, as well as normalization of the models), we keep the cosmological parameters constant and simply adjust the normalization of models by the factors shown in the legend of Figure 5.8b in order to find the best fit values preferred by the data at each redshift. Our findings show that with the exception of $z = 0.2$, the data appear to prefer lower mass function amplitudes relative to the Tinker et al. (2008) predictions with the difference between the observations and predictions being higher at $z > 0.35$. While this comparison provides a preliminary indication of the divergence of observations to predictions of the model, a more comprehensive analysis of the systematic and statistical uncertainties on the ATLAS cluster mass function (with errors estimated from the data using jackknife or bootstrap techniques or using mock catalogues) is needed before the statistical significance of the divergence between the observations and the predictions can be quantified. We leave this, as well as comparison of the observations to different mass function models, and obtaining constraints for a larger set of cosmological parameters from the ATLAS cluster mass functions to future works.

5.5 Conclusions

In this chapter, we converted our cluster richness (N_{200}) values which were presented in Chapter 3 to estimates of cluster mass (M_{200}) based on a mass-richness scaling relation calibrated to cluster masses from the SDSS RedMapper, MCXC, Planck and AdvACT samples.

We then compared the cluster mass functions of ATLAS, RedMapper, Planck and AdvACT samples to the theoretical predictions of Tinker et al. (2008) models (assuming a Planck Collaboration et al. 2020 ΛCDM cosmology), in the $0.05 < z < 0.55$ redshift range. The summary of our findings is as follows:

- At $z < 0.35$, ATLAS cluster mass functions have a higher amplitude compared to those of the SZ samples and the RedMapper mass functions. This places the ATLAS measurements in better agreement with ΛCDM predictions with $\sigma_8 = 0.811 \pm 0.006$ (based on the CMB analysis of Planck Collaboration et al. 2020), rather than some of the previous constraints from the Planck SZ cluster counts, which depending on the SZ mass calibrations, can give σ_8 measurements as low as 0.71 ± 0.03 (Planck Collaboration et al., 2016d).

- Incompleteness of the SDSS RedMapper cluster sample at lower redshifts is likely to be a contributing factor to the lower amplitude of its mass functions relative to the predictions of ΛCDM.

- While systematics in SZ mass calibrations are likely to be the dominant contributing factor to the lower mass function amplitude of SZ samples relative to the models, the current incompleteness of SZ samples are also likely to have a non-negligible impact on the lower than expected mass function amplitudes.

- Follow-up spectroscopic observations of SZ clusters guided by optical cluster catalogues such as ATLAS and RedMapper could improve the completeness of SZ samples. Furthermore, future detailed studies of rich optical clusters which remain undetected in SZ samples could help with the identification of any unknown issues impacting the completeness of SZ catalogues.

- Fitting the ATLAS mass functions over the full redshift range of the sample with σ_8 treated as a free parameter yields a best-fit value of $S_8 = 0.77 \pm 0.33$. While this value in good agreement with the values obtained from the weak lensing and clustering analyses of DES and KiDS surveys, as well as measurements from Planck, SPT and

REFLEX II cluster samples, it is $\approx 2\sigma$ lower than the Planck CMB constraint. This discrepancy increases to 4.6σ when the Planck CMB S_8 measurement is compared to the mean S_8 value obtained from the combination of constraints from the DES and KiDS weak lensing and LSS clustering analyses and the ATLAS, SPT, REFLEX II and Planck SZ cluster counts results. The source of this tension is an important topic of investigation for future works.

- Focusing on the redshift evolution of ATLAS cluster mass functions, we found the ATLAS mass functions to generally prefer lower values of normalisation relative to the Tinker et al. (2008) model predictions (by up to a factor of ~ 2 at $z > 0.35$). This is with the exception of the $z = 0.2$ redshift bin, where the ATLAS mass function normalisation appeared to be $1.11\times$ higher than that of the Tinker et al. (2008) model prediction. In future, better characterisation of the statistical and systematic uncertainties on the ATLAS cluster mass functions (e.g. based on analysis of simulated mocks), will allow for a rigorous statistical analysis of these deviations between the observations and theoretical predictions.

Chapter 6

Cross-correlating Planck with VST ATLAS LRGs: a new test for the ISW effect

6.1 Introduction

Based on the latest observational evidence, the universe is believed to be spatially flat (Planck Collaboration et al. 2016b) and undergoing a late-time accelerating state of expansion (Riess et al. 1998; Alam et al. 2017). In the current standard model of cosmology ΛCDM, dark energy, parameterised as a cosmological constant (Λ), is believed to be the driving force behind this late-time accelerating expansion. Various alternatives to the cosmological constant have been proposed including modified gravity (Clifton et al. 2012), scale-invariant (Maeder 2017) or spatially inhomogeneous cosmological models (see e.g. Dunsby et al. 2010; Rácz et al. 2017). As a consequence of the accelerated expansion of the universe, cosmic microwave background (CMB) photons passing through gravitational potential wells, caused by large-scale structure such as galaxy clusters, are left with a net gain of energy as the potential wells become shallower as the photons cross them. In a matter-dominated universe, the net gain of energy due to gravitational blueshifting of a CMB photon as it "falls into" gravitational potential wells is cancelled out by the photon's gravitational redshifting as it "climbs out" of the potential well. However, as the Universe becomes dark energy dominated (at $z < 1$ according to the ΛCDM model), its accelerating expansion causes the gravitational potential well to decay and become shallower on the time scale it takes for the photon to pass through it. This results in a boost to the energy of CMB photons leaving them with a slightly higher

temperature than the average temperature of the CMB. The opposite effect takes place as the photons pass through gravitational potential peaks (i.e. voids) with the photons undergoing a net loss of energy and a slightly lower than average temperature. The combination of these phenomena leads to secondary anisotropies on the CMB temperature map known as the (late-time) Integrated Sachs-Wolfe (ISW; Sachs & Wolfe 1967) effect. The change in the CMB temperature $\Delta T(\hat{n})$ resulting from the ISW effect in direction $\hat{n}$ is linked to the change in the gravitational potential $\dot{\Phi}(\hat{n}, \tau)$ with respect to conformal time τ, integrated from the surface of last scattering to the observer:

$$\delta T(\hat{n}) = \frac{\Delta T(\hat{n})}{\bar{T}} = 2 \int_{\tau_{\rm LS}}^{\tau_0} \dot{\Phi}(\hat{n}, \tau) d\tau, \tag{6.1.1}$$

where $\delta T(\hat{n})$ is the observed CMB temperature anisotropy due to the ISW effect measured at the present day (τ_0), $\bar{T}$ is the mean CMB temperature and $\tau_{\rm LS}$ is the time of the matter-radiation decoupling when the CMB was emitted. In matter-dominated Universe, Φ is constant in the linear perturbation limit (as large-scale density perturbations grow at the same rate as the scale factor of the Universe). However, in a dark energy dominated Universe, the scale factor grows faster than the linear perturbations resulting in the gravitational potential to decay with time (see Crittenden & Turok 1996; Nadathur et al. 2012; Huterer et al. 2015).

The signature of the ISW effect can be observed as a non-zero signal in the cross-correlation between the distribution of foreground tracers of mass (such as galaxies) and the temperature of CMB, providing a direct probe of the late-time expansion of the universe. Early attempts at measuring the ISW signal using the cross-correlation method, include an analysis of the COBE CMB map by Boughn & Crittenden (2002) followed by detections of the signal using the WMAP CMB data, albeit often at relatively low to moderate levels of significance (Scranton et al. 2003; Nolta et al. 2004; Boughn & Crittenden 2004; Corasaniti et al. 2005; Padmanabhan et al. 2005; Giannantonio et al. 2006; Cabré et al. 2006; Rassat et al. 2007; Raccanelli et al. 2008; Granett et al. 2009; Bielby et al. 2010; Sawangwit et al. 2010; Kovács et al. 2013). Other studies have however claimed detections in the range of $3-5\sigma$ (Fosalba et al. 2003; Fosalba & Gaztañaga 2004; Vielva et al. 2006; McEwen et al. 2006; Giannantonio et al. 2008; Ho et al. 2008; Granett et al. 2008; Giannantonio et al. 2012; Goto et al. 2012; Planck Collaboration et al. 2016c).

Another common approach in measuring the ISW signal is by stacking of voids and superclusters. Similar to the cross-correlation method, studies using this approach have obtained detection significances ranging from low to moderate (Granett et al. 2015; Kovács et al.

2017), to 3σ or higher (Pápai et al. 2011; Nadathur & Crittenden 2016; Cai et al. 2017; Planck Collaboration et al. 2016c). Interestingly, a number of these studies have reported a signal with a higher amplitude than expected based on ΛCDM predictions.

Here, we follow the work of Sawangwit et al. (2010) where the ISW analysis was performed on photometrically selected Luminous Red Galaxies (LRGs) from SDSS in the Northern Hemisphere. In that work, three redshift-limited LRG samples were created allowing the measurement the ISW signal at redshifts of $\bar{z} = 0.35$, 0.55 and 0.68. Although an ISW signal consistent with ΛCDM was detected at $\bar{z} = 0.35$ and 0.55, no such signal was detected at $\bar{z} = 0.68$ albeit, as in the other two cases, the uncertainties were large relative to the expected signal. Given the implications of any ISW deviations from ΛCDM predictions (which could provide evidence for modified gravity or inhomogeneous cosmological models), the lack of detection of the ISW signal at $\bar{z} = 0.68$ in SDSS, is a particularly important topic for investigation using independent samples of LRGs. Sawangwit et al. (2010) also detected the ISW effect in three magnitude limited galaxy samples ($18 < r < 19$, $19 < r < 20$ and $20 < r < 21$), peaking in redshift at $z \approx 0.20$, 0.27 and 0.36, providing some confirmation of the ISW measurements in the two lower redshift LRG samples but not in the third, highest redshift, sample.

In this work we measure the ISW signal in the cross-correlation of similar samples of galaxies to those of Sawangwit et al. (2010) but now selected from the VST ATLAS Survey (Shanks et al. 2015), with the Planck CMB temperature map (Planck Collaboration et al. 2016a). The VST ATLAS survey has the advantage of covering large areas (~ 4070 deg^2) of the previously unexplored Southern sky, making it an ideal dataset for improving ISW constraints. This is because most of the available area in the North has already been covered by SDSS and, since the ISW signal weakens beyond $z \approx 1$, there is limited option to increase the signal at larger distances. Indeed, with these Southern VST ATLAS data we may be approaching the upper limit to the significance of ISW detection due to cosmic variance in our limited 'local' volume (see Francis & Peacock 2010).

VST ATLAS is thus located wholly in the Southern Hemisphere and is split into two areas by the Galactic Plane. In the Northern Galactic Cap (NGC[1]), the survey covers an area of $\sim 1450\,\mathrm{deg}^2$, while the Southern Galactic Cap (SGC) covers an area of $\sim 2620\,\mathrm{deg}^2$. In these regions, the survey provides imaging data in *ugriz* bands to similar depths as SDSS in

[1]We note that at the time of conducting this research, observations of the ATLAS survey in the g and r-bands were incomplete in the DEC<-20 region of the NGC. The analyses presented in this Chapter are therefore limited to the DEC>-20 region of the NGC.

the North, but with superior seeing. We shall use these data to select three LRG samples and three magnitude limited samples, closely analogous to those created by Sawangwit et al. (2010) using SDSS.

In order to test our LRG selections, we shall first compare the angular auto-correlation functions of our VST ATLAS LRG samples to those of Sawangwit et al. (2011). After cross-checking our photometric selections, we shall perform the ISW measurements and combine our results with those of Sawangwit et al. (2010), to obtain better constraints on the ISW effect at each redshift. As a further verification of the SDSS ISW measurements at $\bar{z} = 0.35$, $\bar{z} = 0.55$ and $\bar{z} = 0.68$ we repeat the measurements using the LOWZ and CMASS LRG samples from Data Release 12 (DR12; Alam et al. 2015) of the SDSS BOSS survey and the eBOSS DR14 LRG sample (Prakash et al., 2016) respectively. Unlike photometrically selected samples, these spectroscopically confirmed samples do not suffer from contamination due to stars, or from galaxies outside the redshift range. This makes them ideal datasets for further testing the SDSS photometric ISW measurements, in particular. We note however, that while spectroscopic samples are not affected by stellar contamination or systematics related to photometric redshifts, they are not immune to targeting systematics which could introduce artificial correlations between the inferred density field and factors including stellar density, fiber collisions and observing conditions. In this work, when using spectroscopic samples, we account for these potential systematics by applying the BOSS/eBOSS weights (where available), as described in Section 6.3.2.

To test the robustness of our ISW detections, we perform rotation tests similar to those previously implemented by Sawangwit et al. (2010) and Giannantonio et al. (2012), where the ISW cross-correlation measurement is performed on incremental rotations of the LRG overdensity maps (about the galactic pole) with respect to the CMB to test for systematics. In their analysis, Sawangwit et al. (2010) found that in approximately 1 or 2 out of 8 cases, the rotated maps produce a more significant ISW detection than the un-rotated map. Using a similar approach, Giannantonio et al. (2012) claimed that the results of their rotation tests, were consistent with the statistical variance of their associated datasets. Here we shall apply the rotation test to the ISW measurements obtained from the BOSS LOWZ and CMASS spectroscopic LRG samples, to check their robustness and compare our findings with those of Giannantonio et al. (2012).

Hence, our aims are first to use ATLAS to test the reproducibility of the ISW measurements in the three LRG and the three magnitude limited galaxy samples as selected by Sawangwit

et al. (2010) in SDSS. Of particular interest, is whether the VST ATLAS data independently reproduce the null detection of the ISW effect in the highest redshift LRG sample at $\bar{z} = 0.68$. Our second aim is to check the robustness of the previous SDSS LRG results using new spectroscopically confirmed SDSS LRG samples, particularly in the two lower redshift ranges. The final aim is to apply the rotation test to the BOSS LRG samples to assess the robustness of such ISW measurements.

The layout of this Chapter is as follows: we present a description of the selected datasets in Section 6.2, followed by an outline of all relevant methodology in Section 6.3. We present the results of our analysis and a discussion of our findings in Section 6.4 and conclude this work in Section 6.5.

Throughout this work all magnitudes are given in the AB system, and for consistency, we assume the fiducial ΛCDM cosmology adopted by Sawangwit et al. (2010) with $\Omega_\Lambda = 0.7$, $\Omega_\mathrm{m} = 0.3$, $f_\mathrm{baryon} = 0.167$, $\sigma_8 = 0.8$ and $h = 0.7$.

6.2 Datasets

6.2.1 Planck 2016 CMB temperature map

In our ISW analysis, we use the full Planck 2016 `COMMANDER` CMB temperature map (described in Planck Collaboration et al. 2016a), downgraded to a `HEALpix`[2] (Górski et al. 2005) resolution of $N_{side} = 512$ (FWHM=20 arcmin). This is consistent with the `HEALpix` resolution used in the analysis of Sawangwit et al. (2010). We apply the associated `COMMANDER` "confidence" mask to remove sections of the sky where the temperature and polarization CMB solution cannot be trusted. The masked Planck CMB maps corresponding to coverage area of VST ATLAS Northern and Southern Galactic Caps are shown in Figure 6.5. In this Figure, we also show the overdensity maps for our $\bar{z} = 0.68$ LRG and $20 < r < 21$ magnitude limited galaxy sample, as described in Sections 6.2.5 and 6.2.6 respectively. Here we show the overdensity maps of our faintest and highest redshift samples, as they are the most challenging to obtain due to their susceptibility to residual stellar contamination and artificial inhomogeneities caused by factors such as varying observing conditions.

[2]http://healpix.sourceforge.net

6.2.2 VST ATLAS luminous red galaxies

Following the photometric selection criteria of Sawangwit et al. (2010), which was used to extract LRGs from the SDSS Data Release 5 (DR5; Adelman-McCarthy et al. 2007) data, we use the VST ATLAS survey (described in Chapter 2) to define three LRG samples at low ($\bar{z} = 0.35$), intermediate ($\bar{z} = 0.55$) and high ($\bar{z} = 0.68$) redshifts. Sawangwit et al. (2010) in turn adopted their selection criteria based on those of the SDSS LRG (Eisenstein et al. 2001), 2DF-SDSS LRG and QSO (2SLAQ; Cannon et al. 2006) and Anglo-Australian Telescope (AAT)-AAOmega (Ross et al. 2008) spectroscopic redshift surveys, corresponding to the low, intermediate and high redshift LRG samples respectively. In Appendix C.1 we compare the ATLAS and SDSS $g - r$, $r - i$ and $i - z$ colours, finding a reasonably tight scatter with no major systematic offsets in all cases. This enables us to adopt the above mentioned SDSS-based photometric selection criteria in defining our redshift limited ATLAS LRG samples.

As observations for the VST ATLAS survey are taken in one band at a time and the telescope has a 1 deg^2 field of view (henceforth referred to as a 'tile'), it is possible that different bands are observed on separate nights with varying atmospheric conditions. Although ATLAS has a relatively tight seeing distribution, in a small number of cases, variations in seeing could result in fewer objects being detected in one band (especially at fainter magnitudes). This is because unlike SDSS, forced photometry is currently unavailable for the VST ATLAS catalogue and in this work we only have access to colours for objects with $> 5\sigma$ detection in each band. Consequently, when the selection is applied, regions of the sky covered by these tiles will appear under-dense. Conversely, a few tiles could have a much higher than average number density due to residual stellar contamination (particularly in the NGC where the edge of the survey approaches the Galactic plane).

In order to reduce the impact of these factors on our clustering measurements, we impose a lower and an upper limit on the number of objects per tile, which masks any significantly under and over-dense tiles. This ensures the LRG samples used in our cross-correlation analysis do not contain artificial inhomogeneities due to photometric artefacts or residual stellar contamination. We select these lower and upper limits based on comparing the auto-correlation function of the LRG samples to the measurements of Sawangwit et al. (2011), thus ensuring that such artefacts and contaminations do not impact our ability to recover the true clustering of the LRGs.

6.2.3 $\bar{z} = 0.35$ low redshift LRG sample

Objects in our low redshift LRG sample are selected based on satisfying the following conditions:

$$17.5 < r_{\rm Kron} < 19.2, \tag{6.2.1}$$

$$r_{\rm Kron} < 13.1 + c_{\parallel}/0.3, \tag{6.2.2}$$

$$c_{\perp} < 0.2, \tag{6.2.3}$$

corresponding to 'Cut I' of Eisenstein et al. (2001), or 'Cut II' of the same study as defined by:

$$17.5 < r_{\rm Kron} < 19.5, \tag{6.2.4}$$

$$c_{\perp} > 0.45 - (g_{\rm A5} - r_{\rm A5})/6, \tag{6.2.5}$$

$$g_{\rm A5} - r_{\rm A5} > 1.3 + 0.25(r_{\rm A5} - i_{\rm A5}). \tag{6.2.6}$$

The colour variables $c_{\parallel}$ are and $c_{\perp}$ are given by:

$$c_{\parallel} = 0.7(g_{\rm A5} - r_{\rm A5}) + 1.2(r_{\rm A5} - i_{\rm A5} - 0.18), \tag{6.2.7}$$

$$c_{\perp} = (r_{\rm A5} - i_{\rm A5}) - (g_{\rm A5} - r_{\rm A5})/4.0 - 0.18. \tag{6.2.8}$$

We note that our use of SDSS cuts in our LRG sample selection is justified given the similarity between ATLAS and SDSS bands (see Figure C.1 for comparison of ATLAS and SDSS colours). Figure 6.1 shows the cuts used to selected our $\bar{z} = 0.35$ LRG sample in the $r - i$ vs. $g - r$ colour space.

To restrict our sample to galaxies we require the CASU r-band morphological classification `Classification_r`=1, and we remove noisy regions (due to remaining ghost reflections from bright stars or large galaxies) by requiring `sky_rms_r`<0.2. We further remove residual stellar contamination via visual inspection of the $r_{\rm A3}$ vs $r_{\rm Kron}$ diagram (see Figure 6.2) by requiring:

$$r_{\rm A3} > 0.909 r_{\rm Kron} + 2. \tag{6.2.9}$$

In the case of our low redshift sample we mask tiles with fewer than 5 deg^{-2} and more than 100 deg^{-2} LRGs. This results in the removal of 10 tiles in the NGC and 8 in the SGC, leaving 31,531 (~ 22 deg^{-2}) and 63,245 (~ 24 deg^{-2}) LRGs in the NGC and SGC respectively.

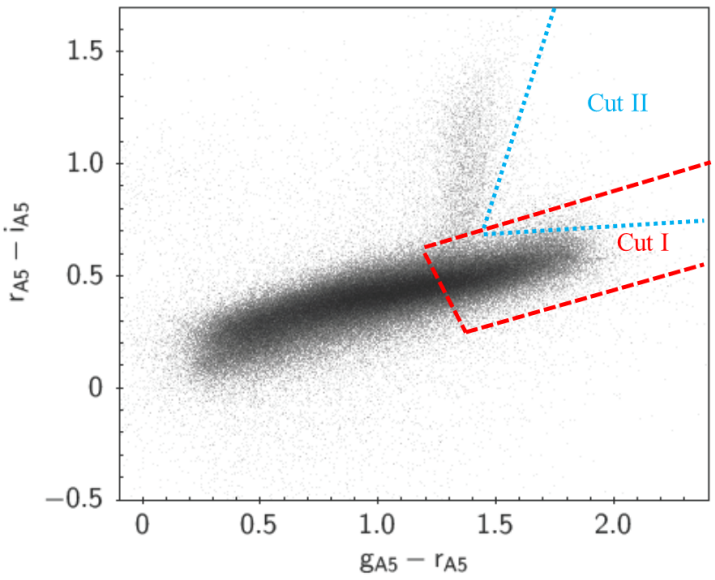

Figure 6.1: Our $\bar{z} = 0.35$ LRG photometric selection, based on 'Cut I' and 'Cut II' of Eisenstein et al. (2001), used in photometric selection of SDSS LRGs. Here, as in subsequent plots, the colour gradient illustrates the density of the points, with darker shades representing a higher number of data points occupying a region of the colour space. The objects shown in this plot are classified as galaxies based on their VST ATLAS r-band morphological classification and lie within a magnitude limit of $17.5 < r_{\mathrm{Kron}} < 19.5$.

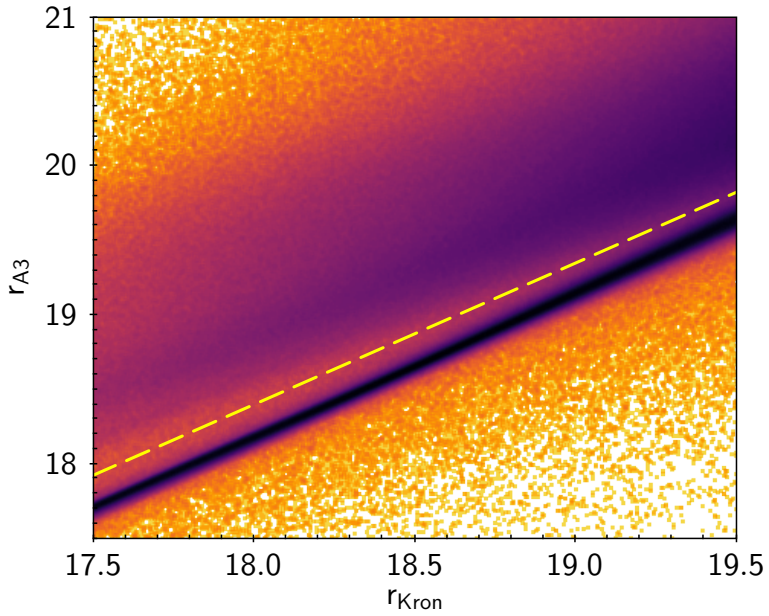

Figure 6.2: Further removal of residual stellar contamination from our $\bar{z} = 0.35$ LRG sample. The dashed line is described by equation 6.2.9, separating the stars (below the line) from galaxies (above the line).

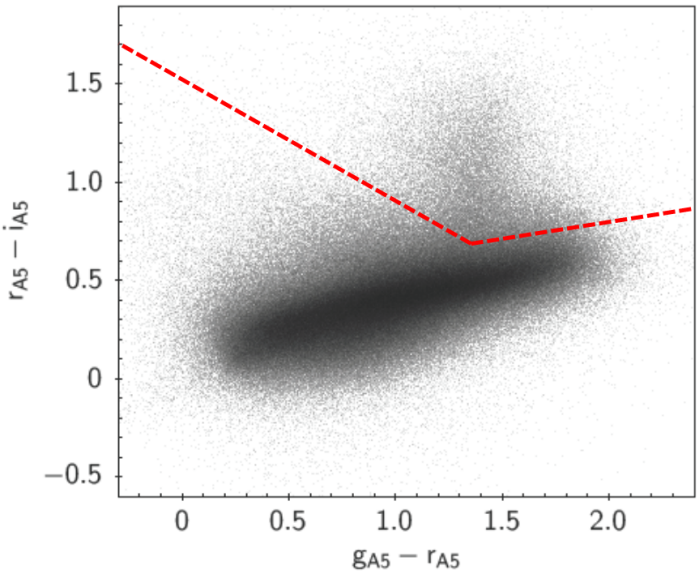

Figure 6.3: Our $\bar{z} = 0.55$ LRG photometric selection, following the colour cuts of Cannon et al. (2006) used in the selection of the 2SLAQ LRG sample. The objects shown here are classified as galaxies based on their VST ATLAS i-band morphological classification and lie within a magnitude limit of $17.5 < i_{\rm Kron} < 19.8$.

6.2.4 $\bar{z} = 0.55$ intermediate redshift LRG sample

We select our intermediate redshift LRG sample based on the following criteria which is an adaption of the photometric cuts of Cannon et al. (2006) used in the selection of the 2SLAQ LRG sample (see Figure 6.3):

$$17.5 \leq i_{\rm Kron} < 19.8, \tag{6.2.10}$$

$$c_{\parallel} \geq 1.6, \tag{6.2.11}$$

$$d_{\perp} > 0.55, \tag{6.2.12}$$

$$0.5 \leq (g_{\rm A5} - r_{\rm A5}) \leq 3.0, \tag{6.2.13}$$

$$(r_{\rm A5} - i_{\rm A5}) < 2, \tag{6.2.14}$$

where $c_{\parallel}$ is defined in equation (6.2.7) and $d_{\perp}$ is given by:

$$d_{\perp} = (r_{\rm A5} - i_{\rm A5}) - (g_{\rm A5} - r_{\rm A5})/8. \tag{6.2.15}$$

We restrict our selection to galaxies using the CASU i-band morphological classification (`Classification_i`=1), limit `sky_rms_i`<0.2 and remove residual stellar contamination by imposing:

$$i_{\rm A3} > 0.8 i_{\rm Kron} + 4.4, \tag{6.2.16}$$

in the NGC for $i_{\rm Kron} < 19.6$ and in the SGC for $i_{\rm Kron} < 19.1$, while imposing:

$$i_{\rm A3} > 1.3 i_{\rm Kron} - 4.95 \tag{6.2.17}$$

for the NGC in the range $i_{\rm Kron} > 19.6$ and

$$i_{\rm A3} > 1.8 i_{\rm Kron} - 14.7 \tag{6.2.18}$$

for the SGC in the range $i_{\rm Kron} > 19.1$. Here we require different slopes for removing residual stars in the NGC compared to the SGC, as the edge of the survey lies closer to the Galactic plane in the NGC resulting in an increase in the level of contamination from residual stars.

We mask tiles with fewer than 10 and more than 130 LRGs in the NGC and those with fewer than 10 and more than 150 LRGs in the SGC. This results in the removal of 21 tiles in the NGC and 8 tiles in the SGC, leaving 78,102 (~ 55 deg^{-2}) and 172,744 (~ 66 deg^{-2}) LRGs in the NGC and SGC respectively.

6.2.5 $\bar{z} = 0.68$ high redshift LRG sample

The high redshift LRG sample is selected based on the following criteria (see Figure 6.4):

$$19.8 < i_{\rm Kron} < 20.5, \tag{6.2.19}$$

$$e_{\parallel} \geq 1.95, \tag{6.2.20}$$

$$0.5 \leq (r_{\rm A5} - i_{\rm A5}) \leq 1.8, \tag{6.2.21}$$

$$0.6 \leq (i_{\rm A5} - z_{\rm A5}) \leq 1.5, \tag{6.2.22}$$

or

$$0.2 \leq (i_{\rm A5} - z_{\rm A5}) \leq 0.6, \tag{6.2.23}$$

$$x \leq (r_{\rm A5} - i_{\rm A5}) \leq 1.8, \tag{6.2.24}$$

with x being the smaller of $e_{\parallel} = (i_{\rm A5} - z_{\rm A5}) + (9/7)(r_{\rm A5} - i_{\rm A5})$ or 1.2 at a given $(i_{\rm A5} - z_{\rm A5})$. The sample is restricted to galaxies using the CASU i-band morphological classification (`Classification_i`=1) and stellar contamination is removed by imposing:

$$i_{\rm A3} > 1.2 i_{\rm Kron} - 3.45, \tag{6.2.25}$$

in the NGC for $i_{\rm Kron} < 20.02$, otherwise:

$$i_{\rm A3} > 1.4 i_{\rm Kron} - 7.42. \tag{6.2.26}$$

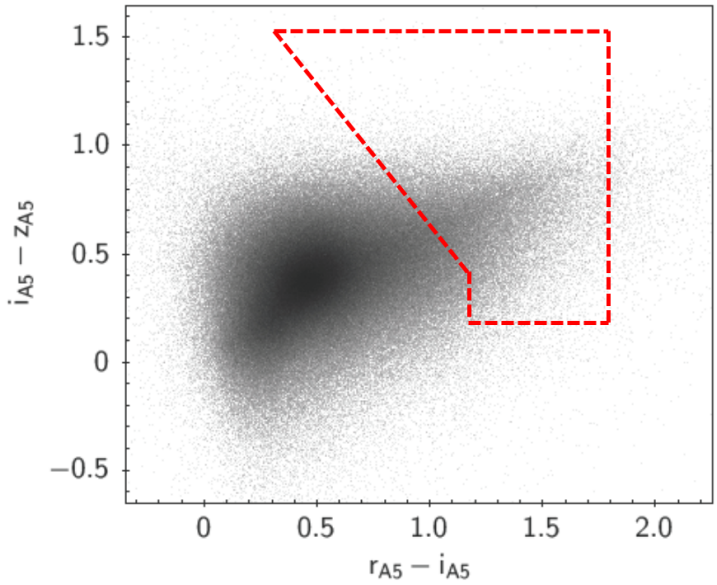

Figure 6.4: Our $\bar{z} = 0.68$ LRG photometric selection, following the colour cuts of Ross et al. (2008) used in the selection of the AAOmega LRG sample. The objects shown here are classified as galaxies based on their VST ATLAS i-band morphological classification and lie within a magnitude limit of $19.8 < i_{\rm Kron} < 20.5$.

In the SGC the imposed cuts are:

$$i_{\rm A3} > 1.2 i_{\rm Kron} - 3.55, \tag{6.2.27}$$

for $i_{\rm Kron} < 20.23$, otherwise:

$$i_{\rm A3} > 1.4 i_{\rm Kron} - 7.55. \tag{6.2.28}$$

For this sample we mask tiles with fewer than 10 and more than 90 LRGs in both NGC and SGC. This excludes 101 tiles in the NGC and 192 in the SGC, leaving 62,379 (~ 46 deg^{-2}) and 138,977 (~ 57 deg^{-2}) LRGs in the NGC and SGC respectively.

6.2.6 Magnitude limited galaxy samples

To select our three magnitude limited galaxy samples we require objects to be classified as galaxies using the CASU r-band morphological classification (`Classification_r`=1). We then simply select objects satisfying $18 < r_{\rm Kron} < 19$, $19 < r_{\rm Kron} < 20$ and $19 < r_{\rm Kron} < 20$. In all cases we apply the additional cut of $r_{\rm A5} > 0.94 r_{\rm Kron} + 1.08$ to remove any residual stellar contamination from our samples. For the $18 < r_{\rm Kron} < 19$ sample this results in 507,813 (~ 350 deg^{-2}) and 839,208 (~ 320 deg^{-2}) galaxies in the NGC and SGC respectively, with the $19 < r_{\rm Kron} < 20$ sample containing 1,567,450 (~ 1100 deg^{-2}) galaxies in the NGC

Table 6.1: Details of the VST ATLAS, BOSS LOWZ and CMASS, and eBOSS LRG samples used in our cross-correlation analyses. For comparison we have included the same information for the SDSS LRG samples used in the analysis of Sawangwit et al. (2010). *Other magnitude limits used in the selection of the eBOSS sample can be found in Prakash et al. (2016).

Sample ($\bar{z}$)	Number of LRGs	Masked Area (deg^2)	Sky Density (deg^{-2})	Magnitude (AB)
ATLAS (0.35)	94,776	≈ 4060	≈ 23	$17.5 < r < 19.5$
ATLAS (0.55)	250,846	≈ 4050	≈ 62	$17.5 < i < 19.8$
ATLAS (0.68)	201,356	≈ 3800	≈ 53	$19.8 < i < 20.5$
SDSS (0.35)	106,699	≈ 8210	≈ 13	$17.5 < r < 19.5$
SDSS (0.55)	655,775	≈ 7715	≈ 85	$17.5 < i < 19.8$
SDSS (0.68)	800,346	≈ 7622	≈ 105	$19.8 < i < 20.5$
LOWZ (0.32)	313,446	≈ 8337	≈ 38	$16.0 < r < 19.6$
CMASS (0.57)	849,637	≈ 9376	≈ 91	$17.5 < i < 19.9$
eBOSS (0.70)	141,000	≈ 1670	≈ 84	$19.9 < i < 21.8$*

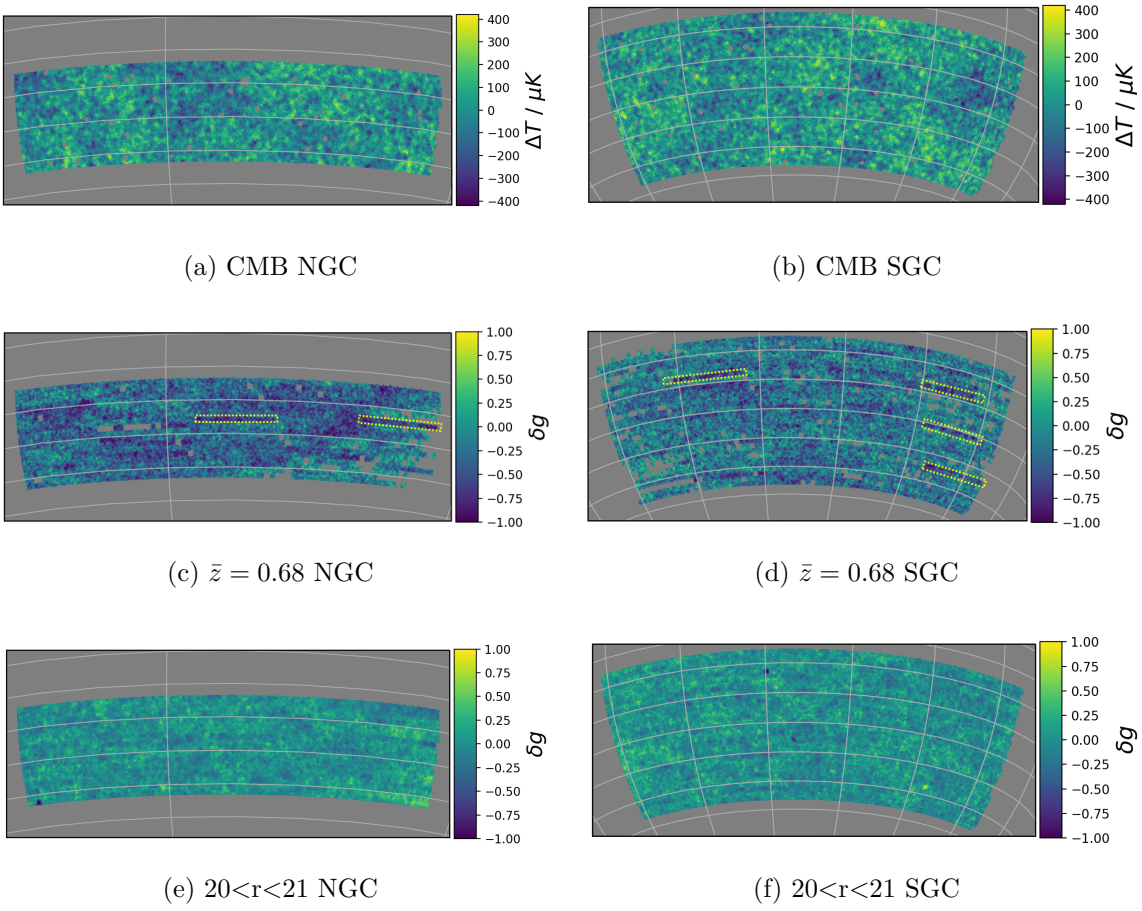

(a) CMB NGC

(b) CMB SGC

(c) $\bar{z} = 0.68$ NGC

(d) $\bar{z} = 0.68$ SGC

(e) 20<r<21 NGC

(f) 20<r<21 SGC

Figure 6.5: The Planck CMB temperature anisotropy map covering the NGC (a) and SGC (b) of the VST ATLAS survey (described in Section 6.2.1). (c & d) The VST ATLAS $\bar{z} = 0.68$ LRG overdensity maps. Although we have included a number of under-dense concatenations in the final sample (marked by dotted boxes), our tests show that our auto and cross-correlation measurements are insensitive to masking these. (e & f) The VST ATLAS galaxy overdensity maps for our $20 < r < 21$ magnitude limited sample (described in Section 6.2.6).

and 2,589,744 ($\sim$ 1000 deg^{-2}) galaxies in the SGC. For the $19 < r_{\rm Kron} < 20$ sample, we find 6,072,488 ($\sim 2,314$ deg^{-2}) and 3,522,801 ($\sim 2,426$ deg^{-2}) galaxies in the NGC and SGC. The mean redshift of our 18-19, 19-20 and 20-21 magnitude limited samples are $\bar{z} \approx 0.20 \pm 0.09, 0.27 \pm 0.13$ and 0.36 ± 0.16 respectively.

6.2.7 BOSS DR12 LOWZ, CMASS and eBOSS DR14 LRG samples

The LOWZ samples covers an area of ~ 8337 deg^2 with a number density of ~ 38 deg^{-2}. As $z \lesssim 0.4$ LRGs were targeted in the LOWZ sample, we remove the lower redshift objects by imposing a redshift cut of $z > 0.23$, thus achieving a subset of the LOWZ sample with a mean redshift of $\bar{z} = 0.35$. The CMASS sample covers an area of ~ 9376 deg^2 with a number density of ~ 91 deg^{-2} and an effective redshift of $z \approx 0.57$. A full description of the target selection criteria for these samples is provided by Reid et al. (2016).

The eBOSS LRG target selection is fully described in Prakash et al. (2016), with the sample used here containing $\sim 141,000$ LRGs, covering an area of ~ 1670 deg^2, resulting in an LRG number density of ~ 84 deg^{-2} with a median redshift of $z \approx 0.7$. A summary of the above information for our BOSS and eBOSS LRG samples is provided in Table 6.1.

6.3 Methodology

6.3.1 Measuring LRG angular auto-correlation function

We measure the angular correlation function $\omega(\theta)$ of our LRG samples using the Landy-Szalay estimator (Landy & Szalay 1993):

$$\omega(\theta) = 1 + \left(\frac{N_{\rm r}}{N_{\rm d}}\right)^2 \frac{DD(\theta)}{RR(\theta)} - 2\left(\frac{N_{\rm r}}{N_{\rm d}}\right) \frac{DR(\theta)}{RR(\theta)}, \tag{6.3.1}$$

where $DD(\theta)$, $DR(\theta)$ and $RR(\theta)$ are data-data, data-random, and random-random pair counts at an angular separation of θ. We perform this calculation using the CUTE[3] algorithm (Alonso 2012). The correlation function is calculated up to $\theta = 100$ arcmin (using 19 logarithmically spaced bins), to match the range covered by Sawangwit et al. (2011) and allow for the comparison of the two results. For each sample we generate random catalogues with 20$\times$ the mean number density of LRGs in the NGC and SGC and apply the same masks as applied to the data.

[3]https://github.com/damonge/CUTE

In order to obtain an estimate of the errors on the correlation functions we divide each sample into $N_{\rm s} = 6$ non-overlapping subsamples (with 2 in the NGC and 4 in the SGC), each ~ 668 deg^2 in area. The mean number of LRGs in each subsample are $\sim 15,800$, $\sim 41,800$ and $\sim 33,600$ for our $\bar{z} = 0.35, 0.55$ and 0.68 samples respectively. We then calculate the mean of these measurements, $\bar{\omega}(\theta)$, for each sample and simply take the standard error on the mean $\sigma_{\bar{\omega}(\theta)}$, as the uncertainty on the correlation function:

$$\sigma_{\bar{\omega}(\theta)} = \frac{\sigma_{N_{\rm s}-1}}{\sqrt{N_{\rm s}}} = \sqrt{\frac{\sum(\omega_i(\theta) - \bar{\omega}(\theta))^2}{N_{\rm s}^2 - N_{\rm s}}}. \tag{6.3.2}$$

Here the sample standard deviation $\sigma_{N_{\rm s}-1}$ is normalized to $N_{\rm s}-1$ (as the mean is determined from the same dataset, reducing the number of degrees of freedom by one), and $\omega_i(\theta)$ is the correlation function of the i-th subsample.

6.3.2 Measuring LRG-CMB cross-correlation

We adopt a similar approach to Sawangwit et al. (2010) in calculating the LRG-CMB cross-correlation, a summary of which is presented here. In this work, we use the NPT (N-point spatial statistic; Gray et al. 2004) code to perform the cross-correlation analysis. First `HEALpix` (Górski et al. 2005) is used to create LRG distribution maps by dividing our LRG samples into spherical pixels of equal area, matching the resolution of our Planck CMB temperature map ($N_{\rm side} = 512$; FWHM=20 arcmin). We combine our LRG mask with the Planck CMB temperature mask and apply it to both the LRG distribution and CMB temperature maps.

The LRG distribution map is then used to calculate the LRG number over-density, $\delta_{\rm L}(\hat{n})$, per pixel:

$$\delta_{\rm L}(\hat{n}) = \frac{n_{\rm L}(\hat{n}) - \bar{n}_{\rm L}}{\bar{n}_{\rm L}}, \tag{6.3.3}$$

where $n_{\rm L}$ is the number of LRGs in a given pixel and $\bar{n}_{\rm L}$ is the mean number of LRGs for the sample being studied.

In the case of CMASS and eBOSS spectroscopic samples, we include the associated weights when calculating the LRG over-density:

$$\delta_{\rm L}(\hat{n}) = \frac{n_{\rm L}(\hat{n}) - w_{\rm tot} \times \bar{n}_{\rm L}}{w_{\rm tot} \times \bar{n}_{\rm L}}, \tag{6.3.4}$$

where $w_{\rm tot} = w_{\rm systot} \times (w_{\rm cp} + w_{\rm noz} - 1)$. Here $w_{\rm systot} = w_{\rm see} \times w_{\rm star}$, is the angular systematic weight, introduced to account for non-cosmological fluctuations in target density with stellar density and seeing, $w_{\rm cp}$ accounts for fibre collisions and $w_{\rm noz}$ corrects for redshift failures

by up-weighting the nearest neighbour. A more detailed description of these weights is presented by Ross et al. (2012). We do not include any weights when measuring the ISW amplitude using the LOWZ sample, as systematic weights were not supplied with the DR12 LOWZ catalogue. As inclusion of weights do not appear to have a significant impact on our CMASS and eBOSS ISW measurements however, the impact of weights on our LOWZ ISW measurement is also likely to be small.

We then calculate the LRG-CMB two-point angular cross-correlation function, $\omega_{\rm LC}(\theta)$, using:

$$\omega_{\rm LC}(\theta) = \frac{\sum_{ij} f_i \delta_{\rm L}(\bar{n_i}) f_j \Delta_{\rm T}(\hat{n}_j)}{\sum_{ij} f_i f_j}, \tag{6.3.5}$$

with f_i representing the fraction of the i-th pixel located within the unmasked area, $\hat{n_i}.\hat{n_j} = cos(\theta)$ and $\Delta_{\rm T}$ being the Planck CMB temperature anisotropy after removing the monopole and dipole contribution. As we are using a high pixel resolution however, the contribution from the factors weighting for unmasked fractions become negligible, and we simplify equation (6.3.5) to $\omega_{\rm LC}(\theta) = \langle \delta_{\rm L}(\hat{n_1}) \Delta_{\rm T}(\hat{n}_2) \rangle$. Here we measure the cross-correlation function using 14 logarithmically spaced bins covering the range of $\theta < 1400$ arcmin.

In order to account for the correlation between the bins in the correlation function and obtain an accurate estimation of the significance of the results, we have to consider the full covariance matrix C_{ij} when fitting a model to the data. Ideally, the covariance matrix is calculated based on thousands of simulated mock catalogues. However, creating such mock catalogues is a complex and computationally extensive task which lies beyond the immediate scope of this work. As a result, here we follow the technique used by Sawangwit et al. (2010) and obtain the covariance matrix using the jackknife re-sampling technique, dividing the masked Planck CMB temperature and ATLAS LRG over-density maps into 36 fields of equal area (24 in SGC and 12 in NGC). Based on these $N_{\rm JK} = 36$ jackknife subsamples are generated, omitting one field at a time. The covariance matrix is then given by:

$$C_{ij} = \frac{N_{\rm JK} - 1}{N_{\rm JK}} \sum_{n=1}^{N_{\rm JK}} [(\omega_{{\rm LC},n}(\theta_i) - \bar{\omega}_{\rm LC}(\theta_i))(\omega_{{\rm LC},n}(\theta_j) - \bar{\omega}_{\rm LC}(\theta_j))], \tag{6.3.6}$$

where $\omega_{{\rm LC},n}(\theta_i)$ is the measured cross-correlation of the n-th subsample, $\bar{\omega}_{\rm LC}(\theta_i)$ is the mean of the measurements from all subsamples and i and j denote the i-th and j-th bins. The $N_{\rm JK} - 1$ factor is required in order to account for the fact that the subsamples are not independent and the uncertainty on each angular bin of the cross-correlation function $\sigma_{\omega_{\rm LC}}(\theta)$, is given by the square root of the diagonal elements of the covariance matrix.

For each of our samples, we obtain separate measurements of $\omega_{\rm LC}(\theta)$ in the NGC and SGC

which are combined by taking the weighted mean $\hat{\omega}_{\rm LC}(\theta)$, of the two measurements:

$$\hat{\omega}_{\rm LC}(\theta) = \frac{\sum_m \omega_{{\rm LC},m}(\theta)/\sigma^2_{\omega_{{\rm LC},m}(\theta)}}{\sum_m 1/\sigma^2_{\omega_{{\rm LC},m}(\theta)}}, \tag{6.3.7}$$

where m denotes the measurement from NGC/SGC and the error on the weighted mean $\sigma_{\hat{\omega}_{\rm LC}(\theta)} = \sqrt{1/\sum_m 1/\sigma^2_{\omega_{{\rm LC},m}(\theta)}}$.

Given that our samples cover the same range of redshifts as those of Sawangwit et al. (2010), and we have assumed the same fiducial cosmology, in this work we do not generate independent theoretical predictions for the ISW signal. Instead we simply compare our results with the models calculated in Section 3 of Sawangwit et al. (2010) based on ΛCDM predictions.

Using the covariance matrix, we then calculate the χ^2 parameter providing a statistical measure of the quality of the fit provided by the model to our observations. The χ^2 is given by:

$$\chi^2 = [\hat{\omega}_{\rm LC,obs}(\theta) - \omega_{\rm LC,mod}(\theta)]^T C^{-1} [\hat{\omega}_{\rm LC,obs}(\theta) - \omega_{\rm LC,mod}(\theta)], \tag{6.3.8}$$

where $\hat{\omega}_{\rm LC,obs}(\theta)$ is our measured cross-correlation and $\omega_{\rm LC,mod}(\theta)$ is the prediction from the model[4].

6.4 Results and Discussion

6.4.1 VST ATLAS LRG angular auto-correlation function

The angular auto-correlation functions for our low, intermediate and high redshift LRG samples are presented in Figure 6.6. For all three samples we find a reasonable agreement between our results and the SDSS measurements of Sawangwit et al. (2011). In all cases the agreement between the auto-correlation function amplitudes of the ATLAS and SDSS LRGs (and best-fit double power law models), is an indication of the success of our applied photometric selection criteria at extracting similar LRG samples from the VST ATLAS survey as those extracted from SDSS. Given the sensitivity of the auto-correlation function amplitude to stellar contamination, these results also show that our cuts have succeeded in efficiently reducing stellar contamination in our three LRG samples. Furthermore, even though our LRG samples have different number densities compared to those of Sawangwit et al. (2010), the agreement between the ATLAS and SDSS auto-correlation functions suggests that the LRG clustering

[4]See Section 6.4.2 for a discussion of why we ultimately adopt an alternative approach to χ^2, in accessing the level of agreement between our results and the model.

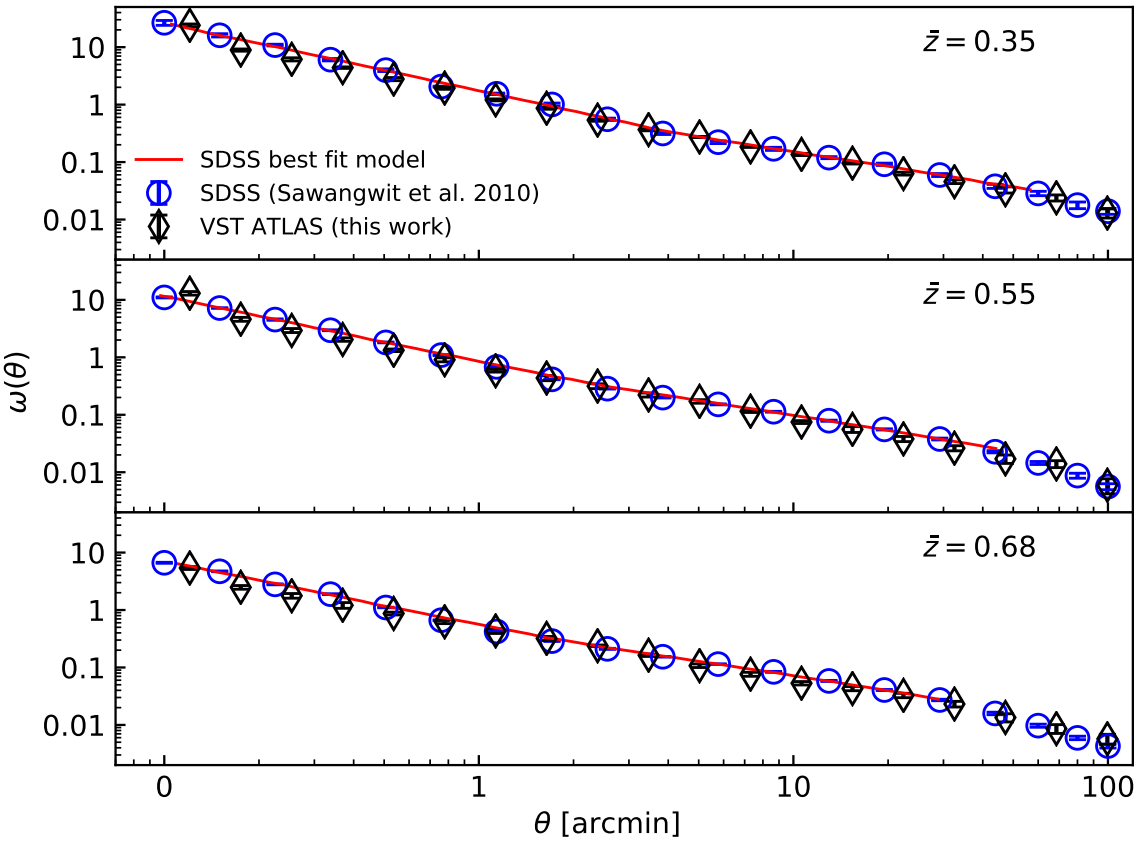

Figure 6.6: The VST ATLAS LRG angular auto-correlation functions, for our low, intermediate, and high redshift samples (diamonds). The SDSS measurements of Sawangwit et al. (2011) (circles) and their best-fit double power-law models (solid lines) are added for comparison. Here, the error bars are shown inside the open data points. The good agreement between the measurements from the two datasets is an indication of the success of our LRG photometric selection in limiting the samples to the correct redshift range as well as efficient removal of stellar contamination.

amplitude is preserved in our samples. As a result, we do not expect our measurements of the ISW amplitude to be influenced by our different sample number densities. We believe our lower LRG densities are in part due to the slightly larger scatter in the VST ATLAS colours used in the LRG sample selections, compared to the colour scatter in SDSS. Another factor influencing our lower number density could be our additional Aperture vs Kron magnitude cuts applied to remove residual stellar contamination as described in Section 6.2.2.

Further tests of impact of survey systematics due to excess stellar contamination, galactic dust extinction and variations in airmass and seeing are presented in Appendix C.2. Our tests indicate that these systematics do not have a significant effect on our ISW measurements.

6.4.2 VST ATLAS LRG-Planck CMB cross-correlation

Figure 6.7a shows a comparison of our ISW measurements based on the cross-correlation of VST ATLAS LRGs and Planck CMB temperature anisotropy map, to the results of Sawangwit et al. (2010) (where the same analysis was perform using SDSS LRGs and the WMAP temperature map). We find a good agreement between the two measurements in terms of ISW amplitude at all redshifts. Our error bars are however larger than those of Sawangwit et al. (2010), which can be partially attributed to the $\sim 2\times$ lower sky coverage of the ATLAS survey compared to SDSS, as well as the lower number density of LRGs, at least in the case of our $\bar{z} = 0.55$ and $\bar{z} = 0.68$ samples (see Table 6.1).

As on large scales relevant to ISW measurements the statistical error is limited by sample variance, one would expect the errors on our ISW measurements to scale with $\sigma_{\rm ATLAS}/\sigma_{\rm SDSS} \approx \sqrt{(A_{\rm SDSS}/A_{\rm ATLAS})}$ where A represents the area of each sample. We therefore expect the ATLAS error bars to be $\sim 1.4\times$ larger than those of SDSS. However, we find that the errors on our VST ATLAS LRG ISW measurements do not obey the above scaling with SDSS and are $\sim 1.9\times$, $\sim 2.4\times$ and $\sim 3.0\times$ larger than those from SDSS, for our $\bar{z} = 0.35$, 0.55 and 0.68 samples respectively. Assuming the SDSS ISW errors of Sawangwit et al. (2010) are not under-estimated, the reason behind the larger than expected errors on our LRG ISW measurements remains unknown.

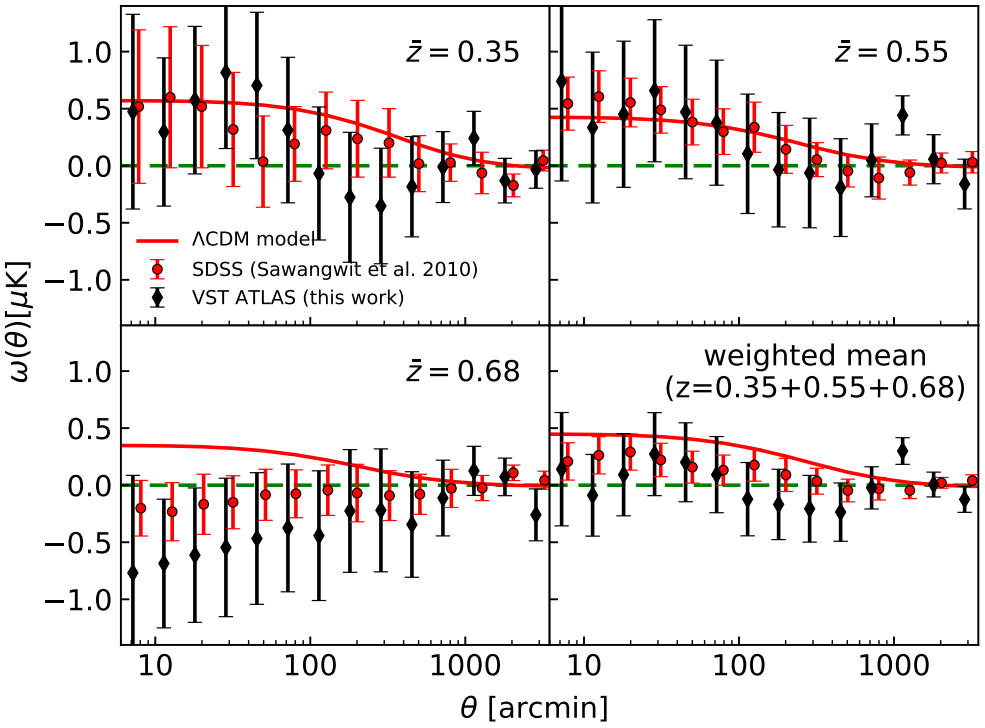

(a) VST ATLAS vs. SDSS.

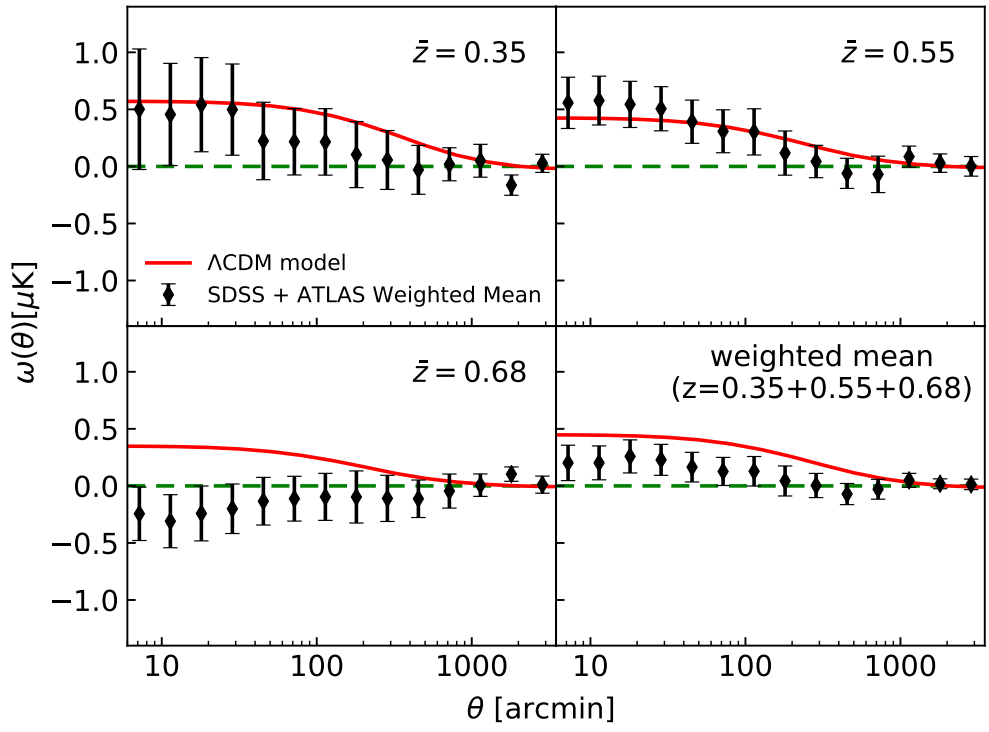

(b) VST ATLAS + SDSS.

Figure 6.7: (a) The VST ATLAS LRG-Planck CMB cross-correlation signal from our low, intermediate and high redshift samples compared to SDSS LRG-WMAP CMB measurements of Sawangwit et al. (2010). The predictions of the ΛCDM model are shown by the red solid lines. (b) The weighted mean of the two measurements in (a).

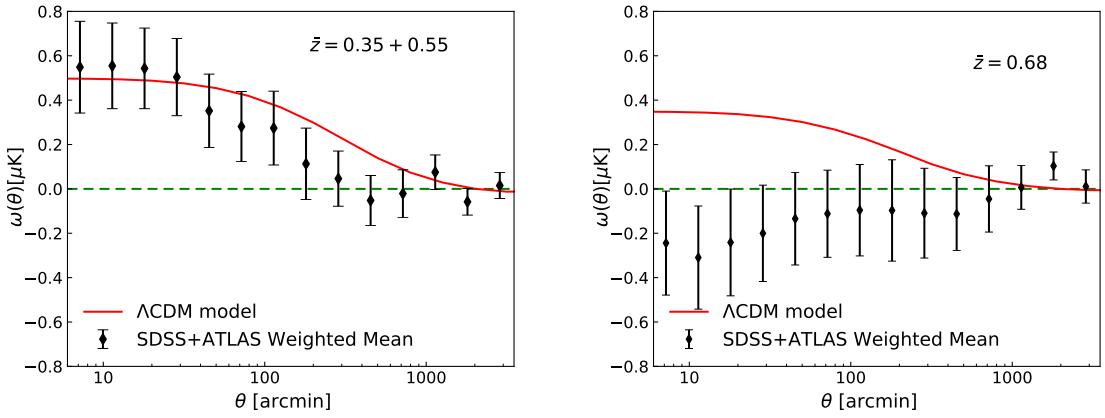

(a) (b)

Figure 6.8: (a) The weighted mean of the SDSS+ATLAS ISW measurements at $\bar{z} = 0.35$ and 0.55 (i.e the top panels of Figure 6.7b). (b) The $\bar{z} = 0.68$ measurement (bottom left panel of Figure 6.7b). As shown in Table 6.2, when combining the $\bar{z} = 0.35$ and 0.55 measurements, we detect the ISW signal at 2.6σ and we note the result is in agreement with the predictions of ΛCDM. However, at $\bar{z} = 0.68$ the ISW amplitude is close to zero and deviates from the ΛCDM predictions by 2.0σ.

Similarly to Sawangwit et al. (2010), when fitting our measurements to the ΛCDM model, we find the resulting χ^2 values (given by equation 6.3.8) to be unreliable. This is likely due to our use of the jackknife technique in estimating the covariance matrices (see equation 6.3.6) and the failure of this technique in accurately estimating the off-diagonal covariance matrix elements, which in turn impacts the χ^2 fitting results. As mocks are currently not available for the VST ATLAS survey (and the Bootstrap technique was also unsuccessful in improving our covariance matrix estimations), we follow the approach of Sawangwit et al. (2010) and simply assess the deviation of our measurements from the ΛCDM predictions and a null ISW amplitude, based on a single large bin covering the $12 < \theta < 120$ arcmin range.

Table 6.2 contains a summary of the our single bin ISW measurements, those of Sawangwit et al. (2010) and also the weighted mean of the results from the two studies (see Figure 6.7b). In the case of the $\bar{z} = 0.35$ and 0.55 LRG samples we found our detected ISW amplitude to be in agreement with the predictions of ΛCDM, supporting the late-time accelerated expansion of the Universe. As seen in Table 6.2, upon combining the ATLAS and SDSS measurements, at these redshifts we detect the ISW effect at 1.2σ and 2.3σ (or 2.6σ combined[5] - see Figure 6.8a). In the case of the $\bar{z} = 0.68$ LRG sample however, where the ISW measurement from VST ATLAS has a similar negative amplitude to SDSS, we find a $\sim 2\sigma$ deviation from the ΛCDM prediction, when combining the results from the two studies (Figure 6.8b).

[5]Based on the weighted mean of the results from the two redshifts.

Table 6.2: Summary of our VST ATLAS and BOSS/eBOSS LRGs-Planck CMB cross-correlation measurements of the ISW amplitude (based on a single bin covering the $12 < \theta < 120$ arcmin range). The SDSS LRG-WMAP CMB measurements of Sawangwit et al. (2010) and weighted mean of the results from the various datasets are also included. The final column shows the deviation of each measurement from the predictions of the ΛCDM model and a null amplitude. In all cases, we use the weighted mean to combine the results from different redshifts.

Sample	$\bar{z}$	ω(12-120 arcmin) [μK]	Deviation significance (ΛCDM, null)
VST ATLAS (this work)	0.35	0.47 ± 0.62	(0.0σ, 0.8σ)
	0.55	0.41 ± 0.51	(0.1σ, 0.8σ)
	0.68	-0.49 ± 0.59	(1.3σ, 0.8σ)
	0.35+0.55+0.68	0.11 ± 0.33	(0.8σ, 0.3σ)
SDSS (Sawangwit et al., 2010)	0.35	0.33 ± 0.33	(0.5σ, 1.0σ)
	0.55	0.44 ± 0.21	(0.5σ, 2.1σ)
	0.68	-0.13 ± 0.20	(2.0σ, 0.6σ)
	0.35+0.55+0.68	0.21 ± 0.14	(1.2σ, 1.5σ)
BOSS/eBOSS (this work)	0.35	0.32 ± 0.38	(0.4σ, 0.9σ)
	0.55	0.73 ± 0.38	(1.1σ, 2.0σ)
	0.68	0.50 ± 0.76	(0.3σ, 0.7σ)
	0.35+0.55+0.68	0.52 ± 0.25	(0.6σ, 2.1σ)
VST ATLAS+SDSS (weighted mean)	0.35	0.36 ± 0.29	(0.5σ, 1.2σ)
	0.55	0.43 ± 0.19	(0.5σ, 2.3σ)
	0.68	-0.17 ± 0.19	(2.3σ, 0.9σ)
	0.35+0.55	0.41 ± 0.16	(0.1σ, 2.6σ)
	0.35+0.55+0.68	0.20 ± 0.12	(1.4σ, 1.7σ)
VST ATLAS+BOSS/eBOSS (weighted mean)	0.35	0.36 ± 0.32	(0.4σ, 1.1σ)
	0.55	0.62 ± 0.31	(0.9σ, 2.0σ)
	0.68	-0.12 ± 0.47	(0.8σ, 0.3σ)
	0.35+0.55	0.49 ± 0.22	(0.4σ, 2.2σ)
	0.35+0.55+0.68	0.38 ± 0.20	(0.1σ, 1.9σ)

In these measurements, the signal is mostly dominated by SDSS and combining the VST ATLAS and SDSS results only yields a small increase in the significance of detection (or rejection) of the ΛCDM ISW predictions, compared to the results previously obtained from

SDSS alone. We note however, that the errors in the ATLAS ISW measurements would be 50-70% smaller if they had scaled correctly with sample size, which may explain the unexpectedly good agreement between SDSS and ATLAS results in all three redshift ranges. Overall, the results of this study offer a valuable confirmation of the measured ISW amplitudes of Sawangwit et al. (2010) based on SDSS and WMAP, using the cross-correlation of two independent datasets (VST ATLAS and Planck) that also cover completely separate areas of the sky.

6.4.3 Comparison to BOSS DR12 LOWZ, CMASS and eBOSS LRGs samples

To further verify the SDSS measurements at $\bar{z} = 0.35$, 0.55 and 0.68 we compare the results with those obtained using the LOWZ, CMASS and eBOSS LRG redshift samples (see Section 6.2.7). As shown in Figure 6.9 with the exception of the $\theta > 100$ arcmin higher BOSS ISW amplitude at $\bar{z} = 0.55$, the BOSS measurements provide a general confirmation of the SDSS results at $\bar{z} = 0.35$ and $\bar{z} = 0.55$. The $\bar{z} = 0.35$ results show particularly good agreement between the photometric and spectroscopic samples. The reason behind the higher than expected $\bar{z} = 0.55$ BOSS amplitude at large separations remains unknown. At $\bar{z} = 0.68$, the ISW amplitude is more positive in the eBOSS LRG sample than observed in SDSS or ATLAS (see Figures 6.9 and 6.10a). Nevertheless, the eBOSS result shows a qualitatively different form to that of the lower redshift results generally rising towards larger separations rather than falling. This behaviour is also similar to that seen in SDSS and ATLAS at the same redshift, just with a higher amplitude for eBOSS.

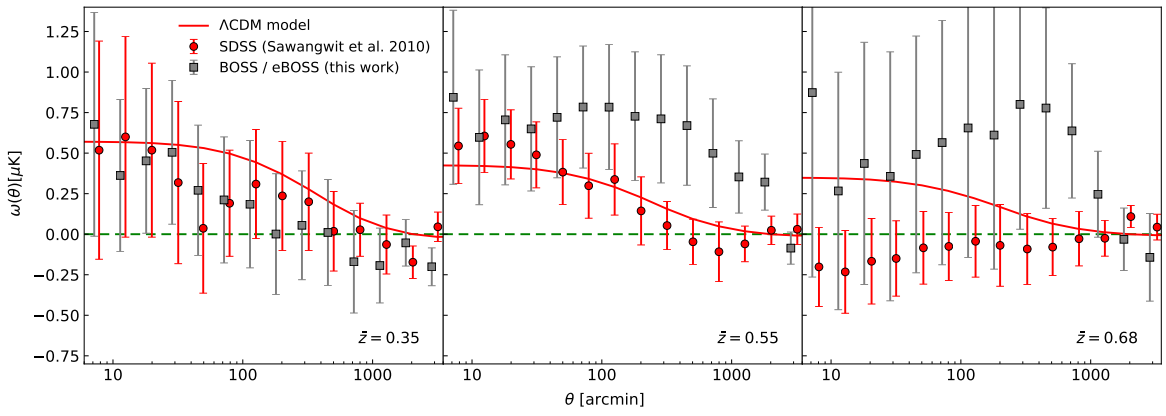

Figure 6.9: Comparison of the SDSS and BOSS/eBOSS ISW measurements.

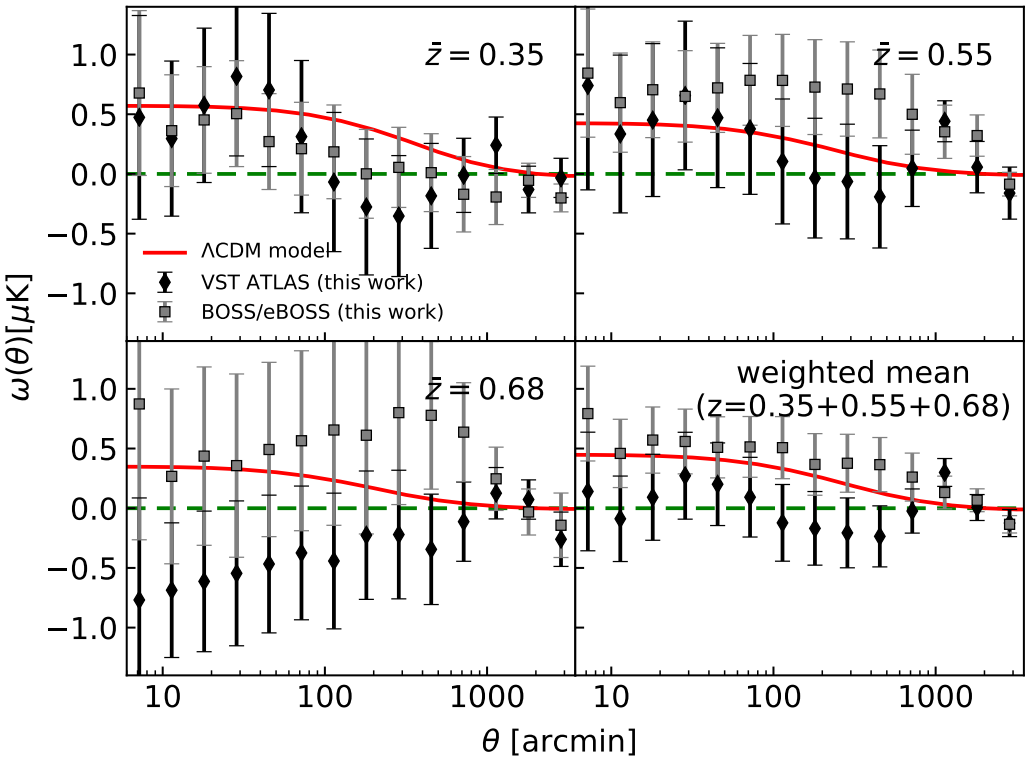

(a) VST ATLAS vs. BOSS/eBOSS.

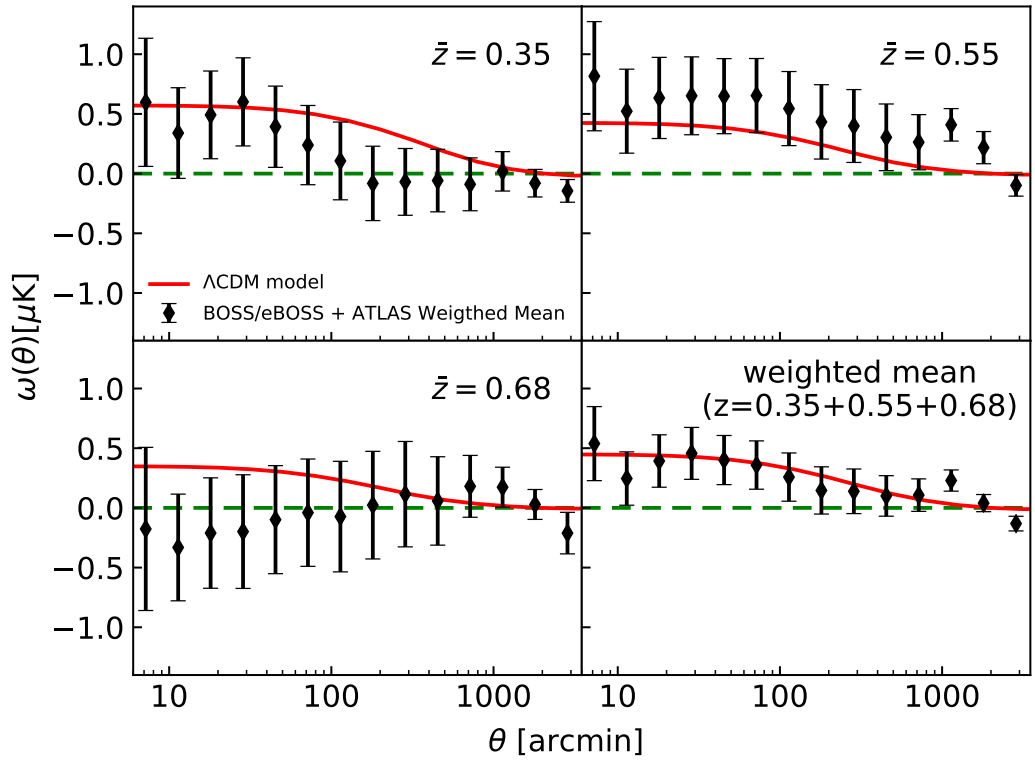

(b) VST ATLAS + BOSS/eBOSS.

Figure 6.10: (a, b) same as (6.7a, 6.7b) but comparing / combining the VST ATLAS ISW measurements to those based on BOSS/eBOSS.

At $\bar{z} = 0.35$ and $\bar{z} = 0.55$, we therefore find similar results whether we combine ATLAS with SDSS photometric, or BOSS/eBOSS spectroscopic LRG samples. For example, in Table 6.2, at $\bar{z} = 0.35$ and 0.55, the null amplitude is rejected at 1.1 and 2.0σ when combining the ATLAS+BOSS measurements (Figure 6.10b); similar to the 1.2 and 2.3σ ATLAS+SDSS ISW detection. When combining the measurements at $\bar{z} = 0.35$ and 0.55, the ATLAS+BOSS result rejects the null signal at 2.2σ, compared to the 2.6σ null rejection obtained from ATLAS+SDSS.

At $\bar{z} = 0.68$ however, Table 6.2 shows a 0.8σ deviation from ΛCDM rather than 2.3σ, when the ATLAS measurement is combined with eBOSS instead of SDSS. Similarly, the ATLAS+BOSS/eBOSS weighted mean of the results from the 3 redshift bins appears to be in better agreement with ΛCDM compared to ATLAS+SDSS (a 0.1σ deviation compared to 1.4σ). However, in both cases this lower rejection significance of ΛCDM is mainly due to the larger eBOSS errors, rather than any intrinsically improved agreement of the *form* of the high redshift result to the ISW model.

These larger errors on the eBOSS ISW measurements are due to its lower sky coverage than that of the equivalent SDSS LRG sample, and SDSS thus remains the $\bar{z} = 0.68$ measurement with the highest signal in this sky area. We therefore conclude that ATLAS+SDSS measurement shown in Figure 6.8b provides the best estimate of the ISW effect using $\bar{z} = 0.68$ LRGs, in the full North+South combined sample. Similarly, in Figure 6.8a we use the ATLAS and SDSS data to provide the best $\bar{z} = 0.35$ plus $\bar{z} = 0.55$ ISW measurement in the full North+South sample. The difference between the two appears clear, although the $\bar{z} = 0.68$ deviation significance from ΛCDM, is currently only at a moderate level of $\sim 2.3\sigma$. It is therefore important to re-measure the high redshift ISW signal using the complete eBOSS survey, as well as future surveys such as DESI (DESI Collaboration et al., 2016) and LSST (Ivezić et al., 2019), which will offer large, high-purity LRG samples that could assess any potential deviations from ΛCDM at a higher statistical significance.

6.4.4 Magnitude limited samples

Figure 6.11a shows a comparison of our measurements of the three r-band magnitude limited samples to the SDSS measurements of Sawangwit et al. (2010). Once again a general agreement is found between the two sets of measurements. Unlike our redshift limited LRG samples, here the number of galaxies in our three samples are in line with theoretical expectations, and we find the VST ATLAS error bars to be comparable to those of Sawangwit

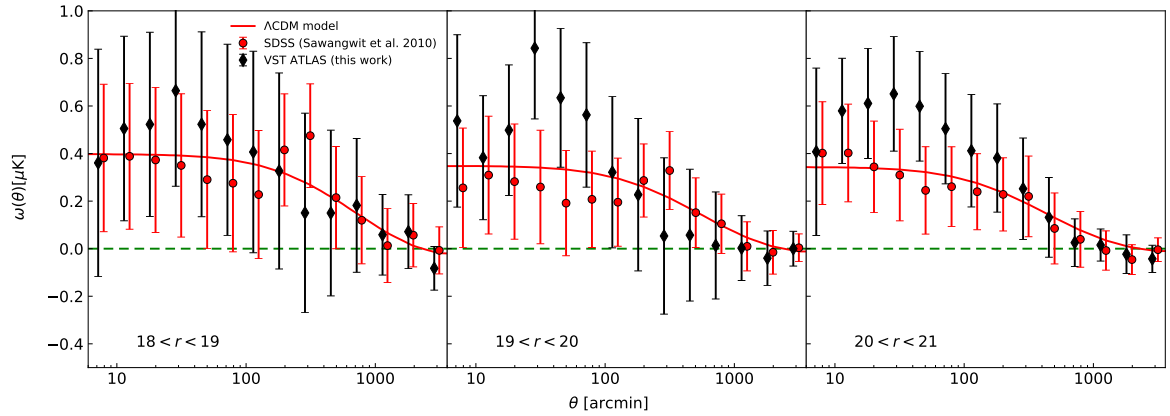

(a) VST ATLAS vs. SDSS.

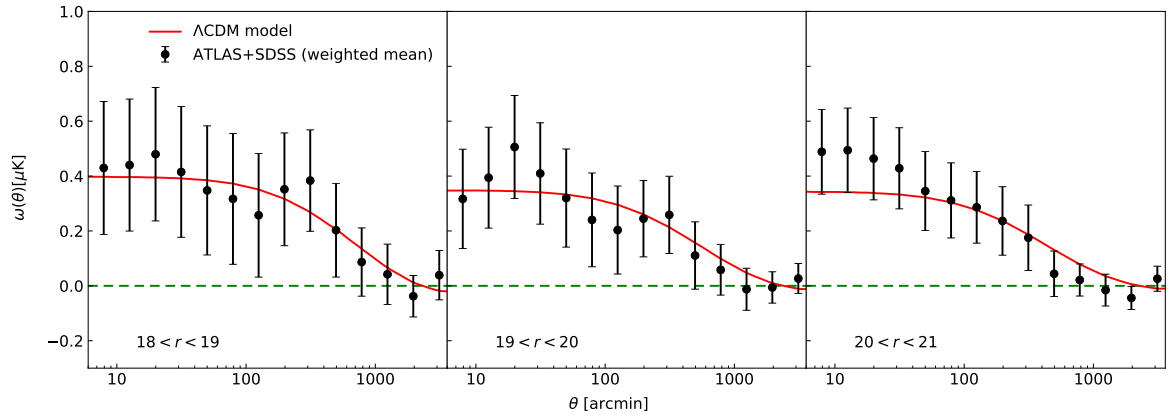

(b) VST ATLAS + SDSS.

Figure 6.11: (a) The ISW signal from our three VST ATLAS r-band magnitude limited galaxy samples (diamonds) in comparison with the SDSS results of Sawangwit et al. (2010) (circles) and ΛCDM model prediction (solid lines). (b) weighted mean of the results from the two studies. Here the mean redshifts of the $18 < r < 19$, $19 < r < 20$ and $20 < r < 21$ samples are $\bar{z} \approx 0.20, 0.27$ and 0.36 respectively.

et al. (2010) based on SDSS, once the difference in survey areas is accounted for.

Upon combining the two sets of measurements by taking their error-weighted mean (see Figure 6.11b), we find that on scales of $12 < \theta < 120$ arcmin, the null amplitude is rejected at moderate levels of $\sim 1.3\sigma$, $\sim 1.9\sigma$ and $\sim 2.0\sigma$ for the $18 < r < 19$, $19 < r < 20$ and $20 < r < 21$ samples respectively. Recalling that these samples have mean redshifts of $\bar{z} \approx 0.20 \pm 0.09, 0.27 \pm 0.13$ and 0.36 ± 0.16, we note that the $\sim 2.0\sigma$ ISW detection obtained from the $20 < r < 21$ ATLAS+SDSS galaxy samples, provides a further confirmation of our 1.2σ ISW detection based on the $\bar{z} = 0.35$ ATLAS+SDSS LRG samples.

6.4.5 ISW rotation test

Following the approach of previous works including Sawangwit et al. (2010) and Giannantonio et al. (2012), we test for presence of systematic effects and the robustness of our measurements by rotating the LRG data with respect to the CMB map in increments of 40° about the Galactic pole (by adding 40° to the Galactic longitude). Here we perform the rotation test on the LOWZ and CMASS samples, as they provide contamination-free samples of spectroscopically confirmed LRGs. Given the current low sky coverage and large uncertainties on the eBOSS measurement, we do not include this sample in our rotation tests.

Figure 6.12a shows the results of our single-bin ($12 < \theta < 120$ arcmin) rotation tests for the LOWZ and CMASS samples. Statistically, one would expect 32 and 5 per cent of the rotations to exceed the 1 and 2σ thresholds. In the case of the LOWZ sample we find that 4/8 and 2/8 (50 and 25 per cent) of the rotations result in amplitudes that lie above the 1 and 2σ thresholds respectively. Furthermore, we find that 2/8 (25 per cent) of the rotations produce a more significant rejection of null, than the zero-rotation value.

For the CMASS sample we find that 4/8 and 1/8 (50 and 12.5 per cent) of the points are further than 1 and 2σ away from zero respectively, while 1/8 (12.5 per cent) of the rotations produces a more significant null rejection than our zero-rotation result. In order to ensure the single-bin measurements in Figure 6.12a do not appear to be artificially deviated from zero due to the presence of outliers in the full-range cross-correlation functions, in Figure 6.12b we show the full-range cross-correlation function for the 240° rotation of the CMASS sample (which resulted in the highest deviation from zero). Here, we can see that the 240° rotation appears to have produced an ISW amplitude which is consistently high in our $12 < \theta < 120$ arcmin range of interest, resulting in a higher null rejection when compared to the 2σ rejection obtained from the zero-rotation CMASS result as shown in Table 6.2.

Here our results are in agreement with those of Sawangwit et al. (2010), who found that in 1 to 2/8 cases, the rotated maps produced a more significant null rejection than the zero-rotation result. However, we find our results to be in contrast to the findings of Giannantonio et al. (2012) (as shown in their Table 3), where in their 6 studied samples only 23 and 2 per cent of their rotations exceeded the 1 and 2σ thresholds (fully consistent with the 32 and 5 per cent statistical expectations), with none exceeding the null rejection significance of the unrotated map. Similarly, Giannantonio et al. (2012) found that across all 7 samples studied by Sawangwit et al. (2010), only 39 and 11 per cent of rotations exceeded the 1 and 2σ thresholds.

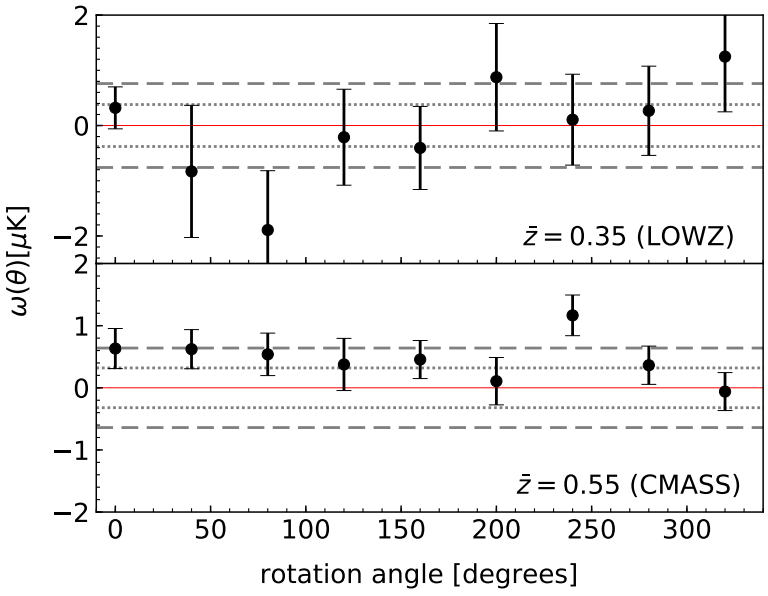

(a)

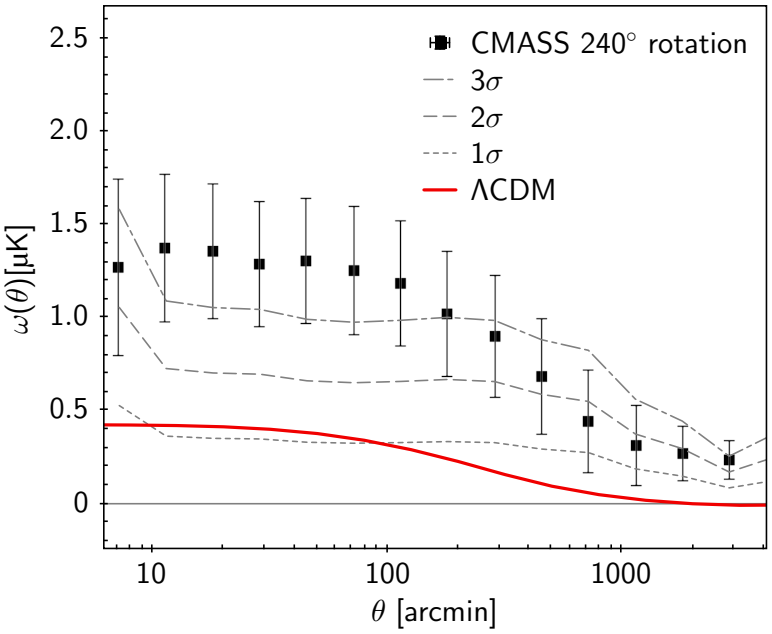

(b)

Figure 6.12: (a) The BOSS LOWZ and CMASS single-bin ($12 < \theta < 120$ arcmin) ISW amplitudes as a function of rotation angles (see text for details). The 1 and 2σ error regions around the null amplitude are shown by dotted and dashed lines. These are based on the error bars of the zero rotation data points and represent level of variance in the data. (b) The full-range 240° rotation result for the CMASS sample showing that in the $12 < \theta < 120$ arcmin range used to extract our single bin measurement, the ISW amplitude is consistently high and is not merely due to the presence of a few outliers.

Giannantonio et al. (2012) suggest that the higher percentage of points exceeding the 1 and 2σ thresholds, found by Sawangwit et al. (2010) could be due to their use of the jackknife method in estimating the errors, which has been shown to produce somewhat smaller errors

(see Cabré et al. 2007) than those obtained from simulated mocks (as used by Giannantonio et al. 2012). This could in part also explain the higher than expected percentages found in our rotation tests. However, given that for the LOWZ and CMASS samples, 50 percent of our rotations exceeded the 1σ threshold, 25 and 12.5 percent exceeded the 2σ threshold, and 2/8 and 1/8 rotations produced a more significant rejection of null than the unrotated map; our findings suggest that the robustness of current ISW detections is still not completely secure even at $\bar{z} = 0.35$ and $\bar{z} = 0.55$. Consequently, as well as any remaining statistical gains, improvements in reducing systematics on ISW measurements should still be sought in future works.

6.5 Conclusions

We have presented our measurements of the ISW signal in the cross-correlation of the Planck CMB temperature map with three photometrically selected LRG samples with mean redshifts of $\bar{z} = 0.35$, $\bar{z} = 0.55$ and $\bar{z} = 0.68$, selected from the VST ATLAS survey. We then combine our measurements with those of Sawangwit et al. (2010), where the same analysis was performed using the WMAP CMB temperature map and LRG samples selected from SDSS.

Upon combining the measurements from ATLAS and SDSS, at $\bar{z} = 0.35$ and $\bar{z} = 0.55$, we detect the ISW signal at 1.2σ and 2.3σ respectively (i.e. a combined detection of 2.6σ). This is in agreement with the predictions of ΛCDM supporting the late-time accelerated expansion of the Universe. We further verify our results at these redshifts by repeating the measurements using the BOSS DR12 LOWZ and CMASS spectroscopic LRG samples. This time upon combining the ATLAS and BOSS measurements, we detect the ISW signal at 1.1σ and 2.0σ (with a combined significance of 2.2σ). Furthermore, we detect the ISW effect in 3 magnitude limited galaxy samples, with mean redshifts of $\bar{z} \approx 0.20$, 0.27 and 0.36, at $\sim 1.3, 1.9$ and 2.0σ respectively.

However, we do not detect the ISW signal at $\bar{z} = 0.68$ when combining the ATLAS and SDSS results. Further tests using eBOSS LRGs at this redshift remain inconclusive (with an amplitude of 0.50 ± 0.76) due to the large uncertainties, caused by the current relatively low sky coverage of the survey. If the ISW signal is shown to be inconsistent with the predictions of ΛCDM at high redshifts, it could open the door to alternative theories such as modified gravity models. It is therefore important to repeat the $z \sim 0.7$ ISW measurement upon

the completion of the eBOSS survey and using data from upcoming surveys such as DESI and LSST which will provide the statistics and reduced systematics required to assess any deviations from the predictions of ΛCDM.

Finally, we test the robustness of our ISW measurements at $\bar{z} = 0.35$ and $\bar{z} = 0.55$ by rotating the LRG overdensity map with respect to the CMB temperature map in 8 increments about the Galactic pole. Here, in contrast to the findings of Giannantonio et al. (2012), we find that a higher percentage of rotations result in amplitudes 1 and 2σ away from zero than statistically expected. Furthermore, we find that in the case of LOWZ and CMASS samples 2/8 and 1/8 rotations result in more significant rejections of the null amplitude than obtained from our unrotated maps. Consequently, our results indicate that the robustness and significance of ISW detections still warrant further examination in future works. Similarly rotation tests could serve as a useful tool for determining the level of systematics in ISW measurements obtained from future surveys.

In summary, the results of this study provide a confirmation of previous ISW measurements from Sawangwit et al. (2010). However, despite the visual impressions given by the cross-correlation measurements, our detections of the ISW signal at $\bar{z} = 0.35$, $\bar{z} = 0.55$ and in 3 magnitude limited samples remain at low to moderate levels of significance. However, previous works such as Francis & Peacock (2010) have demonstrated that the ISW signal could remain evasive in $\gtrsim 10$ per cent of cases, even with the availability of the best possible data. Nonetheless, given the cosmological implications of any significant deviations from the predictions of ΛCDM, repeating the ISW measurement at $z \sim 0.7$, where our results point to the possibility of such deviations, using the next generation of large sky surveys, remains a worthwhile and important endeavour.

Chapter 7

An ALMA investigation of SMG dust heating mechanisms

7.1 Introduction

Sub-millimetre galaxies (SMGs) were first detected as highly luminous Far-infrared (FIR) sources (see, e.g. Smail et al. 1997; Barger et al. 1998; Hughes et al. 1998; Dey et al. 1999) using the James Clerk Maxwell Telescope's (JCMT) Submillimetre Common-User Bolometer Array (SCUBA; Holland et al. 1999). These objects were soon found to be high-redshift, dust-obscured sources which contribute to a significant fraction of the energy output of all galaxies in the early Universe (Blain et al., 2002). Sub-millimetre observations, therefore, opened a new window for studies of galaxy formation and evolution since the cosmic dawn (see Casey et al. 2014 for a detailed review).

The identification of the dominant fueling mechanism which powers SMGs is an ongoing topic of research. The standard view is that SMGs are predominantly hyper-luminous starburst galaxies, seen during an obscured phase of their evolution (see, e.g. Alexander et al. 2005; Dudzevičiūtė et al. 2020). However, it was also found that due to their high mass and star formation rates (SFR) they present a problem for the ΛCDM model, with the Semi-Analytic Model of Baugh et al. (2005) under-predicting the abundance of SMGs and requiring the adoption of a top-heavy stellar initial mass function in starbursts to account for the observed SMG number counts.

An alternative view is that Active Galactic Nuclei (AGN) are the dominant mechanism that power SMGs. Although many SMGs are known to host AGN, they are usually viewed to be

subdominant to star-formation in fueling these sources (see, e.g. Laird et al. 2010; Johnson et al. 2013; Wang et al. 2013).

On the other hand, there are various arguments for considering obscured AGN as the primary power source for SMGs. For instance, a population of heavily obscured quasars could explain the missing hard X-ray background (Comastri et al. 1995; Worsley et al. 2005; Polletta et al. 2007), while their dust-rich nature would mean that they would have large emissions in the infra-red (IR) due to the emission of reprocessed light from the AGN. Indeed, obscured AGN models have been shown to provide a reasonable fit to the bright end of the SMG source counts (Hill & Shanks, 2011), removing the need for top-heavy IMF for high-redshift starbursts, while at fainter fluxes, star-forming galaxies are expected to dominate the SMG number counts. For AGN to be the dominant source of powering the sub-mm emission rather than star formation, the dust torus must lie far enough (on $\sim$ kpc scales) from the nucleus to maintain a cool temperature of $\sim$ 35K and produce spectra consistent with observations; a picture which is feasible if one assumes a torus model similar to Kuraszkiewicz et al. (2003).

In recent years the unprecedented sensitivity and angular resolution of Atacama Large Millimetre/Submillimetre Telescope (ALMA) has enabled the study of the dust heating mechanisms of SMGs up to very high redshifts. Using $0.3''$ imaging from ALMA, Simpson et al. (2015) found that most of their targeted $z \sim 2$ SMGs are just resolved, with their imaging probing scales of $\approx 2h^{-1}$kpc. Furthermore, they found the K-band optical extent of these SMGs to be roughly four times larger than their extent in sub-mm. Using higher resolution ($0.16''$) ALMA imaging, Hodge et al. (2016) found sub-mm sizes of $\sim$ 1.3 kpc for a sample of 16 $z \sim 2.5$ SMGs. Similarly, Gullberg et al. (2019) studied a sample of $\sim$ 150 SMGs with $0.18''$ ALMA observations, finding a compact sub-mm dust continuum emission extended to just $\sim$ 1kpc, in comparison to the Hubble Space Telescope (HST) imaging of the optical/UV emissions of the same sources extending to $\sim 8 - 10$ kpc. These works attributed the compact size of the sub-mm emitting region of these sources to a central starburst evolving into a galactic bulge or bars. However, an alternative interpretation could be the presence of AGN which are fueling the inner regions of these SMGs, producing luminosities comparable to quasar emissions.

Measuring the star formation rate surface densities $\sum_{\rm SFR}$ of SMGs is one way to determine whether the observed emission from the inner regions of SMGs can be entirely explained by star formation or if the emission exceeds the "Eddington limit" of star formation set by

radiation pressure on dust[1] ($\sum_{\rm SFR} \approx 1000$ M$_\odot$ yr^{-1} kpc^{-2}; see, e.g. Thompson et al. 2005; Walter et al. 2009; Hopkins et al. 2010; Decarli et al. 2018; Hodge et al. 2019), indicating an AGN dominated fueling mechanism. In this Chapter, we present $\sum_{\rm SFR}$ based on the continuum emission from four $z > 6$ and seven $z \sim 2$ SMGs observed with ALMA. Our $z > 6$ ALMA observations were conducted with a resolution of $0.3''$ while our $z \sim 2$ observations had a resolution of $0.1''$. The higher resolution of our observations relative to previous studies is a clear advantage, as this will enable us to measure the area of the small inner regions of our targeted SMGs where the bulk of the sub-mm emission is produced. As a result, unlike observations with lower angular resolutions (where the sources may only be marginally resolved), the high resolution of our data reduces the risk of over-estimating the sub-mm emitting regions of these SMGs which could, in turn, result in an under-estimation of their $\sum_{\rm SFR}$ values. In the case of the seven $z \sim 2$ SMGs, Shanks et al. (in prep.) also present a comparison of AGN and star-forming fits to the spectral energy distributions (SEDs) of these sources, constructed using multi-wavelength data ranging from X-ray to radio bands.

For two of our four $z > 6$ SMGs, we also obtain estimates of $\sum_{\rm SFR}$ based on star formations calculated using their [CII] line emissions. The FIR fine-structure [CII] line at 158 μm is known to be one of the brightest cooling lines in local galaxies, and has been shown to be an efficient tracer for star-formation at high redshifts (e.g. Wang et al., 2013; Knudsen et al., 2016). The first [CII] detection in a high redshift quasar was presented by Maiolino et al. (2005), finding evidence for an intense burst of star-formation in the host galaxy. More recently, a small but growing number of studies have presented [CII] detections for high redshift quasars, (e.g. Venemans et al., 2012; Cicone et al., 2015; Bañados et al., 2015; Willott et al., 2015; Venemans et al., 2016; Decarli et al., 2018; Bethermin et al., 2020).

The outline of this chapter is as follows; in Section 7.2 we describe the X-Shooter observations of our $z > 6$ SMGs which were initially identified as quasars in the VST ATLAS survey. We then describe the ALMA observations of these sources and our $z \sim 2$ SMGs. In Section 7.3, we describe our measurements of the sizes and fluxes of our ALMA sources, as well as our calculations of the SFR surface densities based on continuum and [CII] fluxes. We present our results in Section 7.4 and conclude this chapter by presenting a summary of our findings and planned future works in Section 7.5. Throughout, we adopt a fiducial ΛCDM cosmology with $H_0 = 70$ km s^{-1} Mpc^{-1}, $\Omega_{\rm m} = 0.3$, $\Omega_\Lambda = 0.7$ and present all magnitudes in the AB

[1]The Eddington limit on $\sum_{\rm SFR}$ arises due to the momentum deposited due to radiation pressure from stars blowing the star-forming gas and dust out of the system.

system.

7.2 Observations

7.2.1 Identification of our four $z > 6$ and seven $z \sim 2$ SMGs

The four $z > 6$ SMGs studied in this Chapter were initially identified as quasar candidates in the VST ATLAS survey using the colour selection criteria of (Carnall et al., 2015). These candidates were confirmed as $z \sim 6$ quasars using low-resolution spectroscopy on the LDSS-3 instrument on the Magellan 6.5m telescope, and later with moderate resolution X-Shooter (Vernet et al., 2011) spectra by Chehade et al. (2018). A summary of the properties of these quasars including their black hole masses inferred from the [CIV] broad emission-line width $M_{\rm BH}[{\rm C_{IV}}]$ reported by Chehade et al. (2018) is presented in Table 7.1.

All four sources are amongst the most optically luminous known quasars at $z > 6$, with their redshifts placing them within the first Gyr of cosmic history. As these QSOs represent some of the most massive super-massive black holes (SMBHs) at this epoch, their study could reveal valuable insights into the growth of black holes at early times, given that they will be the hardest to produce in so short a time-frame.

The $z \sim 2$ SMGs studied here, were initially detected in a $S_{870\mu m} > 3$ mJy survey of the central region of the William Herschel Deep Field (WHDF), which was conducted using the LABOCA instrument of the APEX telescope (Siringo et al., 2009). A full description of these observations which resulted in the $> 3\sigma$ detection of 11 sub-mm sources is presented by Bielby et al. (2012). In this work, we study 7 of these sources which were targeted by ALMA (as described in the next Section). Two of these sources LAB-05 and LAB-11 have been identified as quasars by Bielby et al. (2012) with redshifts of $z = 2.12$ and $z = 1.32$ respectively. A summary of the redshifts and coordinates of these sources can be found in Table 7.1.

7.2.2 ALMA observations

As shown in Figure 7.1, due to the reduction of the angular diameter distance D_A at redshifts $z > 1.5$, for a fixed angular resolution, at $z \sim 6$ we are able to probe proper distances as small as those at $z \sim 0.5$. Taking advantage of this property of the Universe, we were able to resolve 3/4 of our $z \sim 6$ SMGs using our Band 6 (211–275 GHz) ALMA observations with a resolution of $0.3''$.

Table 7.1: Summary of SMG properties.

Name	Short Name	RA J2000.0	DEC J2000.0	z	$M_{1450Å}$ (Mag)	$M_{BH}[C_{IV}]$ ($10^9 M_\odot$)	Reference(s)
(1)	(2)	(3)	(4)	(5)	(6)	(7)	(8)
VST-ATLAS J332.8017-32.1036	J332-23	22:11:12.41	-32:06:12.96	6.32 ± 0.03	-26.79 ± 0.06	2.7	1
VST-ATLAS J158.6938-14.4211	J158-14	10:34:46.51	-14:25:15.96	6.07 ± 0.03	-27.23 ± 0.08	2.4	1
VST-ATLAS J025.6821-33.4627	J025-33	01:42:43.70	-33:27:45.72	6.31 ± 0.03	-27.50 ± 0.06	2.2	2
VST-ATLAS J029.9915-36.5658	J029-36	01:59:57.96	-36:33:56.88	6.02 ± 0.03	-26.97 ± 0.08	1.4	2
WHDF-LAB-01	LAB-01	00:22:37.58	+00:19:18.4	2.60 ± 0.15	—	—	3,4
WHDF-LAB-02	LAB-02	00:22:28.44	+00:21:47.6	3.00 ± 0.30	—	—	3,4
WHDF-LAB-03	LAB-03	00:22:45.96	+00:18:41.2	2.70 ± 0.35	—	—	3,4
WHDF-LAB-04	LAB-04	00:22:29.19	+00:20:24.8	3.00 ± 0.60	—	—	3,4
WHDF-LAB-05	LAB-05	00:22:22.87	+00:20:13.5	2.12 ± 0.03	—	—	3,4
WHDF-LAB-10	LAB-10	00:22:35.23	+00:24:07.5	2.12 ± 0.10	—	—	3,4
WHDF-LAB-11	LAB-11	00:22:24.84	+00:20:11.4	1.32 ± 0.03	—	—	3,4

Notes. (1) AGN name, (2) Short Name, (3) Right ascension, (4) Declination, (5) Inferred Lyα redshift in case of ATLAS $z \sim 6$ AGN, and redshift based on 2-Power-Law AGN template fit presented in Table 2 of Shanks et al. (2020, in prep.) (6) 1450Å rest-frame absolute magnitude, (7) Blackhole mass estimated from the CIV broad emission-line width, (8) References: 1.-Chehade et al. (2018); 2.-Carnall et al. (2015),3.-Bielby et al. (2012),4.-Shanks et al. (in prep.).

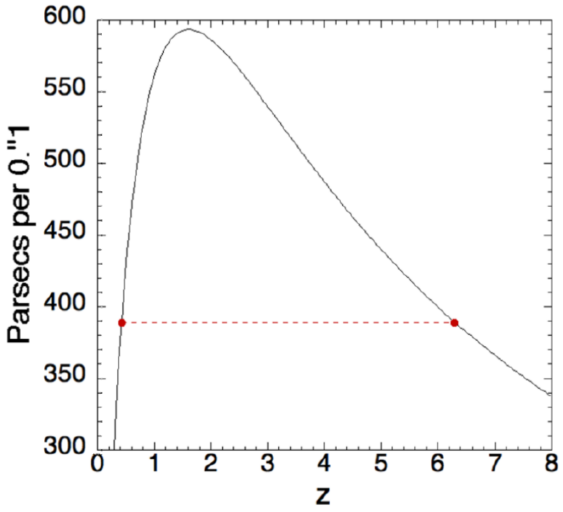

Figure 7.1: Due to the evolution of the angular diameter distance with redshift, for a fixed instrumental angular resolution, we are able to probe physical scales at $z \sim 6$ which are as small as those at $z \sim 0.5$.

Although all four of our $z \sim 6$ ALMA observations were targeted for [CII], due to the low resolution of their Magellan spectra, the uncertainties in the measured redshifts of two of these sources (J332-23 and J029-36) resulted in the [CII] line being at a frequency which was missed from our targeted window. In the case of J025-33 the [CII] line was located at the edge of our detection window missing some of the [CII] flux. However, Decarli et al. (2018) have presented ALMA [C II] observations of J025-33 (albeit with a larger angular resolution of $0.8''$), and we make use of these measurements in order to obtain an estimate of the size of the [CII] emitting region and [CII] SFR surface density for this object.

Our $z \sim 2$ WHDF SMGs were observed with 25 minute ALMA band 7 (275–373GHz) exposures with an angular resolution of $0.1''$. All 7 sources were strongly detected and resolved in these observations. In all cases, we make use of the standard ALMA data reduction and calibration pipelines, which are part of the Common Astronomy Software Application (CASA v4.7.2; McMullin et al. 2007) package[2].

[2]The ALMA observations of the SMGs studied in this Chapter were conducted by T. Shanks and R. Bielby in October and November 2016, while the data reduction and scientific analyses of these sources was performed by B. Ansarinejad.

7.3 Methodology

7.3.1 Source sizes and fluxes with IMFIT

In Fig. 7.2 we show the FIR continuum emission detected in our ALMA observations for each of our four $z > 6$ SMGs. Overlaid are the fitted elliptical sizes estimated using the IMFIT routine, which is part of the CASA package. As well as a measurement of the extent of the sources, IMFIT provides the integrated flux for each object which is used to calculate their SFR as detailed in Section 7.3.2. Fig. 7.2 also shows the clean beam size for each object which in all cases is larger than the fitted elliptical area of our sources.

With the exception of J025-33 which was identified as a point source by IMFIT with a FWHM major axis $< 0.2''$, all our other sources appear to be resolved. Given the relatively circular shape of J025-33 as shown in Fig. 7.2 we assume a circular shape with a radius $0.2''$ in order to obtain an upper-limit on the area of this source. Consequently, in Section 7.4 we only present a conservative lower limit for the star formation rate surface density ($\sum_{\rm SFR}$) of this object. We note that J025-33 lies closer to the edge of the field in the ALMA observations and therefore has a lower S/N compared to the other detections, which lie closer to the field centre. We believe this to be the mostly likely contributing factor for this source remaining unresolved.

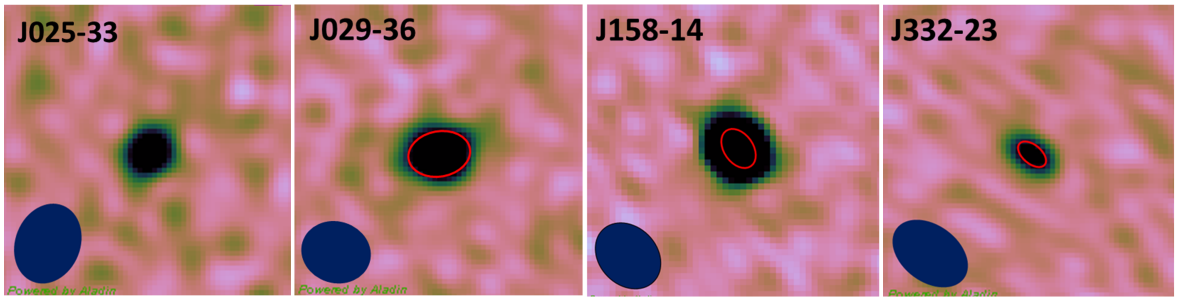

Figure 7.2: $3'' \times 3''$ ALMA postage stamps with a resolution of $0.3''$, showing the continuum emitting regions of the $z \sim 6$ SMGs. The red outline is the beam-deconvolved elliptical fit given by IMFIT with the major and minor axes presented in Table 7.3. The solid oval in the bottom left indicates the ALMA clean beam size. There is no fitted ellipse to J025-33 as this source was identified as a point source by IMFIT and remains unresolved.

Figure 7.3a shows FIR continuum emission of the 7 WHDF SMGs with the red ellipses marking the fitted IMFIT profiles. In Figure 7.3b we show the HST Advanced Camera for Surveys (ACS) i-band coverage of these sources with a resolution of $0.2''$, with the ALMA FIR continuum and the Spitzer IRAC Equatorial Survey (SpIES; Timlin et al. 2016) 3.6 micron profiles over-plotted as red and yellow contours respectively. Also shown as light

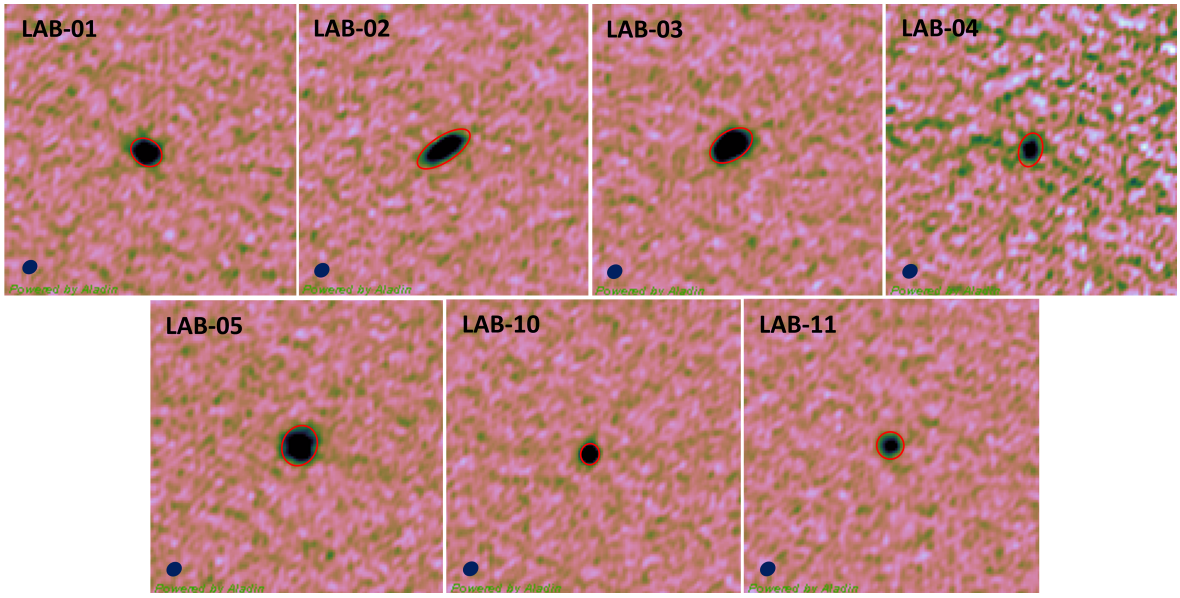

(a)

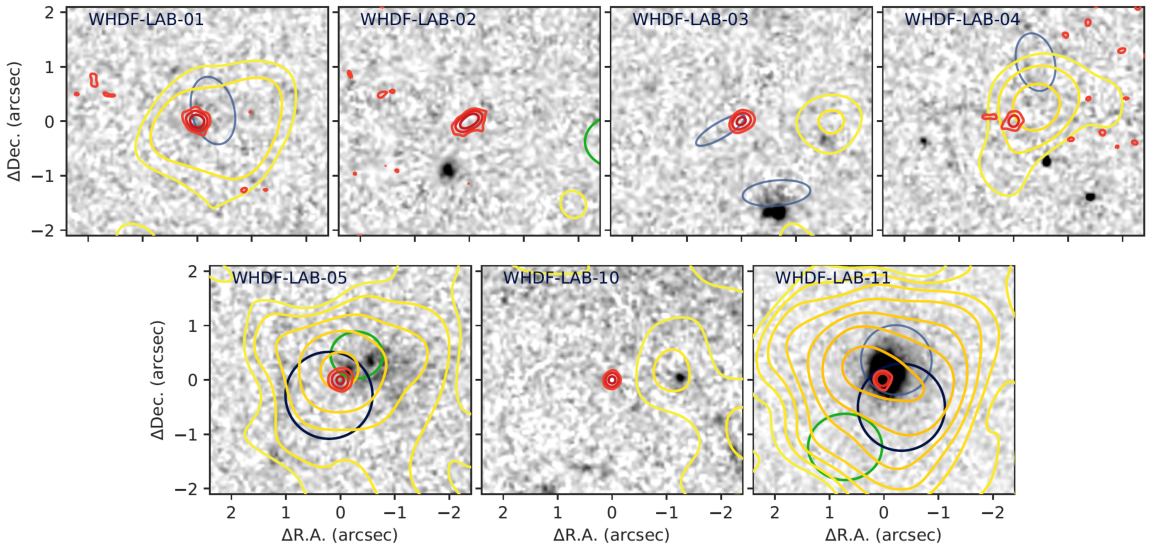

(b)

Figure 7.3: (a) $3'' \times 3''$ ALMA postage stamps with a resolution of $0.1''$, showing the continuum emitting regions of our $z \sim 2$ SMGs. The red outline is the beam-deconvolved elliptical fit given by IMFIT with the major and minor axes (FWHM) presented in Table 7.3. The solid oval in the bottom left indicates the ALMA clean beam size. (b) HST i-band images for the SMGs in (a) with the ALMA and SPIES 3.6μ profiles (with a resolution of $1.2''$) over-plotted as red and yellow contours, respectively. Also marked are detected sources in Chandra X-ray, Calar Alto H-band and EVLA 8.4GHz imaging in dark blue, light blue and green respectively.

blue ellipses are the H-band detections of Metcalfe et al. (2006), obtained with the Calar Alto Omega Prime camera (Bizenberger et al., 1998), as well as Chandra X-ray (Shanks et al., in prep.) and EVLA 8.4GHz (Heywood et al., 2013) source detections, marked by

dark blue and green ellipses respectively. On average, we find the ALMA continuum sizes of our sources to be $\sim 6\times$ smaller than their PSF-corrected extent in the H-band. However, in the future, more detailed comparison of the sub-mm and optical extent of these sources can be made using deep ($K \approx 25.7$), high-resolution ($< 0.5''$) imaging with an instrument such as HAWK-I (Pirard et al., 2004), HST or the James Webb Space Telescope (JWST; Gardner et al. 2006), while accurate redshifts for these sources could be obtained with X-Shooter. Such observations would enable us to determine if the sub-mm emission of these sources predominantly originates from their central regions and is therefore more consistent with an AGN power source, or if the optical and sub-mm emissions follow a similar larger scale galactic profile favouring the star-burst origin for the sub-mm emission.

7.3.2 Continuum luminosity and SFR surface density

Following Decarli et al. (2018) and the references therein, we calculate the IR Luminosity of our objects by modeling the dust continuum emission as a modified black body and integrating the following equation between $\nu = 3$ and 1000μm:

$$L_{\nu,\mathrm{dust}} = \frac{2h\nu^3}{c^2}\kappa_\nu(\beta)\frac{M_{\mathrm{dust}}}{e^{h\nu/k_b T_{\mathrm{dust}}} - 1}, \tag{7.3.1}$$

where $\kappa_\nu = 0.77(\nu/352\mathrm{GHz})^\beta$ is the opacity law, with the dust emissivity index $\beta = 1.6$ and the dust temperature set to $T_{\mathrm{dust}} = 47$K in the case of our $z > 6$ quasars (see e.g. Willott et al. 2017) and 35K (e.g. Cooke et al. 2018) for our WHDF $z \sim 2$ sources. Here we select a value of dust mass M_{dust}, which results in an L_ν that corresponds to the peak flux of each object. In line with Decarli et al. (2018) we calculate the far-IR luminosity using $L_{\mathrm{FIR}} = 0.75 L_{\mathrm{IR}}$ and obtain the SFR following Kennicutt & Evans (2012):

$$\frac{\mathrm{SFR_{FIR}}}{M_\odot \mathrm{yr}^{-1}} = 1.49^{-10}\frac{L_{\mathrm{FIR}}}{L_\odot}. \tag{7.3.2}$$

Our main quantity of interest, the star formation rate surface density $\sum_{\mathrm{SFR}}$, is then obtained by dividing $\mathrm{SFR_{FIR}}$ by the area of the ellipse fitted to the continuum emitting region using IMFIT.

7.3.3 [C$_{\rm II}$] luminosity and SFR surface density

Following Decarli et al. (2018) and Carilli & Walter (2013) we convert the [C$_{\rm II}$] integrated line flux $F_{[\rm C_{II}]}$ to line luminosity using:

$$\frac{L_{[\rm C_{II}]}}{L_\odot} = 1.04 \times 10^{-3} \frac{F_{[\rm C_{II}]}}{\rm Jy\ km\ s^{-1}} \frac{\nu_{\rm obs}}{\rm GHz} \left(\frac{d_{\rm L}(z)}{\rm Mpc}\right)^2. \tag{7.3.3}$$

$L_{[\rm C_{II}]}$ is in turn converted to $SFR_{[\rm C_{II}]}$ using the relation presented by De Looze et al. (2014):

$$\log SFR_{[\rm C_{II}]} = -8.52 + 1.18 \times \log L_{[\rm C_{II}]}. \tag{7.3.4}$$

7.4 Results and discussion

The results of fitting the [C$_{\rm II}$] and continuum emission maps of our sources using the IMFIT algorithm, are presented in Table 7.2. These include the clean ALMA beam size, as well as beam deconvolved minor and major axes FWHM of the fits which are used to estimate the area of the continuum and [C$_{\rm II}$] emitting regions. Also included is the integrated flux of each source as measured by IMFIT. Interestingly, we find the area of J158-14 and J025-33 to be more extended in [C$_{\rm II}$] than in continuum by factors of ~ 4 and ~ 12 respectively. Although a number of recent studies have reported similar results (see, e.g. Fujimoto et al. 2019; Fujimoto et al. 2020; Carniani et al. 2020), the exact mechanism leading to the formation of these extended [C$_{\rm II}$] halos around SMGs remains unknown.

Table 7.3 shows the dust mass, FIR or [C$_{\rm II}$] luminosities, star formation rates and star formation rate surface densities of our SMGs. Here we can see that in all of the four $z > 6$ SMGs, as well as LAB-02 and LAB-10, the FIR SFR surface densities ($\sum_{\rm SFR}$, shown in column 5 of the table) exceed or approach the theoretical Eddington limit of $\sim 1000 M_\odot {\rm yr}^{-1}{\rm kpc}^{-2}$, which has a lower limit[3] of $\sim 650 M_\odot {\rm yr}^{-1}{\rm kpc}^{-2}$. This supports the hypothesis that AGN are the dominant fueling mechanism of these SMGs. We also find that for J158-14 and J025-33, the lower values of SFR obtained from [C$_{\rm II}$] emission, combined with the more extended size of the [C$_{\rm II}$] emitting region, results in $\sum_{\rm SFR}$ values which are much smaller than those obtained from the continuum emissions of these sources. In the case of Lab-1, 3, 4, 5 and 11

[3] A derivation of the Eddington lower limit is presented in Section 4.1 of Hodge et al. (2019). In summary, this lower limited is obtain by converting the Eddington flux for optically thick starbursts (as given by Andrews & Thompson 2011) to the Eddington limited SFR density: $(\sum_{\rm SFR})_{\rm Edd} \sim 7.2 M_\odot {\rm yr}^{-1}{\rm kpc}^{-2} f_{\rm gas}^{-1/2} f_{\rm dg}^{-1}$. Here, the gas fraction $f_{\rm gas}$ is taken to be unity as the most extreme scenario, while the dust-to-gas ratio $f_{\rm dg}$ is assumed to be 1/90.

Table 7.2: IMFIT measurements of the SMG size and fluxes.

Object	Clean beam size	Position angle	Major axis	Minor axis	Position angle	Area	Flux
	[″]	[°]	[″]	[″]	[°]	(kpc^2)	(mJy)
(1)	(2)	(3)	(4)	(5)	(6)	(7)	(8)
J332-23	0.40×0.28	56	0.16 ± 0.07	0.09 ± 0.05	43 ± 89	$0.4 \pm .3$	0.47 ± 0.03
J158-14	0.36×0.29	65	0.20 ± 0.02	0.14 ± 0.02	12 ± 14	0.7 ± 0.1	3.21 ± 0.07
J158-14[C$_{\rm II}$]	0.36×0.31	73	0.34 ± 0.05	0.32 ± 0.05	179 ± 65	2.8 ± 0.6	0.17 ± 0.01
J025-33	0.38×0.34	−13	< 0.2	< 0.2	—	< 1.0	0.70 ± 0.03
J025-33[C$_{\rm II}$]†	1.28×0.90	−49	0.98	0.48	—	11.9	4.29 ± 0.24
J029-36	0.34×0.31	73	0.33 ± 0.02	0.22 ± 0.02	101 ± 9	1.8 ± 0.2	1.99 ± 0.09
LAB-01	0.11×0.09	−57	0.18 ± 0.01	0.135 ± 0.009	63 ± 9	1.3 ± 0.1	3.84 ± 0.18
LAB-02	0.11×0.09	−56	0.31 ± 0.01	0.100 ± 0.006	122 ± 1	1.5 ± 0.2	4.68 ± 0.19
LAB-03	0.11×0.09	−57	0.222 ± 0.007	0.135 ± 0.005	124 ± 2	1.6 ± 0.2	7.16 ± 0.21
LAB-04	0.11×0.09	−56	0.18 ± 0.03	0.13 ± 0.03	165 ± 42	1.2 ± 0.4	1.97 ± 0.28
LAB-05	0.10×0.09	−57	0.19 ± 0.01	0.17 ± 0.01	22 ± 37	1.8 ± 0.2	5.46 ± 0.27
LAB-10	0.11×0.09	−55	0.094 ± 0.008	0.074 ± 0.009	6 ± 21	0.4 ± 0.1	2.30 ± 0.10
LAB-11	0.11×0.09	−56	0.14 ± 0.02	0.13 ± 0.02	180 ± 74	1.0 ± 0.2	1.55 ± 0.08

Notes. (1) AGN short name, (2) Alma clean beam size, (3) Clean beam position angle, (4) Major axis FWHM of the continuum emitting region deconvolved from beam, (5) Minor axis FWHM, (6) Beam deconvolved source component position angle, (7) Surface area of continuum emitting region, (8) IMFIT Integrated (peak) fluxes for resolved (unresolved) objects, (in case of [C$_{\rm II}$] flux the units are Jy Km s^{-1}).†: Measurement from Decarli et al. (2018).

however, the $\sum_{\rm SFR}$ values appear below the Eddington lower limit of star formation, offering no direct evidence that AGN are the dominant power source of these SMGs. We note however that with the exception of Lab-11 the rest of the WHDF SMGs are within a factor of ∼2-3 of the Eddington lower-limit. Furthermore, Shanks et al. (in prep.) found the SED of these WHDF SMGs to be more consistent with AGN rather than star-forming models (with the exception of LAB-10, where the SED comparison was inconclusive).

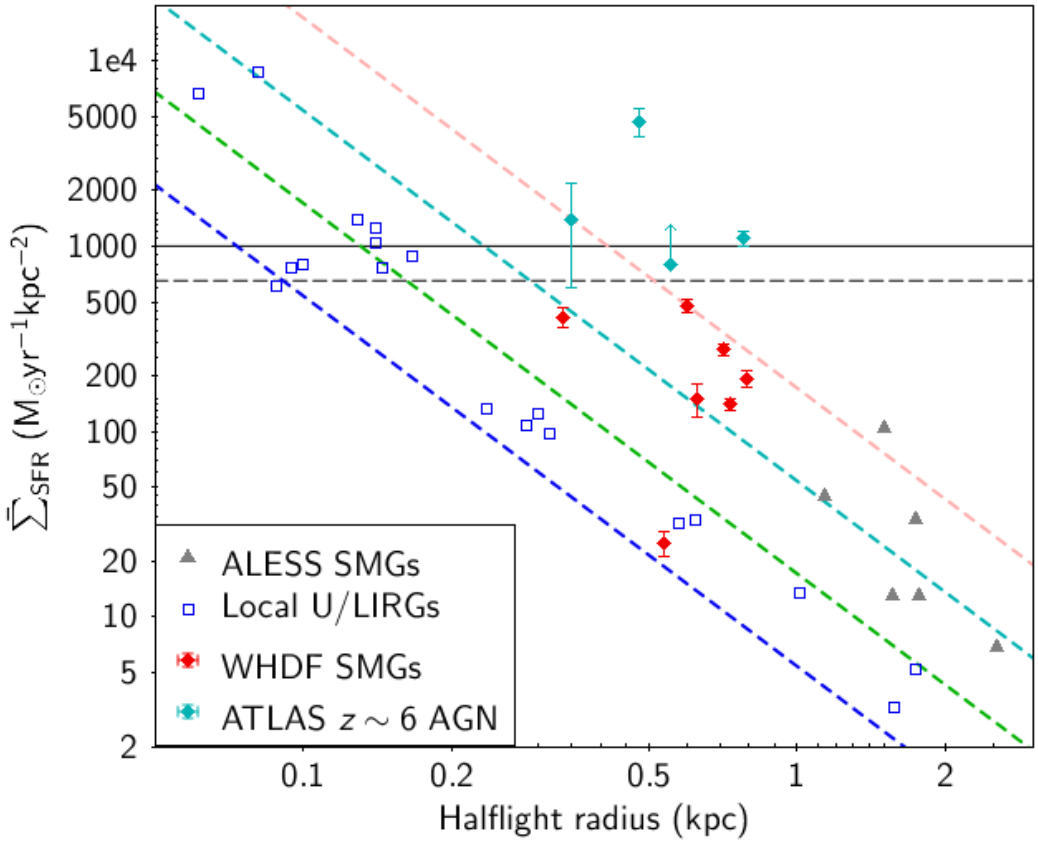

Figure 7.4: The galaxy-averaged star formation rate surface density ($\sum_{\rm SFR}$) as a function of half-light radius for local U/LIRGs of Barcos-Muñoz et al. (2017), the ALESS SMGs of Hodge et al. (2019), compared to the WHDF SMGs and the $z\sim6$ AGN presented in this work. The solid horizontal line indicates the Eddington limit for star formation with its lower limit shown by the horizontal dotted line. The dashed diagonal lines represent lines of constant Far-IR luminosity ranging from $\log(L_{\rm FIR})\sim 11.75, 12.25, 12.75, 13.25 L_\odot$ from left to right respectively. Elements of this plot have been replicated from Figure 6 of Hodge et al. (2019).

In Figure 7.4, we show the galaxy-averaged star formation rate surface density of our sources given by $\bar{\sum}_{\rm SFR} = 0.5\times SFR/(\pi R_e^2)$ following (Hodge et al., 2019), where the half-light radius R_e is taken as the mean of the major and minor axes FWHM of our sources divided by 2 (see column 6 of Table 7.2). For comparison, we also plot the $\bar{\sum}_{SFR}$ measurements of the local U/LIRG sample of Barcos-Muñoz et al. (2017) and high resolution ($\sim 0.07''$) observations of

Table 7.3: Parameters used in the calculation of our SMG star formation rate surface densities.

Object	$M_{\rm dust}$ ($10^9 M_\odot$)	$L_{\rm FIR\ (or\ C_{II})}$ ($10^{13} L_\odot$)	SFR ($10^3 M_\odot {\rm yr}^{-1}$)	$\sum_{\rm SFR}$ ($10^3 M_\odot {\rm yr}^{-1} {\rm kpc}^{-2}$)	Half-light radius (kpc)	$\bar{\sum}_{\rm SFR}$ ($10^3 M_\odot {\rm yr}^{-1} {\rm kpc}^{-2}$)
(1)	(2)	(3)	(4)	(5)	(6)	(7)
J332-23	0.44 ± 0.04	0.73 ± 0.04	1.08 ± 0.07	3.1 ± 0.2	0.3 ± 0.1	1.4 ± 0.8
J158-14	2.72 ± 0.06	4.50 ± 0.10	6.71 ± 0.14	9.6 ± 0.2	0.48 ± 0.04	4.7 ± 0.8
J158-14[C$_{\rm II}$]	—	1.64 ± 0.01	6.396 ± 0.003	0.54 ± 0.004	0.9 ± 0.1	1.2 ± 0.2
J025-33	0.65 ± 0.03	1.08 ± 0.04	1.61 ± 0.06	> 1.7	< 0.6	> 0.8
J025-33[C$_{\rm II}$]†	—	36.3 ± 0.2	0.577 ± 0.001	0.048 ± 0.004	1.8	0.3
J029-36	1.66 ± 0.07	2.74 ± 0.12	4.09 ± 0.17	2.24 ± 0.08	0.89 ± 0.04	1.1 ± 0.1
LAB-01	0.8 ± 0.2	0.26 ± 0.07	0.38 ± 0.07	0.32 ± 0.08	0.63 ± 0.03	0.15 ± 0.03
LAB-02	1.55 ± 0.06	0.13 ± 0.01	0.73 ± 0.03	1.28 ± 0.04	0.79 ± 0.02	0.19 ± 0.02
LAB-03	1.87 ± 0.05	0.59 ± 0.01	0.89 ± 0.02	0.60 ± 0.02	0.71 ± 0.02	0.28 ± 0.02
LAB-04	0.66 ± 0.09	0.21 ± 0.01	0.31 ± 0.05	0.28 ± 0.04	0.46 ± 0.08	0.48 ± 0.04
LAB-05	0.79 ± 0.04	0.25 ± 0.01	0.37 ± 0.02	0.21 ± 0.01	0.73 ± 0.03	0.14 ± 0.01
LAB-10	0.61 ± 0.03	0.19 ± 0.01	0.29 ± 0.01	0.84 ± 0.08	0.34 ± 0.02	0.41 ± 0.05
LAB-11	0.070 ± 0.004	0.022 ± 0.001	0.033 ± 0.002	0.032 ± 0.004	0.54 ± 0.06	0.025 ± 0.004

Notes. (1) AGN short name, (2) Dust mass, (3) Luminosity (in case of $L_{\rm C_{II}}$ the units are $10^8 L_\odot$), (4) Star formation rate (in case of C$_{\rm II}$ the units are $M_\odot {\rm yr}^{-1}$), (5) Star formation rate surface density (in case of C$_{\rm II}$ the units are $M_\odot {\rm yr}^{-1} {\rm pc}^{-2}$). †: Measurement from Decarli et al. (2018). (6) Half-light radius (based on the source major axis FWHM), (7) Galaxy-averaged star formation rate surface densities (see text for details).

the ALMA follow-up of the LABOCA ECDFS submillimeter survey (ALESS; Hodge et al. 2013) SMG sample, as presented in Figure 6 of Hodge et al. (2019). Here, we find all of our $z \sim 6$ AGN to have $\sum_{\rm SFR}$ values that exceed or approach the Eddington limit of star formation as shown by the solid horizontal line. In the case of the $z \sim 2-3$ WHDF SMGs, we find the $\bar{\sum}_{\rm SFR}$ values to be slightly higher than those of the ALESS SMG sample (which have redshifts in the range $z \sim 1.5-5$), but still below the Eddington lower limit on star formation. We note however, that 3/7 of these sources have galaxy-averaged star formation rate surface densities within a factor of $\sim 2-3$ of the Eddington lower-limit.

7.5 Conclusions

In this Chapter, we presented our ALMA band 6 observations targeting the [C II] emission in 4, $z > 6$ SMGs, which were initially detected as quasars in the VST ATLAS survey. We detected significant continuum dust emission in all four sources, and strong [C II] emission was detected in two of the targets (see also Decarli et al., 2018). Intriguingly, all four sources are either not resolved or only marginally spatially resolved (at an angular resolution of $0.3''$) in the dust continuum emission. Additionally, we presented our high resolution ($0.1''$), band 7, ALMA observations of seven $z \sim 2-3$ SMGs originally detected in the William Herschel Deep Field (WHDF).

Similar to a number of previous studies, we found our sources to have significantly more extended profiles in [C II] than in continuum, with the origin of this phenomenon being an area of ongoing research. The null [C II] detections in our $z > 6$ SMGs were most likely due to uncertainties in the measured redshifts of these sources, and it may be that the observations simply missed the [C II] emission from the host galaxy. Indeed, one of the strong [C II] line detections was found to be on the edge of our chosen ALMA spectral window, limiting our ability to ascertain the line flux.

Our primary goal in this Chapter was to identify the dominant fueling mechanism behind the observed sub-mm emission of the SMGs. To this end, we used our ALMA observations of these sources to perform measurements of their sizes and star formation rates based on their continuum (and where available [C II]) fluxes. We then used these measurements to calculate the star formation rate surface densities ($\sum_{\rm SFR}$) of the sub-mm emitting regions of these SMGs. In the case of our $z > 6$ SMGs we found their $\sum_{\rm SFR}$ values to approach or exceed the theoretical Eddington limit on star formation (≈ 1000 M$_\odot$ yr^{-1} kpc^{-2}), favouring an AGN-dominated fueling source behind their sub-mm emission.

In the case of our seven WHDF SMGs however, we found the $\sum_{\rm SFR}$ values of two SMGs to exceed the Eddington limit, while an additional four are within a factor of $\sim 2-3$ of the Eddington lower-limit of ≈ 650 $\rm M_{\odot}$ $\rm yr^{-1}$ $\rm kpc^{-2}$. Furthermore, Shanks et al. (in prep.) have found the SED of 6/7 of these sources to be more consistent with an AGN rather than a star-forming model. In future, high-resolution (sub-0.5″) and deep imaging of these sources in IR bands (e.g. with JWST), could provide another means of testing the AGN vs. star-formation hypothesis, by revealing whether the sub-mm and IR profiles of these sources extend to similar scales, or if the sub-mm emission is focused in the central regions of these SMGs, a picture which would favour the AGN dust heating model.

Chapter 8

Conclusions & Future Work

8.1 Summary of results & the scope for future work

In this thesis, we exploited the recently completed VST ATLAS survey of the Southern sky to test the predictions of the standard model of cosmology (ΛCDM) based on clustering analyses of the large-scale structure of the Universe. In particular, we investigated the tension between the CMB and late-Universe measurements of σ_8 based on our ATLAS cluster mass functions, as well as potential deviations from the standard ΛCDM predictions of the cosmological constant via the Integrated Sachs-Wolfe effect. In Chapter 3, we introduced the VST ATLAS galaxy cluster catalogue comparing it to existing optical, SZ and X-ray cluster samples. In Chapter 4, we presented our follow-up spectroscopic observations of cluster counterparts to Planck SZ sources with no previous identifications, which were detected in the ATLAS cluster catalogue. Chapter 5 focused on our calibration of the ATLAS cluster mass-richness scaling relation to masses from external optical, X-ray and SZ surveys. We then compared the observed cluster mass functions of ATLAS, SDSS RedMapper, Planck and AdvACT SZ samples to the predictions of ΛCDM. In Chapter 6, we presented the cross-correlation of various photometrically selected galaxy samples from ATLAS with the Planck CMB temperature map, providing new measurements of the Integrated Sachs-Wolfe (ISW) effect in the Southern sky. We then compare these measurements as well as those given by SDSS, BOSS and eBOSS surveys to the predictions of ΛCDM. Finally, in Chapter 7, we examined the dust heating mechanism of intermediate and high-redshift sub-mm galaxies (SMGs) based on high-resolution, high S/N ALMA observations of these sources.

We now present a summary of our key findings and discuss possible extensions to these research topics in future works.

8.1.1 Galaxy cluster cosmology

- While the ATLAS and SDSS RedMapper cluster catalogues probe a similar range of redshifts and cluster masses, based on comparison to external catalogues we found ATLAS to be more complete than RedMapper at $z < 0.35$, with ATLAS and RedMapper recovering $\sim 80\%$ and $\sim 60\%$ of Abell clusters in this redshift range respectively. At $z < 0.35$, We also found the majority ($> 85\%$) of ATLAS detections with a richness $N_{200} > 20$ to be genuine cluster detections. At $z > 0.35$ we found RedMapper to detect a larger number of clusters in the $M_{200} < 3 \times 10^{14} h^{-1} \mathrm{M}_{\odot}$ mass range compared to ATLAS.

- Comparison of ATLAS and RedMapper cluster mass functions to models based on a Planck Collaboration et al. (2020) ΛCDM cosmology, showed a better agreement between the ATLAS cluster mass functions and the predictions of ΛCDM, (with RedMapper underestimating the mass function amplitude at $z < 0.35$). In line with our earlier findings this is likely due to the incompleteness of the RedMapper sample at these redshifts, while as discussed in DES Collaboration et al. (2020), under-estimation of RedMapper weak-lensing calibrated masses may also be a contributing factor to these lower mass function amplitudes.

- We also found the amplitude of Planck and AdvACT SZ mass functions to be lower than the predictions of ΛCDM at all considered redshifts ($z < 0.55$). While the lower SZ mass function amplitudes are likely to be predominantly due to systematics in the current calibration of SZ flux-cluster mass scaling relations, we showed that the incompleteness of SZ samples is also likely to be a non-negligible contributing factor to their lower than predicted mass function amplitudes.

- We measure the value of $S_8 = \sigma_8 \sqrt{\Omega_{\mathrm{m}}/0.3} = 0.77 \pm 0.03$ from our analysis of ATLAS cluster mass functions at $z < 0.55$. This is in good agreement with the mean value of $\bar{S}_8 = 0.761 \pm 007$ obtained from the combination of various late-Universe S_8 measurements from the DES, KiDS, BOSS, Planck and SPT surveys. However, our value is $\sim 2\sigma$ lower than the early-Universe measurement from the Planck 2018 analysis of the CMB ($S_8 = 0.830 \pm 0.013$), which is in turn 4.6σ higher than the $\bar{S}_8$ constraint from the late-Universe probes.

- Comparing the normalisation of the ATLAS cluster mass functions to the predictions of the Tinker et al. (2008) models, we found that in general ATLAS observations tend

to prefer lower normalisations than the models (by up to a factor of ~ 2 at $z > 0.35$). In future works, we shall perform an in-depth analysis of the systematic and statistical uncertainties on the ATLAS mass functions, allowing us to assess the statistical significance of any deviations between the redshift evolution of the observed cluster mass functions and theoretical predictions.

The agreement between SZ cluster mass functions and theoretical predictions may improve in the future via improvements in the calibration of the SZ flux-cluster mass scaling relations. These calibrations can benefit from a sample of SZ clusters with 5% mass measurements given by a combination of strong and weak lensing techniques (e.g. von der Linden et al. 2014; Hoekstra et al. 2015; Niemiec et al. 2020), as well as CMB lensing methods which could yield cluster masses with a similar level of precision (e.g. Raghunathan et al. 2017; Gupta & Reichardt 2020). Spectroscopic follow-up campaigns of SZ clusters with no current counterpart identifications (such as the observations presented in Chapter 4), could also improve the completeness of SZ samples as well as providing precise constraints on cluster masses which could be used to improve SZ cluster mass calibrations. Optical cluster samples such as ATLAS and RedMapper are ideal for guiding such future observations. Furthermore, in the coming years X-ray cluster masses from the eROSITA survey will provide a large sample of clusters extending to $z \sim 1$, while probing a wide range of cluster masses. X-ray masses from eROSITA will therefore play a key role (alongside other mass calibration techniques) in improving the current SZ mass calibrations and bringing SZ clusters to the era of precision cosmology.

Another interesting topic for future work is the measurement of the stacked SZ signal by cross-correlating optical cluster samples, including ATLAS or the RedMapper samples from DES and SDSS, with high angular resolution SZ maps from surveys such as ACT or SPT. Such analyses provide a statistical measure of the SZ signal for lower mass halos which would otherwise be hard to measure on an individual basis due to their weak SZ signal. A combined analysis of the stacked SZ and lensing signals, in particular, can provide a powerful tool for calibration of the SZ signal-cluster mass scaling relation as a function of mass and redshift (see Oguri & Takada 2011; Fang et al. 2012; Vikram et al. 2017). Similarly, cross-correlation of SZ and optical data can aid with the identification of clusters that may be missed by red-sequence cluster detection techniques due to containing large fractions of blue galaxies.

Besides the applications mentioned here, the ATLAS cluster catalogue can be used for many other science goals. For instance, Eltvedt et al. (in prep.) have cross-correlated the ATLAS

cluster and quasar catalogues in order to study quasar weak lensing magnification bias, finding an anti-correlation at faint quasar magnitudes (19<g<22), and a positive cross-correlation amplitude at brighter quasar magnitudes (17<g<19). These measurements provide a general confirmation of results from previous works including those of Myers et al. (2003) and Scranton et al. (2005). In addition, the ATLAS cluster catalogue has been used by the ACT team to provide optical confirmation and photometric redshifts for a sample of ~ 50 AdvACT SZ clusters (Hilton et al., 2020). In the future, the ATLAS cluster catalogue can also provide a basis for comparison to the next generation of cluster samples from eROSITA, Euclid and 4MOST, providing a valuable tool for characterising the selection functions of these surveys, as well as their implemented cluster detection techniques. These surveys can in turn be used to improve the cluster mass calibrations of the ATLAS and RedMapper catalogues, and to further investigate the completeness of current SZ samples. In the coming years, these efforts shall enable us to isolate contributions of systematics to the current σ_8 tension from genuine signatures of physics beyond the standard ΛCDM model.

8.1.2 The Integrated Sachs-Wolfe effect

- In order to study the late-time accelerating expansion of the Universe via the ISW effect, we take advantage of data from the ATLAS survey, which covers previously unmapped areas of the southern sky.

- Based on the combination of ATLAS and SDSS LRG-CMB cross-correlation measurements, at $z = 0.35$ and 0.55, we detected the ISW signal at 1.2σ and 2.3σ respectively. At these redshifts, we found the ISW amplitude to be in good agreement with the predictions of ΛCDM. We then verified these results by repeating the measurements using the BOSS LOWZ and CMASS, spectroscopically confirmed LRG samples.

- We also detected the ISW effect in three magnitude-limited ATLAS+SDSS galaxy samples extending to $z \approx 0.4$ at $\sim 2\sigma$ per sample.

- However, we did not detect the ISW signal at $z = 0.68$ in either ATLAS or SDSS, or the combined data from the two surveys, finding a slightly negative ISW amplitude with a $\sim 2\sigma$ deviation from ΛCDM predictions. Further tests using spectroscopically confirmed eBOSS LRGs at this redshift remained inconclusive due to the low sky coverage of the eBOSS LRG sample at the time of conducting this research.

- Finally, we confirmed the robustness of our ISW measurements against observational and survey systematics including seeing, stellar density and galactic dust extinction.

If the ISW signal is shown to be redshift-dependent in a manner inconsistent with the predictions of ΛCDM, it could open the door to alternative cosmological models that predict such ISW amplitudes. Examples of such models include 'Kinetic Gravity Braiding' as introduced by Deffayet et al. (2010), in which the late-time ISW effect is expected to anti-correlate with large-scale structure (Kimura et al., 2012); a 'Galileon' model of modified gravity as first proposed by Nicolis et al. (2009), different variations of which predict a negative ISW amplitude or lower ISW power relative to ΛCDM (Barreira et al., 2014). However, given the ISW observations presented in this thesis, the 'backreaction' model based on the AvERA simulation of Rácz et al. (2017) could be the most promising alternative to ΛCDM. In this model $\Omega_{Lambda} = 0$ and instead, local inhomogeneities are treated as different Universes which evolve according to their local set of cosmological parameters, averaging out on large scales to produce the observed expansion of the Universe. As demonstrated by Beck et al. (2018), such models could produce a change of sing of the ISW amplitude as a function of redshift, similar to that found in this work. Given the large cosmological implications, repeating the high-redshift ISW measurement presented in this work using the completed eBOSS sample, as well as upcoming surveys such as DESI, Euclid, 4MOST and LSST would therefore be an important topic for future works. Additionally, future ISW measurements using the radio data provided by SKA (Dewdney et al., 2009), can be used to check for any undetected systematics in our $z \sim 0.7$ ISW analysis.

8.1.3 AGN vs. star formation fueling of SMGs

- Based on high-resolution (0.3") continuum ALMA observations, we found the star formation rate surface densities of four $z > 6$ SMGs to exceed the Eddington limit of star formation. This suggests that AGN, rather than star formation, are the dominant dust heating mechanism in these objects.

- Our (0.1") ALMA observation of the continuum emission of a sample of seven $z \sim 2$ SMGs revealed star formation rate surface densities exceeding the Eddington limit in 2/7 sources, with 4/7 sources being within a factor of $\sim 2-3$ of the Eddington lower-limit.

In the future high-resolution ALMA imaging and spectroscopic follow-up observations of a

larger sample of SMGs could allow for accurate constraints on the star formation rate surface brightness of these sources, providing us with a better understanding of the power source of this galaxy population. Furthermore, deep, high resolution (sub-0.5") imaging of our $z \sim 2$ SMGs with instruments such as JWST, can reveal whether the sub-mm and IR profiles of these sources extend to similar scales, or if the sub-mm emission is limited to the inner regions of these SMGs, a picture which would favour the AGN dust heating hypothesis.

8.2 Cosmology in the coming decade

Today cosmology is at a pivotal moment. A flat ΛCDM model has so far proven to be our best approximation for the observed large-scale structure and cosmic evolution of the Universe. Over the past decade, however, the increased statistical power of our observations has revealed potential tensions between measurements of various key cosmological parameters based on probes in the early and local Universe. Furthermore, the physical nature of dark matter and dark energy, the two main components of the ΛCDM model have so far remained elusive.

In the coming decade, the availability of an enormous wealth of multi-wavelength data from various state-of-the-art astronomical surveys including DESI, Euclid, LSST, 4MOST, eROSITA, SKA, SPT-3G (Benson et al., 2014), and CMB-S4 (Abazajian et al., 2016), may finally provide us with the statics needed to unravel the nature of the mysterious dark sector. Analysis of the Baryon Acoustic Oscillations (BAO) feature using Euclid, DESI and 4MOST data will soon extend our ability to measure the expansion of the Universe to higher redshifts ($z \sim 2$), with a much higher level of precision than possible today (Laureijs et al. 2011; DESI Collaboration et al. 2016; Richard et al. 2019). Furthermore, these surveys in combination with SKA, will also probe the growth rate of structure via *redshift space distortions* at unprecedented levels of precision, providing new insights into the σ_8 tension.

In the near future, a combination of spectroscopically confirmed quasars from DESI, 4MOST and Euclid, with the latest eROSITA X-ray data will allow us to further test the feasibility of a quasar Hubble diagram based on quasar distances estimated from their X-ray and Ultraviolet emission. This Hubble diagram will extend to high redshifts (up to $z \sim 6$), breaking degeneracies for studies of dark energy by providing complementary measurements to those obtained at lower redshifts ($z < 2$) using supernovae and BAO. This approach follows a novel technique introduced by Risaliti & Lusso (2019), who found the quasar Hubble diagram to

be in a $\sim 4\sigma$ deviation from the predictions of ΛCDM at $z > 1.4$, where the standard model is currently poorly tested. In this work, the authors demonstrated that if one allows the dark energy equation of state to vary with redshift, (with $\omega = \omega_0 + \omega_a(1 - a)$, where the scale factor of the Universe $a = 1/(1 + z)$), the combination of the quasar Hubble diagram and Planck CMB+weak lensing data result in a preference for values of $\omega_0 \approx -1.5$ and $\omega_a \approx 1$ at a $> 3\sigma$ level of significance relative to the ΛCDM model with $\omega = -1$. Interestingly, an evolving dark energy equation of state, as suggested by the quasar Hubble diagram, would also present a solution to the current H_0 tension between local indicators and the measurements form the CMB (see also Zhao et al. 2017; Di Valentino et al. 2016). While the quasar Hubble diagram holds much promise as a novel and independent probe of the expansion history of the Universe at higher redshifts, future studies applying this technique for cosmology need to overcome challenges including quasar X-ray and UV variability which could increase the uncertainties on the distance measurements. Furthermore, more work is still needed to fully constrain the impact of systematics such as intrinsic extinction and host galaxy contamination in the UV, as well as Photoelectric X-ray absorption on these distance measurements. Using an independent and complementary technique, multi-epoch observations provided by LSST, combined with eROSITA quasar X-ray flux measurements can be used to construct a high-redshift Hubble diagram via quasar reverberation mapping (see, e.g. Fine et al. 2013; Czerny et al. 2018).

The next generation of wide-field astronomical surveys will also enable us to adopt a multi-wavelength, multi-probe strategy at measuring key cosmological parameters, an approach that will significantly improve our ability to isolate systematics from genuine deviations from the predictions of cosmological models. At the same time, further advances in simulation techniques and computing, as well as wider adoption of machine learning approaches in astronomy, will also play an instrumental role in our ability to fill the remaining gaps in our current understanding of the Universe. If the promise of the next decade turns into reality, we may now be on the verge of unlocking some of the most fundamental mysteries of the Universe.

Appendix A

A.1 Planck SZ cluster galaxy redshifts and peculiar velocities

The confirmed redshifts and peculiar velocities of our observed Planck SZ clusters are presented in Table A.1. Here our peculiar velocities are calculated based on Equation 4.3.1. In this table the BCG of each cluster is listed as the 0-th member of each group with the remaining galaxies presented in order of decreasing RA.

Table A.1: Planck SZ confirmed cluster members spectroscopic redshifts and peculiar velocities.

Target ID	RA	DEC	Redshift	Peculiar velocity
LOZ-1.0	23:47:32.54	-31:08:50.7	0.400 ± 0.002	119 ± 521
LOZ-1.1	23:47:31.75	-31:08:54.4	0.4018 ± 0.0005	569 ± 297
LOZ-1.2	23:47:30.01	-31:09:02.4	0.39554 ± 0.00004	-764 ± 274
LOZ-1.3	23:47:28.34	-31:09:04.4	0.3995 ± 0.00047	89 ± 292
LOZ-1.4	23:47:25.35	-31:09:55.5	0.3984 ± 0.0001	-151 ± -275
LOZ-1.5	23:47:22.12	-31:07:54.2	0.394 ± 0.002	-1127 ± 421
LOZ-1.6	23:47:21.43	-31:09:24.8	0.397 ± 0.002	-520 ± 422
LOZ-1.7	23:47:20.34	-31:08:54.8	0.3995 ± 0.0006	78 ± 300
LOZ-1.8	23:47:19.02	-31:09:49.5	0.4071 ± 0.0004	1706 ± 288
LOZ-2.0	21:45:29.91	-21:43:22.8	0.2984 ± 0.0003	-51 ± 459
LOZ-2.1	21:45:26.09	-21:42:59.7	0.9528 ± 0.0004	-760 ± 462
LOZ-2.2	21:45:23.08	-21:44:58.5	0.3021 ± 0.0006	811 ± 475
LOZ-3.0	21:38:12.05	-23:58:55.1	0.2439 ± 0.0007	1046 ± 256
LOZ-3.1	21:38:17.73	23:59:13.2	0.2361 ± 0.0006	-855 ± 244
LOZ-3.2	21:38:16.81	-24:00:09.6	0.2384 ± 0.0006	-294 ± 244

Continued on next page

Table A.1 – *Continued from previous page*

Target ID	RA	DEC	Redshift	Peculiar velocity
LOZ-3.3	21:38:15.91	-23:57:29.7	0.2399 ± 0.0009	79 ± 272
LOZ-3.4	21:38:13.49	-23:59:23.5	0.2403 ± 0.0007	177 ± 252
LOZ-3.5	21:38:12.04	-23:57:54.1	0.2392 ± 0.0005	-98 ± 231
LOZ-3.6	21:38:11.29	-23:58:44.1	0.2396 ± 0.0005	-1 ± 231
LOZ-3.7	21:38:11.00	-23:59:18.1	0.235 ± 0.003	-1144 ± 640
LOZ-3.8	21:38:10.37	-23:59:32.0	0.2435 ± 0.0006	952 ± 245
LOZ-3.9	21:38:08.32	-23:58:07.2	0.2392 ± 0.0005	-104 ± 225
LOZ-3.10	21:38:06.92	23:58:06.3	0.2406 ± 0.0006	241 ± 244
LOZ-4.0	21:36:38.80	-10:18:36.3	0.4429 ± 0.0007	643 ± 271
LOZ-4.1	21:36:46.76	-10:20:02.4	0.437 ± 0.002	-546 ± 474
LOZ-4.2	21:36:45.86	-10:18:47.3	0.437 ± 0.001	-693 ± 327
LOZ-4.3	21:36:44.57	-10:19:03.6	0.43473 ± 0.00003	-1067 ± 225
LOZ-4.4	21:36:42.51	-10:19:09.9	0.437 ± 0.002	-679 ± 451
LOZ-4.5	21:36:41.73	-10:18:36.5	0.4348 ± 0.0007	-1045 ± 268
LOZ-4.6	21:36:40.95	-10:18:56.4	0.4443 ± 0.0007	918 ± 269
LOZ-4.7	21:36:39.60	-10:18:25.1	0.4453 ± 0.0008	1130 ± 281
LOZ-4.8	21:36:37.38	-10:18:55.2	0.442 ± 0.001	469 ± 345
LOZ-4.9	21:36:36.30	-10:18:49.6	0.4405 ± 0.0008	127 ± 280
LOZ-4.10	21:36:35.31	-10:20:05.5	0.4402 ± 0.0008	69 ± 280
LOZ-4.11	21:36:31.67	10:18:59.3	0.443 ± 0.001	674 ± 322
LOZ-5.0	13:56:05.41	-34:21:10.6	0.2289 ± 0.0003	-294 ± 299
LOZ-5.1	13:56:15.36	-34:21:13.3	0.2272 ± 0.0005	-707 ± 317
LOZ-5.2	13:56:08.68	-34:20:55.7	0.227 ± 0.002	-689 ± 607
LOZ-5.3	13:56:04.70	-34:21:40.0	0.2349 ± 0.0006	1172 ± 329
LOZ-5.4	13:56:03.92	-34:20:46.6	0.2308 ± 0.0005	176 ± 322
LOZ-5.5	13:55:58.08	-34:20:05.0	0.2315 ± 0.0005	341 ± 317
LOZ-6.0	11:19:05.96	-10:22:52.6	0.1224 ± 0.0003	274 ± 357
LOZ-6.1	11:19:07.04	-10:23:25.6	0.1229 ± 0.0007	582 ± 274
LOZ-6.2	11:19:05.42	-10:22:24.5	0.1211 ± 0.0006	-82 ± 380
LOZ-6.3	11:19:05.02	-10:22:03.0	0.1194 ± 0.0002	-528 ± 351
LOZ-6.4	11:19:03.58	-10:23:59.9	0.1180 ± 0.0002	-906 ± 350

Continued on next page

Table A.1 – *Continued from previous page*

Target ID	RA	DEC	Redshift	Peculiar velocity
LOZ-6.5	11:19:03.35	-10:23:40.8	0.1203 ± 0.0006	-296 ± 382
LOZ-7.0	11:18:58.34	-27:25:33.5	0.1961 ± 0.0003	892 ± 259
LOZ-7.1	11:19:02.79	-27:26:41.3	0.1904 ± 0.0007	-542 ± 305
LOZ-7.2	11:19:00.71	-27:25:32.1	0.1889 ± 0.0007	-919 ± 304
LOZ-7.3	11:18:59.70	-27:25:49.6	0.194 ± 0.002	-348 ± 479
LOZ-7.4	11:18:58.85	-27:25:27.1	0.1905 ± 0.0005	-510 ± 282
LOZ-7.5	11:18:55.84	-27:26:40.5	0.195 ± 0.001	472 ± 346
LOZ-7.6	11:18:55.04	-27:25:36.2	0.194 ± 0.001	259 ± 418
LOZ-8.0	11:05:04.56	-18:56:38.6	0.2214 ± 0.0002	-244 ± 267
LOZ-8.1	11:05:13.88	-18:56:36.0	0.2191 ± 0.0006	-818 ± 303
LOZ-8.2	11:05:12.21	-18:58:12.1	0.2283 ± 0.0004	1441 ± 280
LOZ-8.3	11:05:11.45	-18:58:29.1	0.219 ± 0.001	-792 ± 414
LOZ-8.4	11:05:10.63	-18:57:17.8	0.22340 ± 0.00005	250 ± 262
LOZ-8.5	11:05:08.05	-18:57:49.7	0.2160 ± 0.0004	-1554 ± 282
LOZ-8.6	11:05:08.62	-18:57:50.6	0.226 ± 0.004	955 ± 1015
LOZ-8.7	11:05:05.87	-18:56:50.6	0.2241 ± 0.0004	433 ± 276
LOZ-8.8	11:05:03.78	-18:56:50.4	0.220 ± 0.001	-594 ± 356
LOZ-8.9	11:05:02.77	-18:56:39.4	0.2244 ± 0.0002	490 ± 268
LOZ-8.10	11:05:02.10	-18:56:43.8	0.2266 ± 0.0002	1032 ± 269
LOZ-8.11	11:04:58.81	-18:55:53.4	0.2199 ± 0.0004	-600 ± 279
LOZ-9.0	10:00:20.26	-15:23:43.5	0.2008 ± 0.0001	318 ± 263
LOZ-9.1	10:00:25.88	-15:23:55.4	0.1984 ± 0.0004	-261 ± 220
LOZ-9.2	10:00:22.30	-15:23:28.7	0.2018 ± 0.0001	583 ± 202
LOZ-9.3	10:00:17.2	-15:20:30.3	0.197 ± 0.002	-540 ± 490
LOZ-9.4	10:00:12.1	-15:24:33.9	0.1990 ± 0.0003	-100 ± 212
LOZ-10.0	03:16:27.78	-20:46:32.2	0.2369 ± 0.0004	-59 ± 199
LOZ-10.1	03:16:33.25	-20:48:20.4	0.2381 ± 0.0002	230 ± 186
LOZ-10.2	03:16:33.19	-20:46:20.9	0.2401 ± 0.0004	705 ± 204
LOZ-10.3	03:16:31.30	-20:45:48.3	0.2415 ± 0.0004	1051 ± 204
LOZ-10.4	03:16:30.46	-20:47:07.2	0.2412 ± 0.0003	986 ± 194
LOZ-10.5	03:16:29.46	-20:46:18.2	0.2394 ± 0.0003	554 ± 194

Continued on next page

Table A.1 – *Continued from previous page*

Target ID	RA	DEC	Redshift	Peculiar velocity
LOZ-10.6	03:16:28.68	-20:46:26.9	0.2346 ± 0.0002	-616 ± 185
LOZ-10.7	03:16:27.02	-20:46:37.5	0.2347 ± 0.0009	-592 ± 284
LOZ-10.8	03:16:26.53	-20:46:57.1	0.2348 ± 0.0004	-555 ± 205
LOZ-10.9	03:16:25.90	-20:46:13.1	0.23939 ± 0.00008	542 ± 181
LOZ-10.10	03:16:24.97	-20:48:17.9	0.234 ± 0.001	-658 ± 319
LOZ-10.11	03:16:24.25	-20:46:08.7	0.234 ± 0.001	-736 ± 402
LOZ-10.12	03:16:22.39	-20:45:33.6	0.2368 ± 0.0003	-73 ± 193
LOZ-10.13	03:16:20.30	-20:48:11.0	0.2339 ± 0.0003	-778 ± 193
HIZ-1.0	02:00:16.37	-24:54:51.3	0.71808 ± 0.00007	1408 ± 177
HIZ-1.1	02:00:17.58	-24:54:28.9	0.7064 ± 0.0002	-639 ± 177
HIZ-1.2	02:00:16.93	-24:57:42.5	0.7062 ± 0.0003	-669 ± 183
HIZ-1.3	02:00:16.92	-24:57:42.2	0.70486 ± 0.00002	-909 ± 175
HIZ-1.4	02:00:16.81	-24:54:09.0	0.7095 ± 0.0002	-94 ± 178
HIZ-1.5	02:00:16.79	-24:54:40.4	0.7156 ± 0.0001	-965 ± 177
HIZ-1.6	02:00:16.77	-24:54:40.5	0.7153 ± 0.0003	923 ± 182
HIZ-1.7	02:00:14.71	-24:55:48.5	0.70835 ± 0.00006	-298 ± 175
HIZ-1.8	02:00:14.57	-24:55:23.1	0.7147 ± 0.0002	818 ± 180
HIZ-1.9	02:00:14.09	-24:58:05.9	0.71322 ± 0.00003	558 ± 176
HIZ-1.10	02:00:13.49	-24:55:45.8	0.7078 ± 0.0002	-402 ± 178
HIZ-1.11	02:00:13.02	-24:55:52.8	0.7121 ± 0.0002	376 ± 179
HIZ-1.12	02:00:12.79	-24:52:26.8	0.7181 ± 0.0002	1412 ± 179
HIZ-1.13	02:00:12.73	-24:53:53.6	0.7042 ± 0.0001	-1025 ± 176
HIZ-1.14	02:00:12.20	-24:54:06.7	0.7044 ± 0.0001	-994 ± 176
HIZ-1.15	02:00:11.64	-24:52:29.2	0.70686 ± 0.00006	-558 ± 175
HIZ-1.16	02:00:07.74	-24:56:00.1	0.70713 ± 0.00003	-512 ± 175
HIZ-1.17	02:00:06.06	-24:58:00.8	0.7070 ± 0.0002	-512 ± 175

Appendix B

B.1 Derivation of $\sigma_{M_{200}}$

Here we present a derivation of the error on our cluster mass estimate, as given by Equation 5.2.2. We start with Equation 5.2.1, which provides an expression for our cluster masses:

$$M_{200} = \left(\frac{N_{200}}{20}\right)^{1.1} \times 3\bar{z}^{\,0.9} + 1. \tag{B.1.1}$$

With the uncertainties on our mean cluster redshift $\bar{z}$ and cluster richness N_{200} given by $\sigma_{\bar{z}}$ and $\sigma_{N200} = \sqrt{N_{200}}$ respectively, we can obtain the error on our cluster masses using:

$$\sigma_{M_{200}} = \sqrt{\left(\frac{\partial M_{200}}{\partial N_{200}}\right)^2 \sigma^2_{N_{200}} + \left(\frac{\partial M_{200}}{\partial \bar{z}}\right)^2 \sigma^2_{\bar{z}}}, \tag{B.1.2}$$

with a numerical solution given by:

$$\sigma_{M_{200}} = \sqrt{0.015\sigma^2_{N_{200}} N_{200}^{0.2}\bar{z}^{1.8} + \frac{0.01N_{200}^{2.2}\sigma^2_{\bar{z}}}{\bar{z}^{0.2}}}. \tag{B.1.3}$$

Appendix C

C.1 ATLAS / SDSS colour comparison

Figure C.1 shows a comparison of VST ATLAS Aperture 5 and SDSS model magnitude colours. Upon removing 3σ outliers (as indicated by the dashed lines in the plots), we find a rms scatter of 0.03, 0.04 and 0.13, with ATLAS-SDSS offsets of 0.01, -0.01 and 0.05 for $g-r$, $r-i$ and $i-z$ colors respectively. Here we impose magnitude limits of $g < 21.5$, $r < 19.5$, $i < 20.5$ and $z < 20.0$, corresponding to the range of magnitudes used in our LRG selection. In each case we only impose the magnitude limits of the two bands used to obtain the colours and restrict the sample to galaxies based on the ATLAS morphological classification in those bands. Given the reasonably tight scatter and small systematic offsets, in this work we adopt a photometric selection criteria based on SDSS magnitudes, when defining our LRG samples.

C.2 LRG contamination tests

Adopting a similar approach to Ross et al. (2017), we test for the impact of various sources of survey systematics including airmass, seeing, galactic dust extinction and stellar contamination on our $\bar{z} = 0.35$, 0.55 and 0.68 LRG samples. In the top panel of Figure C.2 we show the four instances where systematic trends due to galactic extinction, seeing and stellar contamination appear to be present in our LRG samples, finding no major systematic trends in the remaining cases. As shown in the bottom panel of Figure C.2, the inclusion of weights correcting for these observed systematics does not appear to have a significant impact on our ISW measurements.

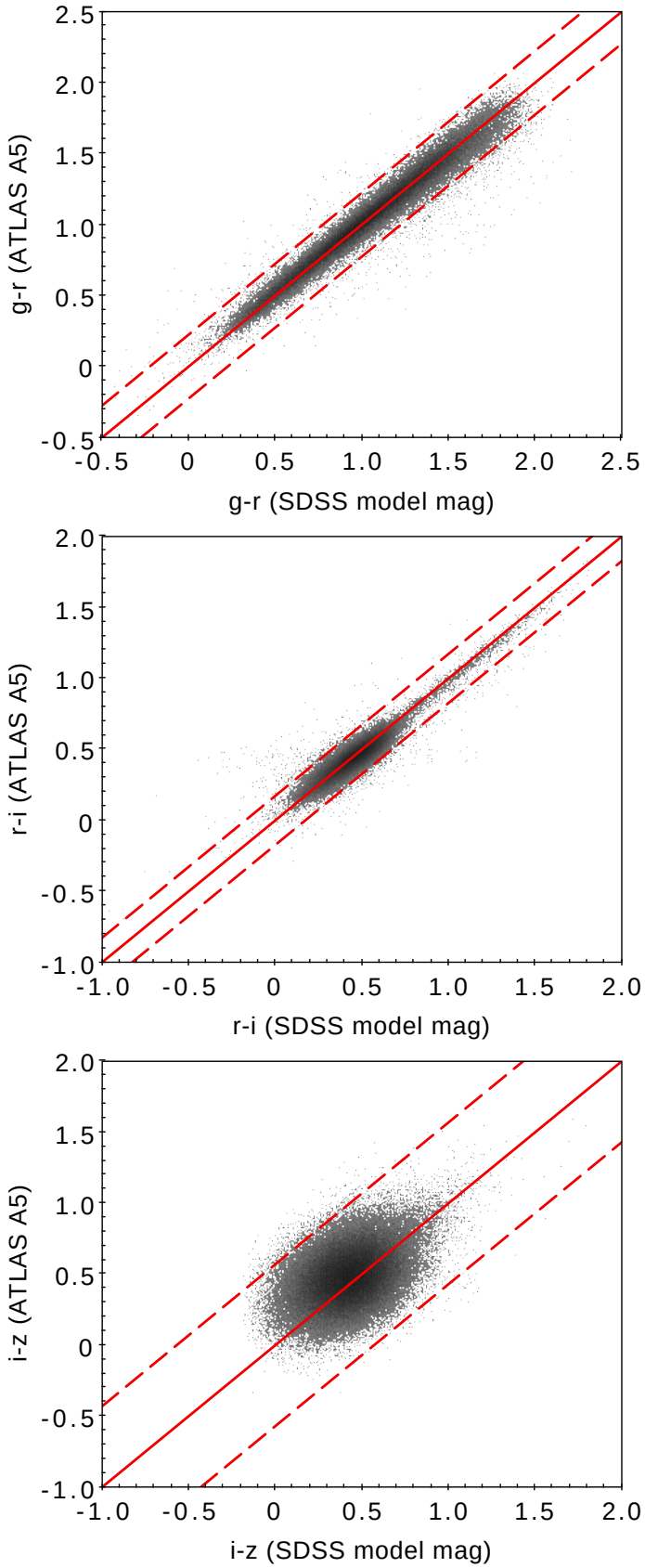

Figure C.1: A comparison of the g-r, r-i and i-z colours based on VST ATLAS Aperture 5 and SDSS model magnitudes. Given the similarity between the colours, we use the SDSS cuts in our LRG sample selections, described in Section 6.2.2. Here the dashed lines indicate the 3σ outliers.

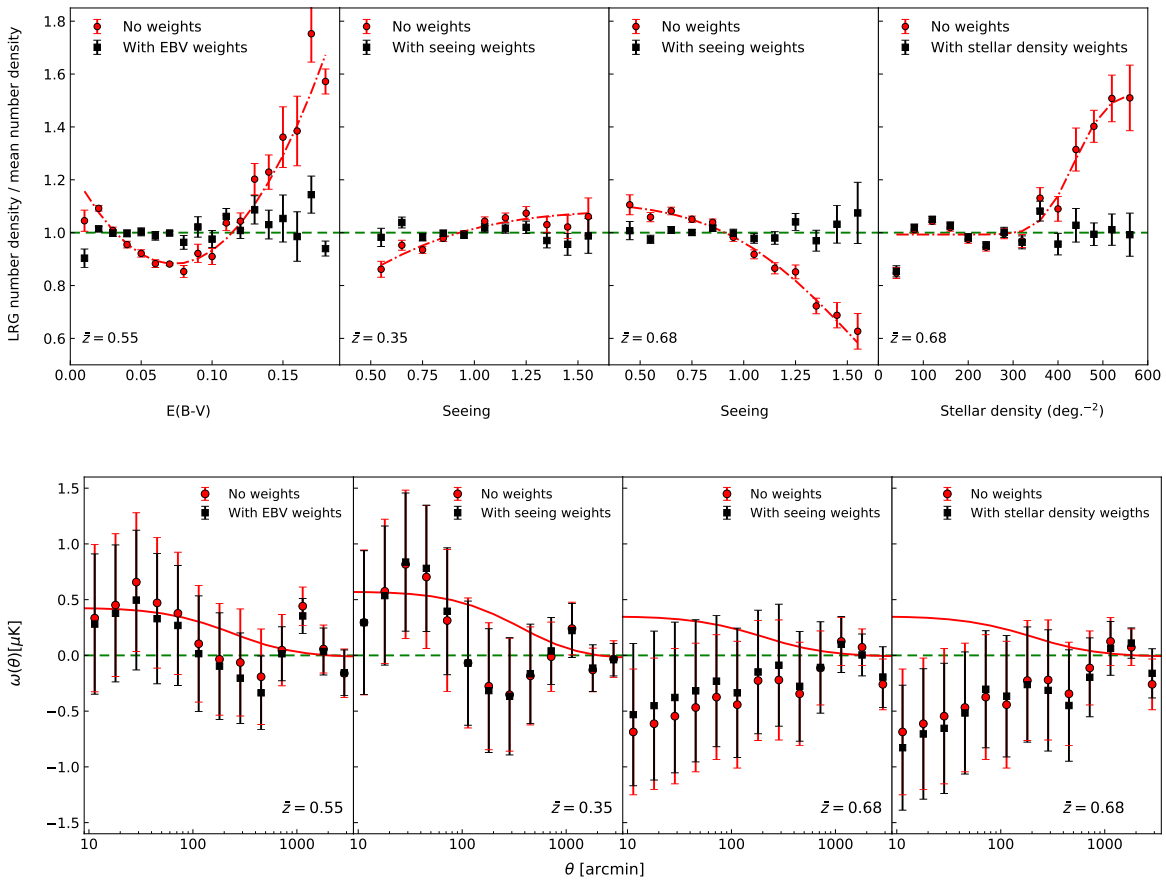

Figure C.2: Top panel: Normalised projected LRG number density as a function of Galactic extinction (in E(B-V)), seeing (in r-band for $\bar{z} = 0.35$ and i-band for $\bar{z} = 0.68$) and projected stellar density (limited to $19.8 < i < 20.5$ corresponding to the magnitude limits of the $\bar{z} = 0.68$ LRG sample). Here the dot-dashed curves are the best-fit relationships used to define the weights correcting for the observed systematic trends. Bottom panel: The impact of including the E(B-V), seeing and stellar density weights from the top panel on our ISW measurements. In all cases, the inclusion of weights do not appear to have a significant impact on our ISW measurements.

Bibliography

Abazajian, K.N., Adshead, P., Ahmed, Z., et al. *CMB-S4 Science Book, First Edition.* arXiv e-prints (2016), arXiv:1610.02743. 1610.02743.

Abazajian, K.N., Arnold, K., Austermann, J., et al. *Inflation physics from the cosmic microwave background and large scale structure.* Astroparticle Physics, **63** (2015), 55. 1309.5381.

Abbott, T.M.C., Abdalla, F.B., Allam, S., et al. *The Dark Energy Survey: Data Release 1.* ApJS, **239**(2) (2018a), 18. 1801.03181.

Abbott, T.M.C., Abdalla, F.B., Annis, J., et al. *Dark Energy Survey Year 1 Results: A Precise H_0 Estimate from DES Y1, BAO, and D/H Data.* MNRAS, **480**(3) (2018b), 3879. 1711.00403.

Abell, G.O. *The Distribution of Rich Clusters of Galaxies.* ApJS, **3** (1958), 211.

Abell, G.O., Corwin, Jr., H.G., Olowin, R.P. *A catalog of rich clusters of galaxies.* ApJS, **70** (1989), 1.

Addison, G.E., Watts, D.J., Bennett, C.L., et al. *Elucidating ΛCDM: Impact of Baryon Acoustic Oscillation Measurements on the Hubble Constant Discrepancy.* ApJ, **853**(2) (2018), 119. 1707.06547.

Adelman-McCarthy, J.K., Agüeros, M.A., Allam, S.S., et al. *The Fifth Data Release of the Sloan Digital Sky Survey.* ApJS, **172** (2007), 634. 0707.3380.

Adler, R.J., Casey, B., Jacob, O.C. *Vacuum catastrophe: An elementary exposition of the cosmological constant problem.* American Journal of Physics, **63**(7) (1995), 620.

Aihara, H., Armstrong, R., Bickerton, S., et al. *First Data Release of the Hyper Suprime-Cam Subaru Strategic Program.* ArXiv e-prints (2017). 1702.08449.

Alam, S., Albareti, F.D., Allende Prieto, C., et al. *The Eleventh and Twelfth Data Releases of the Sloan Digital Sky Survey: Final Data from SDSS-III.* ApJS, **219** (2015), 12. 1501.00963.

Alam, S., Albareti, F.D., Prieto, C.A., et al. *THE ELEVENTH AND TWELFTH DATA RELEASES OF THE SLOAN DIGITAL SKY SURVEY: FINAL DATA FROM SDSS-III.* The Astrophysical Journal Supplement Series, **219**(1) (2015), 12. URL https://doi.org/10.1088%2F0067-0049%2F219%2F1%2F12.

Alam, S., Ata, M., Bailey, S., et al. *The clustering of galaxies in the completed SDSS-III Baryon Oscillation Spectroscopic Survey: cosmological analysis of the DR12 galaxy sample.* MNRAS, **470** (2017), 2617. 1607.03155.

Alestas, G., Kazantzidis, L., Perivolaropoulos, L. *H_0 tension, phantom dark energy, and cosmological parameter degeneracies.* Phys. Rev. D, **101**(12) (2020), 123516. 2004.08363.

Alexander, D.M., Bauer, F.E., Chapman, S.C., et al. *The X-Ray Spectral Properties of SCUBA Galaxies.* ApJ, **632**(2) (2005), 736. astro-ph/0506608.

Allen, S.W., Evrard, A.E., Mantz, A.B. *Cosmological Parameters from Observations of Galaxy Clusters.* ARA&A, **49** (2011), 409. 1103.4829.

Allen, S.W., Schmidt, R.W., Fabian, A.C. *Cosmological constraints from the X-ray gas mass fraction in relaxed lensing clusters observed with Chandra.* MNRAS, **334** (2002), L11. astro-ph/0205007.

Almosallam, I.A., Jarvis, M.J., Roberts, S.J. *GPZ: non-stationary sparse Gaussian processes for heteroscedastic uncertainty estimation in photometric redshifts.* MNRAS, **462**(1) (2016), 726. 1604.03593.

Alonso, D. *CUTE solutions for two-point correlation functions from large cosmological datasets.* ArXiv e-prints (2012). 1210.1833.

Anderson, L., Aubourg, É., Bailey, S., et al. *The clustering of galaxies in the SDSS-III Baryon Oscillation Spectroscopic Survey: baryon acoustic oscillations in the Data Releases 10 and 11 Galaxy samples.* MNRAS, **441**(1) (2014), 24. 1312.4877.

Andrews, B.H., Thompson, T.A. *Assessing Radiation Pressure as a Feedback Mechanism in Star-forming Galaxies.* ApJ, **727**(2) (2011), 97. 1011.0955.

Angulo, R.E., Springel, V., White, S.D.M., et al. *Scaling relations for galaxy clusters in the Millennium-XXL simulation.* MNRAS, **426**(3) (2012), 2046. 1203.3216.

Appenzeller, I., Fricke, K., Fürtig, W., et al. *Successful commissioning of FORS1 - the first optical instrument on the VLT.* The Messenger, **94** (1998), 1.

Arnaud, M., Pratt, G.W., Piffaretti, R., et al. *The universal galaxy cluster pressure profile from a representative sample of nearby systems (REXCESS) and the Y_{SZ} - M_{500} relation.* A&A, **517** (2010), A92. 0910.1234.

Bañados, E., Decarli, R., Walter, F., et al. *Bright [C II] 158 μm Emission in a Quasar Host Galaxy at $z = 6.54$.* ApJ, **805** (2015), L8. 1504.05216.

Bahcall, N.A., Soneira, R.M. *The spatial correlation function of rich clusters of galaxies.* ApJ, **270** (1983), 20.

Bamba, K., Capozziello, S., Nojiri, S., et al. *Dark energy cosmology: the equivalent description via different theoretical models and cosmography tests.* Ap&SS, **342**(1) (2012), 155. 1205.3421.

Banks, T., Dine, M., Motl, L. *On anthropic solutions of the cosmological constant problem.* Journal of High Energy Physics, **2001**(1) (2001), 031. hep-th/0007206.

Barcos-Muñoz, L., Leroy, A.K., Evans, A.S., et al. *A 33 GHz Survey of Local Major Mergers: Estimating the Sizes of the Energetically Dominant Regions from High-resolution Measurements of the Radio Continuum.* ApJ, **843**(2) (2017), 117. 1705.10801.

Barger, A.J., Cowie, L.L., Sanders, D.B., et al. *Submillimetre-wavelength detection of dusty star-forming galaxies at high redshift.* Nature, **394**(6690) (1998), 248. astro-ph/9806317.

Barreira, A., Li, B., Baugh, C.M., et al. *The observational status of Galileon gravity after Planck.* J. Cosmology Astropart. Phys., **2014**(8) (2014), 059. 1406.0485.

Baugh, C.M., Lacey, C.G., Frenk, C.S., et al. *Can the faint submillimetre galaxies be explained in the Λ cold dark matter model?* MNRAS, **356**(3) (2005), 1191. astro-ph/0406069.

Baum, W.A. *Population Inferences from Star Counts, Surface Brightness and Colors.* PASP, **71** (1959), 106.

Beck, R., Csabai, I., Rácz, G., et al. *The integrated Sachs-Wolfe effect in the AvERA cosmology.* MNRAS, **479**(3) (2018), 3582. 1801.08566.

Beers, T.C., Flynn, K., Gebhardt, K. *Measures of Location and Scale for Velocities in Clusters of Galaxies—A Robust Approach.* AJ, **100** (1990), 32.

Benítez, N. *BPZ: Bayesian Photometric Redshift Code.* Astrophysics Source Code Library (2011). 1108.011.

Benson, B.A., Ade, P.A.R., Ahmed, Z., et al. *SPT-3G: a next-generation cosmic microwave background polarization experiment on the South Pole telescope.* In *Millimeter, Submillimeter, and Far-Infrared Detectors and Instrumentation for Astronomy VII*, volume 9153 of *Society of Photo-Optical Instrumentation Engineers (SPIE) Conference Series* (2014), page 91531P. 1407.2973.

Bernal, J.L., Verde, L., Riess, A.G. *The trouble with H_0.* J. Cosmology Astropart. Phys., **2016**(10) (2016), 019. 1607.05617.

Bertin, E., Arnouts, S. *SExtractor: Software for source extraction.* A&AS, **117** (1996), 393.

Bethermin, M., Fudamoto, Y., Ginolfi, M., et al. *The ALPINE-ALMA [CII] Survey: data processing, catalogs, and statistical source properties.* arXiv e-prints (2020), arXiv:2002.00962. 2002.00962.

Beutler, F., Blake, C., Colless, M., et al. *The 6dF Galaxy Survey: baryon acoustic oscillations and the local Hubble constant.* MNRAS, **416**(4) (2011), 3017. 1106.3366.

Bhattacharya, S., Heitmann, K., White, M., et al. *Mass Function Predictions Beyond ΛCDM.* ApJ, **732**(2) (2011), 122. 1005.2239.

Bielby, R., Shanks, T., Sawangwit, U., et al. *Photometric selection of emission-line galaxies, clustering analysis and a search for the integrated Sachs-Wolfe effect.* MNRAS, **403** (2010), 1261. 0902.1098.

Bielby, R.M., Hill, M.D., Metcalfe, N., et al. *Submillimetre observations of X-ray active galactic nuclei in the William Herschel Deep Field.* MNRAS, **419**(2) (2012), 1315. 1108.3934.

Biffi, V., Dolag, K., Merloni, A. *AGN contamination of galaxy-cluster thermal X-ray emission: predictions for eRosita from cosmological simulations.* MNRAS, **481**(2) (2018), 2213. 1804.01096.

Biswas, R., Heitmann, K., Habib, S., et al. *Effects of Massive Neutrinos and Dynamical Dark Energy on the Cluster Mass Function.* arXiv e-prints (2019), arXiv:1901.10690. 1901.10690.

Biviano, A. *From Messier to Abell: 200 Years of Science with Galaxy Clusters.* In *Constructing the Universe with Clusters of Galaxies* (2000). astro-ph/0010409.

Bizenberger, P., McCaughrean, M.J., Birk, C., et al. *Omega Prime: the wide-field near-infrared camera for the 3.5-m telescope of the Calar Alto Observatory.* In A.M. Fowler, editor, *Infrared Astronomical Instrumentation*, volume 3354 of *Society of Photo-Optical Instrumentation Engineers (SPIE) Conference Series* (1998), pages 825–832.

Blain, A.W., Smail, I., Ivison, R.J., et al. *Submillimeter galaxies.* Phys. Rep., **369**(2) (2002), 111. astro-ph/0202228.

Bleem, L.E., Stalder, B., de Haan, T., et al. *Galaxy Clusters Discovered via the Sunyaev-Zel'dovich Effect in the 2500-Square-Degree SPT-SZ Survey.* ApJS, **216**(2) (2015), 27. 1409.0850.

Bocquet, S., Dietrich, J.P., Schrabback, T., et al. *Cluster Cosmology Constraints from the 2500 deg^2 SPT-SZ Survey: Inclusion of Weak Gravitational Lensing Data from Magellan and the Hubble Space Telescope.* ApJ, **878**(1) (2019), 55. 1812.01679.

Bocquet, S., Saro, A., Dolag, K., et al. *Halo mass function: baryon impact, fitting formulae, and implications for cluster cosmology.* MNRAS, **456**(3) (2016), 2361. 1502.07357.

Böhringer, H., Chon, G., Collins, C.A. *The extended ROSAT-ESO Flux Limited X-ray Galaxy Cluster Survey (REFLEX II). IV. X-ray luminosity function and first constraints on cosmological parameters.* A&A, **570** (2014), A31. 1403.2927.

Böhringer, H., Chon, G., Kronberg, P.P. *The Cosmic Large-Scale Structure in X-rays (CLASSIX) Cluster Survey. I. Probing galaxy cluster magnetic fields with line of sight rotation measures.* A&A, **596** (2016), A22. 1610.02887.

Böhringer, H., Schuecker, P., Guzzo, L., et al. *The ROSAT-ESO Flux Limited X-ray (REFLEX) Galaxy cluster survey. V. The cluster catalogue.* A&A, **425** (2004), 367. astro-ph/0405546.

Bolzonella, M., Miralles, J.M., Pelló, R. *Photometric redshifts based on standard SED fitting procedures.* A&A, **363** (2000), 476. astro-ph/0003380.

Bonnarel, F., Fernique, P., Bienaymé, O., et al. *The ALADIN interactive sky atlas. A reference tool for identification of astronomical sources.* A&AS, **143** (2000), 33.

Boughn, S., Crittenden, R. *A correlation between the cosmic microwave background and large-scale structure in the Universe.* Nature, **427** (2004), 45. astro-ph/0305001.

Boughn, S.P., Crittenden, R.G. *Cross Correlation of the Cosmic Microwave Background with Radio Sources: Constraints on an Accelerating Universe.* Physical Review Letters, **88**(2) (2002), 021302. astro-ph/0111281.

Bower, R.G., Lucey, J.R., Ellis, R.S. *Precision photometry of early-type galaxies in the Coma and Virgo clusters: A test of the universality of the colour-magnitude relation. I - The data. II. Analysis.* MNRAS, **254** (1992), 589.

Braatz, J., Condon, J., Henkel, C., et al. *A Measurement of the Hubble Constant by the Megamaser Cosmology Project.* In A. Tarchi, M.J. Reid, P. Castangia, editors, *Astrophysical Masers: Unlocking the Mysteries of the Universe*, volume 336 (2018), pages 86–91.

Brownstein, J.R. *Modified gravity and the phantom of dark matter.* Ph.D. thesis, University of Waterloo, Canada (2009).

Bruzual, G., Charlot, S. *Stellar population synthesis at the resolution of 2003.* MNRAS, **344**(4) (2003), 1000. astro-ph/0309134.

Bull, P., Akrami, Y., Adamek, J., et al. *Beyond Λ CDM: Problems, solutions, and the road ahead.* Physics of the Dark Universe, **12** (2016), 56. 1512.05356.

Burenin, R.A., Vikhlinin, A., Hornstrup, A., et al. *The 400 Square Degree ROSAT PSPC Galaxy Cluster Survey: Catalog and Statistical Calibration.* ApJS, **172** (2007), 561. astro-ph/0610739.

Butcher, H., Oemler, A., J. *The evolution of galaxies in clusters. I. ISIT photometry of Cl 0024+1654 and 3C 295.* ApJ, **219** (1978), 18.

Buzzoni, B., Delabre, B., Dekker, H., et al. *The ESO Faint Object Spectrograph and Camera / EFOSC.* The Messenger, **38** (1984), 9.

Cabré, A., Fosalba, P., Gaztañaga, E., et al. *Error analysis in cross-correlation of sky maps: application to the Integrated Sachs-Wolfe detection.* MNRAS, **381**(4) (2007), 1347. astro-ph/0701393.

Cabré, A., Gaztañaga, E., Manera, M., et al. *Cross-correlation of Wilkinson Microwave Anisotropy Probe third-year data and the Sloan Digital Sky Survey DR4 galaxy survey: new evidence for dark energy.* MNRAS, **372** (2006), L23. astro-ph/0603690.

Cai, Y.C., Neyrinck, M., Mao, Q., et al. *The lensing and temperature imprints of voids on the cosmic microwave background.* MNRAS, **466** (2017), 3364. 1609.00301.

Caldwell, C.E., McCarthy, I.G., Baldry, I.K., et al. *Cosmology with velocity dispersion counts: an alternative to measuring cluster halo masses.* MNRAS, **462**(4) (2016), 4117. 1602.00611.

Cannon, R., Drinkwater, M., Edge, A., et al. *The 2dF-SDSS LRG and QSO (2SLAQ) Luminous Red Galaxy Survey.* MNRAS, **372** (2006), 425. astro-ph/0607631.

Carilli, C.L., Walter, F. *Cool Gas in High-Redshift Galaxies.* ARA&A, **51** (2013), 105. 1301.0371.

Carlstrom, J.E., Ade, P.A.R., Aird, K.A., et al. *The 10 Meter South Pole Telescope.* PASP, **123** (2011), 568. 0907.4445.

Carlstrom, J.E., Holder, G.P., Reese, E.D. *Cosmology with the Sunyaev-Zel'dovich Effect.* ARA&A, **40** (2002), 643. astro-ph/0208192.

Carnall, A.C., Shanks, T., Chehade, B., et al. *Two bright z 6 quasars from VST ATLAS and a new method of optical plus mid-infrared colour selection.* MNRAS, **451** (2015), L16. 1502.07748.

Carniani, S., Ferrara, A., Maiolino, R., et al. *Missing [CII] emission from early galaxies.* arXiv e-prints (2020), arXiv:2006.09402. 2006.09402.

Carroll, S.M. *The Cosmological Constant.* Living Reviews in Relativity, **4**(1) (2001), 1. astro-ph/0004075.

Casey, C.M., Narayanan, D., Cooray, A. *Dusty star-forming galaxies at high redshift.* Phys. Rep., **541**(2) (2014), 45. 1402.1456.

Castorina, E., Sefusatti, E., Sheth, R.K., et al. *Cosmology with massive neutrinos II: on the universality of the halo mass function and bias.* J. Cosmology Astropart. Phys., **2014**(2) (2014), 049. 1311.1212.

Cavaliere, A., Fusco-Femiano, R. *X-rays from hot plasma in clusters of galaxies.* A&A, **49** (1976), 137.

Chambers, K.C., Magnier, E.A., Metcalfe, N., et al. *The Pan-STARRS1 Surveys.* arXiv e-prints (2016), arXiv:1612.05560. 1612.05560.

Chehade, B., Carnall, A.C., Shanks, T., et al. *Two more, bright, z 6 quasars from VST ATLAS and WISE.* MNRAS, **478** (2018), 1649. 1803.01424.

Chen, H.Y., Fishbach, M., Holz, D.E. *A two per cent Hubble constant measurement from standard sirens within five years.* Nature, **562**(7728) (2018), 545. 1712.06531.

Chilingarian, I.V., Melchior, A.L., Zolotukhin, I.Y. *Analytical approximations of K-corrections in optical and near-infrared bands.* MNRAS, **405** (2010), 1409. 1002.2360.

Cicone, C., Maiolino, R., Gallerani, S., et al. *Very extended cold gas, star formation and outflows in the halo of a bright quasar at $z > 6$.* A&A, **574** (2015), A14. 1409.4418.

Clifton, T., Ferreira, P.G., Padilla, A., et al. *Modified gravity and cosmology.* Phys. Rep., **513**(1) (2012), 1. 1106.2476.

Clowe, D., Bradač, M., Gonzalez, A.H., et al. *A Direct Empirical Proof of the Existence of Dark Matter.* ApJ, **648**(2) (2006), L109. astro-ph/0608407.

Clowe, D., Gonzalez, A., Markevitch, M. *Weak-Lensing Mass Reconstruction of the Interacting Cluster 1E 0657-558: Direct Evidence for the Existence of Dark Matter.* ApJ, **604**(2) (2004), 596. astro-ph/0312273.

Colless, M., Peterson, B.A., Jackson, C., et al. *The 2dF Galaxy Redshift Survey: Final Data Release.* arXiv e-prints (2003), astro-ph/0306581. astro-ph/0306581.

Comastri, A., Setti, G., Zamorani, G., et al. *The contribution of AGNs to the X-ray background.* A&A, **296** (1995), 1. astro-ph/9409067.

Comparat, J., Prada, F., Yepes, G., et al. *Accurate mass and velocity functions of dark matter haloes.* MNRAS, **469**(4) (2017), 4157. 1702.01628.

Cooke, E.A., Smail, I., Swinbank, A.M., et al. *An ALMA Survey of the SCUBA-2 Cosmology Legacy Survey UKIDSS/UDS Field: Identifying Candidate $z \sim 4.5$ [C II] Emitters.* ApJ, **861**(2) (2018), 100. 1805.05363.

Cool, R.J., Moustakas, J., Blanton, M.R., et al. *THE PRISM MULTI-OBJECT SURVEY (PRIMUS). II. DATA REDUCTION AND REDSHIFT FITTING.* The Astrophysical Journal, **767**(2) (2013), 118. URL `https://doi.org/10.1088%2F0004-637x%2F767%2F2%2F118`.

Copeland, E.J., Sami, M., Tsujikawa, S. *Dynamics of Dark Energy.* International Journal of Modern Physics D, **15**(11) (2006), 1753. `hep-th/0603057`.

Corasaniti, P.S., Giannantonio, T., Melchiorri, A. *Constraining dark energy with cross-correlated CMB and large scale structure data.* Phys. Rev. D, **71**(12) (2005), 123521. `astro-ph/0504115`.

Costanzi, M., Villaescusa-Navarro, F., Viel, M., et al. *Cosmology with massive neutrinos III: the halo mass function and an application to galaxy clusters.* J. Cosmology Astropart. Phys., **2013**(12) (2013), 012. `1311.1514`.

Crittenden, R.G., Turok, N. *Looking for a Cosmological Constant with the Rees-Sciama Effect.* Phys. Rev. Lett., **76**(4) (1996), 575. `astro-ph/9510072`.

Crocce, M., Fosalba, P., Castand er, F.J., et al. *Simulating the Universe with MICE: the abundance of massive clusters.* MNRAS, **403**(3) (2010), 1353. `0907.0019`.

Croom, S.M., Shanks, T. *Statistical lensing of faint QSOs by galaxy clusters.* MNRAS, **307** (1999), L17. `astro-ph/9905249`.

Czerny, B., Beaton, R., Bejger, M., et al. *Astronomical Distance Determination in the Space Age. Secondary Distance Indicators.* Space Sci. Rev., **214**(1) (2018), 32. `1801.00598`.

Dalal, N., Doré, O., Huterer, D., et al. *Imprints of primordial non-Gaussianities on large-scale structure: Scale-dependent bias and abundance of virialized objects.* Phys. Rev. D, **77**(12) (2008), 123514. `0710.4560`.

Dalton, G.B., Efstathiou, G., Maddox, S.J., et al. *Spatial correlations in a redshift survey of APM galaxy clusters.* ApJ, **390** (1992), L1.

Dalton, G.B., Efstathiou, G., Maddox, S.J., et al. *The APM Galaxy Survey - Part Four - Redshifts of Rich Clusters of Galaxies.* MNRAS, **269** (1994), 151. `astro-ph/9311038`.

Das, S., Louis, T., Nolta, M.R., et al. *The Atacama Cosmology Telescope: temperature and gravitational lensing power spectrum measurements from three seasons of data.* Journal of

Cosmology and Astroparticle Physics, **2014**(04) (2014), 014–014. ISSN 1475-7516. URL http://dx.doi.org/10.1088/1475-7516/2014/04/014.

Davis, M., Efstathiou, G., Frenk, C.S., et al. *The evolution of large-scale structure in a universe dominated by cold dark matter.* ApJ, **292** (1985), 371.

Davis, T.M., Scrimgeour, M.I. *Deriving accurate peculiar velocities (even at high redshift).* MNRAS, **442**(2) (2014), 1117. 1405.0105.

Dawson, K.S., Schlegel, D.J., Ahn, C.P., et al. *The Baryon Oscillation Spectroscopic Survey of SDSS-III.* AJ, **145**(1) (2013), 10. 1208.0022.

de Jong, J.T.A., Kuijken, K., Applegate, D., et al. *The Kilo-Degree Survey.* The Messenger, **154** (2013), 44.

de Jong, R.S., Agertz, O., Berbel, A.A., et al. *4MOST: Project overview and information for the First Call for Proposals.* The Messenger, **175** (2019), 3. 1903.02464.

De Looze, I., Cormier, D., Lebouteiller, V., et al. *The applicability of far-infrared fine-structure lines as star formation rate tracers over wide ranges of metallicities and galaxy types.* A&A, **568** (2014), A62. 1402.4075.

Decarli, R., Walter, F., Venemans, B.P., et al. *An ALMA [C II] Survey of 27 Quasars at z5.94.* ApJ, **854** (2018), 97. 1801.02641.

Deffayet, C., Pujolàs, O., Sawicki, I., et al. *Imperfect dark energy from kinetic gravity braiding.* J. Cosmology Astropart. Phys., **2010**(10) (2010), 026. 1008.0048.

DES Collaboration, Abbott, T., Aguena, M., et al. *Dark Energy Survey Year 1 Results: Cosmological Constraints from Cluster Abundances and Weak Lensing.* arXiv e-prints (2020), arXiv:2002.11124. 2002.11124.

DESI Collaboration, Aghamousa, A., Aguilar, J., et al. *The DESI Experiment Part I: Science,Targeting, and Survey Design.* arXiv e-prints (2016), arXiv:1611.00036. 1611.00036.

Despali, G., Giocoli, C., Angulo, R.E., et al. *The universality of the virial halo mass function and models for non-universality of other halo definitions.* MNRAS, **456**(3) (2016), 2486. 1507.05627.

Dewdney, P.E., Hall, P.J., Schilizzi, R.T., et al. *The Square Kilometre Array.* IEEE Proceedings, **97**(8) (2009), 1482.

Dey, A., Graham, J.R., Ivison, R.J., et al. *Observations of a Z = 1.44 Dusty, Ultraluminous Galaxy and Implications for Deep Submillimeter Surveys.* ApJ, **519**(2) (1999), 610. astro-ph/9902044.

Dey, A., Schlegel, D.J., Lang, D., et al. *Overview of the DESI Legacy Imaging Surveys.* AJ, **157**(5) (2019), 168. 1804.08657.

Di Valentino, E., Holz, D.E., Melchiorri, A.r., et al. *Cosmological impact of future constraints on H_0 from gravitational-wave standard sirens.* Phys. Rev. D, **98**(8) (2018), 083523. 1806.07463.

Di Valentino, E., Melchiorri, A., Linder, E.V., et al. *Constraining dark energy dynamics in extended parameter space.* Phys. Rev. D, **96**(2) (2017), 023523. 1704.00762.

Di Valentino, E., Melchiorri, A., Mena, O., et al. *Interacting dark energy in the early 2020s: A promising solution to the H_0 and cosmic shear tensions.* Physics of the Dark Universe, **30** (2020a), 100666. 1908.04281.

Di Valentino, E., Melchiorri, A., Silk, J. *Reconciling Planck with the local value of H_0 in extended parameter space.* Physics Letters B, **761** (2016), 242. 1606.00634.

Di Valentino, E., Melchiorri, A., Silk, J. *Planck evidence for a closed Universe and a possible crisis for cosmology.* Nature Astronomy, **4** (2020b), 196. 1911.02087.

Diemer, B. *COLOSSUS: A Python Toolkit for Cosmology, Large-scale Structure, and Dark Matter Halos.* ApJS, **239**(2) (2018), 35. 1712.04512.

D'Isanto, A., Polsterer, K.L. *Photometric redshift estimation via deep learning. Generalized and pre-classification-less, image based, fully probabilistic redshifts.* A&A, **609** (2018), A111. 1706.02467.

Domínguez, A., Wojtak, R., Finke, J., et al. *A New Measurement of the Hubble Constant and Matter Content of the Universe Using Extragalactic Background Light γ-Ray Attenuation.* ApJ, **885**(2) (2019), 137. 1903.12097.

Dudzevičiūtė, U., Smail, I., Swinbank, A.M., et al. *An ALMA survey of the SCUBA-2 CLS UDS field: physical properties of 707 sub-millimetre galaxies.* MNRAS, **494**(3) (2020), 3828. 1910.07524.

Dunsby, P., Goheer, N., Osano, B., et al. *How close can an inhomogeneous universe mimic the concordance model?* J. Cosmology Astropart. Phys., **6** (2010), 017. 1002.2397.

Durret, F., Adami, C., Cappi, A., et al. *Galaxy cluster searches based on photometric redshifts in the four CFHTLS Wide fields.* A&A, **535** (2011), A65. 1109.0850.

Ebeling, H., Edge, A.C., Bohringer, H., et al. *The ROSAT Brightest Cluster Sample - I. The compilation of the sample and the cluster log N-log S distribution.* MNRAS, **301** (1998), 881. astro-ph/9812394.

Ebeling, H., Edge, A.C., Burgett, W.S., et al. *X-ray selected galaxy clusters in the Pan-STARRS Medium Deep Survey.* MNRAS, **432** (2013), 62. 1303.0555.

Ebeling, H., Edge, A.C., Mantz, A., et al. *The X-ray brightest clusters of galaxies from the Massive Cluster Survey.* MNRAS, **407**(1) (2010), 83. 1004.4683.

eBOSS Collaboration, Alam, S., Aubert, M., et al. *The Completed SDSS-IV extended Baryon Oscillation Spectroscopic Survey: Cosmological Implications from two Decades of Spectroscopic Surveys at the Apache Point observatory.* arXiv e-prints (2020), arXiv:2007.08991. 2007.08991.

Einstein, A. *Die Grundlage der allgemeinen Relativitätstheorie.* Annalen der Physik, **354**(7) (1916), 769.

Einstein, A. *Kosmologische Betrachtungen zur allgemeinen Relativitätstheorie.* Sitzungsberichte der Königlich Preußischen Akademie der Wissenschaften (Berlin (1917), 142.

Eisenstein, D.J., Annis, J., Gunn, J.E., et al. *Spectroscopic Target Selection for the Sloan Digital Sky Survey: The Luminous Red Galaxy Sample.* AJ, **122** (2001), 2267. astro-ph/0108153.

Eisenstein, D.J., Weinberg, D.H., Agol, E., et al. *SDSS-III: Massive Spectroscopic Surveys of the Distant Universe, the Milky Way, and Extra-Solar Planetary Systems.* AJ, **142**(3) (2011), 72. 1101.1529.

Eke, V.R., Baugh, C.M., Cole, S., et al. *Galaxy groups in the 2dFGRS: the group-finding algorithm and the 2PIGG catalogue.* MNRAS, **348**(3) (2004), 866. astro-ph/0402567.

Eltvedt, A., Ansarinejad, B., Tom, S., et al. *The VST ATLAS Quasar Catalogue* (in prep.).

Evrard, A.E. *The intracluster gas fraction in X-ray clusters - Constraints on the clustered mass density.* MNRAS, **292** (1997), 289. astro-ph/9701148.

Fang, W., Kadota, K., Takada, M. *Cross-correlating the thermal Sunyaev-Zel'dovich effect and the distribution of galaxy clusters.* Phys. Rev. D, **85**(2) (2012), 023007. 1109.4934.

Fine, S., Shanks, T., Green, P., et al. *Stacked reverberation mapping.* MNRAS, **434** (2013), L16. 1305.1803.

Finoguenov, A., Rykoff, E., Clerc, N., et al. *CODEX clusters. Survey, catalog, and cosmology of the X-ray luminosity function.* A&A, **638** (2020), A114. 1912.03262.

Fixsen, D.J. *The Temperature of the Cosmic Microwave Background.* ApJ, **707**(2) (2009), 916. 0911.1955.

Fosalba, P., Gaztañaga, E. *Measurement of the gravitational potential evolution from the cross-correlation between WMAP and the APM Galaxy Survey.* MNRAS, **350** (2004), L37. astro-ph/0305468.

Fosalba, P., Gaztañaga, E., Castander, F.J. *Detection of the Integrated Sachs-Wolfe and Sunyaev-Zeldovich Effects from the Cosmic Microwave Background-Galaxy Correlation.* ApJ, **597** (2003), L89. astro-ph/0307249.

Fowler, J.W., Niemack, M.D., Dicker, S.R., et al. *Optical design of the Atacama Cosmology Telescope and the Millimeter Bolometric Array Camera.* Appl. Opt., **46** (2007), 3444. astro-ph/0701020.

Francis, C.L., Peacock, J.A. *Integrated Sachs-Wolfe measurements with photometric redshift surveys: 2MASS results and future prospects.* MNRAS, **406** (2010), 2. 0909.2494.

Freedman, W.L., Madore, B.F., Hatt, D., et al. *The Carnegie-Chicago Hubble Program. VIII. An Independent Determination of the Hubble Constant Based on the Tip of the Red Giant Branch.* ApJ, **882**(1) (2019), 34. 1907.05922.

Friedmann, A. *Über die Krümmung des Raumes.* Zeitschrift fur Physik, **10** (1922), 377.

Friedmann, A. *On the Curvature of Space.* General Relativity and Gravitation, **31** (1999), 1991.

Fujimoto, S., Ouchi, M., Ferrara, A., et al. *First Identification of 10 kpc [C II] 158 μm Halos around Star-forming Galaxies at z = 57.* ApJ, **887**(2) (2019), 107. 1902.06760.

Fujimoto, S., Silverman, J.D., Bethermin, M., et al. *The ALPINE-ALMA [C II] Survey: Size of Individual Star-forming Galaxies at z = 4-6 and Their Extended Halo Structure.* ApJ, **900**(1) (2020), 1. 2003.00013.

Gaia Collaboration, Brown, A.G.A., Vallenari, A., et al. *Gaia Data Release 2. Summary of the contents and survey properties.* A&A, **616** (2018), A1. 1804.09365.

Gal, R.R., de Carvalho, R.R., Lopes, P.A.A., et al. *The Northern Sky Optical Cluster Survey. II. An Objective Cluster Catalog for 5800 Square Degrees.* AJ, **125** (2003), 2064. astro-ph/0301274.

Gardner, J.P., Mather, J.C., Clampin, M., et al. *The James Webb Space Telescope.* Space Sci. Rev., **123**(4) (2006), 485. astro-ph/0606175.

Garriga, J., Vilenkin, A. *Solutions to the cosmological constant problems.* Phys. Rev. D, **64**(2) (2001), 023517. hep-th/0011262.

Giannantonio, T., Crittenden, R., Nichol, R., et al. *The significance of the integrated Sachs-Wolfe effect revisited.* MNRAS, **426** (2012), 2581. 1209.2125.

Giannantonio, T., Crittenden, R.G., Nichol, R.C., et al. *High redshift detection of the integrated Sachs-Wolfe effect.* Phys. Rev. D, **74**(6) (2006), 063520. astro-ph/0607572.

Giannantonio, T., Scranton, R., Crittenden, R.G., et al. *Combined analysis of the integrated Sachs-Wolfe effect and cosmological implications.* Phys. Rev. D, **77**(12) (2008), 123520. 0801.4380.

Girardi, M., Manzato, P., Mezzetti, M., et al. *Observational Mass-to-Light Ratio of Galaxy Systems from Poor Groups to Rich Clusters.* ApJ, **569**(2) (2002), 720. astro-ph/0112534.

Gladders, M.D., Yee, H.K.C. *A New Method For Galaxy Cluster Detection. I. The Algorithm.* AJ, **120** (2000), 2148. astro-ph/0004092.

Gladders, M.D., Yee, H.K.C., Majumdar, S., et al. *Cosmological Constraints from the Red-Sequence Cluster Survey.* ApJ, **655** (2007), 128. astro-ph/0603588.

González-Solares, E.A., Walton, N.A., Greimel, R., et al. *Initial data release from the INT Photometric Hα Survey of the Northern Galactic Plane (IPHAS).* MNRAS, **388** (2008), 89. 0712.0384.

Górski, K.M., Hivon, E., Banday, A.J., et al. *HEALPix: A Framework for High-Resolution Discretization and Fast Analysis of Data Distributed on the Sphere.* ApJ, **622** (2005), 759. astro-ph/0409513.

Goto, T., Szapudi, I., Granett, B.R. *Cross-correlation of WISE galaxies with the cosmic microwave background.* MNRAS, **422** (2012), L77. 1202.5306.

Granett, B.R., Kovács, A., Hawken, A.J. *The integrated Sachs-Wolfe signal from BOSS superstructures.* MNRAS, **454** (2015), 2804. 1507.03914.

Granett, B.R., Neyrinck, M.C., Szapudi, I. *Dark Energy Detected with Supervoids and Superclusters.* ArXiv e-prints (2008). 0805.2974.

Granett, B.R., Neyrinck, M.C., Szapudi, I. *A Map of the Integrated Sachs-Wolfe Signal from Luminous Red Galaxies.* ApJ, **701** (2009), 414. 0812.1025.

Gray, A.G., Moore, A.W., Nichol, R.C., et al. *Multi-Tree Methods for Statistics on Very Large Datasets in Astronomy.* In F. Ochsenbein, M.G. Allen, D. Egret, editors, *Astronomical Data Analysis Software and Systems (ADASS) XIII*, volume 314 of *Astronomical Society of the Pacific Conference Series* (2004), page 249. astro-ph/0401121.

Gullberg, B., Smail, I., Swinbank, A.M., et al. *An ALMA survey of the SCUBA-2 Cosmology Legacy Survey UKIDSS/UDS field: high-resolution dust continuum morphologies and the link between sub-millimetre galaxies and spheroid formation.* MNRAS, **490**(4) (2019), 4956. 1910.01121.

Gunn, J.E., Oke, J.B. *Spectrophotometry of faint cluster galaxies and the Hubble diagram - an approach to cosmology.* ApJ, **195** (1975), 255.

Gupta, N., Reichardt, C.L. *Mass Estimation of Galaxy Clusters with Deep Learning II: CMB Cluster Lensing.* arXiv e-prints (2020), arXiv:2005.13985. 2005.13985.

Hansen, S.M., McKay, T.A., Wechsler, R.H., et al. *Measurement of Galaxy Cluster Sizes, Radial Profiles, and Luminosity Functions from SDSS Photometric Data.* ApJ, **633**(1) (2005), 122. astro-ph/0410467.

Hao, J., McKay, T.A., Koester, B.P., et al. *A GMBCG Galaxy Cluster Catalog of 55,424 Rich Clusters from SDSS DR7.* ApJS, **191** (2010), 254. 1010.5503.

Hasselfield, M., Hilton, M., Marriage, T.A., et al. *The Atacama Cosmology Telescope: Sunyaev-Zel'dovich selected galaxy clusters at 148 GHz from three seasons of data.* J. Cosmology Astropart. Phys., **7** (2013), 008. 1301.0816.

Henning, J.W., Sayre, J.T., Reichardt, C.L., et al. *Measurements of the Temperature and E-mode Polarization of the CMB from 500 Square Degrees of SPTpol Data.* ApJ, **852**(2) (2018), 97. 1707.09353.

Heymans, C., Tröster, T., Asgari, M., et al. *KiDS-1000 Cosmology: Multi-probe weak gravitational lensing and spectroscopic galaxy clustering constraints.* arXiv e-prints (2020), arXiv:2007.15632. 2007.15632.

Heywood, I., Bielby, R.M., Hill, M.D., et al. *Sub-millimetre source identifications and the microjansky source population at 8.4 GHz in the William Herschel Deep Field.* MNRAS, **428**(2) (2013), 935. 1209.4660.

Hezaveh, Y.D., Perreault Levasseur, L., Marshall, P.J. *Fast automated analysis of strong gravitational lenses with convolutional neural networks.* Nature, **548**(7669) (2017), 555. 1708.08842.

Hildebrandt, H., Viola, M., Heymans, C., et al. *KiDS-450: cosmological parameter constraints from tomographic weak gravitational lensing.* MNRAS, **465**(2) (2017), 1454. 1606.05338.

Hill, M.D., Shanks, T. *The contribution of AGN to the submillimetre population.* MNRAS, **410**(2) (2011), 762. 1007.1659.

Hilton, M., Sifón, C., Naess, S., et al. *The Atacama Cosmology Telescope: A Catalog of > 4000 Sunyaev-Zel'dovich Galaxy Clusters.* arXiv e-prints (2020), arXiv:2009.11043. 2009.11043.

Hinshaw, G., Larson, D., Komatsu, E., et al. *Nine-year Wilkinson Microwave Anisotropy Probe (WMAP) Observations: Cosmological Parameter Results.* ApJS, **208**(2) (2013), 19. 1212.5226.

Hinton, S.R., Davis, T.M., Lidman, C., et al. *MARZ: Manual and automatic redshifting software.* Astronomy and Computing, **15** (2016), 61. 1603.09438.

Ho, S., Hirata, C., Padmanabhan, N., et al. *Correlation of CMB with large-scale structure. I. Integrated Sachs-Wolfe tomography and cosmological implications.* Phys. Rev. D, **78**(4) (2008), 043519. 0801.0642.

Hodge, J.A., Karim, A., Smail, I., et al. *An ALMA Survey of Submillimeter Galaxies in the Extended Chandra Deep Field South: Source Catalog and Multiplicity.* ApJ, **768**(1) (2013), 91. 1304.4266.

Hodge, J.A., Smail, I., Walter, F., et al. *ALMA Reveals Potential Evidence for Spiral Arms, Bars, and Rings in High-redshift Submillimeter Galaxies.* ApJ, **876**(2) (2019), 130. 1810.12307.

Hodge, J.A., Swinbank, A.M., Simpson, J.M., et al. *Kiloparsec-scale Dust Disks in High-redshift Luminous Submillimeter Galaxies.* ApJ, **833**(1) (2016), 103. 1609.09649.

Hoekstra, H., Bartelmann, M., Dahle, H., et al. *Masses of Galaxy Clusters from Gravitational Lensing.* Space Sci. Rev., **177** (2013), 75. 1303.3274.

Hoekstra, H., Herbonnet, R., Muzzin, A., et al. *The Canadian Cluster Comparison Project: detailed study of systematics and updated weak lensing masses.* MNRAS, **449**(1) (2015), 685. 1502.01883.

Høg, E., Fabricius, C., Makarov, V.V., et al. *The Tycho-2 catalogue of the 2.5 million brightest stars.* A&A, **355** (2000), L27.

Hogg, D.W. *Distance measures in cosmology.* arXiv e-prints (1999), astro-ph/9905116. astro-ph/9905116.

Holland, W.S., Robson, E.I., Gear, W.K., et al. *SCUBA: a common-user submillimetre camera operating on the James Clerk Maxwell Telescope.* MNRAS, **303**(4) (1999), 659. astro-ph/9809122.

Hopkins, P.F., Murray, N., Quataert, E., et al. *A maximum stellar surface density in dense stellar systems.* MNRAS, **401**(1) (2010), L19. 0908.4088.

Huang, X., Storfer, C., Ravi, V., et al. *Finding Strong Gravitational Lenses in the DESI DECam Legacy Survey.* ApJ, **894**(1) (2020), 78. 1906.00970.

Hubble, E. *A Relation between Distance and Radial Velocity among Extra-Galactic Nebulae.* Proceedings of the National Academy of Science, **15**(3) (1929), 168.

Hubble, E.P. *Cepheids in Spiral Nebulae.* Popular Astronomy, **33** (1925), 252.

Hughes, D.H., Serjeant, S., Dunlop, J., et al. *High-redshift star formation in the Hubble Deep Field revealed by a submillimetre-wavelength survey.* Nature, **394**(6690) (1998), 241. astro-ph/9806297.

Hunter, J.D. *Matplotlib: A 2D Graphics Environment.* Computing in Science and Engineering, **9**(3) (2007), 90.

Huterer, D., Kirkby, D., Bean, R., et al. *Growth of cosmic structure: Probing dark energy beyond expansion.* Astroparticle Physics, **63** (2015), 23. 1309.5385.

Ivezić, Ž., Kahn, S.M., Tyson, J.A., et al. *LSST: From Science Drivers to Reference Design and Anticipated Data Products.* ApJ, **873** (2019), 111. 0805.2366.

Jacobs, C., Glazebrook, K., Collett, T., et al. *Finding strong lenses in CFHTLS using convolutional neural networks.* MNRAS, **471**(1) (2017), 167. 1704.02744.

Jenkins, A., Frenk, C.S., White, S.D.M., et al. *The mass function of dark matter haloes.* MNRAS, **321**(2) (2001), 372. astro-ph/0005260.

Johnson, S.P., Wilson, G.W., Wang, Q.D., et al. *X-ray detections of submillimetre galaxies: active galactic nuclei versus starburst contribution.* MNRAS, **431**(1) (2013), 662. 1302.0842.

Kaiser, N., Aussel, H., Burke, B.E., et al. *Pan-STARRS: A Large Synoptic Survey Telescope Array.* In J.A. Tyson, S. Wolff, editors, *Survey and Other Telescope Technologies and Discoveries*, volume 4836 of Proc. SPIE (2002), pages 154–164.

Kennicutt, R.C., Evans, N.J. *Star Formation in the Milky Way and Nearby Galaxies.* ARA&A, **50** (2012), 531. 1204.3552.

Kimura, R., Kobayashi, T., Yamamoto, K. *Observational constraints on kinetic gravity braiding from the integrated Sachs-Wolfe effect.* Phys. Rev. D, **85**(12) (2012), 123503. 1110.3598.

Knudsen, K.K., Richard, J., Kneib, J.P., et al. *[C II] emission in $z \sim 6$ strongly lensed, star-forming galaxies.* MNRAS, **462**(1) (2016), L6. 1603.02277.

Koester, B.P., McKay, T.A., Annis, J., et al. *A MaxBCG Catalog of 13,823 Galaxy Clusters from the Sloan Digital Sky Survey.* ApJ, **660** (2007), 239. astro-ph/0701265.

Kovács, A., Sánchez, C., García-Bellido, J., et al. *Imprint of DES superstructures on the cosmic microwave background.* MNRAS, **465** (2017), 4166. 1610.00637.

Kovács, A., Szapudi, I., Granett, B.R., et al. *Cross-correlation of WMAP7 and the WISE full data release.* MNRAS, **431** (2013), L28. 1301.0475.

Kozmanyan, A., Bourdin, H., Mazzotta, P., et al. *Deriving the Hubble constant using Planck and XMM-Newton observations of galaxy clusters.* A&A, **621** (2019), A34. 1809.09560.

Kravtsov, A.V., Borgani, S. *Formation of Galaxy Clusters.* ARA&A, **50** (2012), 353. 1205.5556.

Kravtsov, A.V., Klypin, A.A., Khokhlov, A.M. *Adaptive Refinement Tree: A New High-Resolution N-Body Code for Cosmological Simulations.* ApJS, **111**(1) (1997), 73. astro-ph/9701195.

Kreisch, C.D., Cyr-Racine, F.Y., Doré, O. *Neutrino puzzle: Anomalies, interactions, and cosmological tensions.* Phys. Rev. D, **101**(12) (2020), 123505. 1902.00534.

Kuijken, K. *OmegaCAM: ESO's Newest Imager.* The Messenger, **146** (2011), 8.

Kuraszkiewicz, J.K., Wilkes, B.J., Hooper, E.J., et al. *The Far-Infrared Spectral Energy Distributions of X-Ray-selected Active Galaxies.* ApJ, **590**(1) (2003), 128. astro-ph/0302572.

Lacey, C., Cole, S. *Merger Rates in Hierarchical Models of Galaxy Formation - Part Two - Comparison with N-Body Simulations.* MNRAS, **271** (1994), 676. astro-ph/9402069.

Laird, E.S., Nandra, K., Pope, A., et al. *On the X-ray properties of sub-mm-selected galaxies.* MNRAS, **401**(4) (2010), 2763. 0910.2464.

Landy, S.D., Szalay, A.S. *Bias and variance of angular correlation functions.* ApJ, **412** (1993), 64.

Laureijs, R., Amiaux, J., Arduini, S., et al. *Euclid Definition Study Report.* ArXiv e-prints (2011). 1110.3193.

Lemaître, G. *Un Univers homogène de masse constante et de rayon croissant rendant compte de la vitesse radiale des nébuleuses extra-galactiques.* Annales de la Société Scientifique de Bruxelles, **47** (1927), 49.

Lemaître, G. *Expansion of the universe, A homogeneous universe of constant mass and increasing radius accounting for the radial velocity of extra-galactic nebulae.* MNRAS, **91** (1931), 483.

Lin, Y.T., Mohr, J.J., Gonzalez, A.H., et al. *Evolution of the K-Band Galaxy Cluster Luminosity Function and Scaling Relations.* ApJ, **650**(2) (2006), L99. astro-ph/0609169.

Lin, Y.T., Mohr, J.J., Stanford, S.A. *Near-Infrared Properties of Galaxy Clusters: Luminosity as a Binding Mass Predictor and the State of Cluster Baryons.* ApJ, **591**(2) (2003), 749. astro-ph/0304033.

Liske, J., Baldry, I.K., Driver, S.P., et al. *Galaxy And Mass Assembly (GAMA): end of survey report and data release 2.* MNRAS, **452** (2015), 2087. 1506.08222.

Llinares, C., Mota, D.F. *Shape of Clusters of Galaxies as a Probe of Screening Mechanisms in Modified Gravity.* Physical Review Letters, **110**(15) (2013), 151104. 1205.5775.

Loveday, J., Norberg, P., Baldry, I.K., et al. *Galaxy and Mass Assembly (GAMA): ugriz galaxy luminosity functions.* MNRAS, **420**(2) (2012), 1239. 1111.0166.

LSST Dark Energy Science Collaboration. *Large Synoptic Survey Telescope: Dark Energy Science Collaboration.* ArXiv e-prints (2012). 1211.0310.

Lucey, J.R. *An assessment of the completeness and correctness of the Abell catalogue.* MNRAS, **204** (1983), 33.

Lukić, Z., Heitmann, K., Habib, S., et al. *The Halo Mass Function: High-Redshift Evolution and Universality.* ApJ, **671**(2) (2007), 1160. astro-ph/0702360.

Lumsden, S.L., Nichol, R.C., Collins, C.A., et al. *The Edinburgh-Durham Southern Galaxy Catalogue. IV - The Cluster Catalogue.* MNRAS, **258** (1992), 1.

Maeder, A. *An Alternative to the ΛCDM Model: The Case of Scale Invariance.* ApJ, **834** (2017), 194. 1701.03964.

Maiolino, R., Cox, P., Caselli, P., et al. *First detection of [CII]158 μm at high redshift: vigorous star formation in the early universe.* A&A, **440** (2005), L51. astro-ph/0508064.

Markevitch, M., Gonzalez, A.H., Clowe, D., et al. *Direct Constraints on the Dark Matter Self-Interaction Cross Section from the Merging Galaxy Cluster 1E 0657-56.* ApJ, **606**(2) (2004), 819. astro-ph/0309303.

Marsh, D.J.E. *Axion cosmology.* Phys. Rep., **643** (2016), 1. 1510.07633.

McEwen, J.D., Vielva, P., Hobson, M.P., et al. *Detection of the ISW effect and corresponding dark energy constraints made with directional spherical wavelets.* ArXiv Astrophysics e-prints (2006). astro-ph/0602398.

McMahon, R.G., Banerji, M., Gonzalez, E., et al. *First Scientific Results from the VISTA Hemisphere Survey (VHS).* The Messenger, **154** (2013), 35.

McMullin, J.P., Waters, B., Schiebel, D., et al. *CASA Architecture and Applications*. In R.A. Shaw, F. Hill, D.J. Bell, editors, *Astronomical Data Analysis Software and Systems XVI*, volume 376 of *Astronomical Society of the Pacific Conference Series* (2007), page 127.

Mehrtens, N., Romer, A.K., Hilton, M., et al. *The XMM Cluster Survey: optical analysis methodology and the first data release*. MNRAS, **423** (2012), 1024. 1106.3056.

Menanteau, F., González, J., Juin, J.B., et al. *The Atacama Cosmology Telescope: Physical Properties and Purity of a Galaxy Cluster Sample Selected via the Sunyaev-Zel'dovich Effect*. ApJ, **723** (2010), 1523. 1006.5126.

Merloni, A., Predehl, P., Becker, W., et al. *eROSITA Science Book: Mapping the Structure of the Energetic Universe*. ArXiv e-prints (2012). 1209.3114.

Metcalfe, N., Shanks, T., Weilbacher, P.M., et al. *Galaxy number counts - VI. An H-band survey of the Herschel Deep Field*. MNRAS, **370**(3) (2006), 1257. astro-ph/0509540.

Milkeraitis, M., van Waerbeke, L., Heymans, C., et al. *3D-Matched-Filter galaxy cluster finder - I. Selection functions and CFHTLS Deep clusters*. MNRAS, **406** (2010), 673. 0912.0739.

Morandi, A., Sun, M. *Probing dark energy via galaxy cluster outskirts*. MNRAS, **457** (2016), 3266. 1601.03741.

Murphy, D.N.A., Geach, J.E., Bower, R.G. *ORCA: The Overdense Red-sequence Cluster Algorithm*. MNRAS, **420** (2012), 1861. 1109.3182.

Muzzin, A., Yee, H.K.C., Hall, P.B., et al. *Near-Infrared Properties of Moderate-Redshift Galaxy Clusters. II. Halo Occupation Number, Mass-to-Light Ratios, and* Ω_m. ApJ, **663**(1) (2007), 150. astro-ph/0703369.

Myers, A.D., Outram, P.J., Shanks, T., et al. *The 2dF QSO Redshift Survey - X. Lensing of background QSOs by galaxy groups*. MNRAS, **342**(2) (2003), 467. astro-ph/0211624.

Nadathur, S., Crittenden, R. *A Detection of the Integrated Sachs-Wolfe Imprint of Cosmic Superstructures Using a Matched-filter Approach*. ApJ, **830** (2016), L19. 1608.08638.

Nadathur, S., Hotchkiss, S., Sarkar, S. *The integrated Sachs-Wolfe imprint of cosmic superstructures: a problem for* Λ*CDM*. J. Cosmology Astropart. Phys., **2012**(6) (2012), 042. 1109.4126.

Nagai, D., Kravtsov, A.V., Vikhlinin, A. *Effects of Galaxy Formation on Thermodynamics of the Intracluster Medium.* ApJ, **668**(1) (2007), 1. astro-ph/0703661.

Newton, I. *The Principia: mathematical principles of natural philosophy* (1999).

Nicolis, A., Rattazzi, R., Trincherini, E. *Galileon as a local modification of gravity.* Phys. Rev. D, **79**(6) (2009), 064036. 0811.2197.

Niemiec, A., Jauzac, M., Jullo, E., et al. *hybrid-LENSTOOL: a self-consistent algorithm to model galaxy clusters with strong- and weak-lensing simultaneously.* MNRAS, **493**(3) (2020), 3331. 2002.04635.

Nolta, M.R., Wright, E.L., Page, L., et al. *First Year Wilkinson Microwave Anisotropy Probe Observations: Dark Energy Induced Correlation with Radio Sources.* ApJ, **608** (2004), 10. astro-ph/0305097.

Nozawa, S., Itoh, N., Kawana, Y., et al. *Relativistic Corrections to the Sunyaev-Zeldovich Effect for Clusters of Galaxies. IV. Analytic Fitting Formula for the Numerical Results.* ApJ, **536**(1) (2000), 31. astro-ph/9912008.

Oguri, M., Takada, M. *Combining cluster observables and stacked weak lensing to probe dark energy: Self-calibration of systematic uncertainties.* Phys. Rev. D, **83**(2) (2011), 023008. 1010.0744.

O'Raifeartaigh, C., O'Keeffe, M., Nahm, W., et al. *Einstein's 1917 static model of the universe: a centennial review.* European Physical Journal H, **42**(3) (2017). 1701.07261.

Padmanabhan, N., Hirata, C.M., Seljak, U., et al. *Correlating the CMB with luminous red galaxies: The integrated Sachs-Wolfe effect.* Phys. Rev. D, **72**(4) (2005), 043525. astro-ph/0410360.

Pápai, P., Szapudi, I., Granett, B.R. *Integrated Sachs-Wolfe Imprint of Superstructures on Linear Scales.* ApJ, **732** (2011), 27. 1012.3750.

Peebles, P.J.E. *The large-scale structure of the universe* (1980).

Peebles, P.J.E. *Principles of Physical Cosmology* (1993).

Perez, F., Granger, B.E. *IPython: A System for Interactive Scientific Computing.* Computing in Science and Engineering, **9**(3) (2007), 21.

Piffaretti, R., Arnaud, M., Pratt, G.W., et al. *The MCXC: a meta-catalogue of x-ray detected clusters of galaxies.* A&A, **534** (2011), A109. 1007.1916.

Pillepich, A., Porciani, C., Reiprich, T.H. *The X-ray cluster survey with eRosita: forecasts for cosmology, cluster physics and primordial non-Gaussianity.* MNRAS, **422**(1) (2012), 44. 1111.6587.

Pirard, J.F., Kissler-Patig, M., Moorwood, A., et al. *HAWK-I: A new wide-field 1- to 2.5-μm imager for the VLT.* In A.F.M. Moorwood, M. Iye, editors, *Ground-based Instrumentation for Astronomy*, volume 5492 of *Society of Photo-Optical Instrumentation Engineers (SPIE) Conference Series* (2004), pages 1763–1772.

Planck Collaboration, Abergel, A., Ade, P.A.R., et al. *Planck 2013 results. XI. All-sky model of thermal dust emission.* A&A, **571** (2014a), A11. 1312.1300.

Planck Collaboration, Adam, R., Ade, P.A.R., et al. *Planck 2015 results. IX. Diffuse component separation: CMB maps.* A&A, **594** (2016a), A9. 1502.05956.

Planck Collaboration, Ade, P.A.R., Aghanim, N., et al. *Planck early results. VIII. The all-sky early Sunyaev-Zeldovich cluster sample.* A&A, **536** (2011), A8. 1101.2024.

Planck Collaboration, Ade, P.A.R., Aghanim, N., et al. *Planck 2013 results. XV. CMB power spectra and likelihood.* A&A, **571** (2014b), A15. 1303.5075.

Planck Collaboration, Ade, P.A.R., Aghanim, N., et al. *Planck 2013 results. XX. Cosmology from Sunyaev-Zeldovich cluster counts.* A&A, **571** (2014c), A20. 1303.5080.

Planck Collaboration, Ade, P.A.R., Aghanim, N., et al. *Planck 2013 results. XXIX. The Planck catalogue of Sunyaev-Zeldovich sources.* A&A, **571** (2014d), A29. 1303.5089.

Planck Collaboration, Ade, P.A.R., Aghanim, N., et al. *Planck 2015 results. XIII. Cosmological parameters.* A&A, **594** (2016b), A13. 1502.01589.

Planck Collaboration, Ade, P.A.R., Aghanim, N., et al. *Planck 2015 results. XXI. The integrated Sachs-Wolfe effect.* A&A, **594** (2016c), A21. 1502.01595.

Planck Collaboration, Ade, P.A.R., Aghanim, N., et al. *Planck 2015 results. XXIV. Cosmology from Sunyaev-Zeldovich cluster counts.* A&A, **594** (2016d), A24. 1502.01597.

Planck Collaboration, Ade, P.A.R., Aghanim, N., et al. *Planck 2015 results. XXVII. The second Planck catalogue of Sunyaev-Zeldovich sources.* A&A, **594** (2016e), A27. 1502.01598.

Planck Collaboration, Aghanim, N., Akrami, Y., et al. *Planck 2018 results. VI. Cosmological parameters.* A&A, **641** (2020), A6. 1807.06209.

Planck Collaboration, Aghanim, N., Arnaud, M., et al. *Planck 2015 results. XI. CMB power spectra, likelihoods, and robustness of parameters.* A&A, **594** (2016f), A11. 1507.02704.

Planck Collaboration, Akrami, Y., Ashdown, M., et al. *Planck 2018 results. IV. Diffuse component separation.* arXiv e-prints (2018), arXiv:1807.06208. 1807.06208.

Polletta, M., Tajer, M., Maraschi, L., et al. *Spectral Energy Distributions of Hard X-Ray Selected Active Galactic Nuclei in the XMM-Newton Medium Deep Survey.* ApJ, **663**(1) (2007), 81. astro-ph/0703255.

Popesso, P., Biviano, A., Böhringer, H., et al. *RASS-SDSS galaxy cluster survey. VII. On the cluster mass-to-light ratio and the halo occupation distribution.* A&A, **464**(2) (2007), 451. astro-ph/0606260.

Postman, M., Huchra, J.P., Geller, M.J. *The distribution of nearby rich clusters of galaxies.* ApJ, **384** (1992), 404.

Postman, M., Lauer, T.R. *Brightest cluster galaxies as standard candles.* ApJ, **440** (1995), 28.

Prakash, A., Licquia, T.C., Newman, J.A., et al. *The SDSS-IV Extended Baryon Oscillation Spectroscopic Survey: Luminous Red Galaxy Target Selection.* ApJS, **224**(2) (2016), 34. 1508.04478.

Press, W.H., Schechter, P. *Formation of Galaxies and Clusters of Galaxies by Self-Similar Gravitational Condensation.* ApJ, **187** (1974), 425.

Price-Whelan, A.M., Sipőcz, B.M., Günther, H.M., et al. *The Astropy Project: Building an Open-science Project and Status of the v2.0 Core Package.* AJ, **156** (2018), 123.

Raccanelli, A., Bonaldi, A., Negrello, M., et al. *A reassessment of the evidence of the Integrated Sachs-Wolfe effect through the WMAP-NVSS correlation.* MNRAS, **386** (2008), 2161. 0802.0084.

Rácz, G., Dobos, L., Beck, R., et al. *Concordance cosmology without dark energy.* MNRAS, **469** (2017), L1. 1607.08797.

Radovich, M., Puddu, E., Bellagamba, F., et al. *Searching for galaxy clusters in the Kilo-Degree Survey.* A&A, **598** (2017), A107. 1701.02954.

Raghunathan, S., Patil, S., Baxter, E.J., et al. *Measuring galaxy cluster masses with CMB lensing using a Maximum Likelihood estimator: statistical and systematic error budgets for future experiments.* J. Cosmology Astropart. Phys., **2017**(8) (2017), 030. 1705.00411.

Ramella, M., Boschin, W., Fadda, D., et al. *Finding galaxy clusters using Voronoi tessellations.* A&A, **368** (2001), 776. astro-ph/0101411.

Rassat, A., Land, K., Lahav, O., et al. *Cross-correlation of 2MASS and WMAP 3: implications for the integrated Sachs-Wolfe effect.* MNRAS, **377** (2007), 1085. astro-ph/0610911.

Reed, D., Gardner, J., Quinn, T., et al. *Evolution of the mass function of dark matter haloes.* MNRAS, **346**(2) (2003), 565. astro-ph/0301270.

Reed, D.S., Bower, R., Frenk, C.S., et al. *The halo mass function from the dark ages through the present day.* MNRAS, **374**(1) (2007), 2. astro-ph/0607150.

Reichardt, C.L., Stalder, B., Bleem, L.E., et al. *Galaxy Clusters Discovered via the Sunyaev-Zel'dovich Effect in the First 720 Square Degrees of the South Pole Telescope Survey.* ApJ, **763** (2013), 127. 1203.5775.

Reid, B., Ho, S., Padmanabhan, N., et al. *SDSS-III Baryon Oscillation Spectroscopic Survey Data Release 12: galaxy target selection and large-scale structure catalogues.* MNRAS, **455**(2) (2016), 1553. 1509.06529.

Reid, M.J., Pesce, D.W., Riess, A.G. *An Improved Distance to NGC 4258 and Its Implications for the Hubble Constant.* ApJ, **886**(2) (2019), L27. 1908.05625.

Reiprich, T.H., Böhringer, H. *The Mass Function of an X-Ray Flux-limited Sample of Galaxy Clusters.* ApJ, **567** (2002), 716. astro-ph/0111285.

Reyes, R., Mandelbaum, R., Hirata, C., et al. *Improved optical mass tracer for galaxy clusters calibrated using weak lensing measurements.* MNRAS, **390**(3) (2008), 1157. 0802.2365.

Richard, J., Kneib, J.P., Blake, C., et al. *4MOST Consortium Survey 8: Cosmology Redshift Survey (CRS).* The Messenger, **175** (2019), 50. 1903.02474.

Riess, A.G., Casertano, S., Yuan, W., et al. *Milky Way Cepheid Standards for Measuring Cosmic Distances and Application to Gaia DR2: Implications for the Hubble Constant.* ApJ, **861**(2) (2018), 126. 1804.10655.

Riess, A.G., Casertano, S., Yuan, W., et al. *Large Magellanic Cloud Cepheid Standards Provide a 1% Foundation for the Determination of the Hubble Constant and Stronger Evidence for Physics beyond ΛCDM.* ApJ, **876**(1) (2019), 85. 1903.07603.

Riess, A.G., Filippenko, A.V., Challis, P., et al. *Observational Evidence from Supernovae for an Accelerating Universe and a Cosmological Constant.* AJ, **116** (1998), 1009. astro-ph/9805201.

Riess, A.G., Macri, L.M., Hoffmann, S.L., et al. *A 2.4% Determination of the Local Value of the Hubble Constant.* ApJ, **826**(1) (2016), 56. 1604.01424.

Rigault, M., Aldering, G., Kowalski, M., et al. *Confirmation of a Star Formation Bias in Type Ia Supernova Distances and its Effect on the Measurement of the Hubble Constant.* ApJ, **802**(1) (2015), 20. 1412.6501.

Rines, K., Geller, M.J., Diaferio, A., et al. *CAIRNS: The Cluster and Infall Region Nearby Survey. II. Environmental Dependence of Infrared Mass-to-Light Ratios.* AJ, **128**(3) (2004), 1078. astro-ph/0402242.

Risaliti, G., Lusso, E. *Cosmological Constraints from the Hubble Diagram of Quasars at High Redshifts.* Nature Astronomy, **3** (2019), 272. 1811.02590.

Robertson, H.P. *Kinematics and World-Structure.* ApJ, **82** (1935), 284.

Roncarelli, M., Carbone, C., Moscardini, L. *The effect of massive neutrinos on the Sunyaev-Zel'dovich and X-ray observables of galaxy clusters.* MNRAS, **447** (2015), 1761. 1409.4285.

Rosati, P., Borgani, S., Norman, C. *The Evolution of X-ray Clusters of Galaxies.* ARA&A, **40** (2002), 539. astro-ph/0209035.

Rose, B.M., Garnavich, P.M., Berg, M.A. *Think Global, Act Local: The Influence of Environment Age and Host Mass on Type Ia Supernova Light Curves.* ApJ, **874**(1) (2019), 32. 1902.01433.

Ross, A.J., Beutler, F., Chuang, C.H., et al. *The clustering of galaxies in the completed SDSS-III Baryon Oscillation Spectroscopic Survey: observational systematics and baryon acoustic oscillations in the correlation function.* MNRAS, **464**(1) (2017), 1168. 1607.03145.

Ross, A.J., Percival, W.J., Sánchez, A.G., et al. *The clustering of galaxies in the SDSS-III Baryon Oscillation Spectroscopic Survey: analysis of potential systematics.* MNRAS, **424**(1) (2012), 564. 1203.6499.

Ross, A.J., Samushia, L., Howlett, C., et al. *The clustering of the SDSS DR7 main Galaxy sample - I. A 4 per cent distance measure at z = 0.15.* MNRAS, **449**(1) (2015), 835. 1409.3242.

Ross, N.P., Shanks, T., Cannon, R.D., et al. *Luminous red galaxy clustering at z ˜= 0.7 - first results using AAOmega.* MNRAS, **387** (2008), 1323. 0704.3739.

Rubin, V.C., Ford, W. K., J., Thonnard, N. *Extended rotation curves of high-luminosity spiral galaxies. IV. Systematic dynamical properties, Sa -> Sc.* ApJ, **225** (1978), L107.

Ruel, J., Bazin, G., Bayliss, M., et al. *Optical Spectroscopy and Velocity Dispersions of Galaxy Clusters from the SPT-SZ Survey.* ApJ, **792**(1) (2014), 45. 1311.4953.

Rykoff, E.S., Rozo, E., Busha, M.T., et al. *redMaPPer. I. Algorithm and SDSS DR8 Catalog.* ApJ, **785** (2014), 104. 1303.3562.

Rykoff, E.S., Rozo, E., Hollowood, D., et al. *The RedMaPPer Galaxy Cluster Catalog From DES Science Verification Data.* ApJS, **224** (2016), 1. 1601.00621.

Sachs, R.K., Wolfe, A.M. *Perturbations of a Cosmological Model and Angular Variations of the Microwave Background.* ApJ, **147** (1967), 73.

Sadeh, I., Abdalla, F.B., Lahav, O. *ANNz2: Photometric Redshift and Probability Distribution Function Estimation using Machine Learning.* PASP, **128**(10) (2016), 104502. 1507.00490.

Sahni, V. *The cosmological constant problem and quintessence.* Classical and Quantum Gravity, **19**(13) (2002), 3435. astro-ph/0202076.

Sanchez, A.G. *Let us bury the prehistoric h: arguments against using* h^{-1}Mpc *units in observational cosmology.* arXiv e-prints (2020), arXiv:2002.07829. 2002.07829.

Saro, A., Mohr, J.J., Bazin, G., et al. *Toward Unbiased Galaxy Cluster Masses from Line-of-sight Velocity Dispersions.* ApJ, **772**(1) (2013), 47. 1203.5708.

Sawangwit, U., Shanks, T., Abdalla, F.B., et al. *Angular correlation function of 1.5 million luminous red galaxies: clustering evolution and a search for baryon acoustic oscillations.* MNRAS, **416** (2011), 3033. 0912.0511.

Sawangwit, U., Shanks, T., Cannon, R.D., et al. *Cross-correlating WMAP5 with 1.5 million LRGs: a new test for the ISW effect.* MNRAS, **402** (2010), 2228. 0911.1352.

Schechter, P. *An analytic expression for the luminosity function for galaxies.* ApJ, **203** (1976), 297.

Schipani, P., Capaccioli, M., Arcidiacono, C., et al. *VST: from commissioning to science.* In *Ground-based and Airborne Telescopes IV*, volume 8444 of Proc. SPIE (2012), page 84441C.

Schlafly, E.F., Meisner, A.M., Green, G.M. *The unWISE Catalog: Two Billion Infrared Sources from Five Years of WISE Imaging.* ApJS, **240**(2) (2019), 30. 1901.03337.

Schneider, D.P., Hall, P.B., Richards, G.T., et al. *The Sloan Digital Sky Survey Quasar Catalog. IV. Fifth Data Release.* AJ, **134** (2007), 102. 0704.0806.

Schuecker, P., Caldwell, R.R., Böhringer, H., et al. *Observational constraints on general relativistic energy conditions, cosmic matter density and dark energy from X-ray clusters of galaxies and type-Ia supernovae.* A&A, **402** (2003), 53. astro-ph/0211480.

Scranton, R., Connolly, A.J., Nichol, R.C., et al. *Physical Evidence for Dark Energy.* ArXiv Astrophysics e-prints (2003). astro-ph/0307335.

Scranton, R., Ménard, B., Richards, G.T., et al. *Detection of Cosmic Magnification with the Sloan Digital Sky Survey.* ApJ, **633**(2) (2005), 589. astro-ph/0504510.

Sereno, M., Covone, G., Izzo, L., et al. *PSZ2LenS. Weak lensing analysis of the Planck clusters in the CFHTLenS and in the RCSLenS.* MNRAS, **472**(2) (2017), 1946. 1703.06886.

Shanks, T., Ansarinejad, B., Bielby, R.M., et al. *The nature of sub-millimetre galaxies I: A comparison of AGN and star-forming galaxy SED fits* (in prep.).

Shanks, T., Hogarth, L.M., Metcalfe, N. *Gaia Cepheid parallaxes and 'Local Hole' relieve H_0 tension.* MNRAS, **484**(1) (2019), L64. 1810.02595.

Shanks, T., Metcalfe, N., Chehade, B., et al. *The VLT Survey Telescope ATLAS.* MNRAS, **451** (2015), 4238. 1502.05432.

Shapley, H., Curtis, H.D. *The Scale of the Universe.* Bulletin of the National Research Council, **2**(11) (1921), 171.

Sheth, R.K., Tormen, G. *Large-scale bias and the peak background split.* MNRAS, **308**(1) (1999), 119. astro-ph/9901122.

Simet, M., McClintock, T., Mandelbaum, R., et al. *Weak lensing measurement of the mass–richness relation of SDSS redMaPPer clusters.* Monthly Notices of the Royal Astronomical Society, **466**(3) (2016), 3103. ISSN 0035-8711. https://academic.oup.com/mnras/article-pdf/466/3/3103/10903108/stw3250.pdf, URL https://doi.org/10.1093/mnras/stw3250.

Simpson, J.M., Smail, I., Swinbank, A.M., et al. *The SCUBA-2 Cosmology Legacy Survey: ALMA Resolves the Rest-frame Far-infrared Emission of Sub-millimeter Galaxies.* ApJ, **799**(1) (2015), 81. 1411.5025.

Siringo, G., Kreysa, E., Kovács, A., et al. *The Large APEX BOlometer CAmera LABOCA.* A&A, **497**(3) (2009), 945. 0903.1354.

Slipher, V.M. *The radial velocity of the Andromeda Nebula.* Lowell Observatory Bulletin, **1** (1913), 56.

Slipher, V.M. *Spectrographic Observations of Nebulae.* Popular Astronomy, **23** (1915), 21.

Slipher, V.M. *Nebulae.* Proceedings of the American Philosophical Society, **56** (1917), 403.

Smail, I., Ivison, R.J., Blain, A.W. *A Deep Sub-millimeter Survey of Lensing Clusters: A New Window on Galaxy Formation and Evolution.* ApJ, **490**(1) (1997), L5. astro-ph/9708135.

Smail, I., Swinbank, A.M., Richard, J., et al. *A Very Bright, Highly Magnified Lyman Break Galaxy at z = 3.07.* ApJ, **654** (2007), L33. astro-ph/0611486.

Soares-Santos, M., de Carvalho, R.R., Annis, J., et al. *The Voronoi Tessellation Cluster Finder in 2+1 Dimensions.* ApJ, **727** (2011), 45. 1011.3458.

Soares-Santos, M., Palmese, A., Hartley, W., et al. *First Measurement of the Hubble Constant from a Dark Standard Siren using the Dark Energy Survey Galaxies and the LIGO/Virgo Binary-Black-hole Merger GW170814.* ApJ, **876**(1) (2019), L7. 1901.01540.

Sotiriou, T.P., Faraoni, V. *f(R) theories of gravity.* Reviews of Modern Physics, **82**(1) (2010), 451. 0805.1726.

Soucail, G., Foëx, G., Pointecouteau, E., et al. *The matter distribution in z ∼0.5 redshift clusters of galaxies. II. The link between dark and visible matter.* A&A, **581** (2015), A31. 1505.01031.

Springel, V. *The cosmological simulation code GADGET-2.* MNRAS, **364**(4) (2005), 1105. astro-ph/0505010.

Story, K.T., Reichardt, C.L., Hou, Z., et al. *A MEASUREMENT OF THE COSMIC MICROWAVE BACKGROUND DAMPING TAIL FROM THE 2500-SQUARE-DEGREE SPT-SZ SURVEY.* The Astrophysical Journal, **779**(1) (2013), 86. ISSN 1538-4357. URL http://dx.doi.org/10.1088/0004-637X/779/1/86.

Sunyaev, R.A., Zeldovich, I.B. *Microwave background radiation as a probe of the contemporary structure and history of the universe.* ARA&A, **18** (1980), 537.

Sunyaev, R.A., Zeldovich, Y.B. *The Observations of Relic Radiation as a Test of the Nature of X-Ray Radiation from the Clusters of Galaxies.* Comments on Astrophysics and Space Physics, **4** (1972), 173.

Sutherland, W. *The 3-D distribution of Abell clusters.* MNRAS, **234** (1988), 159.

Swinbank, A.M., Smail, I., Longmore, S., et al. *Intense star formation within resolved compact regions in a galaxy at z = 2.3.* Nature, **464** (2010), 733. 1003.3674.

Szabo, T., Pierpaoli, E., Dong, F., et al. *An Optical Catalog of Galaxy Clusters Obtained from an Adaptive Matched Filter Finder Applied to Sloan Digital Sky Survey Data Release 6.* ApJ, **736** (2011), 21. 1011.0249.

Tauber, J.A., Mandolesi, N., Puget, J.L., et al. *Planck pre-launch status: The Planck mission.* A&A, **520** (2010), A1.

Taylor, M.B. *TOPCAT STIL: Starlink Table/VOTable Processing Software.* In P. Shopbell, M. Britton, R. Ebert, editors, *Astronomical Data Analysis Software and Systems XIV*, volume 347 of *Astronomical Society of the Pacific Conference Series* (2005), page 29.

Taylor, M.B. *STILTS - A Package for Command-Line Processing of Tabular Data.* In C. Gabriel, C. Arviset, D. Ponz, S. Enrique, editors, *Astronomical Data Analysis Software and Systems XV*, volume 351 of *Astronomical Society of the Pacific Conference Series* (2006), page 666.

Thanjavur, K., Willis, J., Crampton, D. *K2: A New Method for the Detection of Galaxy Clusters Based on Canada-France-Hawaii Telescope Legacy Survey Multicolor Images.* ApJ, **706** (2009), 571. 0910.4358.

The Dark Energy Survey Collaboration. *The Dark Energy Survey.* ArXiv Astrophysics e-prints (2005). astro-ph/0510346.

The LIGO Scientific Collaboration, the Virgo Collaboration, Abbott, B.P., et al. *A gravitational-wave measurement of the Hubble constant following the second observing run of Advanced LIGO and Virgo.* arXiv e-prints (2019), arXiv:1908.06060. 1908.06060.

Thompson, T.A., Quataert, E., Murray, N. *Radiation Pressure-supported Starburst Disks and Active Galactic Nucleus Fueling.* ApJ, **630**(1) (2005), 167. astro-ph/0503027.

Timlin, J.D., Ross, N.P., Richards, G.T., et al. *SpIES: The Spitzer IRAC Equatorial Survey.* ApJS, **225**(1) (2016), 1. 1603.08488.

Tinker, J., Kravtsov, A.V., Klypin, A., et al. *Toward a Halo Mass Function for Precision Cosmology: The Limits of Universality.* ApJ, **688**(2) (2008), 709. 0803.2706.

Tröster, T., Sánchez, A.G., Asgari, M., et al. *Cosmology from large-scale structure. Constraining ΛCDM with BOSS.* A&A, **633** (2020), L10. 1909.11006.

van Breukelen, C., Clewley, L. *A reliable cluster detection technique using photometric redshifts: introducing the 2TecX algorithm.* MNRAS, **395** (2009), 1845. 0902.4388.

van der Walt, S., Colbert, S.C., Varoquaux, G. *The NumPy Array: A Structure for Efficient Numerical Computation.* Computing in Science and Engineering, **13**(2) (2011), 22. 1102.1523.

Van Rossum, G., Drake, F.L. *Python 3 Reference Manual.* CreateSpace, Scotts Valley, CA (2009). ISBN 1441412697.

Van Rossum, G., Drake Jr, F.L. *Python reference manual.* Centrum voor Wiskunde en Informatica Amsterdam (1995).

Vanderlinde, K., Crawford, T.M., de Haan, T., et al. *Galaxy Clusters Selected with the Sunyaev-Zel'dovich Effect from 2008 South Pole Telescope Observations.* ApJ, **722** (2010), 1180. 1003.0003.

Venemans, B.P., McMahon, R.G., Walter, F., et al. *Detection of Atomic Carbon [C II] 158 μm and Dust Emission from a z = 7.1 Quasar Host Galaxy.* ApJ, **751**(2) (2012), L25. 1203.5844.

Venemans, B.P., Walter, F., Zschaechner, L., et al. *Bright [C II] and Dust Emission in Three $z > 6.6$ Quasar Host Galaxies Observed by ALMA*. ApJ, **816**(1) (2016), 37. 1511.07432.

Verde, L. *Non-Gaussianity from Large-Scale Structure Surveys*. Advances in Astronomy, **2010** (2010), 768675. 1001.5217.

Verde, L., Treu, T., Riess, A.G. *Tensions between the early and late Universe*. Nature Astronomy, **3** (2019), 891. 1907.10625.

Vernet, J., Dekker, H., D'Odorico, S., et al. *X-shooter, the new wide band intermediate resolution spectrograph at the ESO Very Large Telescope*. A&A, **536** (2011), A105. 1110.1944.

Vielva, P., Martínez-González, E., Tucci, M. *Cross-correlation of the cosmic microwave background and radio galaxies in real, harmonic and wavelet spaces: detection of the integrated Sachs-Wolfe effect and dark energy constraints*. MNRAS, **365** (2006), 891. astro-ph/0408252.

Vikhlinin, A., Kravtsov, A.V., Burenin, R.A., et al. *Chandra Cluster Cosmology Project III: Cosmological Parameter Constraints*. ApJ, **692**(2) (2009), 1060. 0812.2720.

Vikram, V., Lidz, A., Jain, B. *A Measurement of the Galaxy Group-Thermal Sunyaev-Zel'dovich Effect Cross-Correlation Function*. MNRAS, **467**(2) (2017), 2315. 1608.04160.

Virtanen, P., Gommers, R., Oliphant, T.E., et al. *SciPy 1.0: Fundamental Algorithms for Scientific Computing in Python*. Nature Methods, **17** (2020), 261.

Voges, W., Aschenbach, B., Boller, T., et al. *The ROSAT all-sky survey bright source catalogue*. A&A, **349** (1999), 389. astro-ph/9909315.

Voit, G.M. *Tracing cosmic evolution with clusters of galaxies*. Reviews of Modern Physics, **77** (2005), 207. astro-ph/0410173.

von der Linden, A., Allen, M.T., Applegate, D.E., et al. *Weighing the Giants - I. Weak-lensing masses for 51 massive galaxy clusters: project overview, data analysis methods and cluster images*. MNRAS, **439**(1) (2014), 2. 1208.0597.

Wainer, H., Thissen, D. . Psychometrika, **41** (1976), 9.

Walker, A.G. *On Milne's Theory of World-Structure*. Proceedings of the London Mathematical Society, **42** (1937), 90.

Walter, F., Riechers, D., Cox, P., et al. *A kiloparsec-scale hyper-starburst in a quasar host less than 1gigayear after the Big Bang.* Nature, **457**(7230) (2009), 699. 0902.0662.

Wang, R., Wagg, J., Carilli, C.L., et al. *Star Formation and Gas Kinematics of Quasar Host Galaxies at z ˜ 6: New Insights from ALMA.* ApJ, **773** (2013), 44. 1302.4154.

Warren, M.S., Abazajian, K., Holz, D.E., et al. *Precision Determination of the Mass Function of Dark Matter Halos.* ApJ, **646**(2) (2006), 881. astro-ph/0506395.

Warren, M.S., Salmon, J.K. *A Parallel Hashed Oct-Tree N-Body Algorithm.* In *Proceedings of the 1993 ACM/IEEE Conference on Supercomputing*, Supercomputing '93. Association for Computing Machinery, New York, NY, USA (1993). ISBN 0818643404, page 12–21. URL https://doi.org/10.1145/169627.169640.

Watson, W.A., Iliev, I.T., D'Aloisio, A., et al. *The halo mass function through the cosmic ages.* MNRAS, **433**(2) (2013), 1230. 1212.0095.

Weinberg, D.H., Mortonson, M.J., Eisenstein, D.J., et al. *Observational probes of cosmic acceleration.* Phys. Rep., **530** (2013), 87. 1201.2434.

Weinberg, S. *Gravitation and Cosmology: Principles and Applications of the General Theory of Relativity* (1972).

Weinberg, S. *The cosmological constant problem.* Reviews of Modern Physics, **61**(1) (1989), 1.

Wen, Z.L., Han, J.L., Liu, F.S. *A Catalog of 132,684 Clusters of Galaxies Identified from Sloan Digital Sky Survey III.* ApJS, **199** (2012), 34. 1202.6424.

Wes McKinney. *Data Structures for Statistical Computing in Python.* In Stéfan van der Walt, Jarrod Millman, editors, *Proceedings of the 9th Python in Science Conference* (2010), pages 56 – 61.

White, S.D.M., Efstathiou, G., Frenk, C.S. *The amplitude of mass fluctuations in the universe.* MNRAS, **262** (1993), 1023.

Willott, C.J., Bergeron, J., Omont, A. *Star Formation Rate and Dynamical Mass of 10^8 Solar Mass Black Hole Host Galaxies At Redshift 6.* ApJ, **801** (2015), 123. 1501.07538.

Willott, C.J., Bergeron, J., Omont, A. *A Wide Dispersion in Star Formation Rate and Dynamical Mass of 10^8 Solar Mass Black Hole Host Galaxies at Redshift 6.* ApJ, **850**(1) (2017), 108. 1710.02212.

Wolf, C., Johnson, A.S., Bilicki, M., et al. *The 2-degree Field Lensing Survey: photometric redshifts from a large new training sample to $r < 19.5$.* MNRAS, **466** (2017), 1582. 1612.00839.

Wong, K.C., Suyu, S.H., Chen, G.C.F., et al. *H0LiCOW XIII. A 2.4% measurement of H_0 from lensed quasars: 5.3σ tension between early and late-Universe probes.* MNRAS(2020). 1907.04869.

Worsley, M.A., Fabian, A.C., Bauer, F.E., et al. *The unresolved hard X-ray background: the missing source population implied by the Chandra and XMM-Newton deep fields.* MNRAS, **357**(4) (2005), 1281. astro-ph/0412266.

Wright, E.L. *A Cosmology Calculator for the World Wide Web.* PASP, **118**(850) (2006), 1711. astro-ph/0609593.

York, D.G., Adelman, J., Anderson, Jr., J.E., et al. *The Sloan Digital Sky Survey: Technical Summary.* AJ, **120** (2000), 1579. astro-ph/0006396.

Yuan, H.B., Liu, X.W., Xiang, M.S. *Empirical extinction coefficients for the GALEX, SDSS, 2MASS and WISE passbands.* MNRAS, **430**(3) (2013), 2188. 1301.1427.

Zhao, G.B., Raveri, M., Pogosian, L., et al. *Dynamical dark energy in light of the latest observations.* Nature Astronomy, **1** (2017), 627. 1701.08165.

Zwicky, F. *Die Rotverschiebung von extragalaktischen Nebeln.* Helvetica Physica Acta, **6** (1933), 110.

Zwicky, F., Herzog, E., Wild, P., et al. *Catalogue of galaxies and of clusters of galaxies, Vol. I* (1961).

Zyla, P.A.P.D.G., Barnett, R.M., Beringer, J., et al. *Review of Particle Physics.* Progress of Theoretical and Experimental Physics, **2020**(8) (2020). ISSN 2050-3911. 083C01, https://academic.oup.com/ptep/article-pdf/2020/8/083C01/33653179/ptaa104.pdf, URL https://doi.org/10.1093/ptep/ptaa104.